30 March 2007 | $10

Science

AAAS

Believe it!

DNA Sequencing for $2.50 per reaction.

- Read length up to 900 bases.
- High quality electropherograms.
- Fast turnaround.
- Plasmid and PCR purification available.

POLYMORPHIC
Polymorphic DNA Technologies, Inc.™

www.polymorphicdna.com
info@polymorphicdna.com

1125 Atlantic Ave., Ste. 102
Alameda, CA 94501

Polymorphic exclusively uses ABI 3730XL sequencers.
Data delivered via secure FTP, email or CD.
No charge for standard sequencing primers.
384 sample minimum order.
96 well plates only—no tubes.

888.362.0888

For more information please visit
www.polymorphicdna.com

MaxPAK™

World's First Competent Mammalian Cells*

Up to 4X Protein Yield Enhancement

- Revolutionary cell culture technology for achieving 4X more cell density
- No cell passaging needed before transfection
- Transfect in 3 hours with less reagent
- Consistent viability and expression results

HEK 293 Passaged

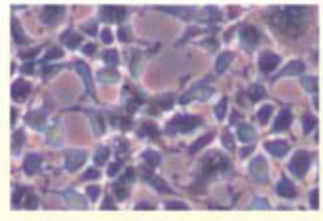

MaxPAK™ HEK 293

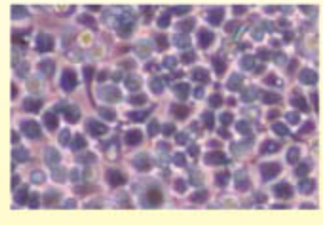

What makes MaxPAK® mammalian cells produce so much more protein?

MaxPAK cells are specially prepared so they can be plated at a 4X higher density than traditional passaged cells while maintaining comparable protein expression per cell. This makes MaxPAX cells ideal for both standard and high-throughput applications. Order today, plate tomorrow to jump start your expression!

Genlantis
a division of Gene Therapy Systems, Inc.

Toll-free: 888-428-0558
Direct: 858-457-1919
For your nearest distributor go to:
www.genlantis.com

MaxPAK® Competent Mammalian Cells	
HeLa S3	C501300
CHO-K1	C502300
HEK 293	C503300

More cell lines coming soon

* Patent Pending

GE Healthcare

Bringing protein analysis to life with Ettan DIGE and Amersham ECL

When it comes to life sciences, GE Healthcare is setting the standard. Tens of thousands of scientists worldwide rely on our products and proven expertise in protein analysis and detection every day. But we're never content to stand still. We're constantly striving for innovations that boost accuracy and deliver quantitative data.

The result is new fluorescence platforms like the Ettan™ DIGE Imager and Amersham ECL Plex™ for quantitative protein analysis.

By continually developing technology that can turn your scientific ideas into reality, we're bringing science to life and helping to transform drug discovery and healthcare.

We call it Protein Analysis Re-imagined.

Discover the full power of Ettan DIGE and the Amersham ECL™ family of Western blotting systems.

www.gehealthcare.com/protein_analysis

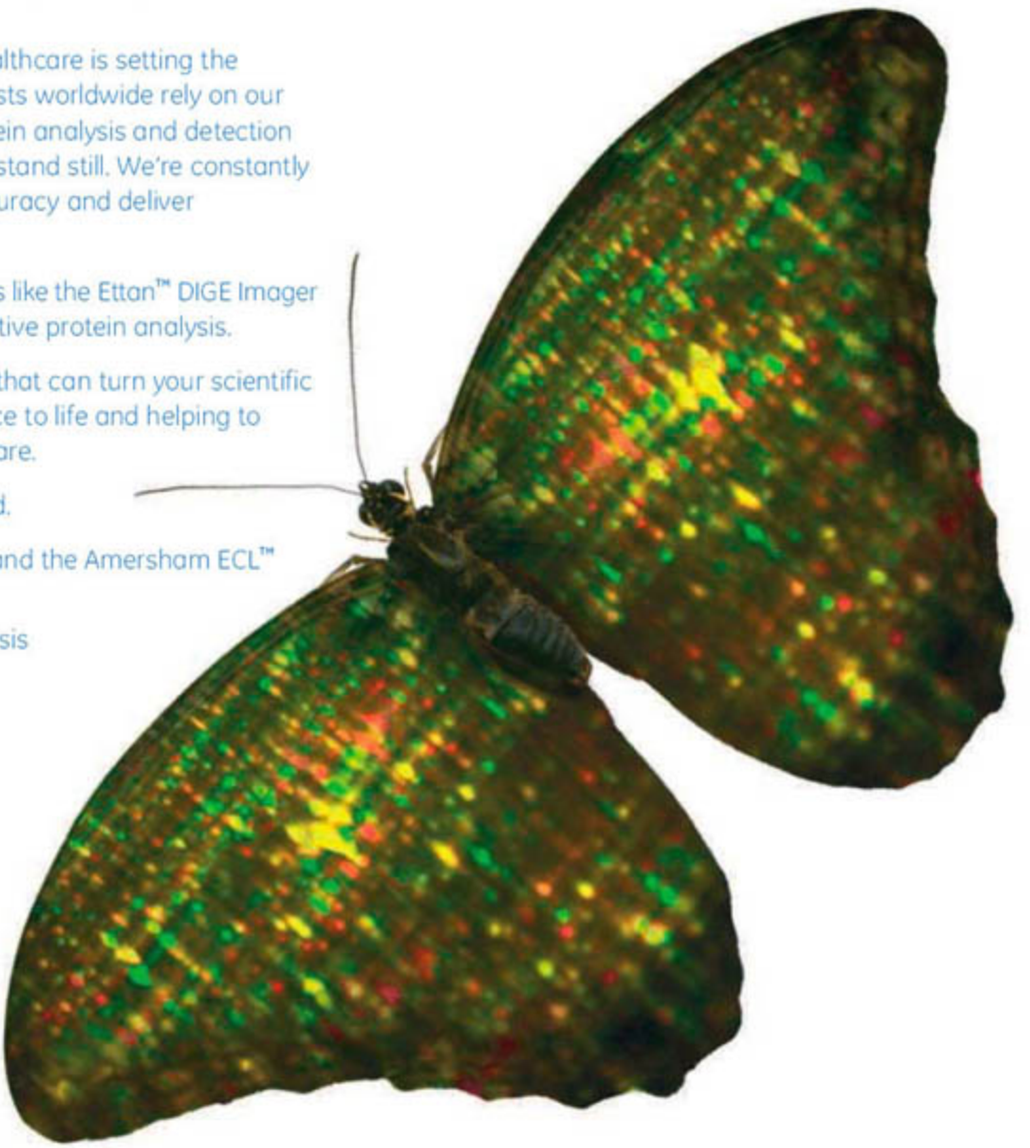

imagination at work

GE Healthcare Bio-Sciences AB, a General Electric Company.
Björkgatan 30, 751 84 Uppsala, Sweden.

GE08-06

Volume 315, Issue 5820

COVER

A bloom of *Rafflesia tuan-mudae* from western Borneo. Rafflesiaceae species produce the world's largest flowers, with blooms up to 1 meter in diameter. Molecular evidence described on page 1812 shows that these enigmatic parasites are members of the spurge family, Euphorbiaceae, hence the enormous flowers of Rafflesiaceae most likely arose from tiny-flowered ancestors.

Photo: © Ch'ien Lee

DEPARTMENTS

EDITORIAL

NEWS OF THE WEEK

NEWS FOCUS


1782

LETTERS

BOOKS *ET AL.*

EDUCATION FORUM

PERSPECTIVES


1794

CONTENTS continued >>

two phase filter

- Maximum protection against aerosols

- Binds biomolecules

- **ep Dualfilter T.I.P.S.** available in ten sizes

NEW! ep Dualfilter T.I.P.S.®

Stop aerosols!

Unique two-phase filter protection with ep Dualfilter T.I.P.S.®

The new Eppendorf ep Dualfilter T.I.P.S., with their unique two-phase filter, provide the perfect shield against contamination.

The filter consists of two visible phases, each with a different pore size. This two-phase filter protection ensures ultimate absorption of aerosols ❶ and biomolecules ❷, outmatching all conventional filters. Rely on it.

For more information go to
www.eppendorf.com/dualfilter

Features of the ep Dualfilter T.I.P.S.
Double protection provided by the two phase filter

- Provides maximum protection for both pipette and sample
- Ultimate absorption of aerosols and biomolecules
- Free from PCR inhibitor additives
- Patent pending two phase filter technology
- Supplied sterile, Eppendorf PCR clean and pyrogen-free
- IvD conformity
- Batch-related certificates available

eppendorf
In touch with life

Your local distributor: www.eppendorf.com/worldwide · Application Support: +49 180-3 66 67 89
Eppendorf AG · Germany · +49 40 538 01-0 • Eppendorf North America, Inc. 800-645-3050

Science

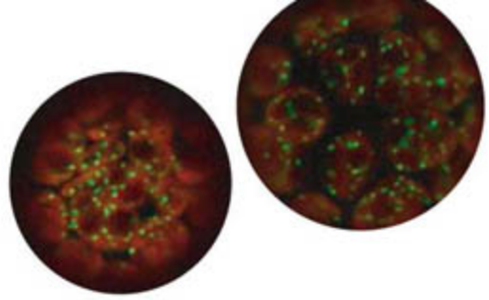

SCIENCE EXPRESS

www.sciencexpress.org

REVIEW

BREVIA

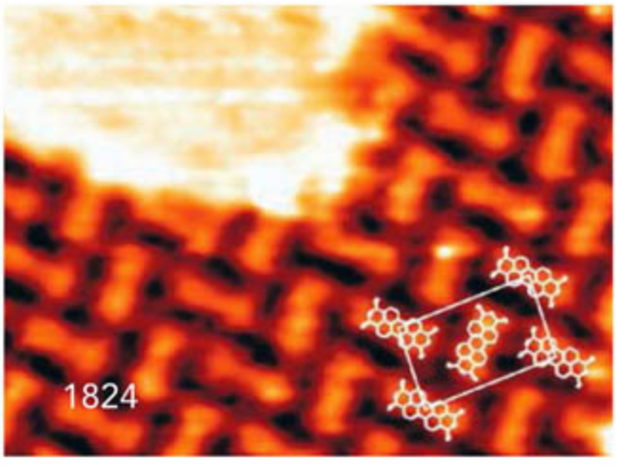

RESEARCH ARTICLES

REPORTS

CONTENTS continued >>

REPORTS *CONTINUED...*

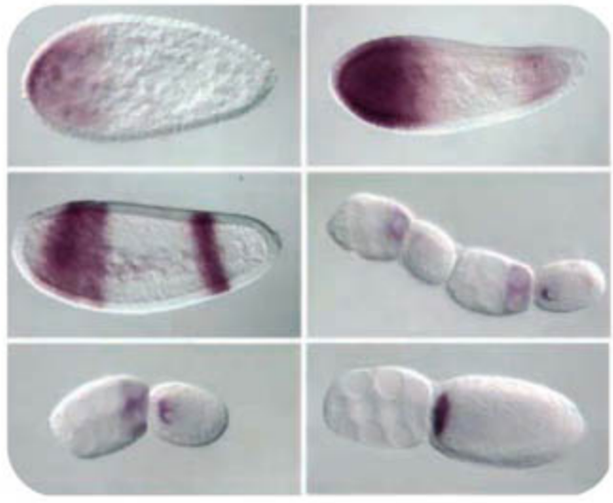

1841

AAAS
ADVANCING SCIENCE, SERVING SOCIETY

SCIENCE (ISSN 0036-8075) is published weekly on Friday, except the last week in December, by the American Association for the Advancement of Science, 1200 New York Avenue, NW, Washington, DC 20005. Periodicals Mail postage (publication No. 484460) paid at Washington, DC, and additional mailing offices. Domestic individual membership and subscription (51 issues): $142 ($74 allocated to subscription). Domestic institutional subscription (51 issues): $710; Foreign postage extra: Mexico, Caribbean (surface mail) $55; other countries (air assist delivery) $85. First class, airmail, student, and emeritus rates on request. Canadian rates with GST available upon request, GST #1254 88122. Publications Mail Agreement Number 1069624. **Printed in the U.S.A.**

Change of address: Allow 4 weeks, giving old and new addresses and 8-digit account number. **Postmaster:** Send change of address to AAAS, P.O. Box 96178, Washington, DC 20090–6178. **Single-copy sales:** $10.00 current issue, $15.00 back issue prepaid includes surface postage; bulk rates on request. **Authorization to photocopy** material for internal or personal use under circumstances not falling within the fair use provisions of the Copyright Act is granted by AAAS to libraries and other users registered with the Copyright Clearance Center (CCC) Transactional Reporting Service, provided that $18.00 per article is paid directly to CCC, 222 Rosewood Drive, Danvers, MA 01923. The identification code for *Science* is 0036-8075. *Science* is indexed in the *Reader's Guide to Periodical Literature* and in several specialized indexes.

CONTENTS continued >>

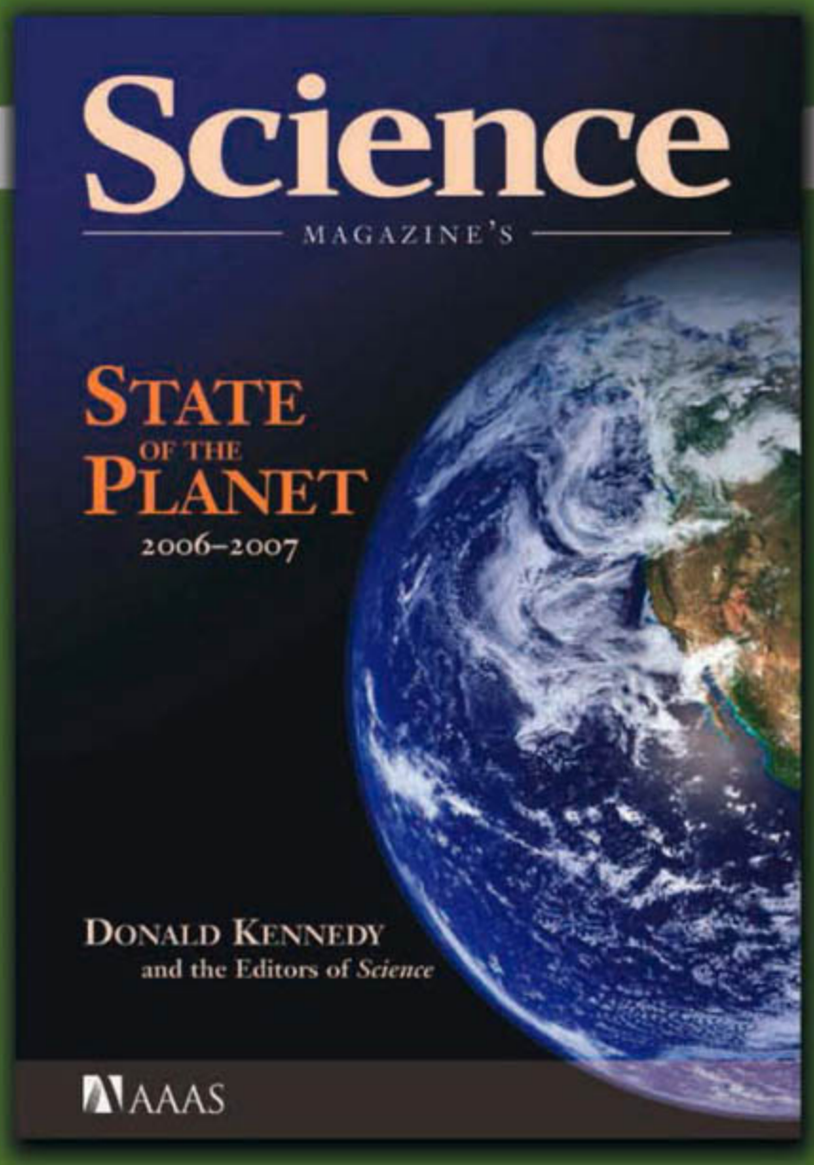

Science Magazine's
State of the Planet 2006-2007

Donald Kennedy, Editor-in-Chief, and the Editors of *Science*

The American Association for the Advancement of Science

The most authoritative voice in science, *Science* magazine, brings you current knowledge on the most pressing environmental challenges, from population growth to biodiversity loss.

COMPREHENSIVE • CLEAR • ACCESSIBLE

ISLANDPRESS

Science
AAAS

islandpress.org

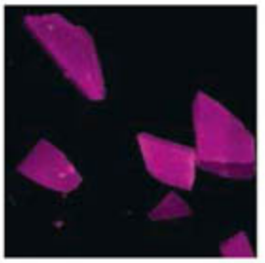

Infrared agent targets evidence of breast cancer.

SCIENCE**NOW**

www.sciencenow.org DAILY NEWS COVERAGE

A Better Breast Cancer Detector
Chemists develop compounds that home in on evidence of malignant cells.

I'll Be a Monkey's Uncle
Chimerism in marmosets allows dads to sire their brother's children.

Defusing the Platelet Time Bomb
Genetic secrets could prolong life of wound-healing blood cells.

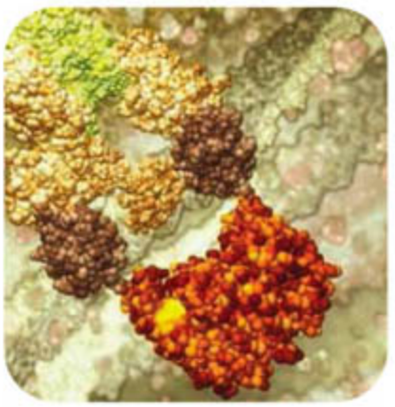

Activating cell death.

SCIENCE'S**STKE**

www.stke.org SIGNAL TRANSDUCTION KNOWLEDGE ENVIRONMENT

PERSPECTIVE: Fat Flies Expanded the Hippo Pathway—A Matter of Size Control
F. Yin and D. Pan
An atypical cadherin contributes to organ size in *Drosophila*.

TEACHING RESOURCE: Molecular Animation of Cell Death Mediated by the Fas Pathway
D. Berry
Using published structures, this movie provides a unique view of the molecular events associated with apoptosis induced by the prototypic death receptor Fas.

New strategy needed.

SCIENCE **CAREERS**

www.sciencecareers.org CAREER RESOURCES FOR SCIENTISTS

MISCINET: Educated Woman, Postdoc Edition, Part 3—Time to Strategize
M. P. DeWhyse
Stuck in a postdoc that doesn't quite fit, Micella considers her options.

US: Announcing GrantsNet 2.0
A. Kotok
The GrantsNet funding database is being updated with new content and features.

UK: Deaf to the Needs of Hearing-Impaired Scientists
N. Anscombe
In the U.K., deaf people seeking careers in science have to overcome many obstacles.

SCIENCE**PODCAST**

Listen to the 30 March *Science* Podcast to hear about the consequences of shark loss in the northwest Atlantic, learning in America's elementary classrooms, and innovations in building design and fabrication.
www.sciencemag.org/about/podcast.dtl

CREDITS: (SCIENCENOW) JOHN V. FRANGIONI AND KUMAR R. BHUSHAN; (SCIENCE CAREERS) COMSTOCK

Separate individual or institutional subscriptions to these products may be required for full-text access.

EDITED BY STELLA HURTLEY AND PHIL SZUROMI

Key to Liver Regeneration>>

The liver is one tissue in mammals that can regenerate. **Passino *et al.*** (p. 1853) now find that hepatocyte proliferation is controlled by the neurotrophin receptor $p75^{NTR}$, known primarily for its role in neurons in regulation of survival, apoptosis, and neuronal regeneration. Mice lacking $p75^{NTR}$ showed impaired hepatocyte proliferation. $p75^{NTR}$ appeared to act on hepatic stellate cells (HSCs), which differentiate in response to $p75^{NTR}$ and then make growth factors and extracellular matrix that support proliferation of hepatocytes. Modulation of the effects of $p75^{NTR}$ on HSCs could thus provide a therapeutic target for management of liver disease.

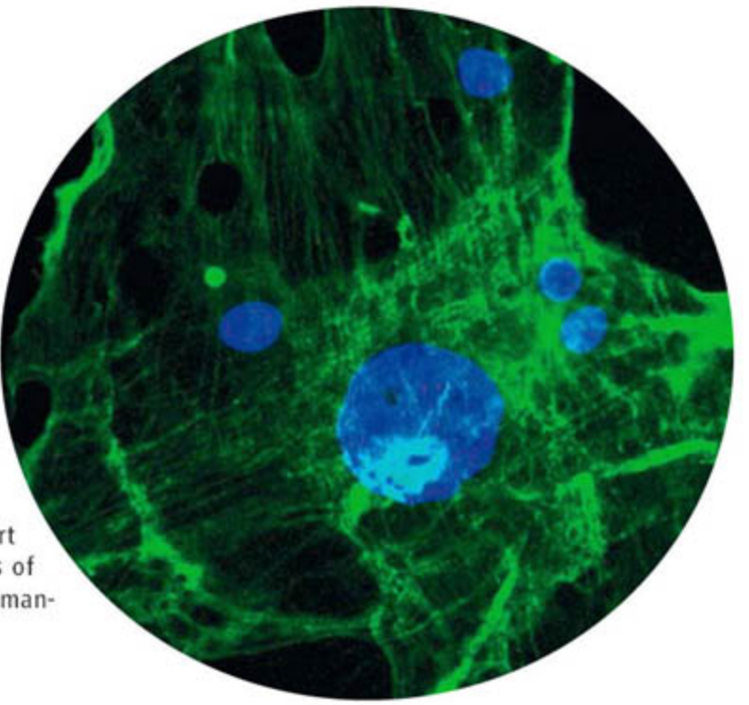

Building Smarter

Building construction is still dominated by traditional materials, and the conservative nature of architects and builders is understandable—it is hard to judge how a material may survive and perform during the 20- to 150-year lifetime of a building. However, the need to improve the energy efficiency and self-diagnostic capabilities of the built environment, along with a desire to improve the quality and functionality found in our interior spaces, has driven the adoption of new materials. **Fernández** (p. 1807) reviews this evolution in building design and fabrication and discusses how partnerships with the materials science community may accelerate the design and adoption of new materials.

Not Polarized Initially

Gamma-ray bursts (GRBs) that last several seconds or longer are thought to arise from the deaths of massive stars. Light from GRBs may be polarized if there are aligned magnetic fields around the collapsing star or in magnetized jets that it generates. Some observations had detected polarized signals from GRBs hours after the burst started. **Mundell *et al.*** (p. 1822; see the Perspective by **Covino**; published online March 15) have looked for polarized optical light just two and a half minutes after the burst GRB 060418 went off with the robotic Liverpool Telescope on La Palma, Canary Islands, which automatically responded to notification of the burst. At this early time, the light emitted came from the initial fireball of the explosion. No polarization was seen, to a limit of less than 8%, which rules out models with large aligned magnetic fields.

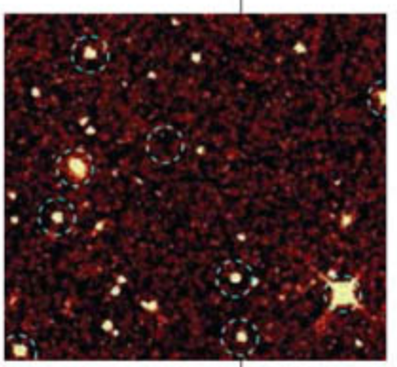

Heat Flow Below

The heat flow between turbulent, flowing liquid metals in the outer core and viscous, slowly convecting silicate magma in the lower mantle can be determined by identifying deep regions of postperovskite, a high-density polymorph of the common mantle mineral perovskite. The depth at which the polymorph forms can be measured seismically, and comparisons with pressure-temperature predictions from lab measurements and theory yield the heat flow at the interface depth. **Van der Hilst *et al.*** (p. 1813; see the Perspective by **Buffett**) have applied a seismic method from oil exploration to map the core-mantle boundary over a large region beneath Central America. They identify several regions where the postperovskite phase transition is seen, including multiple crossings, and infer heat fluxes.

Recovering Plastic Strain

The deformation of nanostructured metals differs from that of more typical coarse-grained metals, but are there also differences in their recovery after deformation? **Rajagopalan *et al.*** (p. 1831) used a micro-electro-mechanical systems device to measure the stress-strain behavior of thin aluminum strips with 65-nanometer (nm) grains. The plastic deformation that remained when the sample was unloaded was very substantially reduced by in situ heating for 7 minutes. Such recovery of plastic strain under zero load was not seen in a similarly sized sample with 200-nm columnar grains. The authors explain the effect by the backward motion of pinned dislocations upon stress release that was aided by thermal energy. These observations, which were also seen in gold samples, could be significant for developing more reliable nanostructures and investigating new deformation mechanisms in nanostructured materials.

Wedges of Stability

Ice-sheet instability and sea level may be connected by a positive feedback that could accelerate sea-level rise in ways previously unexpected. Two reports examine how sedimentation at the grounding line of ice streams, the most distal location where the ice rests on ground and beyond which it floats on water, might affect their stability (see the Perspective by **Anderson**). **Anandakrishnan *et al.*** (p. 1835, published online 1 March) use radar surveys to show that rapid sedimentation of glacial till transported by an Antarctic ice stream is now occurring, and that the sedimentary wedge that has formed at the grounding line resembles the structures that occur on the sea floor at numerous locations nearby that were formed during the retreat of the ice shelves since the Last Glacial Maximum. **Alley *et al.*** (p. 1838, published online 1 March) discuss how this process should affect the stability of ice sheets. Small changes in sea level are not expected to cause rapid retreat, with the implication that the rapid increases in ice loss

CREDITS (TOP TO BOTTOM): M. A. PASSINO AND K. AKASSOGLOU; MUNDELL *ET AL.*

that have been documented recently at the margins of the Antarctic and Greenland ice sheets are caused by dynamic responses to climate warming. However, large sea-level increases, in the range of tens of meters, could overwhelm the stabilizing effects of sedimentation.

Targeting Transmembrane Domains

Reagents such as antibodies that target specific proteins are useful in research and medicine. There are methods to engineer antibody-like molecules that target the soluble regions of proteins, but targeting transmembrane regions remains a challenge. Now **Yin *et al.*** (p. 1817) describe a computational method to design peptides that target specific transmembrane helices. Peptides were designed that were specific for each of two closely related integrins involved in cell adhesion.

Two Ways to Segment an Insect

In the *Drosophila* embryo, the bicoid morphogen serves as a maternal anterior determinant during anterior-posterior axis development; however, this transcription factor is not found among all insects. **Brent *et al.*** (p. 1841) compared the molecular mechanisms of development in the fruit fly *Drosophila* and the wasp *Nasonia*. *Drosophila* bicoid serves both an instructive function during anterior patterning, and a permissive function for the repression of trunk genes in the anterior region. However, in the wasp, these two functions remain discrete: *Nasonia orthodenticle* (*otd*) performs bicoid function for anterior development, while maternal *giant* represses trunk fate. Thus, in the wasp, *otd* and *giant* jointly accomplish bicoid's role in *Drosophila*.

CREDIT: AVA BRENT

Big Fish, Little Fish, Shellfish

The loss of large predators from ecosystems, often caused by human activities, can have effects that cascade through the rest of the food chain. **Myers *et al.*** (p. 1846) quantitatively assess the ecosystem consequences of the functional elimination of top predators from a northwest Atlantic marine environment. The loss of 11 species of large sharks, with numerical declines during a 35-year period of up to >99%, resulted in population increases in 12 out of 13 species of smaller sharks, rays, and skates eaten almost exclusively by large sharks. One of these, the cownose ray, has increased 20-fold since 1970. Its prey, bivalve mollusks, have been reduced to levels where commercial shellfisheries have suffered and where the water-filtering service of their remnant populations has been compromised.

A Fly Model of PolyQ Disease

More than 40 human diseases are known to be caused by the expansion of simple repeat sequences, the majority being trinucleotide repeats such as CAG or CGG. However, few models for repeat instability recapitulate the striking features seen in human patients, and few or no therapeutics to clamp repeat instability. **Jung *et al.*** (p. 1857, published online 1 March; see the Perspective by **Fortini**), in the model organism *Drosophila*, observe striking CAG repeat instability that recapitulates several key features of human disease, including large repeat expansions, with repeat size variations similar to that of human patients. The pathologic CAG/polyglutamine (polyQ) protein, encoded by the expanded CAG repeat, enhanced repeat instability through an inhibitory effect on a regulatory protein involved in DNA repair and replication.

Attention and Information Flow

Cortical neurons modulate their activity with shifts in attention, but the source and flow of attention signals are unclear. **Buschman *et al.*** (p. 1860) used 50 electrodes to record simultaneously the activity from three cortical regions thought to be critical for attention. Bottom-up shifts of attention were first reflected in the parietal cortex, whereas top-down shifts of attention were reflected first in the frontal cortex. Thus, external control of visual attention originates in parietal cortex, but internal control of visual attention is directed from the frontal cortex.

Scott Goetz is a senior scientist at the Woods Hole Research Center, Falmouth, MA, and an adjunct faculty member at the University of Maryland, College Park, MD. E-mail: sgoetz@whrc.org

Crisis in Earth Observation

SATELLITE SENSORS HAVE BEEN IMAGING EARTH'S LAND SURFACE, OCEANS, AND ICE FIELDS since the early 1970s. The data sets derived from these observations have chronicled transformations on the planet's surface, ranging from urban sprawl to tropical deforestation, covering even the most remote regions of the globe. Scientists in the United States, supported by the National Aeronautics and Space Administration (NASA) and other agencies, have demonstrated the utility and societal benefits of the data in a wide range of applications, including community planning, crop monitoring, coral reef mapping, water-quality assessment, disaster management, and homeland security. Sadly, this is about to change.

The workhorses of operational Earth observation, the Landsat series of satellites, now face a crippling data gap. Landsat-7, launched by the United States in 1999 as the latest in the series, suffered a sensor malfunction in 2003 that severely limits its utility. Landsat-5, launched in 1984, has far outlived its 3-year design life and will run out of fuel before the launch of the next satellite in the series, the Landsat Data Continuity Mission (LDCM), which will occur in 2011 at best. If LDCM fails to launch (Landsat-6 pitched into the Pacific in 1993), then the societal benefits that have resulted from the Landsat program will come to an abrupt end. An equally troubling situation faces the next generation of U.S. observational weather satellites. The National Polar-Orbiting Operational Environmental Satellite System (NPOESS) is experiencing large cost overruns, and funding for the instruments designed to fly on these satellites for the study of Earth's climate has been cut.

John Marburger, director of the White House Office of Science and Technology Policy, apparently agrees that a strategy for ensuring future Earth observations is badly needed. In response to a memo he issued in April 2005, a Future of Land Imaging Interagency Working Group was formed. That group's draft recommendations are due out this year. In the meantime, India, China, and Brazil are launching Landsat-class satellites. Others countries, such as Libya and Nigeria, are experimenting with microsatellite systems for Earth observation.

Just at a time when monitoring changes on the land surface (due to changing land use or climate) should be a national priority, how can continued U.S. technological leadership in satellite remote sensing be in question? While other nations are advancing their technologies, the United States appears unable to maintain its own capabilities. The U.S. Department of Agriculture now must resort to buying crop-monitoring data from Indian satellites. This dependence on foreign assets may well increase: Even NASA may buy foreign data to fill the gap in its Landsat data.

This crisis in Earth observation underscores the need for a more strategic approach. The U.S. Integrated Earth Observation System strategic plan, released in 2005, notes the "need for high-quality, global, sustained information on the state of the Earth as a basis for policy and decision making in every sector of our society." Unfortunately, a current focus of NASA—the "new vision" of a manned mission to Mars—is taking priority over securing necessary Earth observations. The U.S. National Research Council's (NRC's) recent assessment of Earth observation capabilities and prospects concludes that $500 million per year is needed to restore NASA's earth science program, and major changes are needed to salvage NPOESS. According to the new chairman of the House Science Committee, Bart Gordon, the United States will be "flying blind" if we don't ensure that its Earth observation satellite system can continually collect data "to guide our policy decisions."

The U.S. Earth-observing strategy should prioritize the NRC recommendations, ensure continuous monitoring, and enable the development of lower-cost experimental systems to measure critical variables. International partnerships in satellite development and operations should also be leveraged to extend limited resources. Society—both the United States and the global community—must have continuous data about our home planet for priority societal applications and policy-making. A clear vision and the associated resources are urgently needed, first to extricate the United States from the current crisis and then to guarantee that a similar situation might not come back to haunt us later.

– Scott Goetz

CREDIT: U.S. GEOLOGICAL SURVEY

10.1126/science.1142466

IMMUNOLOGY

A Bacterial Anticomplement

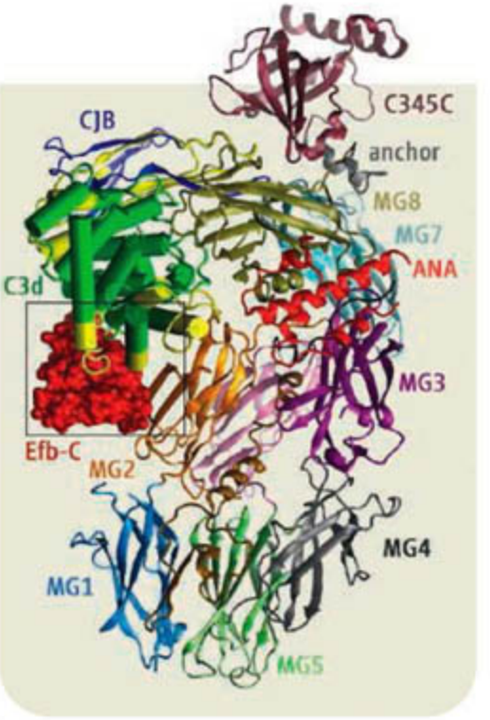

The complement system generates a finely regulated, yet potent antimicrobial response, making it an attractive target for bacterial virulence factors. Most commonly, endogenous regulatory proteins of the complement system are usurped to switch off complement activation, but the widespread human pathogen *Staphylococcus aureus* can inactivate the complement cascade by a more direct means. Previous work has shown that the extracellular fibrinogen-binding protein (Efb-C) generated by *S. aureus* blocks the complement pathway by binding to the thioester-containing domain of the complement C3b protein; indeed, *S. aureus* strains that lack Efb-C display reduced virulence. Hammel *et al.* resolve the crystal structures for the C3-binding domain of Efb-C in its unbound state and in complex with the C3d domain of C3 (shown at right). Structure-based functional studies suggest that native C3 is bound by Efb-C in a way that alters its conformation. As a consequence, conversion to C3b is prevented, and participation in the subsequent activation of the complement cascade is also blocked. As well as binding native C3, Efb-C also had high affinity for C3b, again appearing to induce conformational changes, this time in the already activated form of the complement component. Effective targeting of the interface between Efb-C and the C3d domain by a small molecule could be useful in the treatment of *S. aureus* infection. — SJS

Nat. Immunol. 10.1038/ni1450 (2007).

ARCHAEOLOGY

Fall of the Mitey

Within a century after the arrival of Spanish conquistadors in Peru in the 1530s, the population of the Inca empire fell from an estimated 9 million to around 600,000, due largely to introduced diseases, forced resettlement, and exploitation for labor. It is difficult to reconstruct the demographic history of that collapse because the Inca had no written language. Chepstow-Lusty *et al.* employed a new palaeoenvironmental tool, the abundance of soil-dwelling oribatid mites, to help fill in gaps in the record of population decline. These mites, which are tiny arthropods related to spiders, thrive on a diet rich in animal excrement (in Peru, mostly that of llamas). By measuring the abundance of these creatures' remains in pastures where the animals would have grazed, the authors were able to determine how the abundance of livestock, and by inference the level of human activity, changed in the area around the imperial capital Cuzco from about 800 to 1800 CE. The correspondence of the mite record to the historical accounts of the Spanish invaders bolsters the accuracy of the technique. — HJS

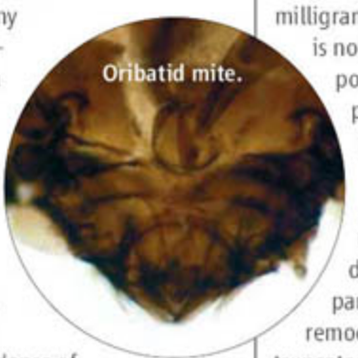
Oribatid mite.

J. Archaeol. Sci. **34**, 1178 (2007).

BIOCHEMISTRY

Making Complexes Simply

Even though proteomic studies may overestimate the number and variety of functionally important protein-protein interactions in cells, most such complexes are not abundant enough to be purified via classical biochemistry. Heterologous expression of well-folded proteins in the milligram amounts needed for structural studies is not straightforward—especially not for posttranslationally modified eukaryotic proteins—and arranging stoichiometric assembly is yet another hurdle.

Fitzgerald *et al.* describe a baculovirus-based system for making multigene expression vectors and demonstrate its utility for producing in parallel a combinatorial set of chromatin-remodeling complexes built of wild-type or truncated subunits. Incorporating a phosphatase into the expression vector quantitatively yielded the de-phospho form of the complex. — GJC

Structure **15**, 275 (2007).

CHEMISTRY

Rearranging Nitriles

Although catalysis of alkene and alkyne metathesis has recently flourished, the analogous transformation of nitriles, which bear C-N triple bonds, has proven more challenging. This reaction is appealing in part because of the relative ease with which CN groups can be introduced to diverse organic molecules. However, the strength of metal nitride bonds can inhibit turnover. Geyer *et al.* have prepared a tungsten complex with trifluoromethyl-substituted alkoxy ligands that acts as an effective catalyst for the metathesis of aryl nitriles R-CN to the corresponding alkynes R-CC-R, with 3-hexyne serving as a N acceptor to yield propionitrile as a co-product; the reaction does not form N_2 in the absence of an acceptor. Alkyne metathesis occurs more rapidly under the reaction conditions than nitrile alkyne cross-metathesis, and the authors note the conserved gas-phase thermodynamic preference for coupling the aryl partners and transferring N to the alkyl moiety. The catalyst tolerates halides, methyl ester, and vinyl groups, as well as thiophene substrates. — JSY

J. Am. Chem. Soc. **129**, 10.1021/ja0693439 (2007).

CREDITS (TOP TO BOTTOM): HAMMEL *ET AL.*, *NAT. IMMUNOL.* 10.1038/NI1450 (2007); CHEPSTOW-LUSTY *ET AL.*, *J. ARCHAEOL. SCI.* **34**, 1178 (2007)

SURFACE SCIENCE

Buckled BN

A covalently bonded overlayer on a metallic surface can be distorted to varying degrees, depending on the extent of lattice mismatch. For example, boron nitride (BN) overlayers can form simple monolayers on close-packed Cu(111) and Ni(111) surfaces, but complex moiré patterns are observed on Pt and Pd surfaces. On Rh(111) and Ru(111) surfaces, scanning tunneling microscopy helped reveal the formation of "nanomeshes" in which 2-nm depressions formed a hexagonal lattice with a 3-nm periodicity. For the Rh system, this pattern was initially attributed to a bilayer structure in which the depressions were holes exposing the underlying metal. Laskowski *et al.* now propose an alternative structure that better explains the ultraviolet photoelectron spectra for this surface and that avoids the energetic penalty posed by the many dangling bonds in the two-layer structure. Density functional calculations were used to create a force field for a BN layer strained by 8%, its lattice mismatch with Rh(111). When this overlayer was allowed to relax on the Rh(111) surface, it adopted a nanomesh geometry of flat depressions ("holes") where the lattice match with the substrate was high, surrounded by a region about 0.6 Å higher, where poor lattice matching led to overlayer repulsion. This steplike corrugation in the surface normal direction relieves strain while maintaining the lateral dimensions of the BN layer. — PDS

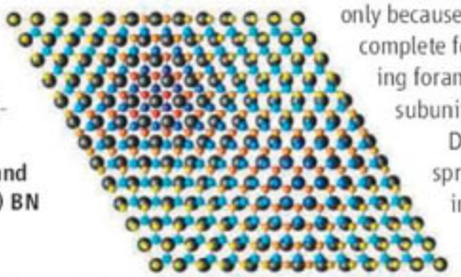

High (blue and red) and low (cyan and yellow) BN on Rh(111) (black).

Phys. Rev. Lett. **98,** 106802 (2007).

ECOLOGY/EVOLUTION

Pelagic Ecology

Investigations of the ecology of planktonic marine organisms run into the problem of reconciling the anonymity of morphological uniformity with the potential for ubiquitous distribution in the continuity of the oceans and the observed genetic diversity. Foraminifera are good model organisms for disentangling protist biogeography, not only because they have left an unusually complete fossil record, but also because living forams display high rates of small-subunit ribosomal RNA evolution. Darling *et al.* find that one widespread morphospecies has evolved into several types with distinct global distribution patterns that seem to have arisen during Northern Hemisphere cooling in the Quaternary. Subsequently, gene flow has been restricted by the equatorial oceans and especially by the Gulf Stream. Adaptations for survival at cold temperatures have since developed and are related to niche: that is, living within ice brine channels, in subpolar oceans, in upwellings, and so on. — CA

Proc. Natl. Acad. Sci. U.S.A. **104**, 5002 (2007).

Science STKE AAAS

www.stke.org

<< Cheering Up with VEGF

Although the molecular mechanisms of antidepressant action remain unclear, one hypothesis suggests that stimulation of growth factor signaling and of adult neurogenesis in the hippocampus may be implicated in their effects. Warner-Schmidt and Duman investigated the effects of different classes of antidepressants on hippocampal expression of the neurotrophic and proangiogenic factor vascular endothelial growth factor (VEGF), which their research group had previously shown to be enhanced by electroconvulsive seizure (ECS) treatment. The abundance of VEGF mRNA increased in the hippocampal granule cell layer of rats treated for 14 days with fluoxetine (a serotonin-reuptake inhibitor) or desipramine (a norepinephrine-reuptake inhibitor), as did the abundance of VEGF in hippocampal homogenates. Pharmacological blockade of the VEGF receptor Flk-1 inhibited the increase in cell proliferation in the hippocampal subgranular zone (SGZ) produced by ECS or by chronic exposure to fluoxetine or desipramine, whereas intracerebroventricular delivery of a VEGF isoform stimulated SGZ cell proliferation. Furthermore, pharmacological blockade of Flk-1 inhibited the effects of desipramine on behavioral responses in chronic and subchronic rat models of depression, whereas VEGF had an antidepressant-like effect. Noting that antidepressants promoted the proliferation of hippocampal endothelial cells as well as hippocampal neurogenesis, the authors speculated that this could play a role in the treatment of certain forms of depression that are associated with vascular abnormalities. — EMA

Proc. Natl. Acad. Sci. U.S.A. **104**, 4647 (2007).

CREDIT: LASKOWSKI *ET AL.*, *PHYS. REV. LETT.* **98**, 106802 (2007)

www.sciencemag.org

Science

1200 New York Avenue, NW
Washington, DC 20005
Editorial: 202-326-6550, FAX 202-289-7562
News: 202-326-6500, FAX 202-371-9227

Bateman House, 82-88 Hills Road
Cambridge, UK CB2 1LQ
+44 (0) 1223 326500, FAX +44 (0) 1223 326501

SUBSCRIPTION SERVICES For change of address, missing issues, new orders and renewals, and payment questions: 866-434-AAAS (2227) or 202-326-6417, FAX 202-842-1065. Mailing addresses: AAAS, P.O. Box 96178, Washington, DC 20090-6178 or AAAS Member Services, 1200 New York Avenue, NW, Washington, DC 20005

INSTITUTIONAL SITE LICENSES please call 202-326-6755 for any questions or information

REPRINTS: Author Inquiries 800-635-7181
Commercial Inquiries 803-359-4578
Corrections 202-326-6501

PERMISSIONS 202-326-7074, FAX 202-682-0816

MEMBER BENEFITS Bookstore: AAAS/BarnesandNoble.com bookstore www.aaas.org/bn; Car purchase discount: Subaru VIP Program 202-326-6417; Credit Card: MBNA 800-847-7378; Car Rentals: Hertz 800-654-2200 CDP#343457, Dollar 800-800-4000 #AA1115; AAAS Travels: Betchart Expeditions 800-252-4910; Life Insurance: Seabury & Smith 800-424-9883; Other Benefits: AAAS Member Services 202-326-6417 or www.aaasmember.org.

science_editors@aaas.org (for general editorial queries)
science_letters@aaas.org (for queries about letters)
science_reviews@aaas.org (for returning manuscript reviews)
science_bookrevs@aaas.org (for book review queries)

Published by the American Association for the Advancement of Science (AAAS), *Science* serves its readers as a forum for the presentation and discussion of important issues related to the advancement of science, including the presentation of minority or conflicting points of view, rather than by publishing only material on which a consensus has been reached. Accordingly, all articles published in *Science*—including editorials, news and comment, and book reviews—are signed and reflect the individual views of the authors and not official points of view adopted by the AAAS or the institutions with which the authors are affiliated.

AAAS was founded in 1848 and incorporated in 1874. Its mission is to advance science and innovation throughout the world for the benefit of all people. The goals of the association are to: foster communication among scientists, engineers and the public; enhance international cooperation in science and its applications; promote the responsible conduct and use of science and technology; foster education in science and technology for everyone; enhance the science and technology workforce and infrastructure; increase public understanding and appreciation of science and technology; and strengthen support for the science and technology enterprise.

INFORMATION FOR AUTHORS

See pages 120 and 121 of the 5 January 2007 issue or access www.sciencemag.org/feature/contribinfo/home.shtml

EDITOR-IN-CHIEF **Donald Kennedy**
EXECUTIVE EDITOR **Monica M. Bradford**
DEPUTY EDITORS **R. Brooks Hanson, Barbara R. Jasny, Katrina L. Kelner**
NEWS EDITOR **Colin Norman**

EDITORIAL SUPERVISORY SENIOR EDITOR Phillip D. Szuromi; SENIOR EDITOR/PERSPECTIVES Lisa D. Chong; SENIOR EDITORS Gilbert J. Chin, Pamela J. Hines, Paula A. Kiberstis (Boston), Marc S. Lavine (Toronto), Beverly A. Purnell, L. Bryan Ray, Guy Riddihough, H. Jesse Smith, Valda Vinson, David Voss; ASSOCIATE EDITORS Jake S. Yeston, Laura M. Zahn; ONLINE EDITOR Stewart Wills; ASSOCIATE ONLINE EDITOR Tara S. Marathe; BOOK REVIEW EDITOR Sherman J. Suter; ASSOCIATE LETTERS EDITOR Etta Kavanagh; EDITORIAL MANAGER Cara Tate; SENIOR COPY EDITORS Jeffrey E. Cook, Cynthia Howe, Harry Jach, Barbara P. Ordway, Jennifer Sills, Trista Wagoner; COPY EDITORS Lauren Kmec, Peter Mooreside; EDITORIAL COORDINATORS Carolyn Kyle, Beverly Shields; PUBLICATIONS ASSISTANTS Ramatoulaye Diop, Chris Filiatreau, Joi S. Granger, Jeffrey Hearn, Lisa Johnson, Scott Miller, Jerry Richardson, Brian White, Anita Wynn; EDITORIAL ASSISTANTS Maris M. Bish, Emily Guise, Patricia M. Moore, Jennifer A. Seibert; EXECUTIVE ASSISTANT Sylvia S. Kihara; ADMINISTRATIVE SUPPORT Maryrose Police

NEWS SENIOR CORRESPONDENT Jean Marx; DEPUTY NEWS EDITORS Robert Coontz, Eliot Marshall, Jeffrey Mervis, Leslie Roberts; CONTRIBUTING EDITORS Elizabeth Culotta, Polly Shulman; NEWS WRITERS Yudhijit Bhattacharjee, Adrian Cho, Jennifer Couzin, David Grimm, Constance Holden, Jocelyn Kaiser, Richard A. Kerr, Eli Kintisch, Andrew Lawler (New England), Greg Miller, Elizabeth Pennisi, Robert F. Service (Pacific NW), Erik Stokstad; John Simpson (intern); CONTRIBUTING CORRESPONDENTS Barry A. Cipra, Jon Cohen (San Diego, CA), Daniel Ferber, Ann Gibbons, Robert Irion, Mitch Leslie, Charles C. Mann, Evelyn Strauss, Gary Taubes, Ingrid Wickelgren; COPY EDITORS Linda B. Felaco, Rachel Curran, Sean Richardson; ADMINISTRATIVE SUPPORT Scherraine Mack, Fannie Groom; BUREAUS Berkeley, CA: 510-652-0302, FAX 510-652-1867, New England: 207-549-7755, San Diego, CA: 760-942-3252, FAX 760-942-4979, Pacific Northwest: 503-963-1940

PRODUCTION DIRECTOR James Landry; SENIOR MANAGER Wendy K. Shank; ASSISTANT MANAGER Rebecca Doshi; SENIOR SPECIALISTS Jay Covert, Chris Redwood; SPECIALIST Steve Forrester; PREFLIGHT DIRECTOR David M. Tompkins; MANAGER Marcus Spiegler; SPECIALIST Jessie Mudjitaba

ART DIRECTOR Kelly Buckheit Krause; ASSOCIATE ART DIRECTOR Aaron Morales; ILLUSTRATORS Chris Bickel, Katharine Sutliff; SENIOR ART ASSOCIATES Holly Bishop, Laura Creveling, Preston Huey; ASSOCIATES Nayomi Kevitiyagala, Jessica Newfield; PHOTO EDITOR Leslie Blizard

***SCIENCE* INTERNATIONAL**

EUROPE (science@science-int.co.uk) EDITORIAL: INTERNATIONAL MANAGING EDITOR Andrew M. Sugden; SENIOR EDITOR/PERSPECTIVES Julia Fahrenkamp-Uppenbrink; SENIOR EDITORS Caroline Ash (Geneva: +41 (0) 222 346 3106), Stella M. Hurtley, Ian S. Osborne, Stephen J. Simpson, Peter Stern; ASSOCIATE EDITOR Joanne Baker EDITORIAL SUPPORT Alice Whaley; Deborah Dennison ADMINISTRATIVE SUPPORT Janet Clements, Jill White; NEWS: EUROPE NEWS EDITOR John Travis; DEPUTY NEWS EDITOR Daniel Clery; CORRESPONDENT Gretchen Vogel (Berlin: +49 (0) 30 2809 3902, FAX +49 (0) 30 2809 8365); CONTRIBUTING CORRESPONDENTS Michael Balter (Paris), Martin Enserink (Amsterdam and Paris), John Bohannon (Vienna); INTERN Krista Zala

ASIA Japan Office: Asca Corporation, Eiko Ishioka, Fusako Tamura, 1-8-13, Hirano-cho, Chuo-ku, Osaka-shi, Osaka, 541-0046 Japan; +81 (0) 6 6202 6272, FAX +81 (0) 6 6202 6271; asca@os.gulf.or.jp; ASIA NEWS EDITOR Richard Stone +66 2 662 5818 (rstone@aaas.org); JAPAN NEWS BUREAU Dennis Normile (contributing correspondent, +81 (0) 3 3391 0630, FAX 81 (0) 3 5936 3531; dnormile@gol.com); CHINA REPRESENTATIVE Hao Xin, + 86 (0) 10 6307 4439 or 6307 3676, FAX +86 (0) 10 6307 4358; cindyhao@gmail.com; SOUTH ASIA Pallava Bagla (contributing correspondent +91 (0) 11 2271 2896; pbagla@vsnl.com)
AFRICA Robert Koenig (contributing correspondent, rob.koenig@gmail.com)

EXECUTIVE PUBLISHER **Alan I. Leshner**
PUBLISHER **Beth Rosner**

FULFILLMENT & MEMBERSHIP SERVICES (membership@aaas.org) DIRECTOR Marlene Zendell; MANAGER Waylon Butler; SYSTEMS SPECIALIST Andrew Vargo; CUSTOMER SERVICE SUPERVISOR Pat Butler; SPECIALISTS Laurie Baker, Tamara Alfson, Karena Smith, Vicki Linton, Latoya Casteel; CIRCULATION ASSOCIATE Christopher Refice; DATA ENTRY SUPERVISOR Cynthia Johnson; SPECIALISTS Tomeka Diggs, Tarrika Hill, Erin Layne

BUSINESS OPERATIONS AND ADMINISTRATION DIRECTOR Deborah Rivera-Wienhold; BUSINESS MANAGER Randy Yi; SENIOR BUSINESS ANALYST Lisa Donovan; BUSINESS ANALYST Jessica Tierney; FINANCIAL ANALYSTS Michael LoBue, Farida Yeasmin; RIGHTS AND PERMISSIONS: ADMINISTRATOR Emilie David; ASSOCIATE Elizabeth Sandler; MARKETING: DIRECTOR John Meyers; MARKETING MANAGERS Darryl Walter, Allison Pritchard; MARKETING ASSOCIATES Julianne Wielga, Mary Ellen Crowley, Catherine Featherston, Alison Chandler, Lauren Lamoureux; INTERNATIONAL MARKETING MANAGER Wendy Sturley; MARKETING EXECUTIVE Jennifer Reeves; MARKETING/MEMBER SERVICES EXECUTIVE Linda Rusk; JAPAN SALES Jason Hannaford; SITE LICENSE SALES: DIRECTOR Tom Ryan; SALES AND CUSTOMER SERVICE Mehan Dossani, Kiki Forsythe, Catherine Holland, Wendy Wise; ELECTRONIC MEDIA: MANAGER Lizabeth Harman; PROJECT MANAGER Trista Snyder; ASSISTANT MANAGER Lisa Stanford PRODUCTION ASSOCIATES Nichele Johnston, Kimberly Oster

ADVERTISING DIRECTOR WORLDWIDE AD SALES Bill Moran

PRODUCT (science_advertising@aaas.org): MIDWEST Rick Bongiovanni: 330-405-7080, FAX 330-405-7081 • WEST COAST/W. CANADA Teola Young: 650-964-2266 EAST COAST/E. CANADA Christopher Breslin: 443-512-0330, FAX 443-512-0331 • UK/EUROPE/ASIA Julie Skeet: +44 (0) 1223-326-524, FAX +44 (0) 1223-325-532 JAPAN Mashy Yoshikawa: +81 (0) 33235 5961, FAX +81 (0) 33235 5852 TRAFFIC MANAGER Carol Maddox; SALES COORDINATOR Deiandra Simms

COMMERCIAL EDITOR Sean Sanders: 202-326-6430

CLASSIFIED (advertise@sciencecareers.org): U.S.: RECRUITMENT SALES MANAGER Ian King: 202-326-6528, FAX 202-289-6742; U.S./INDUSTRY: Darrell Bryant: 202-326-6533; MIDWEST/CANADA: Daryl Anderson: 202-326-6543; NORTHEAST: Allison Millar: 202-326-6572; SOUTHEAST: Fernando Junco: 202-326-6740; WEST: Katie Putney: 202-326-6577; SALES COORDINATORS Erika Bryant, Rohan Edmonson, Shirley Young; INTERNATIONAL: SALES MANAGER Tracy Holmes: +44 (0) 1223 326525, FAX +44 (0) 1223 326532; SALES Christina Harrison, Svitlana Barnes; SALES ASSISTANT Louise Moore; JAPAN: Jason Hannaford: +81 (0) 52 757 5360, FAX +81 (0) 52 757 5361; ADVERTISING PRODUCTION OPERATIONS MANAGER Deborah Tompkins; ASSOCIATES Christine Hall, Amy Hardcastle; PUBLICATIONS ASSISTANTS Robert Buck, Mary Lagnaoui

AAAS BOARD OF DIRECTORS RETIRING PRESIDENT, CHAIR John P. Holdren; PRESIDENT David Baltimore; PRESIDENT-ELECT James J. McCarthy; TREASURER David E. Shaw; CHIEF EXECUTIVE OFFICER Alan I. Leshner; BOARD John E. Dowling, Lynn W. Enquist, Susan M. Fitzpatrick, Alice Gast, Linda P. B. Katehi, Cherry A. Murray, Thomas D. Pollard, Kathryn D. Sullivan

AAAS
ADVANCING SCIENCE, SERVING SOCIETY

Looking for solid ground in the ever-changing landscape of science & technology policy and budget issues?

Join the nation's top S&T experts at the 32nd Annual AAAS Forum on Science & Technology Policy
3–4 May 2007 • Washington DC
International Trade Center in the Ronald Reagan Building

The AAAS Forum on Science and Technology Policy provides a setting for discussion and debate about the federal budget and other policy issues facing the science, engineering, and higher education communities. Initiated in 1976 as the AAAS R&D Colloquium with about 100 participants, the Forum has emerged as the major public meeting in the U.S. devoted to science and technology policy issues. It annually draws upwards of 500 of the nation's top S&T policy experts.

- Get a full analysis of the President's federal R&D funding proposals.
- Have an opportunity to meet directly with key S&T policymakers.
- Learn how the changes in Congress are affecting S&T policy issues.
- Network with colleagues, including top decisionmakers in science and technology policy from all sectors.
- Learn about broader national and international developments that will affect strategic planning in universities, industries, and government.
- Registrants will receive, at the Forum, *AAAS Report XXXII: Research and Development, FY 2008*, a comprehensive analysis of the proposals for the FY 2008 budget, prepared by AAAS and a group of its affiliated scientific, engineering, and higher education associations.

For more complete details on the program, hotel registration and on-line registration, please visit the website: **www.aaas.org/forum.**

www.aaas.org/forum

AAAS
ADVANCING SCIENCE, SERVING SOCIETY

Does your next career step need direction?

There's only one place to go for career advice if you value the expertise of *Science* and the long experience of AAAS in supporting career advancement - ScienceCareers.org. The pages of *Science* and our website ScienceCareers.org offer:

- Thousands of job postings
- Funding information
- Career advice articles and tools
- Networking opportunities

www.sciencecareers.org

Unweaving the Rainbow

From a rare nocturnal rainbow to a shimmering solar halo, the atmosphere can conjure up a host of surprising special effects. A general audience can learn to recognize these tricks of the light and understand their causes at Atmospheric Optics, hosted by retired chemical physicist Les Cowley of Norfolk, U.K.

Lavishly illustrated with photos from sky watchers, the site explains atmospheric phenomena produced when light strikes water droplets, ice crystals, and dust. This early-morning shot (below) from Mount Washington in New Hampshire, for instance, captures two sky spectacles. The photographer's outsized shadow on the mist is a Brocken specter, and the glowing rings surrounding it are a "glory." A rainbow forms because water droplets reflect and refract light, but a glory also requires that light skid along the surface of the droplet before being refracted. Visitors can further probe the effects using free software that simulates light scattering by ice crystals and fine droplets. >> www.atoptics.co.uk

Nanofinger

Nanotechnology is adding a new weapon to the crime fighter's arsenal: a nano-solution for sharpening fingerprints.

For more than a century, crime investigators have sprayed suspect surfaces with a water-based gold or silver solution to detect fingerprints. The metal ions are reduced to a black precipitate along the lines of fatty deposits left by the skin ridges. But "even with the most advanced fingerprint techniques," says chemist Joseph Almog of Hebrew University in Jerusalem, "less than a third" of good prints at crime scenes produce usable evidence.

Almog, who is also a former chief forensic scientist for the Israel National Police, and fellow Hebrew University chemist Daniel Mandler have found that attaching hydrocarbons to gold nanoparticles is the key. The fat-seeking hydrocarbons guide the gold to the skin impression and lay down a metal trail. If this treatment is followed with the conventional solution, the gold catalyzes the precipitation of metal in solution, and the resulting fingerprints are far sharper, the scientists report in the current issue of *Chemical Communications*.

The new method could be "revolutionary" for crime fighting, says Antonio Cantu, chief forensic scientist for the U.S. Secret Service in Washington, D.C. But first, says Almog, it has to be refined, standardized, and field-tested in police labs.

Oregon Sea Monster

Some fossils are rare, but this one recently unearthed in eastern Oregon may be positively mythic. In life, the 2-meter-long Jurassic seagoing crocodile (above), discovered by members of the North American Research Group, sported scales, needlelike teeth, and a fishtail. Some paleontologists, including Stanford University researcher Adrienne Mayor, think similar fossils may have inspired Native American representations of water monsters. Mayor notes the croc's "remarkable" resemblance, for example, to a 19th century Kiowa artist's drawing (inset) of a legendary water serpent.

Modern Humans in Borneo

An international team claims to have nailed the earliest evidence for *Homo sapiens* in Southeast Asia—to about 46,000 years ago.

In 1958, excavators working at Niah Cave on the island of Borneo unearthed a skull cap and upper jaw of an anatomically modern human. Although radiocarbon dating of nearby charcoal fragments put the age at about 40,000 years, many experts suspected the skull was a newer "intrusion" into an older layer.

Since 2000, researchers led by archaeologist Graeme Barker of Cambridge University in the United Kingdom have been reexamining the site. New radiocarbon dates, reported in the March issue of the *Journal of Human Evolution*, show that the cave was continuously occupied between 46,000 and 34,000 years ago. What's more, the group has now been able to date the skull itself, using a technique called uranium series that revealed it was up to 37,000 years old.

The scientists contend that Niah Cave is the earliest securely dated sighting of modern humans in Southeast Asia. They also uncovered evidence that the occupants were sophisticated hunter-gatherers, hunting pigs and monkeys and detoxifying poisonous yams and nuts before eating them.

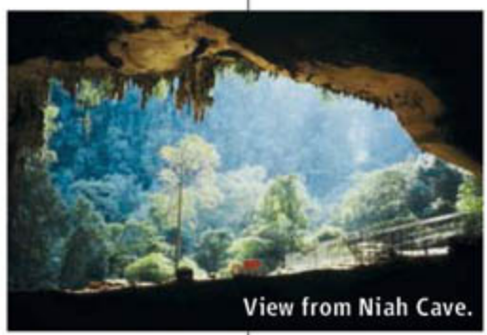

View from Niah Cave.

Sandra Bowdler, an archaeologist at the University of Western Australia in Crawley, says the new dates "suggest that we can forget about the skull being from an intrusive … burial." James O'Connell, an archaeologist at the University of Utah in Salt Lake City, adds that the work shows that the Niah Cave people's sophisticated subsistence activities "were practiced at a surprisingly early date."

CREDITS (TOP TO BOTTOM): JON HUGHES/NARG; SMITHSONIAN INSTITUTION; JIM SALGE/MOUNT WASHINGTON OBSERVATORY; NIAH CAVE PROJECT

Q: Where's the only place you can buy AAAS/*Science* merchandise?

A: Exclusively from the new AAAS Online Store!

AAAS members get your 10% discount

Visit www.apisource.com/aaas

If you're proud to be an AAAS member, here you can find carefully selected quality items that will let you wear your membership with pride. And, as another great benefit of AAAS membership, all members receive a discount of 10% or more on every item! To receive your discount, enter code SBN5 at the checkout.

As with all AAAS programs, a portion of each sale goes toward our vital educational outreach programs.

Don't wait—visit www.apisource.com/aaas and enter SBN5 for your discount.

Science
AAAS

EDITED BY YUDHIJIT BHATTACHARJEE

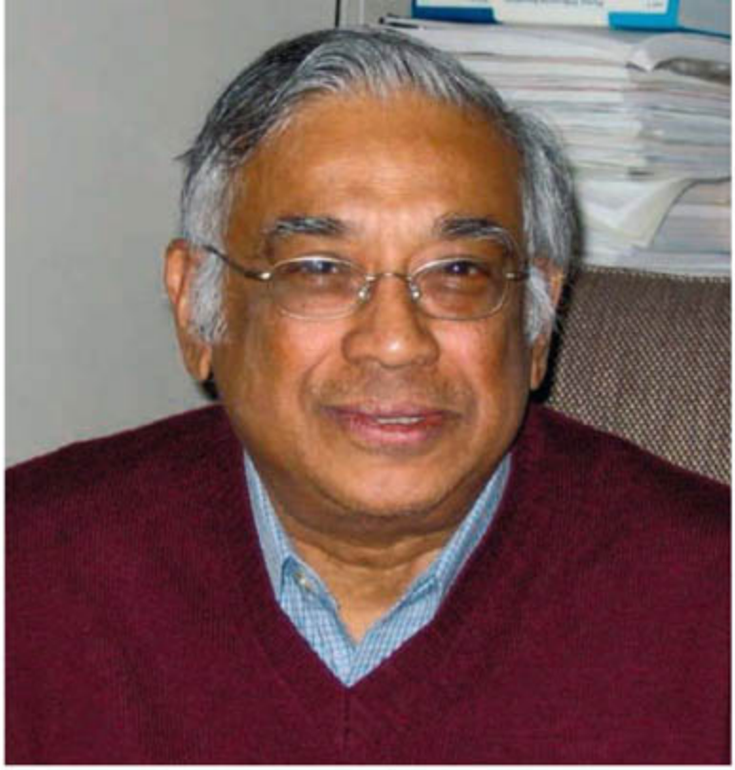

AWARDS

ABEL PRIZE. Srinivasa Varadhan, a probability-theory researcher at New York University (NYU) in New York City, has won the 2007 Abel Prize for mathematics. The $975,000 award—bestowed by the Norwegian Academy of Sciences and Letters—credits the 67-year-old Varadhan for "greatly expand[ing] our ability to use computers to simulate and analyze the occurrence of rare events."

Varadhan, who was born in Madras, India, earned a Ph.D. from the Indian Statistical Institute and since 1966 has taught at NYU's Courant Institute of Mathematical Sciences. His research on probability theory has the potential to benefit disciplines such as quantum field theory and traffic engineering.

Fittingly, in the manner of a random event, the prize announcement last week caught Varadhan by surprise. "It's still like a dream," he told *Science*. "A lot of people deserve it, but so few can get it."

MOVERS

CROSSING BOUNDARIES. Neurobiologist Carla Shatz is returning to her roots. This summer, she will step down as chair of Harvard's neurobiology department and return to California to lead the Bio-X program at Stanford, where she held her first faculty position from 1978 to 1991. "I'm thrilled," says Shatz. "Stanford is really on a roll with an experiment I want to participate in."

Bio-X is an attempt to foster interdisciplinary research in biomedicine. Its flagship building, the James H. Clark Center, has already proved to be fertile ground for interdisciplinary collaborations among its 600 researchers—including 38 faculty members—drawn from 25 departments, Shatz says, and she hopes to encourage more participation from others on campus.

Shatz was the first woman to earn a doctorate in neurobiology from Harvard, in 1976, and in 2000, the first woman to chair Harvard's neurobiology department. It hasn't escaped her notice that only five Clark Center faculty members are women. "I want to do something about that."

SAILING. Having guided the Thomas Jefferson National Accelerator Facility through difficult times, laboratory director Christoph Leemann plans to step down once his replacement is chosen. Leemann, 68, plans to spend more time sailing, including racing a monohull Hobie 33. Last year, Leemann had to batten down the financial hatches at the lab in Newport News, Virginia, to deal with a budget cut from $86 million to $78 million. But the future looks brighter, as the Department of Energy's (DOE's) science budget grows and researchers make progress on an accelerator upgrade.

"One should always leave at the top of one's game," Leemann says. Leemann assembled a top-notch scientific and technical staff, says Dennis Kovar, who directs DOE's nuclear physics program: "He's been a joy to work with."

CREDITS (TOP TO BOTTOM): CHERYL SYLVANT; GREG ADAMS/JEFFERSON LAB; STANFORD UNIVERSITY; SOURCE: HEMA RANGASWAMI

Got a tip for this page? E-mail people@aaas.org

On Campus >>

BLURRED IMAGE. A U.S. journal and an Indian panel have lined up on opposite sides in a case of alleged plagiarism involving a young Indian researcher whose degree hangs in the balance.

Early last year, an anonymous e-mail claimed that a 2005 paper in the *Journal of Biological Chemistry* (*JBC*) co-authored by Hema Rangaswami, then a Ph.D. student at the National Centre for Cell Science in Pune, India, contained images that appeared in an earlier *JBC* paper by the same authors. Last month, *JBC* withdrew the paper. Shelagh Ferguson-Miller, chair of *JBC*'s publications committee, says a computer-assisted analysis found that two control blots were identical to images that had been labeled differently in a 2004 publication. "To us, it seemed there had been deliberate misrepresentation," she says. The paper examines signaling pathways involved in the development of skin cancer.

Five months before the retraction, however, a scientific panel set up by the Indian government to investigate the charge found no evidence of image duplication or misconduct. Govindarajan Padmanabhan, a biologist at the Indian Institute of Science in Bangalore, who headed the Indian panel, says the panelists grilled the researchers and examined original data.

Rangaswami received a provisional degree last year and now works as a postdoc at the University of California, San Diego (UCSD). Her supervisor, UCSD cancer biologist Renate Pilz, says she has reviewed Rangaswami's work and believes the *JBC* paper is valid. Right now, Rangaswami has more on her mind besides completing her defense: This month, she gave birth to her first child.

A famous genome
1780

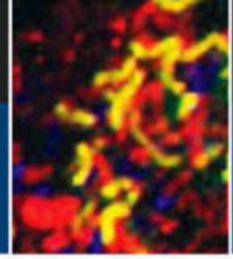

Microbial metagenomics
1781

GENDER EQUITY

U.S. Agencies Quiz Universities On the Status of Women in Science

The U.S. government has begun questioning research universities to determine whether their treatment of women students in science and engineering violates federal law. *Science* has learned that officials from the National Science Foundation (NSF), the Department of Energy (DOE), and NASA have visited four academic departments on three campuses in the past 14 months to monitor their compliance with a 1972 law that prohibits sex discrimination in educational programs and activities receiving federal funds. The law's Title IX has traditionally been used to broaden women's participation in high school and college athletics; educators say it's the first time the government has applied it to long-standing gender imbalances in fields such as physical sciences and engineering.

"I'm delighted that a start has been made," says Debra Rolison, a chemist at the Naval Research Laboratory in Washington, D.C., and longtime advocate for the enforcement of Title IX in academics. "This will push science and engineering departments to work harder to recruit and retain female students and faculty."

Team players. Amber Miller's experimental cosmology lab at Columbia University.

CREDIT: DAVID TAM/COLUMBIA UNIVERSITY

Women are underrepresented in several areas of U.S. science: For example, only 22% of graduate students in engineering, and fewer than 10% of engineering professors, are women. Although some argue that such imbalances merely reflect personal preferences, others blame a male-oriented culture within many science and engineering departments. A 2004 report by the Government Accountability Office, which scolded NSF, DOE, and NASA for not checking to see whether their grantees are complying with Title IX, prompted the current round of reviews. In 2005, Congress also ordered NASA to do two such reviews a year.

In spring of last year, DOE officials visited Columbia University's physics department to conduct the agency's first-ever onsite Title IX compliance review. NSF officials did the same thing around the same time at Columbia's electrical engineering department. And NASA officials looked at the aerospace engineering departments at the University of Michigan, Ann Arbor, and the University of Maryland, College Park. In addition to examining grievance procedures, reviewers interviewed dozens of female students and faculty members about access to laboratory facilities and the general climate of their departments, as well as gathering data on enrollment and faculty composition. NASA's David Chambers says his team deliberately asked "who was in a leadership position and who was doing the note-taking" as well as whether male and female graduate students were equally likely to get research assistantships. NSF has reported its findings to Columbia, whereas DOE and NASA plan to share reports with the universities this spring.

The nature of those interviews was annoying to some. At Columbia, cosmology professor Amber Miller described her DOE interview as "a complete waste of time." The reviewers "made us write down every piece of equipment in the lab," she says, and whether women were permitted to use each item on the list. She says the interviewer responded to her generic complaint about a shortage of lab space to press her on whether she felt discriminated against as a woman. "I wanted to say, 'Leave me alone, and let me get my work done,' " says Miller.

Columbia's Department of Physics Chair Andrew Millis thinks that the reviewers' concern about access to equipment suggests that they don't really understand basic academic science. "For God's sake, everybody is so desperate for good graduate students that gender is the last thing that faculty members are looking at when considering applicants," he says. "Frankly, the process has been a little tedious."

But other academics say that questions about climate are appropriate. "To understand if women face barriers, you have to look at the experiences of individuals in the department," says psychologist Abigail Stewart, head of Michigan's Institute for Research on Women and Gender, who was interviewed during the NASA review. Jocelyn Samuels of the National Women's Law Center, a Washington, D.C., nonprofit that has pushed for compliance reviews, applauds the government for looking beyond obvious metrics such as the number of women students and faculty members in a particular department. "Sex discrimination in labs ranges from outright harassment and sexual overtures to expressions of doubt about women's capabilities and exclusion of women from social gatherings where lab matters may be discussed," Samuels says.

Agency officials did not explain the basis for determining compliance and have not said what would happen if they uncover evidence of discrimination. But one DOE official noted that "this is not a 'Gotcha!' exercise. It is just a matter of ensuring that everybody gets equal opportunity."

Whereas DOE and NASA plan to continue their reviews, NSF's Ronald Branch says that an interagency group within the White House Office of Science and Technology Policy (OSTP) is now leading the Administration's effort to monitor compliance. OSTP did not return calls seeking comment.

–YUDHIJIT BHATTACHARJEE

Back in the enrichment business?
1782

Looming threat to the breadbasket
1786

GENETICS

Selfish Genes Could Help Disease-Free Mosquitoes Spread

"Inspired by a true story"—that could have been the subtitle for a new study that brings the idea of disease-fighting mosquitoes a step closer. Researchers borrowed an idea from real life and, like Hollywood screenwriters, adapted it to suit a different plot.

The paper, published online by *Science* this week (www.sciencemag.org/cgi/content/abstract/1138595), addresses a crucial but often overlooked question: Even if you can make mosquitoes unable to transmit disease, how do you enable them to "replace," or outcompete, the natural population? The study team, led by molecular biologist Bruce Hay and postdoc Chun-Hong Chen at the California Institute of Technology in Pasadena, answered it by producing a set of "selfish" genes in *Drosophila* fruit flies. The same principle could be applied in mosquitoes as well, they say. "This the most exciting thing I have seen [in this area] for a very long time," says Jason Rasgon, an insect geneticist at Johns Hopkins University in Baltimore, Maryland.

The plan to battle disease using transgenic insects has been around for years. Scientists have already spliced into mosquitoes genes that make them unable to transmit dengue, a painful viral disease, and the rodent form of malaria. A malaria-resistant version of *Anopheles gambiae*, the mosquito whose bite kills more than 1 million people a year, is expected to arrive soon. Almost $40 million from the Bill and Melinda Gates Foundation has given the field a big push and may help pay for trials in giant greenhouses within a few years.

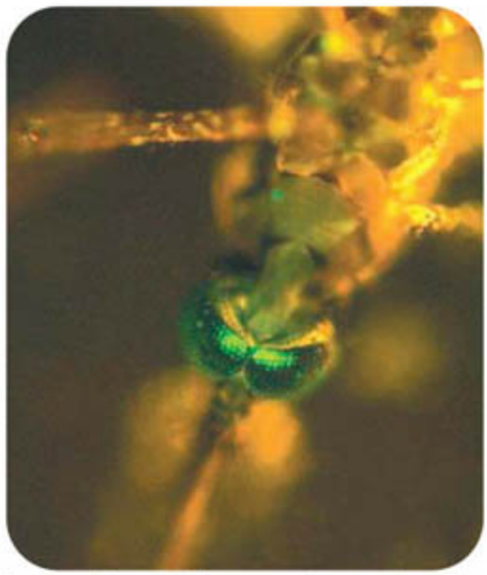

Leg up. A new study suggests a way to make transgenic insects—such as this malaria-resistant mosquito, created by a team at Johns Hopkins University—spread rapidly.

Yet one big question remains: Nobody quite knows how to give an introduced resistance gene an evolutionary leg up so that it becomes widespread. Natural selection alone probably won't do it. It's true that having a virus or parasite reproducing in its body does reduce a mosquito's fitness, and a lab study published in the *Proceedings of the National Academy of Sciences* (*PNAS*) last week showed that malaria-resistant mosquitoes beat out their nonresistant rivals in the struggle for survival—if both were feeding on malaria-infected mice. In real life, however, only a small proportion of mosquito hosts are infected, says Rasgon, one of the *PNAS* paper's authors, so resistance doesn't offer a big enough benefit to make it race through a population. Some sort of active "driver" is needed.

Hay found inspiration for such a mechanism in a bizarre selfish genetic element first described in 1992 in a beetle called *Tribolium castaneum*. When female beetles carry even a single copy of this element, all their viable offspring have it, too; those that don't simply die. As a result, the element, called Medea, spreads through populations rapidly. ▶

PROFESSIONAL SOCIETIES

ACS Drops Iranian Members, Citing Embargo

The American Chemical Society (ACS) has reluctantly rescinded the membership of some 36 Iranian scientists after the society determined that having members in Iran violates U.S. law. The society hopes to reinstate them after obtaining a government license, a step that could set a precedent for other U.S. societies with Iranian members.

U.S. organizations are prohibited from doing business with individuals in Iran, Cuba, and North Korea, but an exemption permits the trade of informational materials. That provision allows U.S. scholarly societies, whose journals are a major benefit to its overseas members, to retain ties to members in those countries.

But ACS's stance changed after Assistant General Counsel David Smorodin reread the embargo rules and concluded that selling publications to members at discount rates, a common practice, represents a service above and beyond the trade of informational materials. He also believes that membership benefits such as "insurance, career counseling, invitation to meetings, and educational opportunities" are not exempt under the rules, although he acknowledges that overseas members typically do not use those privileges. "We had no choice as a federally chartered organization but to comply with the law," says Smorodin, adding that his interpretation of the regulations did not "win [me] any friends within the ACS."

In January, ACS's membership office informed the society's 36 Iranian members that their memberships were being discontinued, although they could still purchase materials from the society at the full rate. The move angered David Rahni, an Iranian-American chemist at Pace University in Pleasantville, New York, and an ACS member, who says ACS should "refrain from allowing politics" to get in the way of scientific openness. Smorodin says the society will soon apply for a license from the Department of Commerce's Office of Foreign Assets Control allowing it to serve its Iranian members.

Other associations are troubled by ACS's proposed solution. "We have no plans to do anything similar," says Judy Franz of the American Physical Society in College Park, Maryland, which also has members in Iran. "We would resist having to obtain a license to the extent we can."

–YUDHIJIT BHATTACHARJEE

CREDIT: M. T. MARRELLI *ET AL.*, *PNAS* 104, 13 (2007)

Researchers have proposed that Medea produces a toxin during egg development, just before meiosis. That way, even if female beetles have only one copy of the element, the toxin ends up in all of their egg cells. After fertilization, the toxin kills the zygote—unless it has inherited the Medea element from either its mother or father. In that case, Medea produces a special antidote just in time to neutralize the toxin.

All of this is just a hypothesis to explain Medea's inheritance pattern, says Richard Beeman of Kansas State University in Manhattan, one of Medea's discoverers, who is still trying to nail down the mechanism. But Hay and Chen decided they didn't need to wait for the answer to build the proposed system, toxin and antidote included, from scratch in fruit flies.

The team spent years engineering flies to produce several kinds of toxins, such as ricin, in their egg cells, along with their respective antidotes. But making the insects produce exactly the right amount of toxin proved difficult. The team was luckier after it realized that the "toxin" didn't need to be a protein at all: It could also be the absence of one. They produced flies whose egg cells contain microRNAs that silence a gene called *Myd88*, whose protein product is crucial to pattern formation in the early embryo. Embryos resulting from these egg cells died. But if the embryos carried the team's Medea element, the "antidote"—in the form of an extra copy of the *Myd88* gene, switched on after fertilization—came to the rescue, and development was normal. "To create a synthetic Medea—what an amazing idea!" says Beeman.

And it worked. In cage experiments where Medea-carrying flies were mated with wild-type counterparts, Medea-carrying flies took over in 10 generations or fewer. By stitching a resistance gene into the genetic element—right between the genes for the toxin and the antidote—it should be easy to make that spread through a population as well, Hay says, although that experiment still needs to be done.

Applying the same strategy in mosquitoes will be quite a bit of work, says Anthony James of the University of California, Irvine. Also, researchers have no idea whether the public will endorse the release of genetically engineered insects. But, says Kenneth Olson of North Carolina State University in Raleigh, the new study is a big step forward in making the notion of transgenic mosquitoes fly.

–MARTIN ENSERINK

CLINICAL RESEARCH

Testing a Novel Strategy Against Parkinson's Disease

One of the largest clinical trials ever for Parkinson's disease, announced last week by the National Institute of Neurological Disorders and Stroke (NINDS) in Bethesda, Maryland, is experimental in more ways than one, officials say. It will use a novel approach to test a nutritional supplement against a disease, with a goal of recruiting 1720 participants (half to receive a placebo). And the method of selecting the test agent, a supposed energy booster called creatine, was unorthodox as well.

In 2000, the institute began canvassing the community for compounds worth testing against Parkinson's disease and whittled a list of dozens down to a handful of candidates for so-called futility trials. Rather than show whether the compounds work, these small studies suggest whether a drug is futile in combating the disease.

Creatine is the only compound of four examined so far to pass. NINDS is beginning to recruit early-stage patients for a large, phase III trial to see whether a purified medicinal version can slow the disease's progress. In another twist, the institute may add more compounds to the trial if they pass futility studies. "The whole thing is unusual," agrees Debra Babcock of NINDS of the creatine trial, for which she is the scientific director. "It's a very new clinical trial for us and a new approach for disease intervention."

Top candidate. A medicinal version of creatine, a popular nutritional supplement, will be tested as an anti-Parkinson's agent.

CREDIT: NAJLAH FEANNY/CORBIS

Babcock declined to give precise numbers on how much the trial will cost. But the entire venture, including futility trials of other potential Parkinson's compounds, is now expected to cost about $60 million, $20 million above the initial estimate, Babcock says. These estimates are "fuzzy," she explained, because NINDS doesn't know how many futility trials it will run or how the creatine trial will evolve in the 7 years it's expected to last.

Creatine, which is available over the counter in health food stores, is thought to help boost ATP levels in cells, giving them more energy and protecting mitochondria, which in Parkinson's patients seem to malfunction, leading to cell death. Whether creatine is promising enough to justify a massive, long-term clinical trial in a time of tight budgets is up for debate. "To be honest, I think the evidence is not tremendously strong" that creatine can help, says J. Timothy Greenamyre, director of the Pittsburgh Institute for Neurodegenerative Diseases at the University of Pittsburgh in Pennsylvania.

Another question is whether enough patients will sign up, because volunteers risk receiving a placebo. Recruiting may be "a major logistical challenge," says Joel Perlmutter, a neurologist at Washington University School of Medicine in St. Louis, Missouri, whose center is one of the 51 participating. Babcock hopes the offer of pure creatine will attract volunteers.

Although Perlmutter considers creatine promising, he's uncertain about its mechanism and how it might work against Parkinson's disease. Still, "even if creatine completely bombs," says Perlmutter, the trial may still help teach researchers how to run large-scale Parkinson's trials and identify new biomarkers.

–JENNIFER COUZIN

With reporting by Eliot Marshall.

RESEARCH FUNDING

Canadian Institutes Get Windfall Without the Bother of Competition

OTTAWA, CANADA—Several Canadian research institutes will receive multimillion-dollar grants from the government this year without having even asked for the money.

The government's unprecedented decision to dispense with peer review in awarding the grants—or even solicit advice on which programs to fund—comes as a huge surprise to the science community, which has questioned the process even as it welcomes the windfall. "I feel like I've been adopted by a rich grandmother," says David Colman, director of the Montreal Neurological Institute and Hospital, which will get nearly $13 million.

The gifts were wrapped in a 2007–08 budget, unveiled last week by Finance Minister James Flaherty, that boosts federal spending overall by nearly 5%. But the biggest twist in a budget that also hikes science and technology spending by a government-projected 5%, to $7.8 billion (*Science*NOW, 20 March, sciencenow.sciencemag.org/cgi/content/full/2007/320/1), is the proposed Centers of Excellence for Commercialization and Research. Finance and Industry ministry officials have already allocated some $130 million to eight institutions deemed best in class in fields that include brain research, stroke recovery, sustainable energy, and optics. The money is designed to help them compete next year for a new $165 million pot of money to support work in areas in which Canada hopes to become a world leader. "It's sort of proof-of-concept stuff," says one ministry official.

Colman says the money will expand fledgling research programs on neural engineering—using engineering techniques to understand and manipulate the behavior of the central and peripheral nervous systems—and neuropalliative care. He also applauds the government's willingness to reward the country's elite researchers with additional resources rather than trying to spread its wealth around. "This is what I like about this government. They're willing to say, 'These things are outstanding. And because they're outstanding, let's give them a little more, not a little less.'"

For one recipient, however, the government's current largess is already more than adequate. Howard Burton is director of the Perimeter Institute for Theoretical Physics in Waterloo, Ontario, which receives $42 million in the new budget. BlackBerry mogul Michael Lazaridis helped create the institute in 2000 with an $85 million endowment (*Science*, 5 December 2003, p. 1650), and the federal government chipped in $21 million. Ministry officials said that favorable reviews from an international panel evaluating that initial 5-year award persuaded them to pony up more money.

CREDIT: MONTREAL NEUROLOGICAL INSTITUTE AND HOSPITAL, MCGILL UNIVERSITY

Brain food. David Colman's Montreal Neurological Institute and Hospital is one of several getting more government funding.

"I'm very happy that we're held as an exemplar in terms of the research and the outreach that we do," says Burton about the institute's ongoing work in foundational theoretical physics, including string theory, quantum gravity, quantum information theory, cosmology, and particle physics. But he says it's "not our intention" to apply for a centers grant because federal and provincial funding is "sufficient" for the next 5 years.

The biggest complaint from scientists is that national politicians and bureaucrats identified and targeted disciplines for investment, and then picked individual winners, without benefit of scientific input and peer review. "It's a dangerous precedent," says Ronald Worton, chair of Research Canada: An Alliance for Health Discovery, a new advocacy group for the research community. "I have no problem with governments prioritizing and saying we're going to support [one discipline or another]," adds Worton, who is CEO and scientific director of the University of Ottawa Health Research Institute. "But there has to be a process to arrive at this that ▶

Stem Cell Results Questioned

The University of Minnesota (UMN), Twin Cities, is looking into a report of an irregularity in the work of researcher Catherine Verfaillie, a stem cell expert whose work has come under previous scrutiny. Fifteen months ago, *New Scientist* reported it had found data plots duplicated in two different Verfaillie publications, as well as confusing data relating to cell types cultivated in her lab from multipotent adult progenitor (MAP) cells. Although the duplication was ascertained to be an honest error, UMN got inconsistent answers from experts it consulted on the other data (*Science*, 2 March, p. 1207).

Earlier this month, *New Scientist* notified the school of a separate problem: The same Western blot image appears twice in a 2001 *Blood* paper—once as a control, then, with the image reversed, representing collagen. A U.S. patent application also contains the same image, this time signifying a bone protein. Verfaillie did not respond to a request for comment, although a Minnesota official says she has been cooperative. UMN is mulling the creation of an inquiry panel, which could recommend a "full investigation."

–CONSTANCE HOLDEN

The Hunt to Capture Carbon Is On

CAMBRIDGE, U.K.—The British government has committed itself to funding a full-scale demonstration of carbon capture and storage. Last year, the Labour government created the $200-million-a-year public-private Energy Technologies Institute, which will be up and running in 2008. In his 2007–08 budget statement delivered last week, Chancellor of the Exchequer Gordon Brown went a step further, promising to hold a competition for a carbon-capture demonstration plant. "We need to understand how the technology works in large, integrated projects so that we can develop it for deployment worldwide," says Hannah Chalmers of Imperial College London. Details will be released in May; the plant is expected to be operational early next decade.

Meanwhile, in the U.S. last week, a powerful group of Democratic and Republican senators proposed legislation to expand coal-sequestration research projects, including $300 million for "large-scale testing of carbon-sequestration systems." The government now runs a smaller-scale injection research program. The legislation (S. 962) incorporates many of the recommendations in a recent Massachusetts Institute of Technology report on coal research (*Science*, 16 March, p. 1481).

–DANIEL CLERY AND ELI KINTISCH

is robust and arrives at conclusions that are logical and transparent."

Worton is also upset with the size of the outlays at a time when the Canadian Institutes of Health Research (CIHR), Canada's leading funder of biomedical research, has seen success rates for competitive grant proposals plummet from 32% to 16% in the past 5 years. "That amount of money added to the CIHR would have solved the whole problem," he avows. The government announced it would raise CIHR's budget by 5%, to $627 million.

Canadian Association of University Teachers Executive Director James Turk says the new initiative not only sets a bad precedent but is also further evidence of the government's preference for strategic initiatives over basic research, both within and outside the granting councils. "Sprinkled through all their discussions on research is a greater focus on targeting," he says, "and the federal government choosing the targets." But Claire Morris, president of the Association of Universities and Colleges of Canada, says that "good things can happen [through] partnerships between the private sector, the public sector, and academia."

Details of the new program are sparse. The winning institutes will have to come up with some outside funding, although the amount will be higher for centers focused on commercialization than for those doing basic research.

–WAYNE KONDRO

Wayne Kondro writes from Ottawa.

GENETICS

Sequencers of a Famous Genome Confront Privacy Issues

A U.S. company has begun to trickle out information on a unique DNA study it calls "Project Jim," a crash effort to sequence the entire genome of a single individual. The results are likely to be made public this summer. Anonymity is out of the question: It has already been announced that the genome belongs to James D. Watson, winner of the Nobel Prize and co-discoverer of DNA's structure.

Watson won't be alone: Harvard Medical School has approved a plan by computational geneticist George Church to sequence and make public the genomes of well-informed volunteers—including his own. And J. Craig Venter says his nonprofit institute will soon release a complete version of his genome. (Venter contributed the largest share of otherwise anonymous DNA in the human genome sequenced by Celera Genomics in 2000.) These projects are adding urgency to an old issue: What constitutes sensitive genome data, and how should those data be safeguarded? As sequencing costs plummet, more and more individuals will be facing those questions.

Watson, 79, says he agreed to have his genome sequenced when he gave a blood specimen 2 years ago to 454 Life Sciences in Branford, Connecticut. His reason was simple: "curiosity about my life." He figures that, "On the whole, I will gain more from people looking at [the genome]" than not.

The company has a new "resequencing" technique that uses public data as a template and relies on massive DNA replication and computerized sorting to lower costs. It would like to show off its prowess. Michael Egholm, 454's vice president of research and development, said in a telephone interview that the company's "fundamental vision" is to make "routine human sequencing" affordable. 454 is one of several firms in a race to claim this territory (*Science*, 17 March 2006, p. 1544). Company staff debated "who should be the first" person to be sequenced, Egholm says. After a dinner with scientific advisers, including DNA sequencer Richard Gibbs, according to Egholm, they decided that "It had to be Watson." Watson not only accepted but also talked about it to the press.

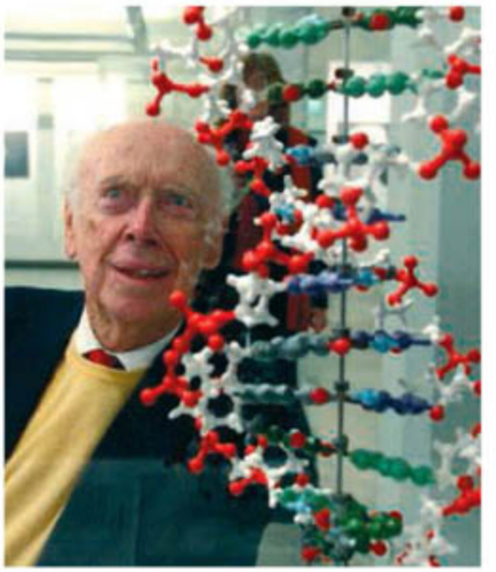

Know thyself. Nobelist James Watson is planning to receive—and possibly share—a complete copy of his own genome sequence this year.

When the project began, 454's equipment wasn't up to the task, Egholm says. But improved technology made it possible to sequence 10 billion bases in multiple overlapping fragments of Watson's DNA "in a space of a few weeks" early this year. Egholm and 454's academic partners discussed preliminary findings at a meeting of sequencers in Marco Island, Florida, in February. For example, according to Egholm, a comparison between the new data and the reference human genome in public databases suggests that the reference genome is "about 97% complete." He adds that Watson's genome has now been sequenced in triplicate, and company leaders and Gibbs—who heads the sequencing center at Baylor College of Medicine in Houston, Texas—estimate that a few weeks' more work would achieve sixfold coverage, enough for a "very high quality diploid genome." The projected cost is "about $1 million."

Still undetermined, however, is precisely what the project will release. Watson agreed that his DNA sequence should be added to public databases. But he requested at the outset that his *ApoE* gene status—which can indicate a risk for Alzheimer's disease—be blanked out. Company staff then realized, Egholm says, that more might need to be blocked—perhaps all genetic loci currently known to be associated with disease risk. Opting to block only high-risk DNA variants would signal that Watson has those variants. Another problem: Some spots now considered innocuous may be linked to disease in the future—a consideration for Watson's sons.

As Baylor scientists got involved, Gibbs and ethicist Amy McGuire of Baylor's Center for Medical Ethics and Health Policy presented the project (without identifying Watson) to the college's Institutional Review Board (IRB). The first step was to obtain a more rigorous consent. That was done, and the IRB gave its approval on 19 March. But public agencies have given "very little guidance," McGuire says, on how to handle privacy and consent issues involving relatives.

Baylor and 454 settled on a "data release pathway," McGuire and Egholm say. The company will put the completed genome on a DVD and hand it over to Watson—perhaps, Egholm says, with a small ceremony. Watson will accept responsibility for discussing the risks of its release with his family, decide what should be blocked, and determine how and when to make the sequence public. Watson declines to say more until the company is ready to publish an article—by July, he expects.

As for Venter, he says he plans simply to release his genome without restrictions.

–ELIOT MARSHALL

CREDIT: MARKUS SCHREIBER/AP PHOTO

METAGENOMICS

Massive Microbial Sequence Project Proposed

Taking stock of the microbial world is like trying to count the stars. But a report* released this week by the U.S. National Academies' National Research Council (NRC) outlines an ambitious program to decipher the incredible diversity of Earth's invisible life. The Global Metagenomics Initiative would be on par with the Human Genome Project in size and relevance. "Understanding the microbiome—human, animal, and 'environmental'—is as important as the human genome," says Michael Ashburner, a geneticist at the University of Cambridge, U.K., and a co-author of the report.

A decade ago, researchers were limited to studying only the microbes they could isolate and grow in the lab—less than 0.1% of Earth's estimated microbial life. Now, they can sequence all the DNA from millions of different microbes in a sample and use powerful computers to pick out the genes. This technology—metagenomics—has enabled them to identify genes from the full complement of microbes in a particular environment, be it the ocean, sewage sludge, or the human colon (*Science*, 16 March 2007, p. 1486; 2 June 2006, p. 1355).

Already, these approaches are revealing that microbes play a far bigger role in human health, agriculture, and the environment than previously realized. "Every process and event on Earth and in its inhabitants is directly or indirectly influenced by microorganisms," says Jo Handelsman, a plant pathologist at the University of Wisconsin, Madison, and co-chair of the NRC panel. Microbial proteins may hold the key to cleaning up toxic wastes; developing "green" fuel sources; catalyzing the production of industrial products, food, and drugs; and protecting against bioterrorism, the report says.

Soaring interest in these possibilities prompted the National Science Foundation (NSF) and other U.S. federal agencies to ask the National Academies to help define the field, establish standards for metagenomics research, and come up with goals for this emerging discipline. The NRC panel calls for a three-pronged approach: single-investigator studies, medium-sized projects, and three large-scale examinations of the microbes that live in particular habitats. The experts suggested that one project cover a natural environment, one look at microbes that live in human or other hosts, and a third focus on a community created by people—such as a sewage treatment plant.

Researchers are already headed in that direction. Last year, NSF awarded the new Center for Microbial Oceanography: Research and Education, based in Hawaii, $19 million over the next 5 years. A human microbiome initiative is under consideration as a priority for the National Institutes of Health in 2008. Researchers from eight European countries have banded together to seek support for a €16 million effort on human gut microbes, and a joint French-Chinese metagenomics project is being planned.

The NRC panel also recommends increased funding to improve the collection, storage, and analysis of the massive amounts of genomic and environmental data involved. "Extracting information from the [sequence] data, that's a hard problem," says Daniel Drell, who coordinates metagenomics projects for the Department of Energy.

As for comparisons with that earlier sequencing effort: "This is not like the human genome project, where you know when you are at the end," says James Anderson, a microbiologist at the National Institute of General Medical Sciences in Bethesda, Maryland. "How big this project might be is anyone's guess." **–ELIZABETH PENNISI**

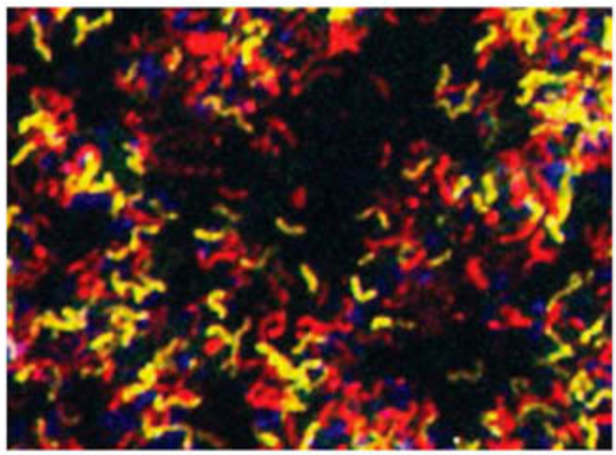

Microbial genes revealed. Researchers can now study many different microbes (in different colors) in a sample at once.

CREDIT: VINCENT DENEF/UC BERKELEY

* *The New Science of Metagenomics: Revealing the Secrets of Our Microbial Planet*, books.nap.edu/catalog/11902.html

Sharing the Flu (Data)

Nations on both sides of the Pacific have established a distributed computing grid to improve research collaborations on avian influenza. The flu project, announced last week in Bangkok, will be managed by the 5-year-old Pacific Rim Applications and Grid Middleware Assembly (PRAGMA) project, based at the San Diego Supercomputer Center (SDSC). Scientists in the United States, Japan, China, South Korea, and Malaysia will be able to remotely operate lab equipment and share access to databases. The grid will have applications for other infectious diseases as well, says Peter Arzberger of SDSC. The project has $350,000 in start-up funding from the U.S. Army.

–MATTHEW BUSSE

Stem Cell Work Restarted

SEOUL—South Korea's National Bioethics Committee has decided to allow scientists to resume studies on human embryonic stem cells, removing a ban imposed in March last year after the Woo Suk Hwang scandal. Last week's decision barred transfers of human cells into animal eggs and egg donations solely for research purposes, allowing donations only of unused eggs collected originally for in vitro fertilization. South Korea's National Assembly will review the rules, which include a 3-year research ban for violators, before incorporating them in an expected bioethics bill later this year. **–D. YVETTE WONG**

Change of FACE?

The U.S. Department of Energy (DOE) is rethinking a move to stop funding long-running studies of the impacts of elevated carbon dioxide levels on various ecosystems. Forest ecologists Ram Oren of Duke University and Richard Norby of Oak Ridge National Laboratory say that DOE told them in January that five of the six sites in the $7-million-a-year Free Air CO_2 Enrichment (FACE) effort—which include forests, a desert, and a farm—could be phased out as soon as 2008. Last year, a DOE panel had suggested that the department allow some projects to continue until 2010, and scientists have been lobbying DOE for a reprieve. This week, DOE official Jerry Elwood told *Science* the department is weighing the 2010 date for some projects but that he wants to make room for new research on what happens when elevated CO_2 levels are combined with other factors such as nutrients or temperature. **–ELI KINTISCH**

Spinning a Nuclear Comeback

A U.S. company is banking on the world's biggest and fastest centrifuges to restore the country's capacity to produce enriched uranium for nuclear power plants at home and abroad

PIKETON, OHIO—It's not easy to get a glimpse of the "American Centrifuge." A visitor must first clear a checkpoint at the edge of the Department of Energy's (DOE's) 1500-hectare Portsmouth reservation in southern Ohio, then pass through several sets of locked and guarded gates. Finally, one reaches the gargantuan, dimly lit centrifuge hall holding the centrifuges themselves—four-story-tall white ghosts, just a few of them so far, looming in the twilight.

Inside each one is a cylinder, called a rotor, that spins faster than the speed of sound. By separating one isotope of uranium from the other, the cylinder slowly increases the concentration of uranium-235. Hooking together thousands of these devices in a cascade yields a fuel rich enough to sustain a nuclear chain reaction.

This technology, a key to acquiring nuclear weapons, is one of the most tightly guarded in the world. In the desert south of Tehran, Iranian engineers are also trying to master the intricacies of the centrifuge. If they succeed, Iran could become one of a handful of nations with a full-scale centrifuge enrichment plant (see map). The United States, currently, is not among that select group. Its membership expired in 1985 when DOE abandoned the centrifuge facility here.

Now the U.S. Enrichment Corporation (USEC), a private company that took over the government's uranium-enrichment operations in 1993, is trying to bring both the building and the technology back to life. The $2.3 billion project would employ thousands of centrifuges and turn the Piketon facility into a source of enriched uranium for nuclear power plants in the United States and around the world. The facility would replace USEC's aging and unprofitable enrichment plant in Paducah, Kentucky, which uses a less efficient technology called gaseous diffusion.

USEC's engineers have retrieved drawings from locked vaults and rediscovered long-forgotten technical skills. "It's like reliving your youth," says Dean Waters, one of the project's leaders. "You almost have to pinch yourself: 'How can I be doing this again?'"

Global demand for enriched uranium is rising, and prices are soaring. Yet the future of the project remains uncertain. A small-scale demonstration of USEC's technology that was due to begin last autumn has fallen nearly a year behind schedule. Even if the technology works, some observers doubt that USEC has the financial muscle to build a full-scale plant. The company also faces increased competition from abroad.

Born in the USSR

The modern gas centrifuge was born in a Soviet camp for captured German and Austrian scientists after World War II. Ordered by Stalin's government to help build an atomic bomb, they took on the job of acquiring uranium-235, an isotope that comprises less than 1% of natural uranium mined from the earth. Low-enriched uranium, with up to 5% uranium-235, is used in power plants. Nuclear weapons contain highly enriched uranium, in which the concentration of U-235 exceeds 90%.

The imprisoned scientists came up with a solution that employs a simple and light tube, balanced on a needle and spinning more than 1000 times each second inside a vacuum chamber. When they fed uranium hexafluoride gas into the cylinder, centrifugal forces pushed the gas outward, against the spinning wall. Atoms of uranium-238, being heavier, concentrated against the wall and also moved toward one end of the rotor. The lighter U-235 moved toward the other end.

The Austrian mechanical engineer Gernot Zippe, one of the leaders of the team, carried this design—in his head, of course—to the West when the Soviets released him in 1956. "At first, I did not want to have anything to do with this highly secret [technology] anymore," said Zippe in a 1992 interview with this reporter. But he soon changed his mind: "I saw that the West was far behind what we did in Russia, and I decided that it would be wrong to leave this to the Russians." Zippe,

Building capacity. Several new centrifuge facilities are under development in anticipation of increased demand.

SOURCE: ISIS, NUCLEAR ENERGY DATA (2003) OECD, *WORLD NUCLEAR HANDBOOK* (2003), AND COMPANY STATEMENTS

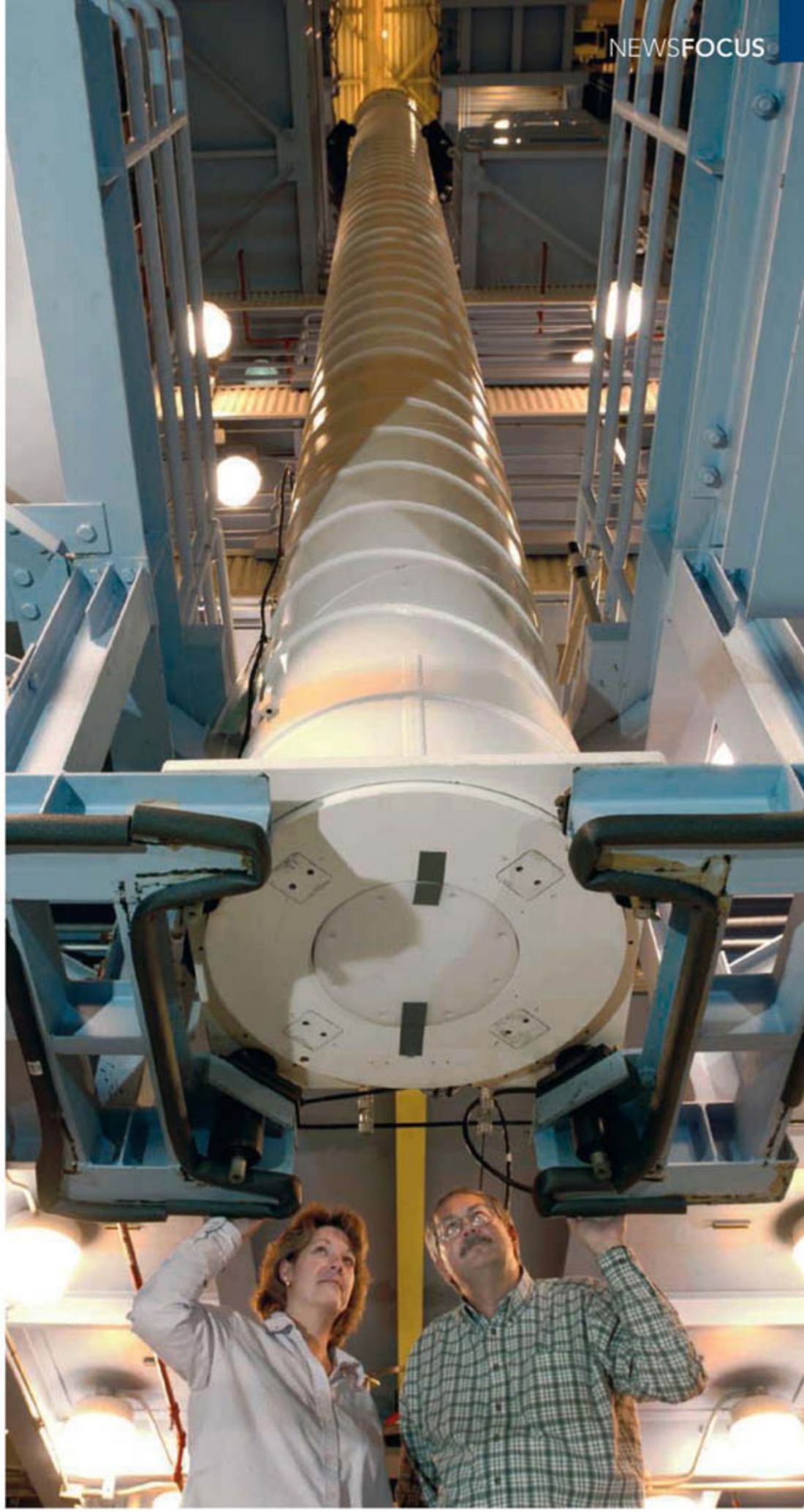

Cylinder of secrets. USEC's Jennifer Slater and Bob Lykowski inspect a centrifuge in Piketon, Ohio. USEC digitally erased some sensitive features from this image.

CREDIT: USEC

who lives near Munich, shared his secrets first with the U.S. government, then with an industrial consortium in Europe called Urenco. The longer a centrifuge's rotor is, and the faster it spins, the more effectively it can separate two isotopes. But this creates huge engineering challenges. Velocities around 600 meters per second, now typical for spinning rotors, test the limits of even the strongest materials. As rotors accelerate, they pass through unstable phases called "critical speeds," where the rotor's shape shifts slightly. The slightest imbalance can cause a rotor to crash catastrophically, and minor stresses will cause bearings to fail.

Each heir to Zippe's invention developed a different version of it. Soviet engineers filled enrichment plants with millions of centrifuges, each one less than 1 meter tall. For many years, they made only small changes to Zippe's original, tried-and-true design. In contrast, Urenco created more powerful machines by increasing both the length and the speed of the rotors. And the U.S. effort, which began in 1960 at Oak Ridge National Laboratory (ORNL) in Tennessee, created the world's largest and most powerful centrifuge. "We started with the original Zippe machine" and improved it, says Waters, who was among the first scientists to work on the centrifuge at ORNL. "Then, within about 6 years, we discovered how to build the kind of machine that we're building today."

That machine, developed during the 1970s and early 1980s, stood about 14 meters tall and could enrich uranium five times faster than any Urenco centrifuge of its time. In the early 1980s, DOE began building a home for it on the Portsmouth reservation, right next to an existing gaseous diffusion enrichment plant. By 1985, more than 1300 machines had been installed in the new facility.

That buildup, however, coincided with the tanking of the U.S. nuclear industry. Faced with plunging estimates of future demand for enriched uranium, DOE officials pulled the plug on the project. For 20 years, the mothballed centrifuges stood idle in silent rows, a mausoleum of secret technology. "We had the feeling that someday those buildings would be like Stonehenge," says Houston Wood III, a centrifuge expert at the University of Virginia in Charlottesville who worked on the project. "People would come and wonder, 'What were they thinking?' "

Recovered memories

There is, in fact, a Stonehengian quality to the Piketon plant. Its scale is massive—the buildings cover 160,000 square meters—and its peculiar architectural features reflect the unique demands of its very tall and very fragile tenants: doors five stories high, for instance, and concrete floors that float on a vibration-absorbing foundation.

From 1985 until last year, these buildings were used only to store containers of waste from the nearby gaseous diffusion plant. Now they are coming back to life. Over the past 2 years, the centrifuges were dismantled, shipped to a classified landfill at the Nevada Test Site, and buried. The first of a new generation of centrifuges, identical-looking but quite different inside, are now arriving.

The revival began in 1999, when USEC decided to bet its future on centrifuges after the rising cost of electricity made USEC's 50-year-old gaseous diffusion plant ruinously expensive to operate. The company went looking for people who knew something about the technology. "A surprising number were still at Oak Ridge," says Waters, one of many nearing retirement. "Frankly, I don't think we would have resurrected this had that not been the case."

USEC signed up ORNL as a partner. Waters helped retrieve piles of old technical reports, computer programs, and centrifuge-related equipment from a laboratory vault. The know-how stored in human brains was even more valuable. "You can never put precisely into a document everything that you know," says Waters.

The team set about recreating its earlier centrifuge, with one crucial difference. The new machine features a rotor made from woven carbon fiber rather than fiberglass. This stronger rotor can spin faster—how much faster, USEC officials won't say. But it has made the world's most powerful centrifuge even more so.

A centrifuge's ability to enrich uranium is measured in "separative work units" (SWU). According to Daniel Rogers, director of the plant in Piketon, each new centrifuge can perform 350 SWU per year. By contrast, the machines that sat unused in the Piketon plant for 20 years were rated at about 200 SWU per year. Julian Steyn, president of the consulting firm Energy Resources International in Washington, D.C., says the latest Urenco centrifuges, which have carbon-fiber rotors about 6 meters long, can run at 70 to 80 SWU per year.

Is tall and fast a winner?

USEC officials like to compare their machine to a Mercedes. In contrast, says one, Urenco's resembles a Volkswagen. A company slide show states it bluntly: "Taller and Faster is Better."

USEC will need only one-fifth the number of centrifuges as Urenco to produce the same amount of enriched uranium. But USEC's large centrifuges may be more costly to manufacture and to maintain. And reliability is even more important, says Steyn. USEC's centrifuges will have to operate flawlessly for decades to hold their own against Urenco's stable of centrifuges.

Waters believes that his new centrifuge will prove the doubters wrong. In the 1970s and 1980s, he says, "we achieved reliability that was on the same order of magnitude as Urenco's. We have several examples of extremely reliable cascades. The people who did that are working on this program today."

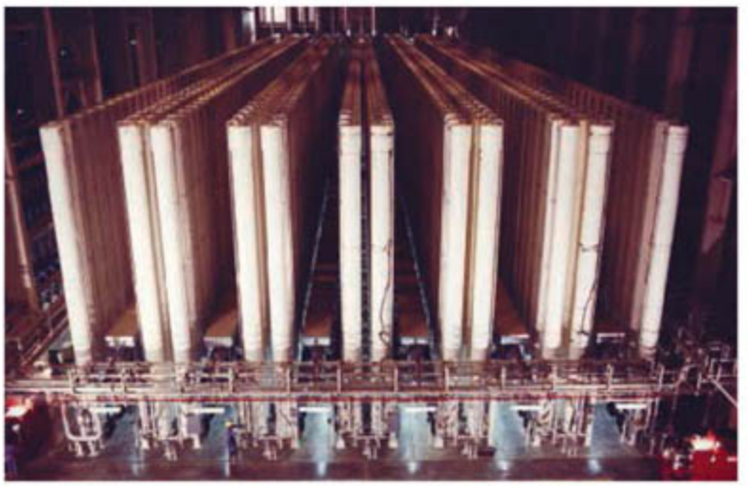

Expired. The 1300 centrifuges at the Piketon facility in 1985 were never used; they are buried in a classified Nevada landfill.

USEC is also facing a financial pinch. In U.S. Securities and Exchange Commission filings last month, USEC estimated that a full-scale centrifuge facility will cost $2.3 billion. The company admitted that it will need "some form of investment or other participation by a third party and/or the U.S. government" to get a new plant running.

Most observers don't think Uncle Sam is likely to help out. Once a tightly held government monopoly, the business of uranium enrichment is now—at least in the United States and Europe—dominated by commercial priorities. Failing companies face bankruptcy rather than a government bailout.

For the first time, USEC also faces possible competition on its own turf. With its eye on the U.S. market, Urenco has acquired preliminary approval for a full-scale centrifuge plant and has broken ground near the town of Eunice, in southeastern New Mexico. Production is scheduled to begin in 2009. Meanwhile, GE Energy is testing another approach to uranium enrichment in Wilmington, Delaware, using lasers that are tuned to excite particular isotopes. GE Energy licensed this technology from an Australian company. "There's not enough enrichment capacity in the West," explains Steyn. Many U.S. power plants currently use fuel that originally came from the Russian stockpile of highly enriched uranium. But the deal that makes this possible will expire in 2013.

Some nuclear proliferation experts worry that the Piketon facility could be a tempting target for nations trying to develop nuclear capabilities. Urenco, the first of the commercial enrichment companies, was the source of centrifuge technology that aided nuclear efforts in Pakistan and other countries. In particular, A. Q. Khan, a Pakistani metallurgist who worked for a Urenco contractor in the Netherlands in the early 1970s, obtained details of centrifuge design before returning to Pakistan, where he led that nation's successful efforts to create a nuclear bomb.

Noting that USEC, like Urenco, plans to rely on contractors to manufacture most of the centrifuge components, Harvard University proliferation researcher Matthew Bunn says that "the more different sets of people have their eyes on parts of the centrifuge, the more chance there is for that technology to leak." Rogers, however, says that USEC has tightened security in recent years to address growing proliferation concerns.

USEC's next step is construction of a small pilot cascade, with up to 240 centrifuges, inside the Piketon plant. The pilot will persuade potential investors that the American Centrifuge is both technically and economically viable, says Rogers. It's running slightly behind schedule: The "lead cascade" was expected to start up last fall, but USEC is now aiming for the end of this summer.

Virginia's Wood hopes that it succeeds, putting the United States back into the big leagues of uranium enrichment. "USEC has a tough road, but I'm pulling for them," he says. "I would hate [for us] to be the only country in the world that doesn't have a centrifuge plant." **–DAN CHARLES**

Dan Charles is a freelance science writer in Washington, D.C.

CREDIT: USEC

CREDIT: COURTESY OF THE SCRIPPS RESEARCH INSTITUTE

Gentle giant. Baran (*center*) is pioneering an effort to streamline the synthesis of natural products.

PROFILE: PHIL BARAN

Chemical High-Flyer's Strategy: Take Away the Safety Net

Synthetic chemists take great pains to ward off unwanted reactions. A young researcher says they can save time—and learn new science—by dropping their defenses

The way synthetic chemists tell it, *three* things in life are unavoidable: death, taxes, and protecting groups. Phil Baran can't do much about death or taxes. But the 29-year-old chemist at the Scripps Research Institute in San Diego, California, is making considerable headway on the third item: a class of molecular stoppers that chemists append to key sites on their molecules to keep unwanted reactions from creating chemical garbage. Among the scientific artisans who craft big, unwieldy molecules—the sort that biology has spent eons perfecting—protecting groups are a must. But they carry a high price tag. Tacking them on and later stripping them off adds so many steps to a typical synthesis that they make the work maddeningly hard and the final yield of the desired compound vanishingly small.

In his young career, Baran has set out to find an alternative to waging this synthetic battle. His solution has been to develop a sort of molecular judo that takes advantage of a molecule's reactive propensities rather than trying to fight them head on. This "gentle way," as a judo master might call it, is beginning to show its strength. Last week, Baran and his students unveiled the latest displays of their technique in papers in *Nature* and the *Journal of the American Chemical Society*, which showed that they could make a variety of highly complex, naturally occurring molecules while either minimizing the number of protecting groups or doing away with them altogether. Earlier this week, such feats also helped Baran reel in this year's National Fresenius Award, which the American Chemical Society gives to a promising chemist under 35.

Baran isn't the first chemist to try to do more with less. But doing away with protecting groups for synthesizing complex natural products is rare. That's because large organic compounds are studded with sites known as functional groups that are difficult to control, says Jie Jack Li, a medicinal chemist at Pfizer in Ann Arbor, Michigan. "For large molecules, there are so many functional groups, it's hard to touch one and not the others," Li says. The typical solution: protecting all but one to avoid the problem.

Baran's gentler display of control is flooring many of his colleagues. "This guy is an off-the-scale youngster who towers above everyone else in his age group," says Elias J. Corey, a chemist at Harvard University who won the 1990 Nobel Prize in chemistry for developing the logical foundations of synthesizing complex molecules. As Baran's former postdoctoral adviser, Corey might have reason to be biased. But other synthetic chemists are equally laudatory, calling Baran "exciting," "impressive," even "a superstar." "Phil is going to be a big name in organic chemistry for a long time to come," concludes Tom Stevenson, a synthetic organic chemist at DuPont in Newark, Delaware.

He's certainly off to a fast start. After blitzing through his undergraduate degree at New York University in 2 years, Baran spent the next 6 years honing his skills with two of the world's leading synthetic organic chemists—earning his Ph.D. at Scripps in the lab of K. C. Nicolaou before settling in with Corey for his postdoc. When Scripps then offered him a position, Baran says he was both excited and concerned about how to focus his research.

After working with Nicolaou and Corey, Baran says he was enamored of synthesizing large, complex molecules. But few young faculty members start out with such complex synthetic projects. "Young people typically start out on [developing novel reaction methods] and move towards synthesis," Baran says. But he recalled a quotation from Corey in a chemistry textbook that said there is still plenty of room for discovering new ways to plan syntheses of complex molecules. That inspired him to see whether he could craft such a plan without protecting groups.

The problem is a tricky one. Take a marine natural product called hapalindole U, one of the molecules Baran and his students reported synthesizing in their *Nature* paper. The compound had been synthesized before. But that approach required 20 steps,

half of which involved either putting on or taking off protecting groups on five different sites around the molecule. At one point in the synthesis, for example, the growing molecule sports an indole group, a five-member ring containing a nitrogen atom that's just begging to react with any electron-hungry compound. The conventional approach caps that nitrogen with a short, chainlike compound called a Boc group to stymie its reactivity.

Baran and his students, however, opted to put the nitrogen's reactivity to use. They reacted the indole with a highly basic compound called LHMDS, which ripped a proton off the nitrogen. They carried out related preparation of another molecular fragment called a terpene. With those groups primed, they then linked two fragments using a specially invented reaction designed to target only the linkage site. By continuing with the strategy, Baran's team cut the synthesis of hapalindole U down to eight steps. Using the same approach, the group turned out another compound in 10 steps that had previously required 25. "This really challenges the rest of us to think that way," Stevenson says.

In addition to making for more efficient syntheses, Baran says he's found that the biggest advantage of using molecular judo is that it forces him to invent new chemistry along the way. Adding protecting groups, Baran says, gives researchers the illusion that they can control the chemistry they are working on. But in reality, protecting groups are added precisely because researchers have not managed to emulate the exquisite knack biological enzymes have for operating on just one bond on a molecule. Removing that safety net forces researchers to find ways to match biology's control. "The point is not to say you should blindly throw away all protecting groups," Baran says. However, he adds, doing so in select cases "is a vehicle for discovery and adventure."

It has a practical upside as well. Fewer synthetic steps mean more of a desired compound at the end, because each added step produces some loss. A 20- to 25-step synthesis typically yields just milligrams of a compound, too little for extensive studies of its biological activity. Baran's approach, by contrast, typically produces final compounds by the gram. Naturally derived compounds, Li points out, remain at least the starting point for about 50% of all new drugs today, excluding small changes to existing compounds. But in many cases, such as with compounds harvested from marine organisms that are difficult to collect, researchers can't get their hands on enough of the naturally occurring compounds for biological tests. Having grams or more of a compound to work with could change things dramatically. "This could potentially revolutionize both [drug] discovery and development," Li says.

Baran, Corey, and others caution that synthetic chemistry's gentle way can't be used in every case. But Baran has already shown that it works with a wide range of complex molecules. That's an achievement in itself and likely a harbinger of many to come.

–ROBERT F. SERVICE

PLANT PATHOLOGY

Deadly Wheat Fungus Threatens World's Breadbaskets

New mutations have put an old killer back on the map. As it spreads, breeders are racing to develop resistant plants

Scientists thought they had beaten *Puccinia graminis* a long time ago, and for good. Before the late 1950s, the fungus was notorious for causing black stem rust, one of the most devastating diseases of wheat. Every few years, outbreaks would lay waste to entire fields somewhere in the world, sometimes sweeping across great swaths of continents in a matter of months.

Salvation came with the development of wheat varieties that resisted the disease, which are widely credited with helping to usher in the green revolution in the 1960s. The new cultivars caught on rapidly, helping ensure bumper crops not just in the United States but in developing countries as well. "Stem rust was something we felt we had solved," says Miriam Kinyua, a plant breeder at the Kenya Agricultural Research Institute (KARI) in Njoro.

But stem rust is back, and it's more dangerous than ever before. In 1999, a new race of the fungus was discovered in Uganda that can defeat the resistance of most varieties of wheat. The fungus spread in northeast Africa for several years while researchers scrambled for funds to study it. In January, pathologists announced that it had jumped the Red Sea into the Arabian Peninsula—on a path to the major wheat-growing regions of Asia. Compounding matters, a new mutation turned up late last year that enables the fungus to infect even more kinds of wheat. "This is the most virulent strain we've seen in 50 years," says Kay Simmons, the national program leader for plant genetics and grain crops at the U.S. Department of Agriculture (USDA).

Against the grain. A new race of stem rust, Ug99, could wipe out wheat fields that were once resistant.

CREDIT: DAVID MOWBRAY/CIMMYT

While pathologists nervously track the spread of the disease, breeders have ramped up their search for varieties that can survive it. Already, they've had initial success with two that might help Ethiopian farmers. But it can take years to complete field-testing and generate enough seed to distribute to farmers. With much of the world in need of resistant varieties, the challenge is enormous, says wheat breeder Rick Ward, who coordinates the Global Rust Initiative.

Stem rust is the worst of three rusts that afflict wheat plants. The fungus grows primarily in the stems, plugging the vascular system so carbohydrates can't get from the leaves to the grain, which shrivels. In the 1950s, when the last major outbreak destroyed 40% of the spring wheat crop in North America, governments started a major effort to breed resistant wheat plants. Led by Norman Borlaug of the Rockefeller Foundation and others, researchers succeeded

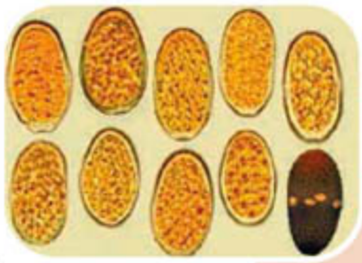

by bundling several genes that conferred powerful resistance in new varieties. One gene, *Sr31*—added later on a large chunk of a rye chromosome—also boosted yield and became widespread in wheat varieties by 1980. *Puccinia*, in contrast, became ever more rare, and fewer new races arose. Researchers turned their attention to the two less devastating wheat rusts, leaf rust and yellow rust, that still cause trouble.

Two decades later, pathologists and breeders were caught off-guard when the new race of stem rust turned up in Uganda. It was first detected in 1999 at a research station, where many varieties of wheat were being studied. Ravi Singh, chief wheat breeder and pathologist at the International Maize and Wheat Improvement Center (CIMMYT) in El Batán, Mexico, recalls being alarmed when he heard how many kinds of wheat were susceptible. Most worrying was that this new race—dubbed Ug99—could even kill wheat plants outfitted with the resistance gene *Sr31*. Still, he says, a few new races had turned up in the past decades without causing epidemics. And Ug99 didn't come back the next year. "If it shows up just for 1 year, you can't make any major commitment. It's hard to justify," Singh says.

In 2001, however, Ug99 started infecting wheat cultivars at a research station in Kenya. It was noticed in Ethiopia 2 years later. Still, the response was minimal; CIMMYT was in a budget crunch, and it had little core funding that it could switch to the problem, Singh says. Enter Borlaug, then 90 years old. He and Christopher Doswell of the Consultative Group on International Agricultural Research wrote a memo in 2004 urging CIMMYT leadership to make Ug99 a priority. "We knew the dangers, and we blew the whistle," Borlaug says.

Shortly thereafter, CIMMYT and a sister institute—the International Center for Agriculture Research in the Dry Areas (ICARDA)—started the Global Rust Initiative (GRI) to coordinate efforts to track and study Ug99 and develop resistant varieties of wheat. With funds that Borlaug helped raise from international donors, CIMMYT and ICARDA began to send more seeds from their collections to be evaluated in Kenya, where the pathogen is now endemic—so many seeds that the seven breeders and pathologists at KARI's Njoro research station are increasingly overwhelmed. "Ug99 is so threatening that other problems have almost been overlooked," says Kinyua.

So far, about 90% of the 12,000 lines tested are susceptible to Ug99. That includes all the major wheat cultivars of the Middle East and west Asia. At least 80% of the 200 varieties sent from the United States can't cope with infection. The situation is even more dire for Egypt, Iran, and other countries in immediate peril.

More bad news arrived last December. Tests on sentinel plots by GRI-funded researchers revealed that Ug99 had mutated. Testing at a USDA laboratory in St. Paul, Minnesota, showed that the new race can now also defeat *Sr24*, another key source of genetic resistance. "That was the worst case scenario," says USDA plant pathologist Yue Jin, who did the work. "It's increased the worldwide vulnerability incredibly." Right now, this identification may only be done in midwinter in Minnesota, so that any spores that might escape will be killed by the temperatures. Researchers are hopeful, however, that the recent sequencing of the *Puccinia* genome will speed development of diagnostic tools that can be easily used in Africa.

Meanwhile, Ug99 continues its march. In January, Jin's Minnesota lab confirmed that Ug99 had reached Yemen. The fear is that the spores will quickly spread via winds north through the Middle East and then head to the bread baskets of India and Pakistan, as an epidemic of yellow rust did in the 1990s. That epidemic caused some $1 billion in damage, and stem rust could easily triple those losses, CIMMYT has estimated.

Fungicides can help control the damage from *Puccinia*, and GRI will begin trials in June to figure out the best way to use them. But chemical treatments are too expensive for many farmers in the developing world, Singh says, so plant breeding is the primary strategy.

Two new kinds of wheat have shown promise in Ethiopia. "The yields are very favorable, comparable to the commercial varieties," says Tsedeke Abate, director general of the Ethiopian Institute of Agricultural Research in Addis Ababa, where a half-dozen scientists are working full-time on Ug99. The immediate challenge is to grow enough seed from these resistant strains to distribute to Ethiopian farmers. Last year, researchers harvested 15 kilograms of precious seed. Then, in a painstaking effort, they hand-planted this wheat to maximize seed production. Spread over 4 hectares, the seedlings had extra room to grow and were carefully watered and weeded by hand. The resulting yield was nearly 4 tons of seed of each variety. "They went to extraordinary efforts," Ward says.

Now, that success must be replicated for other regions. Singh says it's important to come up with resistant varieties for countries that aren't yet infected. Planting those before an epidemic strikes could help slow the spread of the disease. Egypt, for example, has vast tracts of wheat. If stem rust infects those crops, they will send enormous quantities of spores throughout the Middle East and toward west Asia. It's a tight race, as several observers suspect that Ug99 could start reaching Egypt later this year.

Despite the world's initial slow response, Borlaug, who turned 93 last week and is battling lymphoma, says he is optimistic that the fungus will be beaten again.

–ERIK STOKSTAD

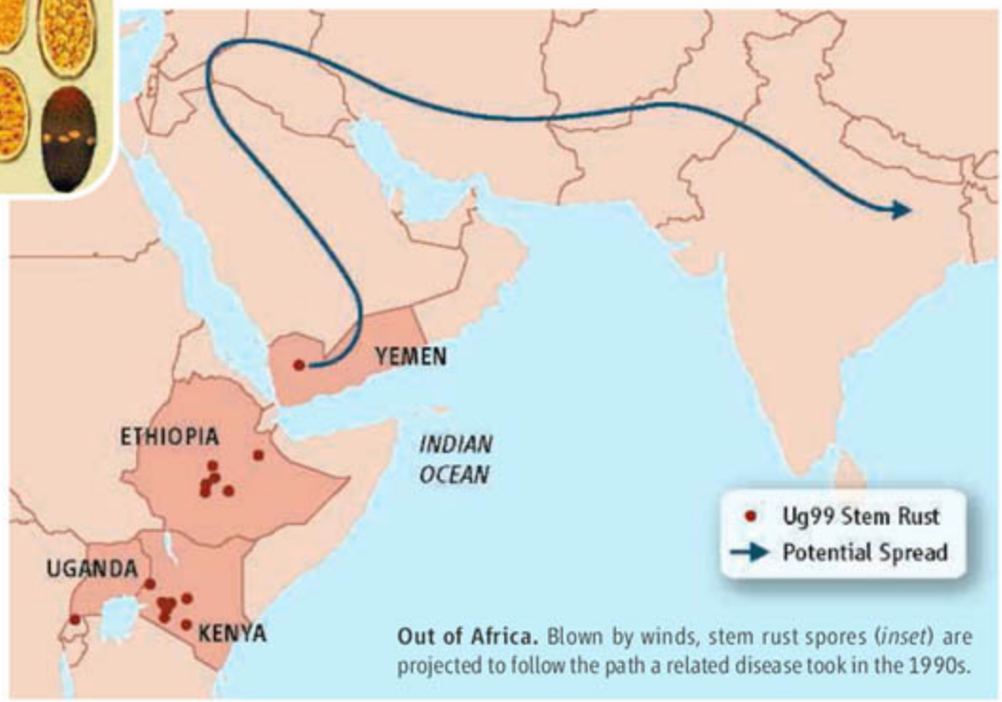

Out of Africa. Blown by winds, stem rust spores (*inset*) are projected to follow the path a related disease took in the 1990s.

CREDITS (TOP TO BOTTOM): T. ELAM AND Y. ANIKSTER; SOURCE: BASED ON SINGH *ET AL.*, *PERSPECTIVES IN AGRICULTURE, VETERINARY SCIENCE, NUTRITION AND NATURAL RESOURCES*, 1 (54), 2006

Nice vantage point. In the Dry Valleys of Antarctica, snowmelt makes Mars-like dark streaks by seeping in and flowing downhill to dampen and darken the surface.

Bringing Martian Streaks And Gullies Down to Earth

For all their dramatic visual appeal, the gullies of Mars are proving mighty enigmatic. They *look* as if they were cut the other day by rivulets of water seeping from crater walls and cliff faces. But in geology, looks aren't everything. Seven years after discovering gullies, planetary geologists still disagree about where the water comes from and even whether water was involved at all. Add in the even more contentious dark streaks that mark other martian slopes, and you've got no end of debate over the recent history of water on the Red Planet.

At the meeting, planetary geologist James Head of Brown University and colleagues offered a down-to-earth resolution of the gully-and-streak conundrum. If a cold, dry Mars works the way the hyperarid and perennially frigid Dry Valleys of Antarctica do, they said, streaks and gullies are both shaped by flowing water, the one from below and the other above and below.

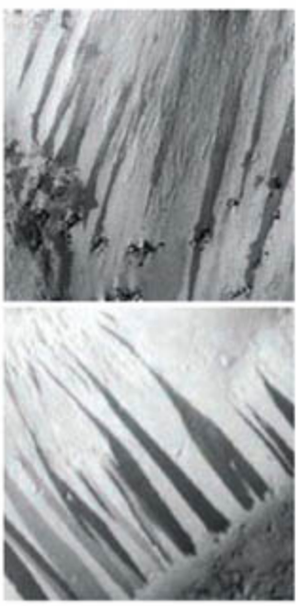

Twins? Streaks in Antarctica (*top*) and on Mars (*bottom*) bear a strong family resemblance.

During a 3-month field season this past austral summer, Head and colleagues took a close look at Dry Valley dark streaks that from orbit and from a helicopter appear "very, very comparable to things seen on Mars," Head said. Like martian streaks, these are dark, stretch down steep slopes, and show no sign of relief across a streak. On Mars, researchers have typically invoked some sort of surface flow: an avalanche of dry dust that unveils a darker substrate, a cascade of wet debris, or the flow of an erosive spring.

In Antarctica, nothing whatsoever flows on the surface to form a streak. Scarce, windblown snow accumulates in pockets near the tops of slopes, melts in the warmest and sunniest part of the summer, seeps down a few tens of centimeters into the loose rocky debris that passes for soil, and runs downhill on top of a layer of ice-encased rock. When the unseen water encounters less-porous, finer-grained soil, it wicks upward to dampen the surface and darken it.

In the next talk, Joseph Levy of Brown spoke for the same group about Dry Valley gullies. A gully works much as a streak does, he said, but with water supplied so fast that it flows both through the soil and on the ground's surface. On higher, steeper slopes, the greater flow cuts a channel, and lower down it deposits fans of sediment.

The Antarctic Dry Valley examples are "the best analogs I've seen," said planetary scientist Oded Aharonson of the California Institute of Technology in Pasadena. And Head's streak presentation was "a great talk," says planetary scientist Robert Sullivan of Cornell University. Still, no one considers the case closed. Sullivan, for one, finds a dearth of snow and ice on the slopes above the martian streaks; he wonders how there would be enough water to even dampen the soil. And Aharonson asks how dark streaks could stay damp for decades on Mars. As Sullivan notes, "We don't have things entirely figured out."

Warped Shorelines On a Rolling Mars

Some planetary scientists see remnants of shorelines where oceans lapped onto land early in Mars's history, but the putative shorelines wander over martian hill and dale. They diverge by a kilometer and more from the single sea-level elevation that an ocean would have traced out. But a group of geophysicists reported at the meeting that they have found a plausible explanation for warped ancient shorelines: Mars rolled on its side, twice, in response to a huge ocean basin emptying.

The new view relies on the ready mutability of vast spinning objects. Tape a penny to the top of a ball floating in water, and the ball will roll over until the penny is at the bottom, the weighted ball's most stable position. Do the same thing to a ball spinning in space, and the ball—while still spinning as before—will roll until the penny is at the ball's rotational "equator," the most stable position for a spinning, weighted ball. Now imagine your spinning ball is a chunk of rock the size of Mars and the added weight is an ocean's worth of water. Because rock is not entirely rigid, the roll that takes the ocean toward the equator will also raise rock into

CREDITS (TOP TO BOTTOM): JAMES HEAD, BROWN UNIVERSITY; IKONOS IMAGE COURTESY OF JAMES GARVIN, NASA/GSFC; MSSS/JPL/NASA

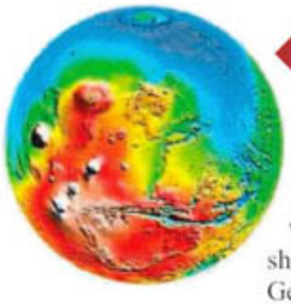

A roller? Northern lowlands (blues) may once have been equatorial and water-filled.

an equatorial bulge, warping the ocean's shorelines in the process. Geophysicist Taylor Perron of Harvard University and colleagues described how they investigated whether such rolling could explain two warped apparent shorelines of different ages that partially enclose the northern lowlands of Mars. They calculated how much Mars would have had to roll, and in which direction, to deform the once-level shoreline of an ancient ocean into the putative shorelines. Working backward in their model, they found that the shorelines become releveled when the lowlands roll in two steps from their present pole-centered position to more equatorial positions. Throughout both steps, Mars's massive Tharsis volcano stayed near the equator—where it is today. If the releveling had moved the dominant Tharsis mass, the calculation would have been obviously erroneous. Keeping Tharsis in place by chance would have been a "pretty incredible" coincidence (about a 0.01% probability), they calculated. The group also calculated that the mass of water in the lowlands would have been great enough to drive such planetary rolling.

"The idea is really interesting and refreshing," says geophysicist Shijie Zhong of the University of Colorado, Boulder. "If the story is true, we can probably make sense of these shorelines." One possible snag, he adds, is the mass of ocean water. It may have been too small to overcome the forces besides Tharsis—such as the thickened crust of southern Mars—that influence the planet's orientation.

Cold, Cold Bodies, Warm Hearts

What would erupting volcanoes, even icy ones, be doing on the coldest bodies in the solar system? Temperatures hover around 50 kelvin on Kuiper belt objects (KBOs), which circle on the frigid dark fringes of the solar system for eons on end. But astronomers recently have seen signs that fresh ice has formed on KBOs in the geologically recent past. Now, researchers have calculated how a KBO, at least a larger one, might husband its primordial allotment of heat until the present day.

At the meeting, theoretical astrophysicist Steven Desch and colleagues at Arizona State University (ASU) in Tempe explained the problem researchers have with some KBOs. Astronomers, including members of the ASU group, have detected the spectroscopic signature of crystalline water ice on KBOs such as 1260-kilometer-diameter Quaoar and 1500-kilometer 2003 EL61. But both cosmic rays and ultraviolet light destroy ice's crystallinity within a few hundred thousand years.

Somehow, relatively warm crystalline ice has formed of late on the largest KBOs, but scientists have had trouble explaining where the necessary heat came from. KBOs have been cooling inside for billions of years, and unlike satellites such as Io or Enceladus, they do not orbit a huge planet that can spare a trickle of tidal energy to heat the smaller body's interior. So the ASU group constructed a mathematical model to simulate the temperature history of a 1200-kilometer KBO, beginning as a cold ball of ice and rock. They included the heat produced by radioactive elements such as potassium-40 as well as the ability of rock and water to separate if the heating goes far enough, a process called differentiation.

The trick to staying warm proved to be differentiating. The test KBO—modeled after Pluto's moon Charon, which is a KBO-type body like Pluto—differentiated within 70 million years of formation, from the inside out. It differentiated just enough to include half the body's mass in a hot, rocky core overlain by a liquid ocean. A thick, cold outer crust remained unchanged while central temperatures rose to 1300 kelvin for 2 billion years. Modelers added a dollop of ammonia "antifreeze" inferred from spectroscopic detections of ammonium dihydrate on the surfaces of large KBOs. Even today, a liquid ammonia-water ocean a few tens of kilometers thick remains in the model KBO, thanks to the antifreeze. Ammonia-water "magma" could still be oozing to the surface of real KBOs, the group calculates, as ongoing freezing and expansion of water initiates cracks that propagate to the surface.

"I'm surprised it stays so hot," commented planetary physicist William McKinnon of Washington University in St. Louis, Missouri. Desch had two explanations. One was the insulating effect of the rock in the undifferentiated outer shell. The other was the large heat stores in the rocky core.

If the real Charon works anything like the model version, there's hope of seeing some lively geology—frozen "lava" flows and flooded plains—when the New Horizons spacecraft reaches Pluto-Charon in 2015. Then on into the Kuiper belt.

–RICHARD A. KERR

Snapshots From The Meeting >>

Springtime on Mars. The Red Planet may be colorful to the eye, but for decades it had been a drab, wintertime landscape to spectroscopists as they searched for new colors denoting new minerals and thus new geology. Now colors are bursting out all over. "Revelation number one is not just a handful of water-related sites but hundreds," Scott Murchie of the Applied Physics Laboratory in Laurel, Maryland, said at the meeting. Murchie is principal investigator of the Compact Reconnaissance Imaging Spectrometer for Mars (CRISM) orbiting on Mars Reconnaissance Orbiter. The most powerful spectrometer ever flown to Mars, CRISM is revealing the intimate details of highly weathered sulfates, clays, and iron minerals deposited in early martian environments where conditions varied dramatically over time. That should give mission planners no end of options when they put the next rover on Mars in 2010.

Big sploshes. Mojave impact crater on Mars is worn beyond its years. Formed in the cold, dry times of later martian history, Mojave looks as if torrential rains stripped its flanks and dumped the debris in great fans (*Science*, 9 April 2004, p. 196). But new images from the HiRISE camera aboard the Mars Reconnaissance Orbiter reveal other drenched-looking craters of about the same age. Planetary geologist Livio Tornabene of the University of Arizona, Tucson, and colleagues reported heavy erosion and fan deposition in and around Tooting, Zunil, and Zumba craters in low northern latitudes. Did four recent icy comets dump their water on Mars? Statistically improbable, the researchers say. Instead, they suggest, the impacts may have unleashed water stored deep beneath the surface. That beats a divining rod on Mars. –R.A.K.

Deep flood. Water to erode young martian craters may have welled up from below.

CREDITS (TOP TO BOTTOM): GSFC/NASA; TORNABENE *ET AL.*, LUNAR AND PLANETARY SCIENCE CONFERENCE XXXVIII (2007)

LETTERS

edited by Etta Kavanagh

Wildlife Population Increases in Serengeti National Park

IN THEIR BREVIA "EFFECTIVE ENFORCEMENT IN A CONSERVATION area" (24 Nov. 2006, p. 1266), R. Hillborn *et al.* report that antipoaching efforts led to increased wildlife populations in the Serengeti National Park. Although these results are compelling, we are not convinced that the documented population increases are a result of these efforts.

First, the data presented demonstrate correlation, but not causation. There may be other reasons for the population recovery, but the authors did not consider alternative hypotheses. Documented increases in buffalo numbers may be explained as a recovery to postdrought conditions rather than the results of antipoaching efforts. This is a plausible alternative hypothesis, because large herbivore populations can be regulated by food availability (*1*–*3*) and experience higher rates of predation during drought periods (*2*, *4*).

Elephants in Serengeti National Park, Tanzania.

Second, the authors show an exponential increase in the number of patrols per day after 1993, but it is unclear what level of patrolling is necessary to realize population recovery. For example, between 1985 and 1993, the buffalo population increased with number of patrols. However, the number of patrols during this period was much lower than during other periods of population increase. It is important to identify how much patrolling is actually needed to minimize poaching such that limited conservation funds are used efficiently.

Finally, the authors argue that community-based conservation could not explain the declines in poaching because the populations were already increasing before community-based programs were in place. Yet community-driven management programs adjoining the park are important for wildlife populations to thrive (*5*). It is possible that an alternative factor, such as postdrought recovery, could have been the impetus for population recovery and that community-based conservation programs then led to a reduction in poaching.

JULIE K. YOUNG, LEAH R. GERBER, CATERINA D'AGROSA

Department of Ecology, Evolution and Environmental Science, School of Life Sciences, Arizona State University, Box 874501, Tempe, AZ 85287–4501, USA.

References

1. N. Georgiadis, M. Hack, K. Turpin, *J. Appl. Ecol.* **40**, 125 (2003).
2. P. J. Funston, M. G. L. Mis, *S. Afr. J. Wildl. Res.* **36**, 9 (2006).
3. M. G. L. Mills, H. C. Biggs, I. J. Whyte, *Wildl. Res.* **22**, 75 (1995).
4. A. J. Loveridge, J. E. Hunt, F. Murindagomo, D. W. Macdonald, *J. Zool.* **270**, 523 (2006).
5. S. Thirgood *et al.*, *Ann. Conserv.* **7**, 113 (2004).

Response

YOUNG *ET AL.* ARGUE THAT CHANGES IN THE intensity of poaching are only one possible explanation for the change in abundance of elephants, buffalo, and rhino in the Serengeti park. They do not appear to question that poaching rates increased dramatically after 1977, when enforcement was reduced. We agree that there are other possible explanations, but within the strict word limit for Brevia, we had little scope for discussion of these factors. In particular, we suspect that the reduction in world price for elephant ivory and rhino horn due to the CITES (Convention on International Trade in Endangered Species of Fauna and Flora) bans contributed to making poaching on these species less profitable. Further, we agree that changes in rainfall can influence year-to-year abundance, as seen by the 1993 drought's impact on buffalo.

However, we formulated a hypothesis about the time trend in poaching intensity from the history of arrests and antipoaching efforts and then tested that hypothesis using the trends in abundance of the three species. This is a reasonably strong test of hypothesis, but clearly not totally definitive. The evidence that poaching pressure in the 1990s is considerably less than in the 1980s is very strong. The annual mortality rates after 1977 from poaching using abundance data alone were 58% for rhinos, 30% for elephants, and 15% for buffalo. These populations could not have recovered if these levels of poaching had continued.

Thus, the only significant question is what caused the dramatic decrease in poaching by 1990. There were no significant community development programs in place until the late 1990s, and community development programs simply cannot explain why poaching had declined by 1990. Young *et al.* argue that the increase in buffalo after the drought could be due to density-dependent factors, ignoring the fact that poaching rates must have been much lower than the 8% maximum rate of increase observed in the 1960s and 1970s. Density dependence does not explain why poaching rates declined so much. Although a multitude of factors, including antipoaching efforts, price of ivory and rhino horn, rainfall, community development projects, and local villagers' cash income and demands for cash, all undoubtedly contribute to poaching and changes in population abundance, the data we present

Origin of domestication
1797

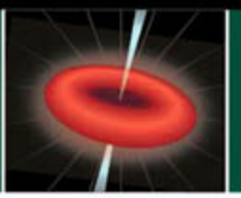

Stellar fireworks
1798

provide undeniable evidence that the poaching mortality rates both increased and decreased, and the timing of these increases and decreases is best explained by the changes in antipoaching efforts.

RAY HILBORN,[1] GRANT HOPCRAFT,[2,3] PETER ARCESE[4]

[1]School of Aquatic and Fishery Sciences, Box 355020, University of Washington, Seattle, WA 98195, USA. [2]Frankfurt Zoological Society, Post Office Box 14935, Arusha, Tanzania. [3]Community and Conservation Ecology, University of Groningen, Post Office Box 14, 9750AA, Haren, Netherlands. [4]Center for Applied Conservation Research, University of British Columbia, Vancouver, BC VLT 1Z4, Canada.

HIV-Malaria Interactions: Don't Forget the Drugs

THE ADVERSE EFFECT OF CO-INFECTION WITH HIV and malaria is becoming increasingly apparent. The importance of these interactions is illustrated by the mathematical modeling of L. J. Abu-Rabbad *et al.* ("Dual infection with HIV and malaria fuels the spread of both diseases in sub-Saharan Africa," 8 Dec. 2006, p. 1603), which predicts significant increases in the prevalence of both diseases due to an interaction between them. Theoretical models suggested that the effect of antimalarial chemotherapy on co-infected individuals would be a decline in both HIV and malaria prevalence. These findings assume that the effect of antimalarial chemotherapy on HIV infection is a shorter duration of raised HIV viral load after malaria infection. Although this is an important consideration, a number of studies have demonstrated direct effects of antimalarial drugs on HIV replication (*1*) and inhibition of *Plasmodiumfalciparum* development by HIV protease inhibitors (PIs) (*2*–*4*). Some HIV PIs act synergistically in vitro in combination with antimalarials (*5*). These direct drug effects have the potential to alter the complex interaction between malaria and HIV in co-infected individuals. Although HIV PIs are not currently recommended for first-line antiretroviral (ARV) therapy, they are likely to assume a greater role in ARV therapy in malaria-endemic regions as thermostable formulations of PIs are made available at significantly reduced cost (*6*), and as the need to combat ARV-induced drug resistance increases (*7*). We endorse the view of Abu-Raddad *et al.* that further studies are required to explore these interactions, particularly with respect to the effect of interventions with potential efficacy against both pathogens.

KATHERINE T. ANDREWS, MICHELLE L. GATTON, TINA S. SKINNER-ADAMS, JAMES S. MCCARTHY, DONALD L. GARDINER

Queensland Institute of Medical Research, Queensland 4029, Australia.

References

1. A. Savarino, J. R. Boelaert, A. Cassone, G. Majori, R. Cauda, *Lancet Infect. Dis.* **3**, 722 (2003).
2. T. S. Skinner-Adams, J. S. McCarthy, D. L. Gardiner, P. M. Hilton, K. T. Andrews, *J. Infect. Dis.* **190**, 1998 (2004).
3. K. T. Andrews *et al.*, *Antimicrob. Agents Chemother.* **50**, 639 (2006).
4. S. Parikh *et al.*, *Antimicrob. Agents Chemother.* **49**, 2983 (2005).
5. T. S. Skinner-Adams, K. T. Andrews, L. Melville, J. McCarthy, D. L. Gardiner, *Antimicrob. Agents Chemother.* **51**, 759 (2007).
6. See "Abbott statement regarding new initiatives to expand access and affordability to lopinavir/ritonavir in the developing world," 14 Feb. 2007 (available at www.abbott.com/global/url/pressRelease/en_US/60.5:5/Press_Release_0341.htm).
7. S. H. Eshleman *et al.*, *J. Infect. Dis.* **192**, 30 (2005).

Response

ANDREWS *ET AL.* INDICATE THOUGHTFUL AND important considerations regarding interventions targeting HIV and malaria and their interactions. Indeed, we only considered one effect of chemotherapy: that of reducing the malaria infectious period and the duration of heightened HIV viral load. We concur with Andrews *et al.* that detailed modeling studies of the impact of single and synergistic interventions warrant further consideration, such as highly active antiretroviral therapy (HAART) (*1*, *2*), HIV protease inhibitors (*3*), malaria prophylaxis (*2*), antimalarials (*4*), and insecticide-impregnated bednets (*2*), in addition to behavioral interventions. This issue assumes particular importance with the expansion of HAART in sub-Saharan Africa as combinations of therapy may become logistically feasible. Moreover, there is evidence for dual beneficial effects of a number of antivirals and antimalarials (*2*–*5*). Finally, data on the biological effects of therapy combinations at the individual level would be of great utility to explore the epidemiological and population level consequences of intervention efforts.

LAITH J. ABU-RADDAD,[1,2] PADMAJA PATNAIK,[3] JAMES G. KUBLIN[4]

[1]Statistical Center for HIV/AIDS Research and Prevention, Fred Hutchinson Cancer Research Center, Seattle, WA 98109, USA. [2]Center for Studies in Demography and Ecology, University of Washington, Seattle, WA 98195, USA. [3]Department of Epidemiology, School of Public Health, University of North Carolina at Chapel Hill, NC 27599, USA. [4]International Health Program, University of Washington, Seattle, WA 98109, USA.

References

1. J. S. Montaner *et al.*, *Lancet* **368**, 531 (2006).
2. J. Mermin *et al.*, *Lancet* **367**, 1256 (2006).
3. K. T. Andrews *et al.*, *Antimicrob. Agents Chemother.* **50**, 639 (2006).
4. A. Savarino, J. R. Boelaert, A. Cassone, G. Majori, R. Cauda, *Lancet Infect. Dis.* **3**, 722 (2003).
5. S. Parikh *et al.*, *Antimicrob. Agents Chemother.* **49**, 2983 (2005).

Coal-Fired Power Plants: Imprudent Investments?

GRANGER MORGAN'S EDITORIAL "DON'T grandfather coal plants" (17 Nov. 2006, p. 1049) wisely suggests not "grandfathering" (i.e., not exempting from regulations) carbon emissions from coal-fired power plants. This is not just a matter of good policy, but it is also sensible in light of a widespread and long-standing principle of utility law.

In most of the United States, state public utilities commissions decide whether costs incurred by utilities can be passed along to ratepayers or whether they will be borne by investors. For decades, commissions have based their decisions on the prudence and usefulness of decisions to build or run power plants and negotiate power contracts. A prudence review occurs after the fact, but seeks to take into account the information available at the time of the action taken. It "determines whether a utility's management decisions… were reasonable in light of all the circumstances that existed at the time the actions in question were taken" and then decides whether costs should be allowed in rates (*1*). In a highly relevant example, many utility commissions ordered major disallowances of nuclear-plant investments, years after allowing the initial construction, and the United States Supreme

Letters to the Editor

Letters (~300 words) discuss material published in *Science* in the previous 3 months or issues of general interest. They can be submitted through the Web (www.submit2science.org) or by regular mail (1200 New York Ave., NW, Washington, DC 20005, USA). Letters are not acknowledged upon receipt, nor are authors generally consulted before publication. Whether published in full or in part, letters are subject to editing for clarity and space.

Court rejected investors' efforts to overturn those regulatory decisions (*2*).

When utilities calculate the life-cycle risks involved in constructing a new coal-fired power plant, the likelihood of federal carbon dioxide regulation is already clearly foreseeable. Thus, as the Coalition for Environmentally Responsible Economies points out, wise investors are already demanding that corporations calculate and inform potential investors about the costs of carbon regulations (*3*). Morgan's Editorial is only one of many indicia that those future liabilities are currently "foreseeable." Imagine utility investors ignoring this possibility, investing in coal technology that does not allow carbon control, and later requesting a rate increase when forced to retrofit or retire the plant. Public utility commissions could well find such decisions imprudent. That would result in the utility's investors footing the bill for expensive retrofits or even more expensive stranded costs (costs that investors cannot recover either from markets or from ratepayers).

Legislators may or may not explicitly forbid grandfathering, but, regardless of that, investors should recognize that utilities that rush to add coal-fired capacity may face not only future compliance costs, but also a reality in which such imprudent costs are paid by investors, and not by ratepayers.

MICHAEL DWORKIN, SHANNA VALE, ELLEN CRIVELLA

The Institute for Energy and the Environment at Vermont Law School, South Royalton, VT 05068, USA.

References

1. Vermont Public Service Board, Docket No. 5983 (1998), and, more generally, "Abandoned Nuclear Plant Recovery," 83 ALR 4th 183 (1991).
2. See, e.g., *Duquesne Light Co. v. Barasch*, 488 U.S. 299 (1989).
3. Coalition for Environmentally Responsible Economies (CERES), "Best Practices in Climate Change Risk Analysis for the Electric Power Sector" (CERES, Boston, MA, Oct. 2006), p. 22.

Response

IN MY EDITORIAL, I SUGGESTED THAT ONE approach to emission constraints would be to mandate controls only on plants constructed after carbon regulations go into effect "while exempting existing plants for some extended period on the grounds that firms would otherwise face large 'stranded costs.'" I suggested that this might be a factor in the current rush to build new conventional coal plants and noted that "[s]ome investors may be counting on this or on the hope that such costs could be passed on to electricity rate payers." In concluding, I observed that while "[a] state-by-state approach is not optimal," it could be undertaken in such a way as to "place future liability on investors, not rate-payers, and thus send a clear message to those planning new plants…"

In their Letter, Dworkin (who is the former Chairman of the Vermont Public Service Board and one of the United States' leading thinkers on utility regulation) and co-authors persuasively elaborate this argument. The message is clear. Unless investors are confident that they will face sympathetic politically appointed state regulators for decades to come, they run a considerable financial risk when they choose today to build a conventional coal plant in the face of what is now compelling evidence of the need to limit future emissions of carbon dioxide, and with technical options, now available, that could control emissions.

M. GRANGER MORGAN

Department of Engineering and Public Policy, Carnegie Mellon University, Pittsburgh, PA 15213–3890, USA.

SOCIAL SCIENCE

What Flowed from "Surveys Say..."

Tom W. Smith

Sarah Igo's *The Averaged American* operates on two levels. The first is a descriptive, largely historical, account of three major social-science developments in the mid-20th century: the Middletown studies of Robert and Helen Lynd (*1*, *2*), the rise of public opinion polls in the 1930s and 1940s (represented by the operations of George Gallup and Elmo Roper), and the studies of male and female sexual behavior by Alfred Kinsey (*3*, *4*). The second advances the conjoint hypotheses that during the 20th century America transformed into a mass society obsessed with the statistical and "averaged" and that these interrelated, survey-based developments notably contributed to that process.

The Averaged American
Surveys, Citizens, and the Making of a Mass Public

by Sarah E. Igo

Harvard University Press, Cambridge, MA, 2007. 408 pp. $35, £22.95, €32.30. ISBN 9780674023215.

Although Igo (a historian at the University of Pennsylvania) clearly stresses the importance of the development of polls and surveys in general, her discussion is largely limited to the examples of Gallup, Roper, and Middletown, and the Kinsey reports. The much larger field of market research is mentioned only in passing; academic survey research—as illustrated by Paul Lazarsfeld's Bureau of Applied Social Research (Columbia University), the National Opinion Research Center (the University of Denver and then the University of Chicago), and the Institute for Social Research (University of Michigan)—gets a few, minor, mentions, and government surveys, such as the establishment of the Current Population Survey, are ignored. This approach creates a biased understanding of the development of survey research and how it shaped American society.

Moreover, Igo's description of survey research contains a number of weakly supported or exaggerated contentions. For example, she asserts that "Pollsters' sponsors delimited not just the form but the content of public opinion." She provides no substantial evidence to back up this claim, and given the many sponsors that surveys had and the comprehensive topics that they covered, this contention is dubious. Also, Igo notes that "On the political front, the U.S. Congress and state governments made numerous attempts to rein in the new technology [of public opinion polls]." She offers a few good examples of such attempts, but these were mostly symbolic exercises, and none came close to regulating the new field. Likewise, the author misses an opportunity to seriously examine the reasons for what she correctly notes as the "quick recovery" of polling from its misprediction of the 1948 presidential election. The cause is not really explored, with only a nod to "the polls' distinct blend of scientific and democratic rhetoric" and a claim that "polling techniques were firmly embedded in American society by 1948."

Despite some rich archival research and many valuable citations of original sources, Igo unfortunately makes a large number of factual errors. For example: (i) It is not true that "the response rate to telephone surveys has steadily declined since 1952." Telephone surveys did not become common until the 1970s, and while telephone response rates have decreased over the last decade or two, no one has solid figures on the rate of decline. (ii) SLOPs are not "selected listener opinion polls," but "self-selected listener opinion polls" (a term coined by Norman Bradburn). (iii) The federal government did not play a role in the 1941 establishment of the National Opinion Research Center.

Regarding the role of surveys in society, Igo argues that surveys in general and her three examples in particular were aimed at finding the "averaged American," the "typical," the "averaged-out," and the "ordinary." But that misrepresents what surveys are designed to do and how they have been used. They were designed to describe American society by examining the distribution of attitudes and behaviors across its population. A mean and a mode come out of such measurements, but those averages are not the sole or even main purpose of surveys. Rather, they are just part of the statistical picture that surveys project. Counter to what Igo asserts, surveys are not primarily about "polling the average populace," nor are they mostly tools for massification or promoting "a fixation on the normal." The distribution of responses of a particular item, the comparison of distributions across different items, the tracking of trends, and (most important) the cross-tabulation of attitudes and behaviors by sociodemographics and other variables reveal the complexity and diversity of American society much more than its unity and sameness.

Also weak are Igo's arguments that "national polls and surveys ... were as much responsible for creating a mass public as they were reacting to its arrival" and that "modern survey methods helped to forge a mass public." Although these are interesting contentions, she offers no real proof. Her account shows that Middletown, the Gallup and Roper polls, the Kinsey reports, and surveys in general attracted a lot of attention, both positive and negative. But her evidence is almost entirely anecdotal; much consists of letters from "average citizens" either praising or attacking the method or specific findings. Quantitative content analysis of the media; detailed investigations of what evidence is used in making governmental, corporate, and other societal decisions; or even survey-based studies of the impact of surveys are needed to test her hypothesis.

Lastly, Igo gives surveys like those she discusses in *The Averaged American* too much credit for the quantification of American society. The increase in statistical information during the 20th century also flowed from many

Middletown citizens. The Lynds' social survey presented Muncie, Indiana, as a "typical" American city of the 1920s.

CREDIT: W. A. SWIFT COLLECTION, ARCHIVES AND SPECIAL COLLECTIONS RESEARCH CENTER, BALL STATE UNIVERSITY LIBRARIES

The reviewer is at the National Opinion Research Center, University of Chicago, Chicago, IL 60637, USA. E-mail: smitht@norc.uchicago.edu

other sources, including national economic accounts, aggregate voting counts, government administrative records, and the expanded U.S. Census.

References

1. R. S. Lynd, H. M. Lynd, *Middletown: A Study in Contemporary American Culture* (Harcourt, Brace, New York, 1929).
2. R. S. Lynd, H. M. Lynd, *Middletown in Transition: A Study in Cultural Conflicts* (Harcourt, Brace, New York, 1937).
3. A. C. Kinsey, W. B. Pomeroy, C. E. Martin, *Sexual Behavior in the Human Male* (Saunders, Philadelphia, 1948).
4. A. C. Kinsey *et al.*, *Sexual Behavior in the Human Female* (Saunders, Philadelphia, 1953).

10.1126/science.1140764

PSYCHOLOGY

How Far Can We Go with Reason?

Robert J. Sternberg

Just as its name implies, *How We Reason* is nominally about how we reason. Its not-so-hidden agenda is actually quite a bit broader: namely, to argue that reasoning can help people lead successful lives and that to the extent that people fail, it is in part because emotions begin to color their reasoning. Beyond establishing the importance of reasoning, Philip Johnson-Laird contends that reasoning can be understood in terms of his theory of mental models—according to which people, in the reasoning process, manipulate abstract mental representations that allow them to reach conclusions.

How We Reason
by Philip N. Johnson-Laird
Oxford University Press, Oxford, 2006. 583 pp. $57.50, £29.95. ISBN 9780198569763.

Johnson-Laird burst upon the cognitive-psychology scene with the publication of *Psychology of Reasoning* (*1*). That book was fairly narrowly focused, primarily on deductive reasoning. A later book (*2*) sought to characterize reasoning as well as other cognitive processes in terms of mental models. The current magnum opus goes quite a bit beyond its predecessors in dealing with problems of induction, creativity, and insight. In past work, Johnson-Laird has devoted quite a bit of effort to battling the theories of his competitors, such as Lance Rips (*3*). In this book, Johnson-Laird's goal is not so much to fight the opposition but to argue that human reason can solve many problems facing the world.

Historically, the study of reasoning has not been at the center of psychology in general or of cognitive psychology in particular. There are far more cognitive psychologists studying perception and memory. Johnson-Laird has strived throughout his career—at the University of Sussex, the Medical Research Council Applied Psychology Unit in Cambridge, and now Princeton University—to raise the profile of the study of reasoning. He has been at least somewhat successful. He, his students, and his collaborators have received international recognition for their work.

Four big questions arise from the book. First, to what extent does Johnson-Laird succeed in describing how we reason? Second, to what extent do the reasoning structures (mental models) Johnson-Laird posits characterize scientific reasoning, a major focus of the book? Third, to what extent does reasoning account for the kinds of thinking artists, writers, composers, and others in the humanities and arts use in their work? Finally, how much help is reasoning of the kind described by Johnson-Laird to us all in our everyday lives?

With regard to how we reason, Johnson-Laird's account may not be entirely correct, and it is certainly not complete. To give two examples: Expert reasoning probably relies more on pattern recognition than would follow from mental models. And the fundamental problem of induction—why we make certain inductions but not others—is scarcely addressed. But no other current theory of reasoning is complete either.

Not that many years ago, students were being taught, for example, that syllogisms were solved by heuristics, such as atmosphere (if there is a negation in a premise, the solution involves a negation; if there is a particular, the solution involves a particular) or conversion (people read "If A, then B" as equivalent to "If B, then A"). Considering how woefully inadequate these past accounts were, Johnson-Laird has brought us very far along in understanding how we reason.

Johnson-Laird gives fascinating accounts of some major examples of scientific reasoning, such as the Wright brothers' designing of the first successful airplane, how the codes underlying the Nazi Enigma machine were broken, and how John Snow discovered the link between fecal contamination of drinking water and outbreaks of cholera. His account of deductive inferences is more compelling than his account of inductive and creative processes. Although his broad characterizations are useful, he does not really solve or even address, for example, the crucial problem of creativity: How do we generate novel ideas in the first place? His theory is better at characterizing how we assess whether our ideas are good ideas.

Thinker on a Rock (Barry Flanagan, 1997).

CREDIT: J. NEWFIELD/SCIENCE

The author believes his theory of mental models would characterize thinking in the humanities and arts as well. That is a leap of faith on his part and would be a bigger leap on the part of a reader. There is no evidence—at least in the book (at its end, Johnson-Laird acknowledges that his case histories include nothing from these fields)—that this is the case.

Lastly, *How We Reason* is at its weakest in showing how Johnson-Laird's model of reasoning—or, really, any model—applies to everyday life. If you want to know how to solve the problems of what to do about the intervention in Iraq, runaway government spending, or a failing marriage, you probably will find little in this book to help. Johnson-Laird believes that many of the world's ills are caused by emotional contamination of reasoning, an idea that goes back to some of the earliest theorists (*4*). He tends to view emotion as the cause of failings in reasoning. Yet, one might instead argue that emotion is what makes the world run round. If we want to understand how to rectify our own, and the world's, problems, we had better understand emotional reasoning in its own right, rather than simply label it as an aberration. Two-process theories of reasoning (*5*), which posit an experiential, a-rational system, as well as the more rational one of which Johnson-Laird writes, seem a large step toward that goal.

References

1. P. C. Wason, P. N. Johnson-Laird, *Psychology of Reasoning: Structure and Content* (Batsford, London, 1972).
2. P. N. Johnson-Laird, *Mental Models: Towards a Cognitive Science of Language, Inference, and Consciousness* (Harvard Univ. Press, Cambridge, MA, 1983).
3. L. J. Rips, *The Psychology of Proof* (MIT Press, Cambridge, MA, 1994).
4. R. J. Woodworth, S. B. Sells, *J. Exp. Psychol.* **18**, 451 (1935).
5. S. A. Sloman, *Psychol. Bull.* **119**, 3 (1996).

10.1126/science.1140812

The reviewer is at the School of Arts and Sciences, Bailou Hall, Tufts University, Medford, MA 02155, USA. E-mail: Robert.Sternberg@tufts.edu

TEACHING

Opportunities to Learn in America's Elementary Classrooms

Analysis of elementary school classrooms in the United States returns a discouraging report on the quality of students' experiences.

Robert C. Pianta,[1]* Jay Belsky,[2] Renate Houts,[3] Fred Morrison,[4] The National Institute of Child Health and Human Development (NICHD) Early Child Care Research Network[5]

America's students are tested regularly, and the results serve as justification for closing schools, firing principals, awarding merits, and focusing professional development and curriculum reform. However, little attention is paid to measuring the opportunities to learn that teachers create in classrooms—the quantity and quality of classroom instruction and relationships between teachers and students. Nearly all state certification standards for "highly qualified teachers" focus on degree status (*1*, *2*). However, despite evidence that teachers' instructional practices and relationships with students account for a substantial portion of the "added value" derived from attending school (*3*–*5*), observations of classroom experiences for large samples of students and teachers are limited.

The Study

Here, we describe results from a study of elementary school classroom experiences for more than 1000 American children recruited at birth from 10 U.S. sites and enrolled in more than 2500 classrooms in more than 1000 elementary schools and 400 school districts. Our investigation approximates an epidemiological study of opportunities to learn in U.S. classrooms, although the sample was not nationally representative. Of teachers observed, 90% were credentialed by their state; all had a bachelor's degree and 44% had a master's degree. These teachers meet many states' standards for highly qualified elementary school teachers (*1*).

Observation of classrooms complements student test performance as a measure of quality in the educational system and can document opportunities to learn that are reflected in students' performances on tests. We observed first, third, and fifth grades. First, we coded the presence of 44 behavioral events for 80 one-minute intervals. In a given school day, intervals were clustered into eight 10-minute cycles of coding, in which 30-second periods of observation alternated with 30-second periods of recording. Next, we rated nine dimensions of the quality of the emotional and instructional climate on the basis of 20 minutes of observation, again across eight cycles during the day. We used these codes and ratings to assess opportunities to learn (*6*, *7*).

Experiences in the Classroom

The results for fifth grade (see chart) are similar to those for first and third grades (*8*, *9*). In fifth grade, children spent most of their time (91.2%) working in whole-group or individual-seatwork settings. Students spent little time (7%) in small-group instruction (two to five students). In fifth grade, 37% of instruction was in literacy and 25% was in math; in first and third grade, more than 50% of instruction was in literacy and less than 10% was in math. Science and social studies activities occurred in 11 and 13% of intervals in fifth grade, respectively. The average fifth grader received five times as much instruction in basic skills as instruction focused on problem solving or reasoning; this ratio was 10:1 in first and third grades. Teachers in fifth grade spent 17% of their time instructing students on managing materials or time.

Classroom emotional and instructional climate was rated with the use of a seven-point scale, in which higher ratings were more positive (*8*, *9*). In correlational studies, relatively higher ratings predicted gains on standardized tests of reading and math in pre-kindergarten (*10*), reading in first grade (*3*), and math in fifth grade (*9*). Emotional climate of classrooms was moderately positive—the mean rating over all classrooms for "teacher sensitivity" and "positive classroom climate" was about 5. Children in the classrooms we observed were often working on assignments, with "productive use of time" rated 4.9. However, quality of instructional climate received a low rating. "Richness of instructional methods," reflecting conceptually focused instruction, averaged 3.6, and "evaluative feedback" on student performance averaged 3.44. Typically, over the course of a 20-minute period, instruction involved only one method or mode (e.g., vocabulary worksheet or watching the teacher do math problems), and teachers gave generic feedback on correctness rather than encouraging extension of student performance or discussing alternative solutions. Ratings of instructional and emotional quality in fifth grade were similar to those for first and third grades.

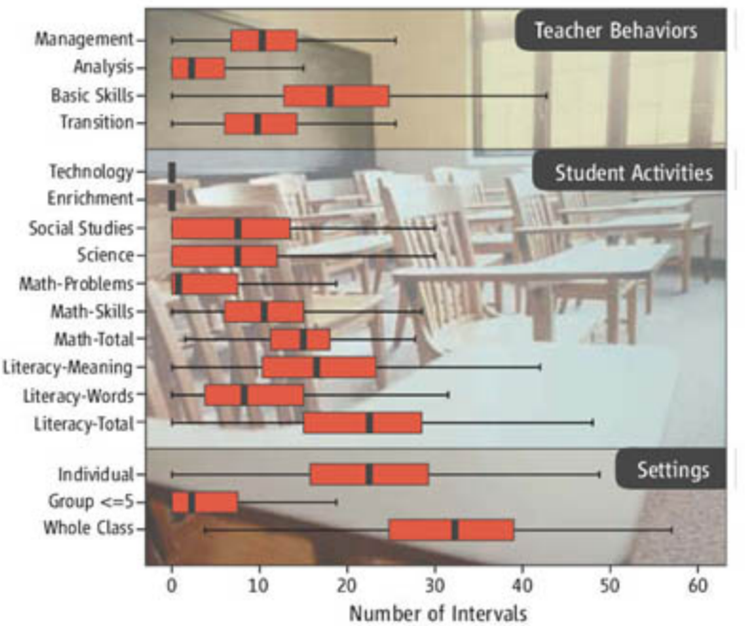

Learning in fifth-grade classrooms. Number of time intervals in which the specified activities were observed. Black whiskers, range; red boxes, 25th to 75th percentiles; gray bars within boxes, overlapping median and mean.

[1]Center for Advanced Study of Teaching and Learning, University of Virginia, Charlottesville, VA 22903, USA. [2]Institute for the Study of Children, Family, and Society, Birkbeck University of London, London, UK. [3]Department of Statistics and Epidemiology, RTI International, Research Triangle Park, NC 27709, USA. [4]Department of Psychology, University of Michigan, Ann Arbor, MI 48103, USA. [5]NICHD Early Child Care and Youth Development Research Network, CRMC, NICHD, 6100 Executive Boulevard, 4B05, Rockville, MD 20852, USA.

*Author for correpondence. E-mail: rcp4p@virginia.edu

Predicting Classroom Climate

Composites reflecting our ratings of the quality of the emotional and instructional climate were examined with various teacher, student, child, and family factors (table S5). Teacher credentialing was not investigated because nearly all teachers met state requirements.

Larger class size was associated with less positive emotional climate. (Class size ranged from 10 to 42 students.) Quality of instructional climate was higher when teachers had fewer years of teaching experience, earned higher salaries, and reported more influence on school policy and efficacy. The magnitude of these significant associations was very small, and causal direction is unknown. The total variance attributed to emotional and instructional climate accounted for less than 10% of the differences in observed quality of the classroom environments. Children with more highly educated mothers and with higher family income were more likely to be enrolled in classrooms with higher observed emotional and instructional climates. These associations with family characteristics were statistically significant but small.

Consistency of a Child's Experience

A child's classroom experience was not particularly consistent from first to third to fifth grade. Results were not a function of (some) children switching schools. Quality of emotional environment was modestly stable from first grade to third grade ($r = 0.17$, $P < 0.05$) and from third grade to fifth grade ($r = 0.25$, $P < 0.05$), but corresponding across-grade analysis for quality of instructional climate did not show statistically supported correlations. We divided climate composites into terciles at each grade. Children were classified as "consistently" in high-quality classrooms if they were enrolled in a high-tercile class in two or more grades and were never enrolled in a classroom in the lowest tercile. Students in "consistently" low-quality classrooms were enrolled in accordingly low-tercile classes and never in the highest tercile. Only 17% of children experienced classrooms with consistently high emotional climate, and 19% experienced classrooms with consistently low emotional climate. Comparable figures for instructional climate were 14 and 20%, respectively. Across all three grades, 7% of children experienced classrooms high on both instructional and emotional climate.

We predicted each child's enrollment in our consistency classifications using the child's scores on standardized tests of reading and math at age 54 months, prior to school entry, and family income-to-needs ratio (using federal guidelines for poor, near poor, and not poor) as predictors. Children from nonpoor families and who scored high on achievement at 54 months were most likely to experience classrooms high in positive emotional or instructional climate throughout elementary school. Poor children were highly unlikely (only 10%) to experience classrooms with high instructional climate across multiple grades.

Discussion

In this multistate observational and longitudinal study of children in U.S. primary-school classrooms, opportunities to learn for this sample of mostly middle-class students proved highly variable and did not appear congruent with the high performance standards expected for students or for teachers as described by most state teacher certification and licensure documents. Rather, experiences in fifth grade, although highly variable, were geared toward performance of basic reading and math skills, not problem-solving or reasoning skills or other content areas. Few opportunities were provided to learn in small groups, to improve analytical skills, or to interact extensively with teachers. This pattern of instruction appears inconsistent with aims to add depth to students' understanding, particularly in mathematics and science. Classroom dynamics were not related to teachers' degree status or experience. Teachers met credentialing standards, but their classrooms, even if emotionally positive, were mediocre in terms of quality of instructional support. Children who needed support were unlikely to receive it consistently. These results are consistent with arguments that a focus on standards-based reform and teacher credentialing may lead to instruction that is overly broad and thin.

It is troubling that opportunities to learn in classrooms are unrelated to features intended to regulate such opportunities and that students most in need of high-quality instruction are unlikely to experience it consistently. If metrics and regulations for high-quality teaching continue to rely on teachers' credentials or school attributes, actual opportunities to learn may not be driven to improve (*2*). These results confirm the need for rigorous designs that test effects on observed instruction of specific knowledge- or skill-focused teacher training interventions.

This study relied on direct observations of classrooms and used instruments that correlate with students' gains in achievement (*11*). Emotional and instructional support contribute to the elimination of the achievement gap in first grade (*3*), predict growth in children's functioning (*10*), and predict reading and math achievement growth and social functioning through fifth grade in our sample (*12*). A study in England reported a similar pattern of effects for elementary students (*5*). Others concur that these features of teacher-child interaction are indicative of good teaching (*13*, *14*). Collectively, these investigations demonstrate that classroom experience can be observed reliably in large numbers of classrooms and that such observations capture a portion of the "value-added" effect of enrollment in a given classroom (*4*, *15*). Experimental interventions that include such observations may yield results useful for improving classroom teaching and the preparation of teachers (*5*) by revealing the mechanisms by which classrooms influence children's development. Science and policy aimed at producing and maintaining effective teaching are needs as pressing as are curriculum reform and assessment of student performance.

References and Notes

1. U.S. Department of Education, *Definitions from the No Child Left Behind Act* (U.S. DOE, Washington, DC, 2002); www.ed.gov/policy/elsec/leg/esea02/pg107.html#sec9101.
2. Educational Testing Service, *Where We Stand on Teacher Quality: An Issue Paper from ETS* (ETS, Princeton, NJ, 2004); http://ftp.ets.org/pub/corp/position_paper.pdf.
3. B. K. Hamre, R. C. Pianta, *Child Dev.* **76** 949 (2005).
4. B. Nye *et al.*, *Educ. Eval. Pol. Anal.* **26**, 237 (2004).
5. P. Sammons *et al.*, *Variations in Teacher and Pupil Behaviors in Year 5 Classes* (Institute of Education, Univ. of London, London, 2006).
6. Methods are available on *Science* Online.
7. Information about methods used in the NICHD Study of Early Child Care and Youth Development is available online (http://secc.rti.org/).
8. NICHD Early Child Care Research Network, *Child Dev.* **71**, 960 (2002).
9. NICHD Early Child Care Research Network, *Elem. Sch. J.* **105**, 305 (2005).
10. C. Howes *et al.*, *Multi-State Pre-K Study* (National Center for Early Development and Learning, Univ. of North Carolina, Chapel Hill, NC, 2005).
11. R. C. Pianta *et al.*, *Elem. Sch. J.* **102**, 225 (2002).
12. NICHD Early Child Care Research Network, *Child Dev.* **74**, 1639 (2004).
13. K. Bogner *et al.*, *Sci. Stud. Reading* **6**, 135 (2002).
14. J. Brophy, T. Good, in *Handbook of Research on Teaching*, M. Wittrock, Ed. (MacMillan, New York, 1986), pp. 328–375.
15. W. L. Sanders, J. C. Rivers, "Cumulative and residual effects of teachers on future student academic achievement" (Univ. of Tennessee Value-Added Research and Assessment Center, Knoxville, TN, 1996).
16. This research is directed by a steering committee (see supporting online material) and supported by NICHD through a cooperative agreement.

Supporting Online Material

www.sciencemag.org/cgi/content/full/315/5820/1795/DC1

10.1126/science.1139719

BEHAVIOR

The Ultimate Ecosystem Engineers

How did human societies initially domesticate plants and animals, and what were the keys to success?

Bruce D. Smith

"Evolution helps those who help themselves" is the basic idea behind the concept of niche construction or ecosystem engineering (*1*). Many animal species attempt to enhance their environments, and humans have been trying to make the world a better place—for themselves—for tens of thousands of years, often with unforeseen consequences. We have long been the ultimate niche constructors in terms of our rich repertoire of ecosystem skills and the magnitude of their impact. Today, as our efforts at ecosystem engineering are beginning to attempt to reduce and reverse human modification of environments, interest is also growing across diverse fields (including archaeology, biology, climatology, genetics, and geography) in the origins of human dominance of Earth's ecosystems. The general concept of niche construction provides an important new window of understanding about how our distant ancestors, through their initial domestication of plants and animals, first gained the ability to significantly alter the world's environments.

Early strategists. Human niche construction, including controlled burning, may date back to as early as 55,000 yr B.P. Shown is an Australian aborigine.

Currently, research on domestication is carried out on two largely disconnected scales—at the level of individual plant and animal species to document the "what, when, and where" of domestication worldwide (*2*), and at a regional or larger scale, to identify causal "macro" variables (such as climate change and population growth) that may account for "why" human societies first domesticated target species (*3*). The theory of niche construction provides a link between research at these two different scales of analysis by offering insights into the intervening "how" of domestication—the general human behavioral context within which macroevolutionary factors forged new human-plant/animal relationships of domestication.

Niche construction or ecosystem engineering activities have been documented in a broad range of different animal species. Beavers, for example, through their tree-cutting, dam building, and pond-creating efforts, generate new landscapes for themselves and many other species. Such efforts at environmental modification are proposed to play an important if underappreciated role in shaping biotic communities and evolutionary processes (*1*).

Studies of human niche construction have usually concentrated on either a particular form of environmental modification, such as controlled burning of vegetation, or on human intervention in the life cycle of a particular target species. Only recently have regional-scale studies offered a fuller appreciation of the extent to which traditional resource-management strategies involve the coherent and integrated manipulation of a broad range of plants and animals and their habitats (*4*).

Documenting the overall niche construction strategies of past human societies, however, remains a difficult challenge. Archaeological evidence for the management of wild plants (sowing, burning, weeding, irrigation, transplanting, and mulching) provides widely scattered clues to the developmental history of integrated systems of human environmental management. Controlled burning of vegetation to maintain a preferred ecosystem state, for example, is documented throughout the Holocene (the last ~10,000 years) in numerous temperate and tropical environments, and may have been present as early as 55,000 years ago in southern Africa (*5*). Yet in many world regions, the appearance of domesticated plants and animals in the archaeological record provides the strongest evidence for integrated strategies of ecosystem engineering.

A number of different aspects of our current understanding of the initial, worldwide domestication of plants and animals points to domestication taking place within a broader behavioral context of niche construction strategies. The development of such human–target species relationships was not a unique event, limited to a particular time or place. Eight to 10 environmentally and culturally diverse world regions have been identified as likely independent centers of domestication and agricultural origin (*2*). Each exhibits a distinct sequence of domestication of different species over millennia. Human societies thus domesticated a diverse array of species at different

The author is in the Archaeobiology Program, National Museum of Natural History, Smithsonian Institution, Washington, DC 20560, USA. E-mail: smithb@si.edu

times and in developmental isolation across a broad range of ecosystems.

In addition, recent research indicates that the initial domestication of plants and animals in these independent centers encompasses a remarkable diversity of species-specific relationships reflecting a wide range of different forms of human intervention. In Asia, for example, the domestication of two utilitarian species—the dog (for hunting) and the bottle gourd (for containers)—by ~12,000 years before the present (yr B.P.), did not so much involve deliberate human intervention as it did allow dogs and bottle gourds to colonize the human niche. In contrast, the initial cultivation of tree crops (such as fig by 11,400 yr B.P. in the Near East and banana by ~10,000 yr B.P. in Southeast Asia) involved the intentional cutting and transplanting of branches, indicating a recognition of the long-term benefits to be gained by a commitment to sustained management.

The initial domestication of goats in the Near East by 10,000 yr B.P., and the subsequent domestication of other livestock species, also called for considerable sustained human intervention, but of a very different kind. Human preemption of herd dominance hierarchies, resulting in human control of animal reproduction, allowed the selective culling of immature males, producing an age and sex profile (that is, a majority of adult females and a few adult males) that is the hallmark of managed domesticated herds. In contrast, the initial domestication of seed-bearing plants (such as wheat, rice, maize, millet, and sunflower), including two species of squash that were domesticated in South America and Mexico by 10,000 yr B.P. (*2*), involved yet another form of human intervention in the life cycle of target species—the sustained planting of stored seed stock in prepared planting areas. Plants with starch-rich underground organs (including manioc, arrowroot, and leren), on the other hand, were brought under domestication in South America by ~9000 to 8000 yr B.P. by replanting fragments of parent plants, paired with sustained selection for desired attributes (larger tubers and preferred starch types, for example) (*2*).

Evidence is also growing for early attempts at domestication that eventually proved unsuccessful. In both the Near East and the Americas, initial efforts at plant management and manipulation were often abandoned, for as yet unknown reasons, and the crops in question were not successfully domesticated until several thousand years later (*6*).

Whatever the exact mixture of macro-evolutionary forces that were in play, humans identified potential domesticates within the broader context of niche construction strategies through endless auditioning and experimentation with a long list of possibilities. Domesticates would not have been different, necessarily, from the many other managed species in either requiring a greater investment of labor, or constituting a greater intellectual challenge. What set humans apart was their recognized potential for open-ended expansion and ever-increasing returns.

References

1. F. Odling-Smee, K. Laland, W. Feldman, *Niche Construction* (Princeton Univ. Press, Princeton, NJ, 2003).
2. M. Zeder *et al.*, Eds., *Documenting Domestication. New Genetic and Archaeological Paradigms* (Univ. of California Press, Berkeley, CA, 2006).
3. M. Zeder. *Evol. Anthropol.* **15**, 105 (2006).
4. M. K. Anderson, *Tending the Wild* (Univ. of California Press, Berkeley, CA, 2005).
5. P. Mellars, *Proc. Natl. Acad. Sci. U.S.A.* **103**, 9381 (2006).
6. E. Weiss, M. Kislev, A. Hartmann, *Science* **312**, 1608 (2006).

10.1126/science.1137740

ASTRONOMY

A Closer Look at a Gamma-Ray Burst

A study of gamma rays produced when stars collapse or collide reveals details of the explosion mechanism, particularly the role of magnetic fields.

Stefano Covino

Gamma-ray bursts are among the most intriguing astrophysical events. Although short-lived, these explosions are the most luminous objects in the universe. However, the detailed mechanisms driving these bursts are still partly unknown. On page 1822 of this issue, the observations reported by Mundell *et al.* (*1*) will allow us to better understand the physical processes that power these celestial sources. By measuring the polarization of the electromagnetic radiation emitted immediately after a burst, Mundell *et al.* can help us unravel the role of magnetic fields in controlling the outflows produced by these explosions.

These burst events were first detected in the 1960s as intense and brief pulses of high-energy photons. They are now observed at photon energies across the whole electromagnetic spectrum and have been located at cosmological distances (that is, more than 10 billion light-years from Earth). They are also possible sources of gravitational waves, ultrahigh-energy cosmic rays, and neutrinos. The most successful description of these events involves a very energetic outflow from an inner engine, either a massive star undergoing core-collapse or the merger of two compact objects (see the figure). Inhomogeneities in the outflow generate a prompt high-energy emission of gamma rays, whereas the later interaction of the outflow with the matter surrounding the progenitor object generates a fainter and softer long-lasting emission, called the afterglow. One of the hottest open topics is to understand what drives the outflow, its composition, and its dynamics. This is where the observations performed by Mundell *et al.* make an important contribution.

Gamma-ray burst outflows are extreme events. Initially they are ultrarelativistic, that is, the flow must have a velocity greater than 99.99% of the speed of light. This allows high-energy photons to escape from the very compact region where they are generated. The hypothesis accepted by most researchers assumes that the outflow is initially hot, with the expansion driven by its internal energy (*2*–*4*). This is known as the matter-dominated scenario, and serves as the reference model for outflows. The most popular alternative scenario requires that the outflow is driven by electromagnetic energy, which is called the Poynting flux–dominated scenario (*5*–*7*). (The Poynting flux is the flux of energy car-

The author is at Osservatorio Astronomico di Brera, via Emilio Bianchi 46, Merate LC, I-23807, Italy. E-mail: stefano.covino@brera.inaf.it

ried by an electromagnetic field.) These two families of models differ in many aspects, although from the observational standpoint, they produce remarkably similar results.

These two scenarios also assume essentially the same emission processes, mainly synchrotron radiation (that is, radiation produced by electrons accelerated to relativistic velocities and usually characterized by a high degree of intrinsic polarization), although the presence of other components, such as inverse Compton scattering (that is, photons scattered to higher energies by the interaction with energetic electrons), has often been invoked. However, one important difference arises—if large-scale magnetic fields are present, they introduce a preferential direction in the system, breaking the spherical symmetry that can be assumed for the first phases of the outflow evolution. Independently of the details of the model, a general prediction for internal energy–dominated outflows is that during the first stages of the event, the polarized flux from the source should be almost negligible. In fact, due to the extreme relativistic effects acting at these stages, the observer sees only a small portion of the emitting outflow, and only very small anisotropies are expected (*8*–*11*). On the contrary, electromagnetic energy–dominated outflows could present initially a rather high-polarized flux, perhaps as high as 30 to 40% (*12*–*14*).

Polarimetric observations performed during the first few minutes of gamma-ray burst evolution are therefore an effective observational test. If a strong polarized flux is measured, the hypothesis of a Poynting flux–dominated outflow is favored. Otherwise, hot, chaotic, internal energy–dominated outflows are to be preferred. Indeed, polarimetric observations of the high-energy emission of the prompt phase were attempted in the past, although none of the results were convincing enough due to the enormous technical difficulties. It is well known that polarimetry allows us to extract all the information carried by the photons we receive, in addition to the simple intensity. However, performing polarimetric observations of astrophysical sources has never been an easy task.

For gamma-ray bursts, these observations must be executed soon after the detection of high-energy photons in order to study a region still spatially close to the inner engine. The only way to cope with the unpredictable time and space location of gamma-ray bursts, and be able to rapidly begin the observations, is with robotic telescopes, such as the 2.0-m Liverpool Telescope used by Mundell *et al.* Thanks to the rapid localization of gamma-ray bursts detected by the Swift satellite (*15*), Mundell *et al.* could observe the gamma-ray burst GRB 060418 only about 3 minutes after the burst. Their remarkable result is that only a rather low 8% upper limit for the linearly polarized flux at optical wavelengths was derived. Moreover, these observations were roughly coincident in time with the onset of the afterglow, as shown by Molinari *et al.* (*16*). The lack of evidence for strong polarization just after the afterglow onset could suggest that large-scale magnetic fields are not likely playing an important role in driving gamma-ray burst outflows. However, if the magnetic fields are carried by the outflow ejected from the central source, as is commonly hypothesized, the prediction of the polarization during the afterglow onset depends on poorly known details of the magnetic energy transfer from the outflow to the shocked medium around the burst (*6*, *17*).

More observations tracing the early time evolution of the polarized flux, and an adequate modeling of these first phases of evolution of the outflow interaction with the matter surrounding the progenitor, will definitively settle the question. In addition, the possibility of carrying out polarimetric observations at high energies, in particular in the x-ray region, is an exciting future possibility. It could open the way for measurements during the prompt event, much closer to the progenitor, in a region where the possible effects of large-scale magnetic fields should be stronger.

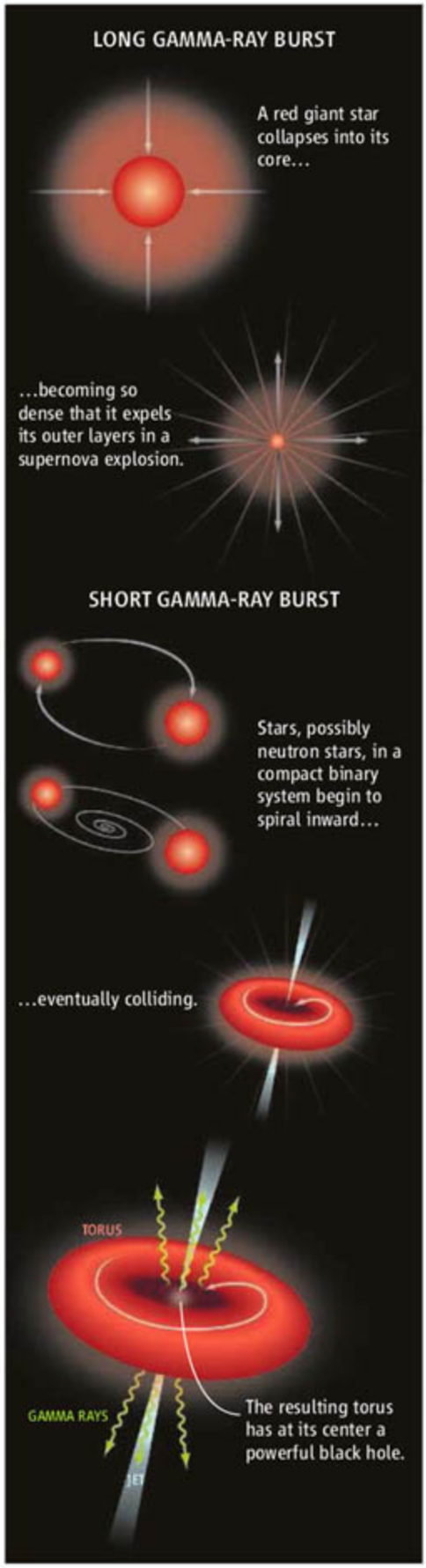

Controlling the flow. Gamma-ray bursts originate either from (**top**) collapsing stars or (**middle**) mergers of binary stars. The resulting high-energy event (**bottom**) creates ultrarelativistic outflows and very bright bursts of gamma radiation.

CREDIT: ADAPTED FROM A NASA IMAGE

References and Notes

1. C. G. Mundell *et al.*, *Science* **315**, 1822 (2007); published online 15 March 2006 (10.1126/science.1140172).
2. T. Piran, *Phys. Rep.* **314**, 575 (1999).
3. P. Meszaros, *Rep. Prog. Phys.* **69**, 2259 (2006).
4. B. Zhang, *Chin. J. Astron. Astrophys.* **7**, 1 (2007).
5. M. Lyutikov, V. I Pariev, R. D. Blandford, *Astrophys. J.* **597**, 998 (2003).
6. B. Zhang, S. Kobayashi, *Astrophys. J.* **628**, 315 (2005).
7. M. Lyutikov, *N. J. Phys.* **8**, 119 (2006).
8. A. Gruzinov, E. Waxman, *Astrophys. J.* **511**, 852 (1999).
9. G. Ghisellini, D. Lazzati, *Mon. Not. R. Astron. Soc.* **309**, L7 (1999).
10. R. Sari, *Astrophys. J.* **524**, L43 (1999).
11. E. Rossi, D. Lazzati, J. D. Salmonson, G. Ghisellini, *Mon. Not. R. Astron. Soc.* **354**, 86 (2004).
12. J. Granot, A. Königl, *Astrophys. J.* **594**, L83 (2003).
13. D. Lazzati *et al.*, *Astron. Astrophys.* **410**, 823 (2004).
14. A. Sagiv, E. Waxman, A. Loeb, *Astrophys. J.* **615**, 366 (2004).
15. N. Gehrels *et al.*, *Astrophys. J.* **611**, 1005 (2004).
16. E. Molinari *et al.*, www.arxiv.org/astro-ph/0612607.
17. Y. Fan, T. Piran, *Mon. Not. R. Astron. Soc.* **369**, 197 (2006)

18. I thank G. Ghisellini, D. Lazzati, and D. Malesani for numerous fruitful discussions.

10.1126/science.1140172

MEDICINE

Anticipating Trouble from Gene Transcription

By forcing the fruit fly to transcribe repeat regions, a model of certain human neurological disorders has been developed, which suggests new possibilities for understanding repeat instability.

Mark E. Fortini

Numerous human neurological and neurodegenerative diseases, including Huntington's disease, spinocerebellar ataxias, and fragile X syndrome, involve expansions of certain trios of nucleotides, such as CAG and CGG, in the genome. These trinucleotide repeats can arise in coding or noncoding sequences in select loci (*1*). Much research has focused on unraveling the consequences of these expansions. In some cases, the repeat lengths are unstable, accounting for a striking clinical feature called "genetic anticipation" in which disease symptoms become progressively more severe in successive generations. On page 1857 of this issue, Jung and Bonini (*2*) show that repeat instability can be replicated for a trinucleotide repeat disorder in the fly *Drosophila melanogaster*. The study provides fresh insights into the role of gene transcription, DNA repair, and the potential complicity of pathogenic polyglutamine proteins in the genetic mechanisms that underlie repeat instability.

Trinucleotide expansions typically encode long stretches of glutamine residues when they occur within the protein-coding regions of genes. In many cases, the expanded polyglutamine domain causes misfolding of the affected protein and its aggregation into visibly abnormal inclusions. Repeat lengths are also unstable, undergoing shrinkages and expansions—in some cases involving tens of CAG repeats—upon transmission from parent to child. Expansion is associated with more severe disease symptoms (*3*). Although several genetic models have been developed to study repeat instability, *Drosophila* has proven recalcitrant to showing the expected genetic instability of the repeats. This has been frustrating, given the fly model's success in revealing cell biological mechanisms of neurodegenerative pathology in the polyglutamine diseases (*4*). Jung and Bonini make a major advance by successfully exploiting this powerful experimental organism to address genetic instability. By showing that in the fly, changes in repeat length that occur over generations can be monitored in weeks rather than decades, the study opens the door for much-awaited genetic analysis.

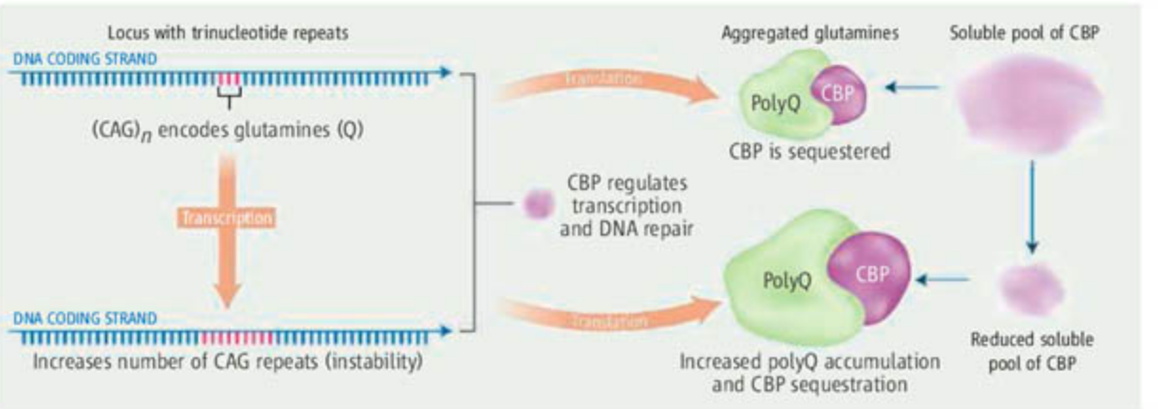

A toxic cycle, accelerated. Polyglutamine (polyQ) proteins interfere with CBP, which influences transcription and DNA repair. This may lead to more genetic instability of the trinucleotide repeats [$(CAG)_n$], increased polyglutamine protein production, more interference with CBP function, and greater instability of expanded trinucleotide repeats.

The breakthrough in developing this new model for unstable polyglutamine expansions was realizing that transcription of CAG repeats might be critical for generating instability. Previous fly models have relied on the expression of transgenes containing CAG repeats in either developing or fully differentiated tissues that are most suitable for investigating the primary neurodegenerative phenotype. However, these models failed to uncover substantial instability of even large repeat expansions (*5*). Because earlier work in *Escherichia coli* and mouse suggested that repeat instability might be linked to transcription of the repeat region (*3*, *6*, *7*), Jung and Bonini reasoned that forcing a repeat-containing transgene to be transcriptionally active in *Drosophila* germ cells might trigger considerable changes in repeat length. Such germline events would also be transmitted from one generation to the next, just as occurs in the genetic anticipation phenomenon of human polyglutamine diseases.

To test this idea, Jung and Bonini expressed a transgene bearing various lengths (51 or 78) of tandem CAG repeats in fly germline cells. Tracking individual transgenes over nine generations revealed an overall rate of instability of up to 20%. The majority of events corresponded to small changes involving expansion or shrinkage of one to three CAG repeat units; 10% of events involved considerably larger repeat expansions or shrinkages (≥10 repeats). Overall, the prevalence of repeat changes in this fly model is still markedly less than that found in humans. However, a striking feature is that the magnitudes of the large shrinkages and expansions are reminiscent of those seen in human patients (*8*, *9*). The fly model shows a consistent bias for expansions over shrinkages, similar to what is observed with paternal transmission in human polyglutamine diseases. Moreover, in flies (as in mammals), larger trinucleotide expansions accelerated the process whereby the increased rate of instability begets even larger expansions. In humans, this scenario has deadly neurological consequences.

How might transcription influence the size of trinucleotide repeats? Such repeats give rise to DNA structures that trigger a DNA repair response (*3*). Jung and Bonini found that *Drosophila* mutants deficient in transcription-coupled repair of DNA exhibited dampened rates of repeat instability. Conversely, mutations in CREB-binding protein (CBP), a protein that interacts with and regulates many transcription factors,

The author is in the Cancer and Developmental Biology Laboratory, National Cancer Institute, Frederick, MD 21702, USA. E-mail: fortini@ncifcrf.gov

CREDIT: P. HUEY/SCIENCE

increased repeat instability. The latter could be reversed by treating flies with trichostatin A, a compound that can counteract loss of CBP activity. Thus, a specific DNA repair mechanism may promote rather than prevent a problem.

The precise role of CBP in influencing repeat expansions is unclear, though. Its ability to modify histones and other protein targets with acetyl groups (*10*) could have global effects on transcription, thereby affecting the expression of key DNA repair enzymes. A lack of major changes in the overall pattern of histone H3 or H4 acetylation in the fly mutants suggests that other CBP targets might be implicated. CBP, which contains a short polyglutamine tract, also accumulates in the pathogenic inclusions with polyglutamine proteins (*11*). It is likely that certain polyglutamine proteins can sequester CBP, reducing its availability in the cell, or can otherwise directly affect CBP function. This interference could increase the rate of repeat instability, which in turn would generate more polyglutamine proteins in a self-reinforcing cycle (see the figure). Whether all polyglutamine disease proteins have similar effects on CBP, and whether such effects extend to disease genes involving other types of expanded trinucleotide repeats, warrants investigation.

The genomic context of trinucleotide repeats is a key determinant in repeat instability (*7*, *12*), an issue that can be systematically addressed using transgenic *Drosophila* approaches. Perhaps most promising is the idea of testing the potential modulatory effects of genetic background with the use of such fly models. In humans, 10 generations span two centuries, with small family sizes and complex environmental and genetic influences. An equivalent longitudinal study using the fly, by contrast, would take just a few months, could be performed under tightly controlled conditions, and could generate much larger numbers of individuals for analysis.

References

1. J. R. Gatchel, H. Y. Zoghbi, *Nat. Rev. Genet.* **6**, 743 (2005).
2. J. Jung, N. Bonini, *Science* **315**, 1857 (2007); published online 1 March 2007 (10.1126/science.1139517).
3. C. E. Pearson, K. Nichol Edamura, J. D. Cleary, *Nat. Rev. Genet.* **6**, 729 (2005).
4. M. M. Muqit, M. B. Feany, *Nat. Rev. Neurosci.* **3**, 237 (2002).
5. S. M. Jackson *et al.*, *Gene* **347**, 35 (2005).
6. R. P. Bowater, A. Jaworski, J. E. Larson, P. Parniewski, R. D. Wells, *Nucleic Acids Res.* **15**, 2861 (1997).
7. L. Mangiarini *et al.*, *Nat. Genet.* **15**, 197 (1997).
8. Y. Takiyama *et al.*, *Hum. Mol. Genet.* **6**, 1063 (1997).
9. R. P. Grewal *et al.*, *Hum. Mol. Genet.* **8**, 1779 (1999).
10. H. M. Chan, N. B. La Thangue, *J. Cell Sci.* **114**, 2363 (2001).
11. A. Kazantsev, E. Preisinger, A. Dranovsky, D. Goldgaber, D. Housman, *Proc. Natl. Acad. Sci. U.S.A.* **96**, 11404 (1999).
12. Y. Zhang, D. G. Monckton, M. J. Siciliano, T. H. Connor, M. L. Meistrich, *Hum. Mol. Genet.* **11**, 791 (2002).

10.1126/science.1141279

GEOPHYSICS

Taking Earth's Temperature

Seismic data and improved analysis techniques allow researchers to measure the temperature at the boundary between Earth's core and the outer mantle.

Bruce A. Buffett

Much of what we know about temperature in the interior of Earth is inferred from phase transitions. Temperature within the rocky mantle (roughly between 30 and 2900 km depth) is of particular interest because it indicates the current state of Earth's heat engine, which powers nearly all geological processes. On page 1813 of this issue (*1*), van der Hilst and colleagues describe new results on the mantle temperature at two depths near the core-mantle boundary (CMB). The difference in temperature gives an estimate of the thermal gradient and heat flow at the base of the mantle. Such estimates are crucial for resolving long-standing questions about the distribution of heat-producing elements, the transport of heat through the interior, and the thermal evolution of the planet.

Changes in pressure and temperature with depth cause transitions in the crystal structure of mantle minerals, which can be detected as abrupt changes (or discontinuities) in the speed of seismic waves (*2*). Researchers typically infer mantle temperature from the depth of these discontinuities using an experimentally determined phase diagram (*3*). Discontinuities at depths of 410 km and 660 km fix the temperature in the upper mantle within experimental uncertainty, whereas the liquid-solid transition at the inner-core boundary anchors the temperature deep in the core. Our ability to interpolate temperature to other depths is compromised by large uncertainties in the core temperature and by an incomplete understanding of the radial structure of convection in the mantle (*4*).

To obtain their results, van der Hilst *et al.* used a seismic imaging technique that maps surfaces of abrupt change in wave speed. Seismic waves that reflect from surfaces near the base of the mantle are recorded mainly before the arrival of the principal reflection from the CMB (see the left panel of the figure). To estimate the spatial structure, magnitude, and even the sign of wave-speed changes, the seismic data are processed by means of numerical methods called "inverse scattering." That is, instead of starting with a geophysical structure and calculating the scattering, the scattered waves are used to reconstruct the scattering structures. These methods were initially developed for hydrocarbon exploration (*5*), but growing interest in other areas of geophysics (*6*, *7*) attests to the utility of high-resolution techniques when spatial sampling of the target region is sufficient.

The reflectors identified by van der Hilst *et al.* are located near the CMB below Central America. They attributed several prominent reflections to a newly discovered transition (*8*, *9*) between the perovskite (pv) phase of the mineral $(Mg,Fe)SiO_3$, the most abundant mineral in the mantle, and the higher-pressure postperovskite (ppv) phase. Published experimental and theoretical estimates for the pressure ($P \approx 110$ to 125 GPa) and temperature ($T \approx 2200$ to 2700 K) of the phase transition suggest that the ppv phase may be present near the base of the mantle. Moreover, the rate of change of pressure with temperature (the Clapeyron slope) is thought to be much larger than values typically reported for the other mantle transitions (*10*–*12*). A steep Clapeyron slope in the vicinity of a thermal boundary layer at the base of the mantle raises the possibility of a double crossing of the pv-ppv phase boundary (*13*). This first transition occurs at the depth where pressure converts pv into the more compact ppv structure. The resulting density increase of 1 to 2% is accompanied by a 2 to 4% increase in the speed of shear waves (*10*, *14*). A second transition occurs

The author is in the Department of Geophysical Sciences, University of Chicago, Chicago, IL 60637, USA. E-mail: buffett@geosci.uchicago.edu

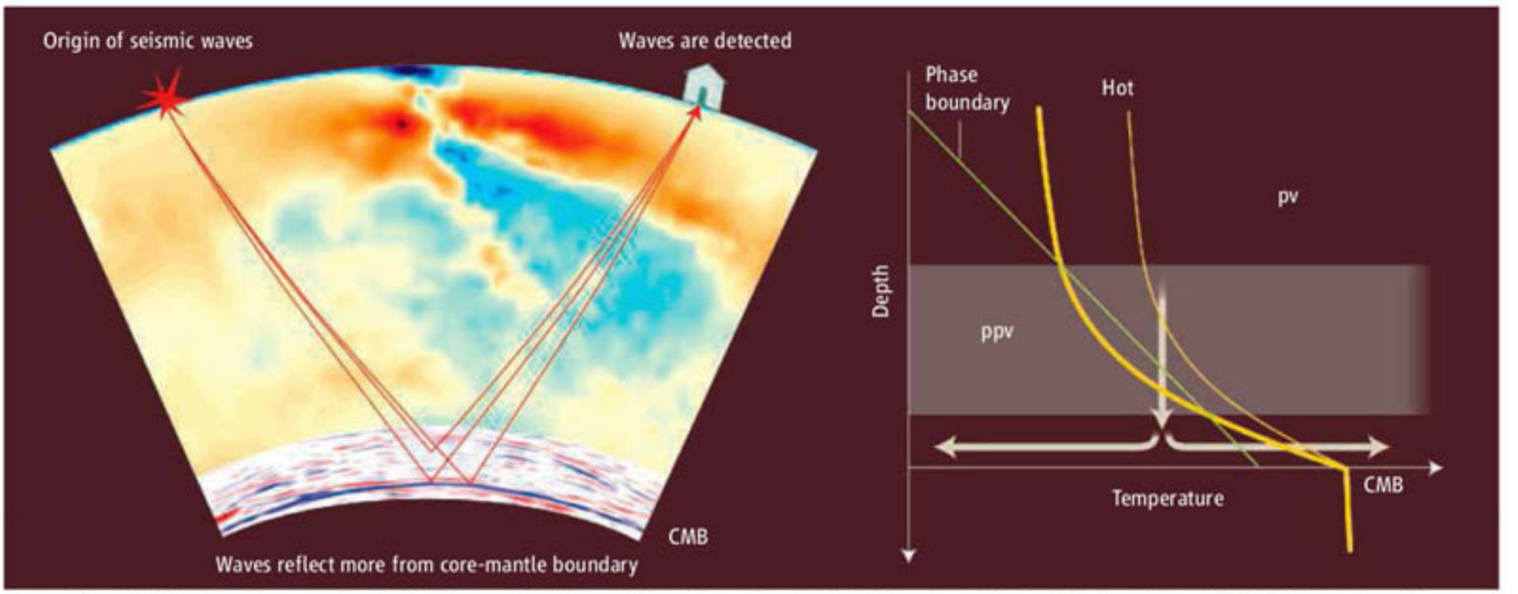

Core values. (**Left**) Waves from a seismic disturbance reflect from different structures in the CMB and are detected at the surface. (**Right**) Intersection of temperature curve (thick yellow line) with the pv phase transition boundary (green line) defines the upper and lower surfaces of the ppv layer. No transition occurs when the overlying mantle is sufficiently hot (thin yellow line). The dense ppv layer (shaded) drives flow toward and along the CMB, altering the temperature gradient due to the effects of latent heat.

within the boundary layer, where a rapid increase in temperature converts the ppv phase back to pv (see the right panel of the figure).

Reflection of shear waves from a double crossing of the pv-ppv phase boundaries should produce characteristic reflections, and the observations support this expectation. The data also reveal substantial variations in the height of the reflectors above the CMB. The upper transition appears to be deflected upward in a region where subduction of the Cocos plate of Central America would presumably lower the temperature. The observed topography is consistent with the positive Clapeyron slope of the pv-ppv transition. The lower transition appears to be deflected downward in this cold region, which is reasonable given that temperature in the boundary layer must adjust to a nearly constant value at the surface of the core; a steeper thermal gradient crosses the phase transition closer to the CMB (*14*).

At the margins of the study area, the upper and lower transitions appear to merge, implying that these regions are too hot to permit the ppv phase. A similar structure (e.g., a region of ppv phase) is present in the central Pacific (*15*), suggesting that double crossings are widespread but not ubiquitous.

So what does this finding mean for Earth's thermal state? The occurrence of a double crossing anywhere indicates that the temperature at the top of the core must exceed the transition temperature at the pressure of the CMB. A lower core temperature permits only a single reflector that must be present everywhere above the CMB.

Conversely, a higher core temperature permits intermittent regions of ppv phase in places where the radial geothermal gradient (rate of change of temperature versus radius) is steeper than the phase boundary (–5 to –8 K/km). Regions where the ppv phase is absent indicate a smaller radial gradient and less heat flow. More specific estimates of temperature and heat flow can be obtained by fitting a simple parametric representation of the boundary layer temperature (*1*, *15*). By matching the points of intersection of thermal gradient with the phase boundary to the height of the observed reflectors, it is possible to calculate the temperature and heat flow at the CMB. Of course, the phase boundary is not well known, and the influence of compositional variations is currently a wild card, but the general relationship between the phase boundary and the local temperature profile should stand the test of time, as long as the reflectors are correctly interpreted as phase transitions. As our knowledge of the phase diagram improves, so will our knowledge of temperature near the base of the mantle.

Another wrinkle is introduced when the dense layer of ppv sinks into the less dense layer of pv. A settling velocity of 1 mm/year is plausible given typical (but uncertain) estimates for the density contrast (*10*), viscosity (*16*), and characteristic dimensions of the ppv region (*1*, *15*), including its height above the CMB. Heat is absorbed at the base of the zone by conversion of ppv to pv, steepening the temperature gradient at the CMB, possibly by a factor of two or more relative to the predictions obtained with the simple boundary-layer model. A higher heat flow would cool the underlying core more rapidly and drive more vigorous convection, increasing the power available to generate Earth's magnetic field. However, additional energy sources in the core may be needed to maintain the higher heat flow.

The important result in this study is the detection of new phase transitions in the mantle with seismic methods that have only recently been applied to the study of the deep interior. Advances in the methodology are likely and better data coverage is expected through the ongoing USArray component of Earthscope. Future work with this and other instruments has the potential to reveal new insights into the inner workings of our planet.

References

1. R. D. van der Hilst *et al.*, *Science* **315**, 1813 (2007).
2. P. Shearer, *J. Geophys. Res.* **96**, 18147 (1991).
3. R. Boehler, *Rev. Geophys.* **38**, 221 (2000).
4. P. J. Tackley, *Science* **288**, 2002 (2000).
5. G. Beylkin, *J. Math Phys.* **26**, 99 (1985).
6. M. G. Bostock, S. Rondenay, J. Shragge, *J. Geophys. Res.* **106**, 30771 (2001).
7. C. Thomas, E. J. Garnero, T. Lay, *J. Geophys. Res.* **109**, B08307 (2004).
8. M. Murakami, K. Hirose, K. Kawamura, N. Sato, Y. Ohishi, *Science* **304**, 885 (2004).
9. A. R. Oganov, S. Ono, *Nature* **430**, 445 (2004).
10. T. Tsuchiya, J. Tsuchiya, K. Umenmoto, R. M. Wetzcovitch, *Earth Planet. Sci. Lett.* **224**, 241 (2004).
11. S. Ono, A. R. Oganov, *Earth Planet. Sci. Lett.* **236**, 914 (2005).
12. K. Hirose, R. Sinmyo, N. Sata, Y. Ohishi, *Geophys. Res. Lett.* **33**, L01310 (2006).
13. J. W. Hernlund, C. Thomas, P. J. Tackley, *Nature* **434**, 882 (2005).
14. J. Wookey, S. Stackhouse, J. M. Kendall, J. Brodholt, G. D. Price, *Nature* **438**, 1004 (2005).
15. T. Lay, J. Hernlund, E. J. Garnero, M. S. Thorne, *Science* **314**, 1272 (2006).
16. J. X. Mitrovica, A. M. Forte, *Earth Planet. Sci. Lett.* **225**, 177 (2004).

10.1126/science.1140470

CLIMATE CHANGE

Ice Sheet Stability and Sea-Level Rise

A wedge of sediments appears to stabilize the Whillans Ice Stream, suggesting that sea-level rise may not destabilize ice sheets as much as previously feared.

John B. Anderson

The base of the West Antarctic Ice Sheet is mostly below sea level. Where the ice is thin enough to float, it spreads seaward into vast ice shelves. The grounding line is the juncture between the ice shelf and the part of the ice sheet that is thick enough to ground on the sea floor. Any increase in water depth or decrease in ice sheet thickness at the grounding line could cause the ice sheet to float off the sea floor. The grounding line will then retreat landward until the water depth decreases or the thickness of the ice sheet increases to the point where it is no longer buoyant.

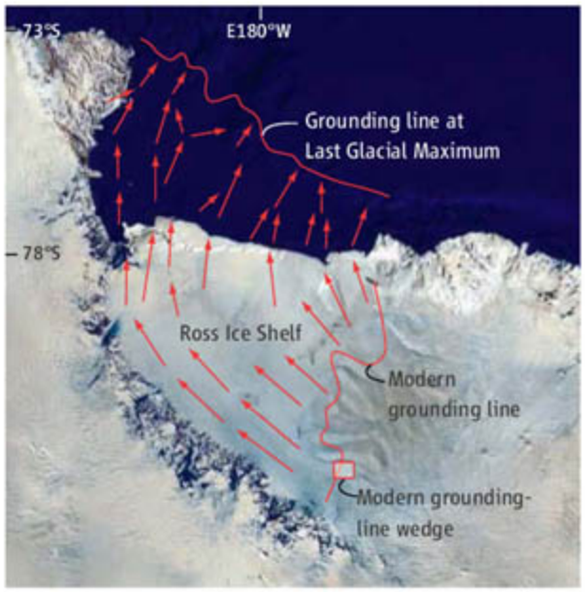

The grounding line, past and present. This satellite image of the Ross Sea and Ross Ice Shelf shows the modern grounding line of the ice sheet, as well as its grounding line ~20,000 years ago (red line). Arrows show flow lines of ice streams. The location of the modern grounding-line wedge identified by Anandakrishnan *et al.* is also shown.

It has long been argued that a rise in sea level or a change in ice sheet thickness can result in rapid grounding-line retreat, thereby increasing the overall rate of sea-level rise (*1*, *2*). Thus, the West Antarctic Ice Sheet may be inherently unstable. The ice sheet has clearly retreated landward since the Last Glacial Maximum (~20,000 years ago) when its grounding line was located at the edge of the continental shelf (*3*) (see the first figure). Recent changes in the ice sheet have raised concern that it may be retreating again.

Two reports in this issue show that at least one threat to the ice sheet's stability—sea-level rise—may not be as serious as has been feared. Anandakrishnan *et al.* on page 1835 (*4*) and Alley *et al.* on page 1838 (*5*) provide evidence that the grounding line of the Whillans Ice Stream, one of the major drainage outlets of the West Antarctic Ice Sheet, rests on a wedge of sediments that will stabilize the ice stream during a sea-level rise of several meters. Thus, in the foreseeable future, sea-level rise should not threaten the ice sheet's stability.

Around West Antarctica, the flow of the ice sheet converges toward the coast as the ice passes through mountain and sea-floor valleys. The converging ice accelerates to form rapidly flowing ice streams, with flow velocities of typically a few hundred meters per year (compared with a few tens of meters per year in nonstreaming parts of the ice sheet). Hence, the ice streams have long been considered the unstable portion of the ice sheet (*6*). Indeed, as the technology for analyzing the behavior of ice streams has evolved, signs of their instability have also emerged (*7*). To assess West Antarctic Ice Sheet stability, it is thus crucial to understand the factors that regulate ice stream behavior over centuries to millennia.

Early discussions of ice stream stability focused on the reason for rapid and potentially episodic flow. Measured velocities of most ice streams far exceed the capacity of ice to flow internally, especially where the ice is not confined by valley walls. Hence, high flow rates must be accounted for by basal sliding. Basal sliding requires a lubricant at the base of the ice sheet, either water or a sediment/water mixture. It is now generally accepted that rapid flow of ice streams is due, at least in part, to flow across a deforming till layer produced by the mixing of basal meltwater with sedimentary material (*8*, *9*).

The deforming till concept implies high rates of sediment transport at the bed. The

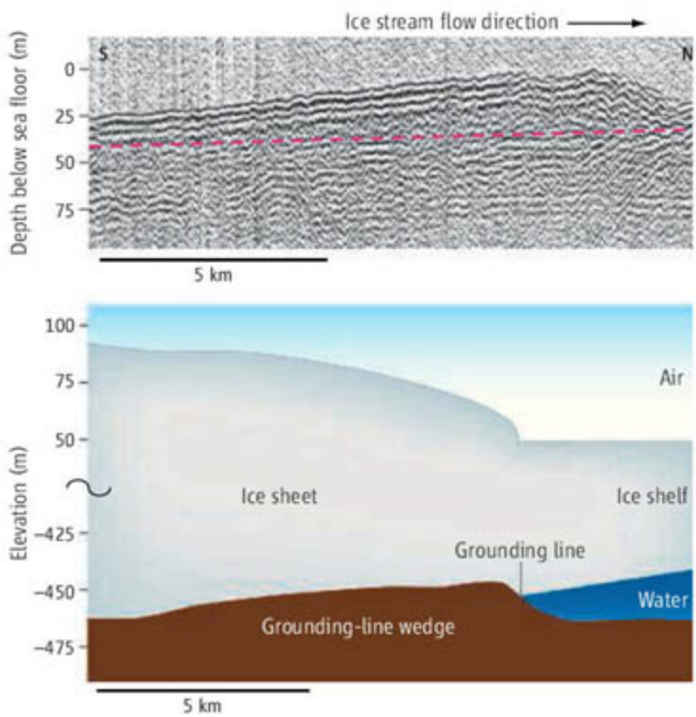

Stabilizing ice sheets. (Top) Seismic image of an ancient ice stream wedge on the Ross Sea continental shelf. The dashed line marks an erosion surface that formed during the advance of the ice sheet onto the continental shelf. The wedge was deposited as the grounding line of the ice sheet became stationary at this location during the overall retreat. [Adapted from (*3*)] **(Bottom)** In the model presented by Alley *et al.*, the wedge elevates the grounding line and manifests itself as an abrupt change in the profile of the ice sheet at this location. It stabilizes the grounding line as sea level rises. The horizontal scale of the model has been adjusted to approximate the wedges on the continental shelf shown at the top.

The author is in the Department of Earth Science, Rice University, Houston, TX 77251, USA. E-mail: johna@rice.edu

PHOTO CREDIT (LEFT) BASEMAP FROM GOOGLE EARTH. ORIGINAL IMAGE FROM NASA

sediment that moves seaward within the subglacial conveyer belt is deposited in wedges of sedimentary material known as grounding-line wedges. Several such wedges have been identified and mapped in broad valleys on the Antarctic continental shelf with detailed images of the sea floor and high-resolution seismic data (see the second figure, top panel) (*10*). Ice streams excavated these valleys when the ice sheet advanced onto these continental shelves. The wedges were formed at locations where the grounding lines stabilized for a while during retreat.

Anandakrishnan *et al.* now provide the first documentation of a grounding-line wedge beneath a modern ice stream, the Whillans Ice Stream. The wedge is likely to have formed during a pause in the overall retreat of the ice sheet. Alley *et al.* describe the wedge in relation to the current ice stream configuration and behavior, and model the response of the ice stream to sea-level rise. The combined results show that the modern grounding line is situated over the crest of the wedge and that the ice thickness increases appreciably upstream of the grounding line (see the second figure, bottom panel). The model results indicate that the ice sheet is thick enough at that point to remain grounded, even with a sea-level rise of several meters. At the current rate of sea-level rise, it would take several thousand years to float the ice sheet off the bed.

The two reports discuss a single ice stream, but relict grounding-zone wedges are common features on the continental shelf, including the Ross Sea shelf (*3*, *10*). In addition, all ice streams of the Siple Coast have an anomalous elevation and stop at the grounding line (*11*). Thus, this mechanism for stabilization of the grounding line is likely to be widespread.

The ice sheets have changed in the past and are changing today. Yet Anandakrishnan *et al.* and Alley *et al.* demonstrate that grounding-line deposition serves to stabilize ice streams, suggesting a decreased role for sea level in explaining these changes. Future research should focus on other ice streams, especially those that currently display signs of instability, to get at the causes of this instability.

References

1. A. Penck, *Sitzungsber. Preuss. Akad. Wiss. Berlin Phys.-Math. Kl.* **6**, 76 (1928).
2. R. H. Thomas, C. R., Bentley, *Quat. Res.* **10**, 150 (1978).
3. A. B. Mosola, J. B. Anderson, *Quat. Sci. Rev.* **25**, 2177 (2006).
4. S. Anandakrishnan, G. A. Catania, R. B. Alley, H. J. Horgan, *Science* **315**, 1835 (2007); published online 1 March 2007 (10.1126/science.1138393).
5. R. B. Alley, S. Anandakrishnan, T. K. Dupont, B. R. Parizek, D. Pollard, *Science* **315**, 1838 (2007); published online 1 March 2007 (10.1126/science.1138396).
6. T. J. Hughes, *Rev. Geophys. Space Phys.* **78**, 1 (1977).
7. D. McAyeal, *Nature* **359**, 29 (1992).
8. R. B. Alley, D. D. Blankenship, S. T. Rooney, C. R. Bentley, *J. Geophys. Res.* **92**, 8931 (1987).
9. B. Kamb, in *The West Antarctic Ice Sheet: Behavior and Environment*, R. B. Alley, R. A. Bindschadler, Eds. (American Geophysical Union, Washington, DC, 2001), pp. 157–199.
10. J. B. Anderson, *Antarctic Marine Geology* (Cambridge Univ. Press, Cambridge, UK, 1999).
11. H. J. Horgan, S. Anandakrishnan, *Geophys. Res. Lett.* **33**, L18502 (2006).

10.1126/science.1140766

ATMOSPHERIC SCIENCE

CO_2 Is Not the Only Gas

About 40% of the heat trapped by anthropogenic greenhouse gases is due to gases other than carbon dioxide, primarily methane.

Keith P. Shine and William T. Sturges

In 1971, one of the first international assessments of the role of humankind in climate change concluded that "because methane has no direct effects on climate…it is considered of no importance" [(*1*), p. 242]. How times change. By the mid-1980s (*2*), methane and a host of other non-CO_2 gases were together recognized to be contributing to climate change by an amount comparable to that of CO_2.

An increase in the concentration of a greenhouse gas causes a change in Earth's energy balance. This change, or radiative forcing, is a simple indicator of the climate change impact. The largest single contributor to radiative forcing is CO_2, with an estimated value of 1.66 W m^{-2} since preindustrial times—enough, on its own, to eventually raise global average surface temperatures by about 1.4°C. The non-CO_2 greenhouse gases contribute an additional 1 W m^{-2} (*3*, *4*).

The Kyoto Protocol to the United Nations Framework Convention on Climate Change recognizes the importance of non-CO_2 greenhouse gases. Emission targets for signatories to the Convention are given in terms of CO_2-equivalent emissions; the signatories can choose to control emissions of several gases—CO_2, methane, nitrous oxide, sulfur hexafluoride (SF_6), the hydrofluorocarbons, and the perfluorocarbons—to meet their targets. There remain issues concerning what emissions are included and excluded in the Kyoto Protocol and the method by which emissions of different gases are placed on a common "carbon-equivalent" scale (*5*). Nevertheless, it is clear that controlling non-CO_2 greenhouse gas emissions can play a very important role in attempts to limit future climate change (*6*, *7*).

The contribution of a given non-CO_2 greenhouse gas to radiative forcing depends on its ability to absorb infrared radiation emitted by Earth's surface and atmosphere. This ability is determined by fundamental spectroscopic properties of the molecule; to be really effective, the molecule must absorb at wavelengths where the atmosphere is not already strongly absorbing. The contribution also depends on the change in the atmospheric concentration of the gas; this change is determined by the size of its emissions and by its atmospheric lifetime. The lifetimes of non-CO_2 greenhouse gases vary from less than a year to thousands of years.

On a per-molecule basis, many non-CO_2 greenhouse gases are far more effective than CO_2 at contributing to radiative forcing. For example, the absorption strength of heavily fluorinated molecules can be 10,000 times that of CO_2. CO_2 has a dominant radiative forcing only because the increase in its atmospheric concentration has been so large—around 100 parts per million (ppm) since preindustrial times. Methane, by contrast, has increased by only 1 ppm; other important non-CO_2 greenhouse gases have increased by parts per billion or even parts per trillion (ppt), yet still contribute appreciably to radiative forcing (*3*, *8*–*10*).

Determining the past and present growth of non-CO_2 greenhouse gases in the atmosphere is not trivial. A global network of surface measurements has only become available since the late 1970s (*8*–*10*). Unraveling earlier histories requires measurements of "firn air" pumped out of deep snow in polar regions, or analysis of tiny bubbles trapped in ice cores. Glacial records of the more abundant gases,

K. P. Shine is in the Department of Meteorology, University of Reading, Reading RG6 6BB, UK. E-mail: k.p.shine@reading.ac.uk W. T. Sturges is in the School of Environmental Sciences, University of East Anglia, Norwich NR4 7TJ, UK. E-mail: w.sturges@uea.ac.uk

CO_2 and methane, are well established, but more complete histories of a wider range of greenhouse gases have only recently become available (*11*–*14*). Some, such as methane, have natural backgrounds due to emissions from, for example, wetlands, soils, and the ocean; methane concentrations have increased dramatically in the 20th century as a result of human activities, including fossil fuel use and agriculture. Other greenhouse gases have been found to be entirely human-made.

Methane poses the biggest challenge to current understanding. Its concentration has increased by a factor of 2.5 since 1800, giving a radiative forcing of almost 0.5 W m^{-2} (*3*, *9*, *10*). Complications arise because methane is chemically reactive, leading to a number of additional effects. For example, rising methane concentrations can cause increases in ozone and stratospheric water vapor concentrations. A recent emissions-based view of methane's radiative forcing that included these additional effects estimated that methane's true contribution was nearer 0.9 W m^{-2} (*15*), equivalent to more than half the radiative forcing caused by CO_2.

The steady rise in methane levels since the mid-19th century has slowed markedly in the past decade (see the figure). There are many possible explanations for this; for example, methane emissions may no longer be increasing, the concentration of oxidizing radicals may have increased because of other emissions, or climate change itself may have hastened methane destruction (via increased temperatures or a greater abundance of oxidizing radicals) (*8*, *9*, *16*). Until this slowdown is properly understood, confidence in projections of future methane changes remains tentative. Questions also persist about the natural emissions of methane; a recent study suggests that plants may constitute a much larger source than hitherto believed (*17*).

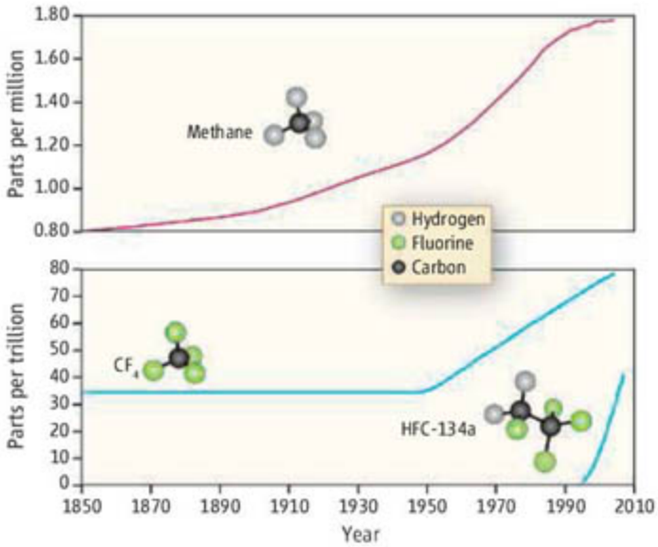

Time histories for the abundances of three non-CO_2 greenhouse gases. Data for methane are from (*6*, *20*) and for the hydrofluorocarbon HFC-134a from (*9*, *10*). The curve for CF_4 is based on a model fit to firn air (*13*) and ice core (*19*) measurements.

Two other major classes of non-CO_2 greenhouse gases are the chlorofluorocarbons and hydrofluorocarbons. Chlorofluorocarbons were widely used in, for example, refrigeration and air conditioning, but have largely been phased out as a result of the Montreal Protocol on Substances that Deplete the Ozone Layer. The concentrations of the most abundant chlorofluorocarbons are nevertheless still high and declining only slowly because of their long lifetimes (*8*). The hydrofluorocarbons have replaced many of the uses of the chlorofluorocarbons; they are benign to stratospheric ozone but are strong greenhouse gases. The concentration of the most abundant of these, HFC-134a, more than doubled every year in the mid-1990s and is still increasing by more than 10% per year; it is now at 40 ppt (see the figure) (*9*, *10*). Its radiative forcing is currently small (about 0.005 W m^{-2}), but if its growth rate is sustained, it will become a significant contributor.

Fully fluorinated gases, including SF_6 and perfluorocarbons such as CF_4, form another distinct group of greenhouse gases. Their sources include aluminum and magnesium smelting, high-voltage dielectrics, and computer chip production. Some, such as SF_5CF_3 (*18*), have origins that remain obscure. These gases have very long lifetimes, in some cases more than 10,000 years (*8*). Once emitted, these "super–greenhouse gases" impart an essentially permanent, although currently very small, change to the atmosphere's ability to absorb infrared radiation. Nearly all are human-made, but CF_4 has a small natural source. It took many millennia for the atmosphere to accumulate 35 ppt of CF_4, and less than 50 years of industrial activity to double it (see the figure) (*8*, *13*, *19*).

It is crucial that researchers continue to monitor non-CO_2 greenhouse gas concentrations and investigate their sources, lifetimes, and spectroscopic properties. These data and insights will enable industry and policymakers to make informed decisions on the desirability and impact of allowing or curbing emissions. CO_2 undoubtedly remains the single most important contributor to greenhouse gas radiative forcing, but the non-CO_2 greenhouse gases are important both collectively and individually. It seems unlikely that we have overlooked a major contributor to radiative forcing, but this was probably what was thought in the early 1970s.

References and Notes

1. *Inadvertent Climate Modification (Report of the Study of Man's Impact on Climate)* (MIT Press, Cambridge, MA, 1971).
2. V. Ramanathan *et al.*, *Rev. Geophys.* **25**, 1441 (1987).
3. The IPCC Working Group I Fourth Assessment Report Summary for Policymakers was released on 2 February 2007 (www.ipcc.ch/SPM2feb07.pdf); the full Working Group I report will be released in May 2007.
4. A cocktail of pollutants, not all of them greenhouse gases, have contributed to higher levels of ozone—which is a greenhouse gas—in the lower part of the atmosphere, indirectly adding a further radiative forcing of 0.35 W m^{-2} (*3*). Through similar effects, ozone in the stratosphere has been reduced, contributing −0.05 W m^{-2} (*3*). Human activity has also changed the concentrations of particles in the atmosphere, leading to a more uncertain cooling effect estimated to be about −1.2 W m^{-2} (*3*). We focus here only on greenhouse gases that are emitted directly into the atmosphere .
5. J. S. Fuglestvedt *et al.*, *Clim. Change* **58**, 267 (2003).
6. J. Hansen, M. Sato, *Proc. Natl. Acad. Sci. U.S.A.* **101**, 16109 (2004).
7. D. P. van Vuuren, J. Weyant, F. de la Chesnaye, *Energy Econ.* **28**, 102 (2006).
8. *Scientific Assessment of Ozone Depletion: 2006* (Global Ozone Research and Monitoring Project, Report No. 50, World Meteorological Organization, Geneva, 2007); the full report is available at www.unep.ch/ozone/Assessment_Panels/SAP/Scientific_Assessment_2006/index.shtml.
9. D. J. Hofmann *et al.*, *Tellus* **58B**, 614 (2006).
10. Updates to gas concentrations can be found at www.esrl.noaa.gov/gmd.
11. J. H. Butler *et al.*, *Nature* **399**, 749 (1999).
12. G. A. Sturrock, D. M. Etheridge, C. M. Trudinger, P. J. Fraser, A. M. Smith, *J. Geophys. Res.* **107**, 10.1029/2002JD002548 (2002).
13. D. R. Worton *et al.*, *Environ. Sci. Technol.* 10.1021/es061710t (2007).
14. See also the report on the CRYOSTAT project at http://badc.nerc.ac.uk/data/cryostat.
15. D. T. Shindell, G. Faluvegi, N. Bell, G. A. Schmidt, *Geophys. Res. Lett.* **32**, L04803 (2005).
16. A. M. Fiore, L. W. Horowitz, E. J. Dlugokencky, J. J. West, *Geophys. Res. Lett.* **33**, L12809 (2006).
17. F. Keppler, J. T. G. Hamilton, M. Brass, T. Röckmann, *Nature* **439**, 187 (2006) .
18. W. T. Sturges *et al.*, *Science* **289**, 611 (2000).
19. J. Harnisch, R. Borchers, P. Fabian, H. W. Gäggeler, U. Schotterer, *Nature* **384**, 32 (1996).
20. For this figure, the data from (*6*) were adjusted using the new internationally accepted gravimetrically prepared scale for methane (*21*).
21. E. J. Dlugokencky *et al.*, *J. Geophys. Res.* **110**, D18306 (2005).

22. Supported by Natural Environment Research Council grant NERC/I/S/00661 (K.P.S.) and the European Commission CRYOSTAT project (W.T.S.). We thank S. Montzka and E. Dlugokencky (NOAA Earth System Research Laboratory) for updated data for HFC-134a and CH_4, and L. Gohar and D. Worton for other assistance with the figure.

10.1126/science.1141677

PUBLIC ENGAGEMENT

AAAS Town Hall Probes Challenges and Opportunities of Climate Change

SAN FRANCISCO—With the United States approaching a tipping point on climate change policy, AAAS brought more than a thousand teachers, students, business executives, and journalists together with top researchers for a town hall forum at the association's Annual Meeting.

Presentations at the event provided educators and students with powerful evidence of climate trends confronting humanity in the century ahead. But a guarded optimism prevailed, and through a creative exercise on greenhouse gas reduction and by exploring possibilities for improved cars, buildings, and power plants, the speakers made clear that science and technology can contribute much to potential solutions.

Researcher Lonnie G. Thompson

AAAS President John P. Holdren, in the Annual Meeting's presidential address, focused on the critical near- and long-term threats from climate change. At the town hall, he opened on a different tack. Climate change is "an immense teaching opportunity," he said, a single framework for delivering lessons in physics, chemistry, biology, meteorology, and technology.

Often the subject is not taught effectively, said P. John Whitsett, president-elect of the National Science Teachers Association (NSTA). While national standards and benchmarks call for teaching it and NSTA and other groups are working to aid teachers, traditional curriculum "dictates science be taught in little boxes," he said. Textbook treatment of climate change "is at best cursory and at worst nonexistent."

AAAS has staked out an ambitious, active profile on global climate change, and the effort culminated in the Annual Meeting from 15 to 19 February under the theme "Science and Technology for Sustainable Well-Being." Environment-related briefings and symposia generated hundreds of news stories in the United States and worldwide. Project 2061, AAAS's science education reform initiative, released a new guide to teaching climate change at the meeting.

Later in February, the United Nations (U.N.) Foundation and Sigma Xi, the Scientific Research Society, issued a climate change report prepared for the U.N. by a panel of 18 experts, including three recent and current AAAS leaders: Holdren, who became chairman of the AAAS Board of Directors at the end of the Annual Meeting; former AAAS President and Chairman Peter H. Raven; and former AAAS Board Member Rosina Bierbaum.

Just before the town hall on Sunday 18 February, the AAAS Board released a statement that drew coverage in the *Washington Post* and other publications. "The growing torrent of information presents a clear message: We are already experiencing global climate change," it said. "It is time to muster the political will for concerted action. Stronger leadership at all levels is needed….We owe this to future generations."

The town hall event, "Communicating and Learning About Global Climate Change," offered participants a half-day of forward-looking briefings and dialogue. It opened with the debut of AAAS's 12-minute video, which describes the science and impact of climate change and focuses on the endangered Inupiat village of Shishmaref in arctic Alaska.

Lonnie G. Thompson, an Ohio State University professor whose study of glaciers has dramatically expanded understanding of climate history, gave the audience a sobering tour of Earth's ice sheets. "Their loss is readily apparent," he said, "and they have no political agenda."

Subsequent speakers suggested creative approaches to climate change, few of them easy.

Paleoclimatologist Margaret Leinen, chief science officer for green-tech startup Climos Inc., described how corporations and venture capital firms are moving more aggressively to invest in potential solutions. "There is no silver bullet for solving this problem," she said, "but we must use every alternative available to us."

Given the enormity of the problem, the challenge is daunting, said two Princeton scholars who presided over a "Stabilization Wedges" exercise. Members of the audience had to develop a portfolio of options for reducing carbon emissions. Voting with electronic clickers, they preferred conservation, increased efficiency, and alternative energy sources, largely rejecting nuclear energy.

Green-tech visionary Amory B. Lovins, chairman of Rocky Mountain Institute, suggested that some climate prescriptions may be too dire. Politicians tend to concentrate on the "cost, burden, and sacrifice" of the effort, he said. "Any practitioner will tell you, empirically, that it's not a costly activity, but a profitable one, because it's cheaper to save fuel than to buy fuel." Further, he said, materials and technology are emerging that will allow extraordinary energy efficiency in jets, cars, and buildings.

Those were the sorts of messages that intrigued many teachers and others who attended.

"I'm concerned that kids will just get depressed about the state of affairs," said Barbara Denny, who teaches environmental science at Miramonte High School in Orinda, California. "I really want to encourage them to start thinking about solutions. So I came for inspiration."

(To see AAAS's climate resources, including town hall presentations, the new video, and the education groups that cosponsored the event, visit www.aaas.org/climate.)

HEALTH SCIENCE

New AAAS Book: Straight Talk on Fighting Obesity

The cover features a brightly colored mélange of vegetables, and the pages inside hold a wealth of plain-spoken anecdotes and science-based advice, making the latest book in AAAS's "Healthy People" an accessible, common-sense guide to fitness and fighting obesity.

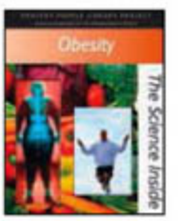

"Obesity: The Science Inside," like the six earlier volumes by AAAS's award-winning Healthy People Library Project, is aimed at providing useful information to minority and disadvantaged communities through public libraries. It steers clear of jargon while emphasizing the importance of good health habits such as eating right and exercising.

With childhood obesity of particular concern, the volume also includes tools for parents to help their children stay healthy, said Kirstin Fearnley, the AAAS Education and Human Resources program associate who researched and wrote much of the booklet.

The booklet was funded in part by the National Center for Research Resources at the U.S. National Institutes of Health. To obtain free copies, visit www.healthlit.org.

— *Carol Viera*

CREDIT (CENTER): THOMAS NASH

Materials for Aesthetic, Energy-Efficient, and Self-Diagnostic Buildings

John E. Fernández

It has become desirable to reduce the nonrenewable content and energy footprint of the built environment and to develop "smart buildings" that allow for inexpensive monitoring and self-diagnostic capabilities. Latest-generation embedded sensors, self-healing composites, and nanoscale and responsive materials may augur a time when buildings can substantially adjust to changing environmental and functional demands. However, faced with the legal liability resulting from unknown lifetime performance, designers and engineers have had little incentive to incorporate new material technologies into building designs. As efficiency issues become more acute, the potential for improvement in performance from new materials, together with partnerships between the materials science community and those entrusted with the design and engineering of the built environment, may offer real breakthroughs for the future.

Buildings satisfy one of the most basic of all human needs: sheltering the diverse collection of human activities. The immutable requirement to provide a reliable and durable built environment has been both a catalyst for and a beneficiary of advances in modern materials science and engineering. Equally enduring is our interest in representing cultural values through our buildings. During much of the 20th century, visions of buildings as "machines for living" were particularly effective in promoting the development of novel material solutions.

Today's buildings contain many materials not available only decades ago, including reinforced concrete, neoprene, silicone, poly(vinyl chloride) (PVC), ethylene tetrafluoroethylene (ETFE), laminated glass using polyvinylbutyral and fiber-reinforced polymer composites, and many others (Fig. 1) (*1*). Many of these materials were discovered and used successfully in industry decades before their application in buildings. For example, PVC was synthesized in its pure form in 1913 and introduced commercially in 1933 but was not used extensively in buildings until the 1970s. ETFE was introduced commercially in 1970 but was not used in buildings until recently, despite very good properties as a glass replacement.

In developed nations, the material throughput devoted to the built environment accounts for 70% (by weight) of national totals. Construction and demolition waste from buildings amounts to 60% of the total nonindustrial waste stream, whereas the global production of concrete alone accounts for about 8% of total CO_2 emissions. In addition, buildings are a component of primary energy use and account for 40% of total energy consumption and 60% of electrical use in developed nations.

Materials for Building Structures

The physical components of a building's structure are responsible for the collection and distribution of the weight of all of the elements of the building and imposed loads from the environment. A building's structure is composed of two subsystems—the superstructure above ground, and the substructure foundation below ground—along with all of the various secondary assemblies that transfer static and dynamic loads to the building frame. Stresses that pass through these components are the result of the cumulative mass of all fixed objects within the building, people using it, the building components themselves, snow and rain, as well as dynamic pressures from the wind that presses on its façade and roof, earthquakes, long-term foundation settlement, and a diverse variety of local conditions. For the most part, the extent of the structure encompasses the enclosed volume of the building, which results in a need for strong, stiff, and inexpensive materials. The selection of economically viable materials for this system is relatively limited and has traditionally included wood, steel, concrete, stone, clays, and a variety of masonry materials. Other nontraditional structural materials such as aluminum, glass, and structural textiles are used only occasionally, with the exception of fiber-reinforced polymers (FRPs), which are widely accepted for short-span bridges and small-building applications (*2*–*4*).

Improving lifetime service reliability has led to intense work in monitoring the health of large-scale structures and providing solutions for damage caused by the environment and age. Our buildings are designed for typical service lives of 50 to 75 years, whereas large civil structures are expected to attain a 120- to 150-year life without additional investment. Monitoring and ensuring the health of these structures includes technologies to provide accurate and inexpensive sensors as well as materials that administer a useful level of repair and self-healing; the latter are variously referred to as "smart," "self-diagnostic," and "self-healing" materials. Another set of concerns are the overall environmental and resource issues that accompany the construction and maintenance of material-intensive building and infrastructure projects. With the awareness of the growing resource consumption involved in the construction and operation of buildings, designers and engineers are in search of techniques and materials that contribute breakthrough gains in material and energy efficiencies.

Structural wood composites, referred to as engineered woods, have been manufactured from a variety of wood waste products, with phenol resorcinol as the most common bonding agent. Wood composites have been used in Europe since around 1890 and today include glue-laminated members, laminated veneer lumber, parallel-strand lumber, and laminated strand lumber. Engineered woods are superior to natural timber in their dimensional stability, use of wood waste, and ease of customization. Current research includes textile and fiber reinforcement using carbon, glass, and aramid materials for higher strength and stiffness (*5*). Research is needed for inexpensive fire treatments and effective, environmentally benign, nontoxic wood preservatives to replace chromated copper arsenate, which has recently come under scrutiny as a source of elevated arsenic levels in areas adjacent

Fig. 1. The ETFE pneumatic double-membrane "pillows" of the façade of the Space and Science Center in Leicester, UK. ETFE, a member of the fluoroplastic family, offers excellent transparency, good mechanical strength, good permeability resistance, and excellent abrasion resistance over a temperature range of −185°C to +150°C. [Photo by J. E. Fernández]

Department of Architecture, MIT Building Technology Program, Massachusetts Institute of Technology, Room 5-418, 77 Massachusetts Avenue, Cambridge, MA 02139, USA. E-mail: fernande@mit.edu

to wood decks, children's playgrounds, and other treated structures.

Research advances in metals for structures have made good progress at improving reliable service under catastrophic conditions. New steel alloys have attained much higher service temperatures while retaining more than 70% of their strength, an important consideration in preventing catastrophic collapse due to fire. Other steels alloyed with various amounts of vanadium, molybdenum, niobium, and copper have shown increased strength over the temperature range in which typical structural steels lose strength, 250° to 550°C (*6*). Also, metal-polymer laminates using elastomeric and natural rubber layers sandwiched between steel or lead plates have been used as isolation bearings for buildings in seismic zones. The bearing surfaces for such devices are as large as 1 m^2 and sustain loads of up to 5 MN. These assemblies are located at the interface between the superstructure and the foundation and take advantage of the nonlinear viscoelastic behavior of rubbers that are capable of deformation up to 300% without permanent damage (*7*).

The development of new concretes, variously reinforced, has been an extremely rich field for materials research for many decades. Major goals of the past several decades have been high strength, lower water and cement content, improved toughness, and resource efficiency. Concretes of various kinds now use a long list of additives for strength, workability, controlled and accelerated curing, compaction, shrink minimization, air entrainment, and the reduction of water and cement content. Mineral additives include sands and coarse aggregates, metakaolin, silica fume, industrial slags, and fly ash; these are used in a variety of concrete mixes for volume fillers, compaction, and cement substitution. Chemical additives include superplasticizers of sulfonated melamine-formaldehyde condensates, sulfonated naphthalene-formaldehyde condensates, modified lignosulfonates, and polycarboxylate derivatives; water-reducing additives include salts and modifications of lignosulfonic acids (lignins), salts and modifications of hydroxylized carboxylic acids, and various polymeric materials. These materials facilitate the production of cement paste at lower water content by deflocculating the cement particles and liberating water. They can also, along with certain sugars and derivatives, retard the curing of concrete.

With these and other improvements, concrete materials have become more workable, durable, and reliable. Impressive gains in strength have accompanied the improvements to these properties. Axial compressive strengths have increased to more than 150 MPa, a threefold rise since 1985. Ultrahigh-performance fiber-reinforced concretes (UHPFRCs) use thin steel whiskers distributed randomly in a highly engineered and compacted concrete matrix composite that displays distinct ductile behavior. Recent work has produced a nano-enabled flexible concrete that uses embedded polyvinyl alcohol microfibers coated with a nanoscale film that controls the fiber-matrix interfacial bond; relative to conventional concrete, this material is 500 times as resistant to cracking and 40% lighter per unit weight (*8*). Aerated autoclaved concrete is a foamed material light and soft enough to be cut with a large bandsaw and stacked like masonry.

Cement research has also considered alternative binders of lower embodied energy. These alternative binders result in "green" concrete, a less resource-intensive material. The use of industrial by-products such as slag and fly ash, along with postconsumer materials such as expanded polystyrene, glass, and recycled concrete, allows the concrete matrix to act as a long-term repository for materials that would otherwise end up in a landfill (*9*).

Current challenges in structural materials continue to be low cost per unit weight, improved strength per unit weight, and strength per unit embodied energy with reliability and durability. In addition, the monitoring of structural behavior deserves special mention. Sensors have been successfully placed in many types of structures, including concrete, steel, wood, and FRP frames (*10*–*12*). Concrete and FRP are particularly amenable to accepting materials and devices that can relay information about the internal stress and strain, as well as moisture content and temperature of concrete and FRP matrices (*13*, *14*). This is important because FRPs, and carbon fiber–reinforced polymers (CFRPs) in particular, are used more intensely as a primary repair system for concrete and masonry structures and carbon fibers become a common reinforcing material directly in the concrete matrix (*15*, *16*). Carbon nanotubes and sheets have potential as monitoring media while providing enormous improvements in strength (*17*, *18*).

Materials for Exterior Enclosures

The building enclosure system controls the flow of mass and energy between the inside and outside. In concert with building services, this system ensures that a reliable and habitable interior environment can be maintained. Air, water, acoustic pressure, and pollutants as well as radiant heat and visible light from the Sun constitute the major elements of these flows. Today, this system includes thermal insulation, air, vapor and radiant barriers, windows, and many other components. In the past, massive walls would ensure that water, air, and heat flow could be controlled to an extent. Over the past decades, the modern building enclosure has delivered a much higher level of predictable service by developing into a multilayered system incorporating a diverse range of materials. These assemblies include the opaque vertical wall, windows, doors, and other openings; the roof, skylights, and water management elements such as flashing and rainwater drains; and any number of elements that negotiate the geometric configuration of the building itself. Separation and specialization of function has been facilitated by the introduction of higher-performing materials targeted at specific barrier needs.

Relative to their mineral wool and natural fiber precursors, modern insulation materials are 1.5 to 3 times as resistant to the flow of heat. Typical materials today include blankets of loose, nonwoven glass fibers; treated cellulose; and polymer foams including polyisocyanurate, polyicynene, polyurethane, and polystyrene. High-performance systems include vacuum- and gas-filled panels encased in aluminized Mylar pillows as well as aerogel materials of foamed silica capable of thermal resistance as low as 0.008 W m^{-1} K^{-1} (Fig. 2). Water vapor resistance is often provided by applying a continuous material layer of limited permeability, most commonly polyethylene sheeting. Air barriers use a variety of sheet materials, and radiant barriers use aluminized paper and Mylar films.

As with structural materials, research for the exterior envelope can also be grouped into two separate lists. First, improved materials for the opaque portion of the exterior envelope—that area of buildings containing all primary barrier systems—can contribute to an overall improvement in energy use. Air, vapor, and radiant barriers as well as materials that are better thermal insulators are critically needed. Smart barriers that can be tuned for a variety of climatic and performance conditions may better address the need to balance energy efficiency with health concerns arising from sick building syndrome. Second, the transparent portion of the envelope—individual window assemblies, curtain walls, and skylights—would benefit from a new generation of materials with precisely tuned properties to allow daylight, avoid glare, and provide controlled heat gain and loss.

Current work includes high-performance thermal insulators of gas-filled panels using argon, krypton, and xenon gas with aerogel (open-cell silica foam) or glass-fiber filler materials. These

Fig. 2. Detail of an unfinished exterior wall assembly showing a waterproof membrane of self-adhering ethylene propylene diene monomer rubber (EPDM) on a structure of precast concrete inset with aluminum window frames. [Photo by J. E. Fernández]

panels have demonstrated effective thermal conductance as low as 0.01 W m^{-1} K^{-1}; that is, they are about 3.5 times as effective as typical glass-fiber batt insulation. Vacuum panels can achieve a value of 0.002 W m^{-1} K^{-1} and lower. However, these systems are relatively expensive and require careful installation. Robust and inexpensive super-insulating materials of thermal conductance below 0.02 W m^{-1} K^{-1} will markedly improve thermal performance of buildings. Additionally, self-repairing air and vapor barriers would greatly advance the energy performance of contemporary buildings by automatically sealing gaps arising from inconsistent quality in the application of these materials.

Material needs for the transparent portion of the envelope require better materials for precisely tuned apertures for a variety of building types and climates. Bringing in daylight is always tempered by the effect of glare and the heat that is transported through infrared radiation. The use of low-emmissivity metal oxide coatings is now widespread in the United States. A full 40% of all windows sold today are coated with a low-emissivity coating that reduces radiative heat flow. Many other materials are being developed for high-performance window assemblies, including spectral-selective glass and polymer sheets and foils; micrometer-scale particles of $CaCO_3$, $BaSO_4$, TiO_2, and ZnS embedded in poly(methyl methylacrylate) (PMMA) and polycarbonate substrates for control of solar radiation; angular-selective thin films; and laser-grooved polymer panels and holographic films (*19*–*22*). There is also a need for inexpensive and efficient reflective mirror surfaces and ultraclear solid polymers for "light pipe" and "light guide" devices that conduct daylight deep into the interiors of buildings and are integrated with anidolic ceiling assemblies (*23*).

In contrast, smart materials for active glazing have been developed but are not currently economically viable for most buildings; many are priced at \$75 to \$250/m^2, 2 to 5 times the cost of double-pane, metal oxide–coated glass. These chromogenic materials display electrochromic, photochromic, and thermochromic behavior and use a wide variety of inorganic and organic materials, including WO_3, NiO, IrO_x, V_2O_5, and others (*24*). Despite the cost, active glazing is a promising field that could lead to effective solutions for low-energy buildings. For example, recent work has resulted in the development of materials that demonstrate a continuously tunable refractive index by varying the use of metal oxide nanoparticles (*25*). Switchable mirrors using transition-metal hydride electrochromics are also being developed, and a number of thermochromic glass laminates may contribute to the production of glazing systems that reject unwanted solar heat gain while maximizing daylighting.

Finally, self-cleaning materials have been developed using biomimetic micro- and nanotextured surfaces that mimic the behavior of several hydrophobic plant leaves, notably *Nelumba nucifera* (lotus) and *Colocasia esculenta*. One example uses micro- and nanopatterned surfaces of PMMA (*26*). Other examples of artificial biomimetic roughness-induced hydrophobic surfaces have shown that a combination of surface coating and roughness determines the level of water repellence and thus the self-cleaning capacity of the material (*27*).

Materials for Building Services

Modern buildings deliver carefully modulated amounts of heat, air, artificial light, water (and sometimes humidity), telecommunications and data, natural light, and other elements to their interior spaces. In addition, buildings evacuate wastes, including heat, stale air, and liquid and solid wastes. This system is analogous to life-support systems in vehicles of all kinds. Building services are intended to create a well-regulated interior environment tailored to serve the needs of occupants in buildings of all types.

Desiccants that support the natural ventilation of buildings and effectively function at a range of dew points and temperatures are needed. Many desiccants are commonly used for low dew points in the range of 50° to 55°C. Passive humidity control materials for improving the mass and heat transfer of desiccant wheels would contribute to low-energy strategies such as natural ventilation and desiccant air conditioning. Porous ceramics are particularly attractive in these applications. Also of interest are materials with high thermal mass, including phase change materials (PCMs), for use in radiant heating and cooling. These materials—salt hydrates (such as $CaCl_2 \cdot 6H_2O$ and $LiNO_3 \cdot 3H_2O$) and paraffin waxes—use their phase transition to store energy over a diurnal cycle (*28*).

As electricity consumption increases, harvesting energy from solar radiation is an important research area. Silicon-based photovoltaics (PVs) account for more than 99% of production. Single-crystal and amorphous cells on the market account for an average efficiency of 12.5% (*29*). Alternative materials, including $CuInSe_2$ and CdTe cells with efficiencies of 20% and organic cells, are providing some novel research pathways. Recently developed PV devices use TiO_2 nanorods together with the conjugated polymer MEH-PPV (poly[2-methoxy-5-(2′-ethyl-hexyloxy)-1,4-phenylene vinylene) (*30*) or use silicon and silicon dioxide to produce quantum dots that absorb a wide range of light wavelengths (*31*).

In the United States, about 8% of total energy and 20% of electrical energy is consumed in artificial lighting. Of the latter, 42% is consumed by incandescent bulbs, a technology that produces light indirectly from a heated filament. Solid-state lighting (SSL), the direct conversion of electricity into light with semiconductor materials, is an extremely promising field of research to reduce this energy consumption. The challenge will be to produce bright white light emission at high efficiencies and low cost. Currently, the cost of SSL devices for architectural lighting exceeds a competitive level by multiples of 10 to 100 (*32*).

The materials science challenge for SSL is primarily in basic research: understanding the behavior and control of light production from light-emitting diodes (LEDs) and organic LEDs (OLEDs), discovering alternative luminescent materials, developing optimal material system and device architectures, and maximizing the extraction of light from all SSL devices (Fig. 3). Today, three- and four-component inorganic materials of aluminum indium gallium phosphide or nitride (AlInGaP or AlInGaN) are most efficient. However, there remain many material combinations that have not been tested and may produce good results. Organic materials of carbon solids have been used for thin-film architecture SSLs, including polymer LEDs (PLEDs), and combined inorganic and organic materials promise real breakthroughs in performance. Currently, industry attention is focused on the application of OLEDs in flat-panel displays because substantial obstacles, such as short service life and high cost, prevent the widespread use of OLEDs in general lighting applications (*33*).

Materials for Interior Construction

Interior construction is primarily meant to delineate interior spaces and to provide privacy through acoustic and visual separation. Research in materials that improve the interior environment may contribute to the health effects of our buildings. Recent work in this area has yielded both virucidal and bactericidal surface coatings. The virucidal coating consists of methylpolyethylenimines (PEIs) and other hydrophobic PEI derivatives (*34*). A bactericidal coating is titanium dioxide exposed to near-ultraviolet light (*35*). More work in this field to develop coatings that effectively eliminate mold and fungus growth may greatly improve indoor air quality in buildings, especially those in humid climates.

A New Era of Material Innovations for Buildings

Recently a new building, the Dives in Misericordia Church in Rome, seemed to be reducing the concentration of urban pollutants in its immediate vicinity (*36*). Upon investigation, it was discovered that the titanium dioxide coating on the large concrete walls of the church was reacting with nitrogen oxide pollutants in a photocatalytic reaction, resulting in a decrease of pollutants in the area. Although the TiO_2 was originally specified for its visual qualities and self-cleaning properties, its effect on local pollutants was a surprise to the architects and engineers of the building. Further research is needed to determine efficacy and real benefits, but proposals are already surfacing for the use of photocatalytic coatings in sidewalks and roads to neutralize the concentration of pollutants found in dense urban conditions.

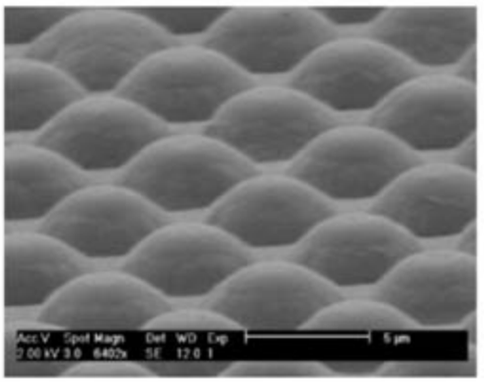

Fig. 3. A polymer microlens array, each lens about 5 μm in diameter and printed on an OLED substrate, extracts 70% more light than a typical white-light OLED. [Photo courtesy of Steve Forrest, University of Michigan]

Also, a "new" material—polyamide, or nylon—has emerged in applications as a "smart" vapor barrier in exterior envelopes. Its water vapor permeability increases by a factor of 10 in conditions of very high humidity. This is particularly useful when moisture is trapped inside a wall assembly. The vapor barrier becomes more permeable and allows moisture to escape, reducing the risk of corrosion, rot, and the growth of mold and mildew. Although nylon was discovered in 1931, its properties as a vapor barrier were not described until 1999, and it was recently commercialized for this purpose (*37*).

Both of these examples illustrate opportunities that arise from addressing the needs of the built environment with materials science and engineering. The first resulted from an unintended consequence of an aesthetic choice, the second from an overlooked property of a common material. Both examples raise the question of why our built environment has been so resistant to change when new materials may offer better performance and more satisfying aesthetic results. The introduction of unfamiliar materials in buildings is difficult because of life safety concerns, first-cost constraints, and the reluctance of builders to adopt new practices in the field. In addition, the very long life of buildings that serve as host to unproven materials compounds the risk of legal exposure for all involved, from researchers to builders. However, it is likely that latent opportunities for achieving a substantially improved built environment await the attention of building experts and the materials science community united in common research goals.

References and Notes

1. J. Fernández, *Material Architecture* (Architectural Press, Oxford, UK, 2006), pp. 44–55.
2. T. Keller, *Use of Fiber Reinforced Polymers in Bridge Construction: Structural Engineering Document No. 7* (International Association of Bridge and Structural Engineering, Zürich, 2003).
3. L. C. Hollaway, *Construct. Build. Mater.* **17**, 365 (2003).
4. L. van den Einde, L. Zhao, F. Seible, *Construct. Build. Mater.* **17**, 389 (2003).
5. D. Dempsey, D. W. Scott, *J. Composites Construct.* **10**, 392 (2006).
6. M. S. Walp, J. G. Speer, D. K. Matlock, *Adv. Mater. Processes* **162**, 34 (2004).
7. J. J. Connor, *Introduction to Structural Motion Control* (Prentice-Hall, Upper Saddle River, NJ, 2003), pp. 286–320.
8. T. Imerito, *JOM* **57**, 18 (December 2005).
9. K. Babu, D. S. Babu, *Cement Concrete Composites* **26**, 605 (2004).
10. K. P. Chong, E. J. Garboczi, *Prog. Struct. Eng. Mater.* **4**, 417 (2002).
11. A. A. Mufti, *Construct. Build. Mater.* **17**, 379 (2003).
12. S.-W. Lu, H.-Q. Xie, *Construct. Build. Mater.* 10.1016/j.conbuildmat.2006.05.062 (2006).
13. A. Norris, M. Saafi, P. Romine, *Construct. Build. Mater.* 10.1016/j.conbuildmat.2006.05.047 (2006).
14. C.-Y. Tang, M. J. O'Brien, G. F. Hawkins, *JOM* **57**, 32 (March 2005).
15. F. Bastianini, M. Corradi, A. Borri, A. di Tommaso, *Construct. Build. Mater.* **19**, 525 (2005).
16. F. Bencardino, V. Colotti, G. Spada, R. N. Swamy, *Cement Concrete Composites* **28**, 832 (2006).
17. V. R. Coluci, D. S. Galvão, A. Jorio, *Nanotechnology* **17**, 617 (2006).
18. R. Dharap, Z. Li, S. Nagarajaiah, E. V. Barrera, *Nanotechnology* **15**, 379 (2004).
19. G. B. Smith, *Solar Energy Mater. Solar Cells* **84**, 395 (2004).
20. M. Kischkoweit-Lopin, *Solar Energy* **73**, 77 (2002).
21. J. Apte, D. Arasteh, Y. J. Huang, paper presented at the annual meeting of the American Society of Heating, Refrigerating and Air-Conditioning Engineers, Honolulu, 22 to 26 June 2006.
22. D. Arasteh, S. Selkowitz, J. Apte, paper presented at the American Council for an Energy-Efficient Economy Summer Study on Energy Efficiency in Buildings, Pacific Grove, CA, 13 to 18 August 2006.
23. S. K. Wittkopf, E. Yuniarti, L. K. Soon, *Energy Build.* **38**, 1120 (2006).
24. C. M. Lampert, *Mater. Today* **7**, 28 (2004).
25. K. C. Krogman, T. Druffel, M. K. Sunkara, *Nanotechnology* **16**, S338 (2005).
26. Y. C. Jung, B. Bhushan, *Nanotechnology* **17**, 4970 (2006).
27. M. Nosonovsky, B. Bhushan, *Microsyst. Technol.* **11**, 535 (2005).
28. H. Weinläder, A. Beck, J. Fricke, *Solar Energy* **78**, 177 (2005).
29. M. Green, *Prog. Photovoltaics* **13**, 447 (2005).
30. Y.-T. Lin *et al.*, *Nanotechnology* **17**, 5781 (2006).
31. N. Lewis, D. G. Nocera, *Proc. Natl. Acad. Sci. U.S.A.* **103**, 15729 (2006).
32. U.S. Department of Energy, *Basic Research Needs for Solid-State Lighting: Report from DOE's Basic Energy Sciences Workshop on SSL, May 22–24, 2006* (available at www.sc.doe.gov/bes/reports/files/SSL_rpt.pdf).
33. U.S. Department of Energy, *The Promise of Solid State Lighting for General Illumination: Conclusions and Recommendations from OIDA Technology Roadmaps Co-sponsored by DOE (BTS) and OIDA* (2001); available at www.netl.doe.gov/ssl/PDFs/oida_led-oled_rpt.pdf.
34. J. Haldar, D. An, L. Álvarez de Cienfuegos, J. Chen, A. M. Klibanov, *Proc. Natl. Acad. Sci. U.S.A.* **103**, 17667 (2006).
35. Z. Haung *et al.*, *J. Photochem. Photobiol. A* **130**, 163 (2000).
36. E. Povoledo, *New York Times*, 28 November 2006, p. 10.
37. H. M. Künzel, *J. Thermal Envelope Building Sci.* **23**, 95 (1999).

38. I thank my colleagues in the Building Technology Program at MIT; M. Andersen, L. Glicksman, and J. Ochsendorf for providing useful suggestions on emerging material technologies for buildings; and A. M. Klibanov and S. R. Forrest for their contributions.

10.1126/science.1137542

Scleractinian Coral Species Survive and Recover from Decalcification

Maoz Fine[1,3]* and Dan Tchernov[2,3]

Increasing global concentrations of atmospheric carbon dioxide (CO_2) enhance hydrolysis of CO_2 in seawater, ultimately decreasing seawater pH (*1*). This has already caused the pH of modern surface waters (8.0 to 8.3) to be about 0.1 pH unit less than in preindustrial times, and geochemical models have estimated further acidification of up to 1.4 pH units over the next 300 years (*1*).

Increased atmospheric CO_2 also reduces carbonate ion concentrations in seawater, which decreases the saturation of aragonite (Ω-arag), the principal mineral deposit of corals. Ω-arag, together with temperature and light, sets boundaries for coral reef biogeography (*2*). Reef communities thrive where Ω-arag is 3.1 to 4.1, but under CO_2 doubling Ω-arag is projected to drop below 3.0. Experiments have shown that CO_2 doubling results in reduced coral calcification (by 44 to 80%) (*3*). A concern has been raised (*4*) that low Ω-arag values and increased chemical dissolution might shift the balance from net accumulation at present to net loss under high-CO_2 conditions.

The geological record suggests that there have been periods with unfavorable conditions for calcification, characterized by absence of fossilized coral (reef gaps) (*5*). The phylogeny of recent corals suggests, however, their origin in the pre-Permian extinction (*6*). These contradicting facts led to the hypothesis that corals have a means of alternating between soft bodies and fossilizing forms (*5*, *7*, *8*), but this has never been tested. We therefore examined the ability of scleractinian corals to survive acidic conditions.

Thirty coral fragments from five coral colonies of the scleractinian Mediterranean species *Oculina patagonica* (encrusting) (Fig. 1A) and *Madracis pharencis* (bulbous) were subjected to pH values of 7.3 to 7.6 and 8.0 to 8.3 (ambient) for 12 months. The corals were maintained in an indoor flow-through system under ambient Mediterranean seawater temperatures (17° to 30°C) and photoperiod (intensity of 250 μmol photons m^{-2} s^{-1}). After 1 month in acidic conditions, morphological changes were seen, initially polyp elongation (Fig. 1B), followed by dissociation of the colony form and complete skeleton dissolution. Surprisingly, the polyps remained attached to the undissolved hard rocky substrate (Fig. 1C).

The biomass of the solitary polyps under acidic conditions was three times as high as the biomass of polyps in the control colonies that continued to calcify and grow. Control and treatment fragments maintained their algal symbionts during the entire experiment, except for six fragments (10%) of *O. patagonica* that partially lost their symbionts (bleached) during July but recovered within 2 months. Gametogenesis in control and experimental corals developed similarly during spring and summer months.

All skeleton-free coral fragments survived to the end of the experiment. After 12 months, when transferred back to ambient pH conditions, the experimental soft-bodied polyps calcified and reformed colonies (Fig. 1D). Hence, in the absence of conditions supporting skeleton building, both species maintained basic life functions as skeleton-less ecophenotypes. This has far-reaching implications for better understanding the natural history of corals (*6*, *8*) but mainly implies that corals might survive large-scale environmental change, such as that expected for the following century.

Physiological, versus geographical, refugia may provide a broader explanation for the existence of corals during times of stress. It is important to note that although survival as soft bodies allows corals to persist, substantial decalcification of reefs will cause major changes to the structure and function of coral reef ecosystems and the services they provide to human society.

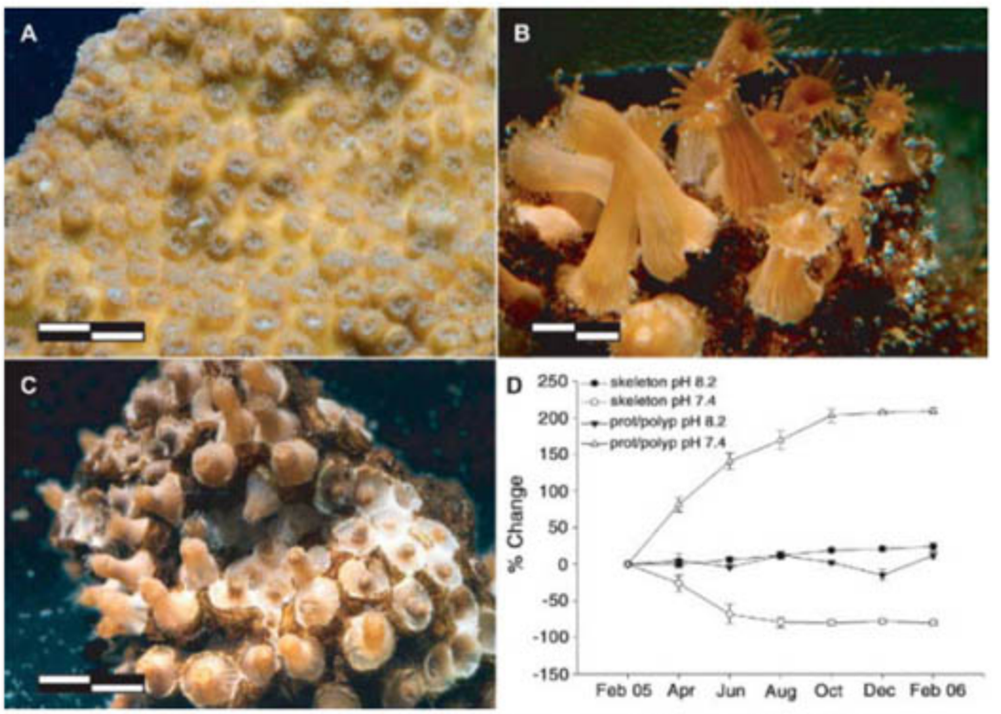

Fig. 1. Photographs of *O. patagonica*. Scale bars indicate 2 mm. (**A**) Control colony. (**B**) Sea anemone–like coral polyps following skeleton dissolution in low-pH conditions. (**C**) Solitary polyps reforming a colony and calcifying after being transferred back to normal seawater following 12 months as soft-bodied polyps in low-pH conditions. (**D**) Time series illustrating percent change (average ± SE) in protein per polyp (biomass) and total buoyant weight over 12 months in experimental (pH = 7.4) and control (pH = 8.2) seawater ($N = 20$). A two-way analysis of variance (time × pH) revealed significant changes ($P < 0.001$) between treatments over time.

References and Notes

1. K. Caldeira, M. E. Wickett, *Nature* **425**, 365 (2003).
2. J. A. Kleypas *et al.*, *Science* **284**, 118 (1999).
3. C. Langdon, M. J. Atkinson, *J. Geophys. Res.* **110**, C09S07 (2005).
4. O. Hoegh-Guldberg, *J. Geophys. Res.* **110**, 11 (2005).
5. G. D. Stanley Jr., *Earth Sci. Rev.* **60**, 195 (2003).
6. S. L. Romano, S. R. Palumbi, *Science* **271**, 640 (1996).
7. M. Medina, A. G. Collins, T. L. Takaoka, J. V. Kuehl, J. L. Boore, *Proc. Natl. Acad. Sci. U.S.A.* **103**, 9096 (2006).
8. G. D. Stanley Jr., D. G. Fautin, *Science* **291**, 1913 (2001).

9. We thank P. Falkowski, K. Caldeira, D. Potts, and A. Genin for their constructive comments; B. Goodman and K. Madmoni for editorial assistance; A. Brietstien for photography; and the School of Marine Sciences and Marine Environment in Michmoret for use of its facilities.

2 November 2006; accepted 21 December 2006
10.1126/science.1137094

[1]Faculty of Life Sciences, Bar-Ilan University, Ramat-Gan, 52900, Israel. [2]Department of Evolution, Systematics, and Ecology, Hebrew University, Givat Ram, Jerusalem 91904, Israel. [3]Interuniversity Institute for Marine Science, Eilat 88103, Israel.

*To whom correspondence should be addressed. E-mail: finema@mail.biu.ac.il

Floral Gigantism in Rafflesiaceae

Charles C. Davis,[1]* Maribeth Latvis,[1] Daniel L. Nickrent,[2] Kenneth J. Wurdack,[3] David A. Baum[4]

The Rafflesiaceae are leafless, stemless, and rootless nonphotosynthetic parasites that live embedded in host plants (*1*). With flowers measuring up to a meter in diameter and weighing up to 7 kg, Rafflesiaceae *sensu stricto* [Supporting Online Material (SOM) text] possess the largest flowers of all angiosperms. Like other holoparasitic angiosperms, the phylogenetic affinities of Rafflesiaceae have proved difficult to resolve because of their reduced vegetative morphology, highly modified reproductive structures (*1*), and anomalous and often accelerated molecular evolution, particularly in plastid (cp) DNA (*2*–*6*).

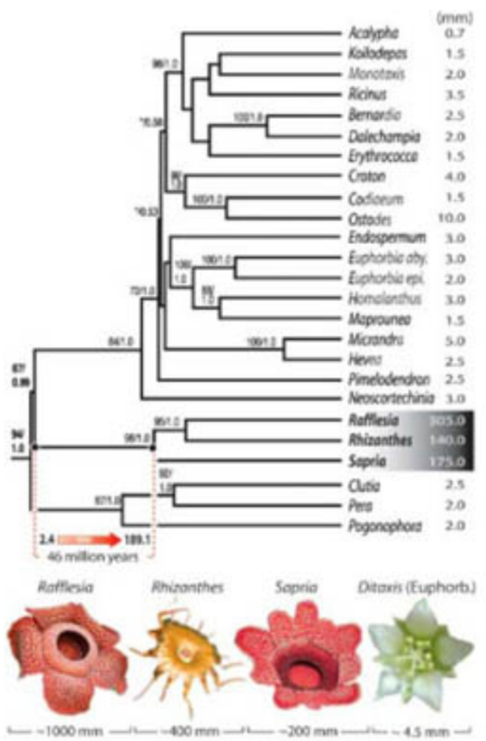

Fig. 1. Phylogeny of Euphorbiaceae [including Rafflesiaceae (bold)] based on a temporally calibrated ML tree (see SOM text for details and fig. S1 for full tree). ML BS and BPP, respectively, are provided. Support values ≤ 50%/0.50 are designated with asterisks. Flower size diameters (in mm) are provided (right), and ancestral flower size estimates are indicated at the stem and crown nodes of Rafflesiaceae. Reconstructions indicate a 79-fold increase in floral diameter for stem lineage Rafflesiaceae (with a 95% confidence interval of 74- to 83-fold). For additional ancestral size estimates see SOM text. Color images with scale bars illustrate the approximate sizes of flowers representative of the three genera of Rafflesiaceae (*Rafflesia arnoldii*, *Rhizanthes lowii*, and *Sapria himalayana*), plus a representative of Euphorbiaceae (*Ditaxis neomexicana*), the latter being similar in size to the inferred ancestral flowers at the stem node of Rafflesiaceae.

By analysis of slowly evolving genes, especially from mitochondrial (mt) DNA, Rafflesiaceae were shown to be members of the Malpighiales (*4*–*6*), a diverse group of circa (ca.) 16,000 species, with 29 major subclades [mostly recognized as families (*7*)]. However, the position of Rafflesiaceae within the order was unclear because of either insufficient taxon sampling (*4*, *6*) or a lack of phylogenetic signal (*5*). We used maximum likelihood (ML) and Bayesian inference (BI) to estimate the phylogeny of Malpighiales from ca. 11,500 base pairs of sequence data (see SOM text for detailed information). Five mt genes (*ccmB*, *cob*, *matR*, *nad6* and *rps3*) and one cp gene [*matK* (*8*)] were sampled from 111 accessions representing all families of Malpighiales (*7*) and 22 outgroup species, including Rafflesiaceae's obligate host, *Tetrastigma* (Vitaceae). Nuclear (nr) small- and large-subunit ribosomal DNA regions were also included for a subset of 40 taxa. Examination of ML bootstrap scores (BS) and Bayesian posterior probabilities (BPP) in the individual analyses of the eight gene regions revealed no significant topological discord, and thus the data were concatenated and analyzed in combination.

Both the ML and BI analyses showed that Rafflesiaceae are nested within Euphorbiaceae (Fig. 1). Strong support was found for both the Rafflesiaceae plus Euphorbiaceae clade (BS = 94% and BPP = 1.0) and the clade that includes Rafflesiaceae and all Euphorbiaceae except *Pera*, *Clutia*, and *Pogonophora* (BS = 87% and BPP = 0.99).

The phylogenetic association of Rafflesiaceae and Euphorbiaceae is robust and not attributable to phylogenetic artifacts (*9*). Although the morphology of Rafflesiaceae prevents identification of unambiguous synapomorphies, some reproductive traits (*10*) are consistent with a placement of Rafflesiaceae within Euphorbiaceae.

We conducted a quantitative analysis of floral size evolution in the context of the estimated phylogeny (SOM text). Flower sizes were determined from the literature and herbarium data. A likelihood ratio test (*11*) rejects the hypothesis that there was a single rate of flower size evolution in the entire Euphorbiaceae-plus-Rafflesiaceae clade. Instead, the optimal model assigns one rate to all Euphorbiaceae lineages and crown-group Rafflesiaceae but a different, higher rate to the stem lineage of Rafflesiaceae. This demonstrates that floral gigantism evolved principally along the stem lineage of Rafflesiaceae, whereas subsequent flower-size evolution within crown group Rafflesiaceae reverted to the original euphorbiaceous rate. Flower size evolved about 91 times faster along the stem lineage than in the rest of the phylogeny. By using Brownie (*12*), we estimated flower diameter to have increased from 2.4 [confidence interval (CI) of 1.1 to 5.3 mm] to 189.1 mm (CI of 91.2 to 392.2 mm) along the stem lineage of Rafflesiaceae (Fig. 1 and SOM text): a ca. 79-fold increase in size in a period of ca. 46 million years (Fig. 1). Thus, a placement of giant-flowered Rafflesiaceae within Euphorbiaceae, whose flowers are nearly all tiny, only increases the evolutionary enigma of "the greatest prodigy of the vegetable world" (*13*).

References and Notes

1. J. Kuijt, *The Biology of Parasitic Flowering Plants* (Univ. of California Press, Berkeley, CA, 1969).
2. D. L. Nickrent, Y. Ouyang, R. J. Duff, C. W. dePamphilis, *Plant Mol. Biol.* **34**, 717 (1997).
3. D. L. Nickrent *et al.*, in *Molecular Systematics of Plants II: DNA Sequencing*, D. E. Soltis, P. S. Soltis, J. J. Doyle, Eds. (Kluwer Academic, Boston, 1998), p. 211.
4. T. J. Barkman, S.-K. Lim, K. Mat Salleh, J. Nais, *Proc. Natl. Acad. Sci. U.S.A.* **101**, 787 (2004).
5. C. C. Davis, K. J. Wurdack, *Science* **305**, 676 (2004).
6. D. L. Nickrent, A. Blarer, Y.-L. Qiu, R. Vidal-Russell, F. E. Anderson, *BMC Evol. Biol.* **4**, 40 (2004).
7. C. C. Davis, C. O. Webb, K. J. Wurdack, C. A. Jaramillo, M. J. Donoghue, *Am. Nat.* **165**, E36 (2005).
8. Plastid *matK* is most likely absent in Rafflesiaceae (SOM text).
9. The phylogenetic placement of Rafflesiaceae is strongly supported by ML and BI methods of both mt and nr data (see SOM text for further evidence).
10. P. F. Stevens, Angiosperm Phylogeny Website, ed. 4 (2001), www.mobot.org/MOBOT/research/APweb.
11. B. C. O'Meara, C. Ane, M. J. Sanderson, P. C. Wainwright, *Evolution* **60**, 922 (2006).
12. Brownie, 2.06b, B. C. O'Meara, University of California, Davis (available by download at www.brianomeara.info/brownie/index.html).
13. R. Brown, *Trans. Linn. Soc. London* **13**, 201 (1822).

14. We thank W. Anderson, H. Cowles, P. Endress, J. Finarelli, J. Hall, A. Knoll, E. Kramer, J. Losos, C. Moreau, B. O'Meara, A. Pringle, B. Ruhfel, and P. Stevens for helpful discussion. C.C.D. was supported by NSF Assembling the Tree of Life (EF 04-31242) and by the Michigan Society of Fellows.

Supporting Online Material

www.sciencemag.org/cgi/content/full/1135260/DC1
SOM Text
Fig. S1
Table S1
References

18 September 2006; accepted 26 December 2006
Published online 11 January 2007;
10.1126/science.1135260
Include this information when citing this paper.

[1]Department of Organismic and Evolutionary Biology, Harvard University Herbaria, 22 Divinity Avenue, Cambridge, MA 02138, USA. [2]Department of Plant Biology, Southern Illinois University, 1125 Lincoln Drive, Carbondale, IL 62901–6509, USA. [3]Department of Botany, Smithsonian Institution, NMNH MRC-166, Washington, DC 20013–7012, USA. [4]Department of Botany, University of Wisconsin, 430 Lincoln Drive, Madison, WI 53706, USA.

*To whom correspondence should be addressed. E-mail: cdavis@oeb.harvard.edu

Seismostratigraphy and Thermal Structure of Earth's Core-Mantle Boundary Region

R. D. van der Hilst,[1]* M. V. de Hoop,[2] P. Wang,[1] S.-H. Shim,[1] P. Ma,[3] L. Tenorio[4]

We used three-dimensional inverse scattering of core-reflected shear waves for large-scale, high-resolution exploration of Earth's deep interior (D″) and detected multiple, piecewise continuous interfaces in the lowermost layer (D″) beneath Central and North America. With thermodynamic properties of phase transitions in mantle silicates, we interpret the images and estimate in situ temperatures. A widespread wave-speed increase at 150 to 300 kilometers above the core-mantle boundary is consistent with a transition from perovskite to postperovskite. Internal D″ stratification may be due to multiple phase-boundary crossings, and a deep wave-speed reduction may mark the base of a postperovskite lens about 2300 kilometers wide and 250 kilometers thick. The core-mantle boundary temperature is estimated at 3950 ± 200 kelvin. Beneath Central America, a site of deep subduction, the D″ is relatively cold (ΔT = 700 ± 100 kelvin). Accounting for a factor-of-two uncertainty in thermal conductivity, core heat flux is 80 to 160 milliwatts per square meter (mW m^{-2}) into the coldest D″ region and 35 to 70 mW m^{-2} away from it. Combined with estimates from the central Pacific, this suggests a global average of 50 to 100 mW m^{-2} and a total heat loss of 7.5 to 15 terawatts.

At a depth of ~2890 km, the core-mantle boundary (CMB) separates turbulent flow of liquid metals in the outer core from slowly convecting, highly viscous mantle silicates. The 200- to 300-km-thick thermo-chemical boundary layer on the mantle side—the so-called D″ layer—is enigmatic (*1*, *2*), but a recently discovered phase transition from perovskite (pv) to postperovskite (ppv) in $(Mg,Fe)SiO_3$ (*3*–*5*) begins to explain seismologically observed complexity [e.g., (*6*)]. If the ppv transition occurs, one can, in principle, estimate in situ variations in temperature from the pressure-temperature dependence (that is, the Clapeyron slope) and the seismologically inferred location of the associated interface (*7*). Steep (conductive) thermal gradients in D″ can produce multiple crossings of the phase boundary, and identification of associated seismic signals offers new opportunities for constraining (local) core heat flux (*8*, *9*).

Seismic (transmission) tomography delineates smooth changes in wave speed associated with mantle convection (Fig. 1A), but one must focus on the scattered wave field to image interfaces associated with transitions in mineralogy or composition. Scattering of *PKP* (the main *P* wave propagating through the core) in D″, first recognized in the early 1970s (*10*), has been used to constrain stochastic models of deep mantle structure [e.g., (*11*)], but the most detailed and accurate constraints on D″ structure to date have come from forward modeling of shear waves reflected at or near the CMB (*12*, *13*). This approach has its drawbacks, however. First, it requires prior knowledge about the target structure and often assumes relatively simple geometries, the uniqueness of which is not easily established. Second, it relies on signal associated with near- and postcritical incidence, which limits radial resolution and the CMB regions that can be studied (*14*). The small distance window can also reduce the available source-receiver azimuths, which can degrade imaging in directions perpendicular to dominant sampling (*15*).

Stacking of data from dense source and receiver arrays can enhance weak signals and has begun to produce tantalizing images of D″ stratification (*9*, *15*, *16*). However, most applications still rely on near-critical data and require strict data selection and visual inspec-

[1]Department of Earth, Atmospheric, and Planetary Sciences, Massachusetts Institute of Technology, Cambridge MA, USA. [2]Center for Computational and Applied Mathematics, Purdue University, West Lafayette, IN, USA. [3]Department of Statistics, University of Illinois, Urbana-Champaign, IL, USA. [4]Mathematical and Computer Sciences, Colorado School of Mines, Golden, CO, USA.

*To whom correspondence should be addressed. E-mail: hilst@mit.edu

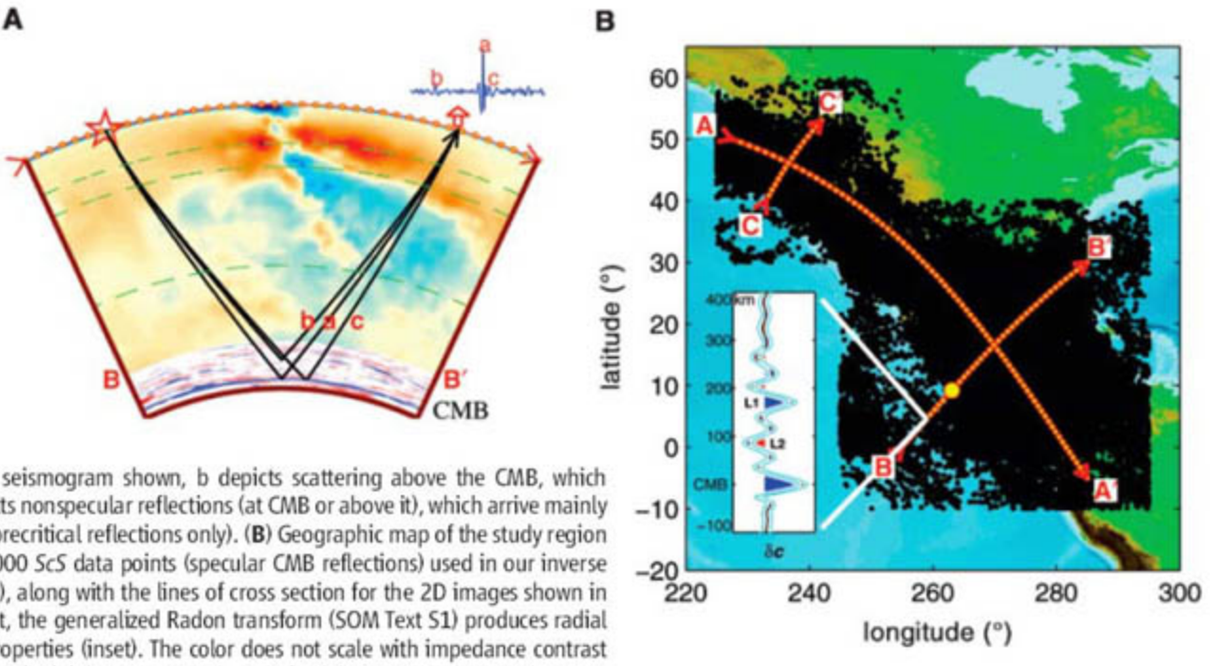

Fig. 1. (**A**) In the mantle, tomography depicts smooth *P*-wave speed variations (*45*) associated with deep subduction (blue structure in center of section) beneath Central America; inverse scattering constrains deep mantle reflections in the lowermost 400 km. Superimposed on the tomography/scattering image are schematic ray paths of *ScS* waves reflecting at and above the CMB: a depicts specular CMB reflections, which contribute to the main *ScS* arrival in the seismogram shown, b depicts scattering above the CMB, which produces precursors, and c depicts nonspecular reflections (at CMB or above it), which arrive mainly in the coda of *ScS* (we consider precritical reflections only). (**B**) Geographic map of the study region with bounce points of the ~80,000 *ScS* data points (specular CMB reflections) used in our inverse scattering study (*17*) (black dots), along with the lines of cross section for the 2D images shown in Figs. 2 and 3. At each yellow dot, the generalized Radon transform (SOM Text S1) produces radial profiles of contrasts in elastic properties (inset). The color does not scale with impedance contrast but with the reflection coefficient (*14*) (blue, $R > 0$; red, $R < 0$). Only structure outside the 75% confidence level (thin lines) is discussed here.

tion, which prohibits application to very large data sets

Large-Scale Deep Earth Exploration Seismology

Systematic three-dimensional (3D) imaging of large D″ regions becomes feasible if one can (i) rely on fewer a priori assumptions, so that structures of unknown geometries can be detected; (ii) use efficient methods to detect, extract, and interpret subtle signals in large volumes of broad-band waveforms available through modern data centers; (iii) use data from more source-receiver distances; and (iv) validate results by means other than labor-intensive forward modeling. To achieve this, we combine inverse scattering—specifically, a generalized Radon transform (GRT) of the wave field comprising core-reflected shear waves (*ScS*) (SOM Text S1)—with statistical methods (SOM Text S2) to produce images of D″ structure and to estimate their uncertainty. This approach benefits from the superior 3D sampling afforded by narrow- and wide-angle data (SOM Text S3) and requires few a priori assumptions about target structures and no visual inspection of data.

For the source-receiver distances considered, specular (mirror-like) reflections of interfaces above the CMB arrive before *ScS* proper, whereas nonspecular CMB reflections arrive after the main phase (Fig. 1A). The GRT uses data redundancy to identify coherent signal from (single) scattering and localizes the causative structures (*17*). Statistical inference, a nonlinear process that replaces stacking, suppresses the effects of uneven source-receiver distribution, incorrect wave-speed models, and multiple scattering, and yields rigorous Bayesian confidence levels (*18*). The latter is used as the initial tool for model validation, which allows routine analysis.

We used ~80,000 broad-band (1 to 20 s) records of the *ScS* wave field for large-scale, high-resolution exploration of the D″ beneath Central and North America (Fig. 1B) (SOM Text S3). The GRT maps data from wide angles [epicentral distances between 43° and 80° (fig. S3)] into multiple images of the same structure (as illustrated in fig. S1), which are then combined into a radial profile of medium contrasts at a specified CMB location (Fig. 1B, inset). These reflectivity profiles are aligned on the CMB and corrected for 3D mantle heterogeneity inferred from global tomography (*19*). Juxtaposition of these radial profiles produces 2D (or 3D) images that reveal the lateral extent of medium contrasts and lowermost mantle stratification (fig. S2). Figure 2 clearly reveals the CMB beneath the Americas, but our subject is the rich pattern of scatterers and interfaces up to 400 km above it.

D″ Structure and Temperature

Figure 3 displays the GRT images (top) along with variations in *S*-wave speed, $d\ln V_S$, derived from tomography (bottom). To emphasize the relations among them, we superimpose the strongest scatterers (at more than 75% confidence) on the wave-speed maps. We focus on the structures labeled L1, L2, and L3.

Postperovskite transition. Structure L1 delineates an increase of wave speed with depth. In most places L1 is unambiguous because the amplitude of the pulses that define it can be a substantial fraction of the CMB peak (Fig. 1B, inset), depending on the angle at which L1 is sampled (fig. S1). Our GRT results pertaining to L1 corroborate more localized previous studies of the main D″ discontinuity beneath Central America [see table 1 in (*15*)], but they also constrain structure far into previously uncharted D″ territory. The depth variation of L1 correlates strongly with changes in *S*-wave speed (*20*). If

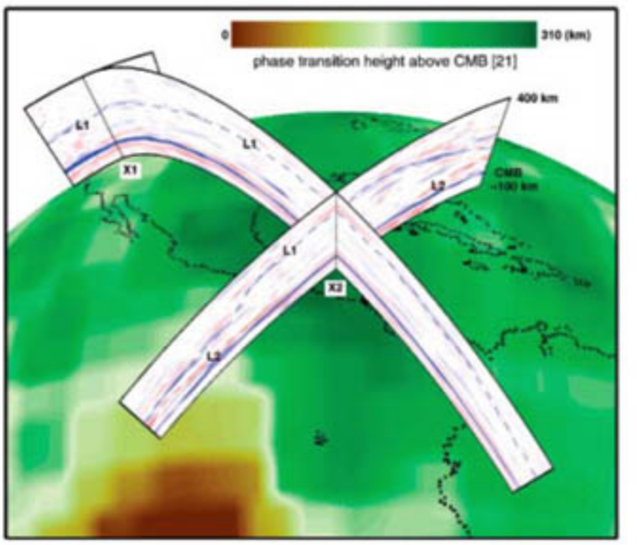

Fig. 2. Three-dimensional exploration seismology of the lowermost mantle. Seismic images of the lowermost mantle (CMB to 400 km above it) are produced by lateral juxtaposition of radial general Radon transform profiles (fig. S2) calculated at image points along the section lines shown in Fig. 1. Structure outside 75% confidence bands (*18*) includes the CMB (at 0 km) and several scatter interfaces above it. Thinly dashed lines indicate scatter interfaces (L1, L2) highlighted in Fig. 3. This 3D rendition illustrates the large spatial scales over which inverse scattering with the *ScS* wave field can be used to explore the lowermost mantle. Points X1 and X2 indicate the section intersections. The background color depicts the prediction of the height above the CMB of a presumed phase transformation with a Clapeyron slope of 6 MPa/K (*21*). In most of this region, the correlation between L1 and the predicted values is very good

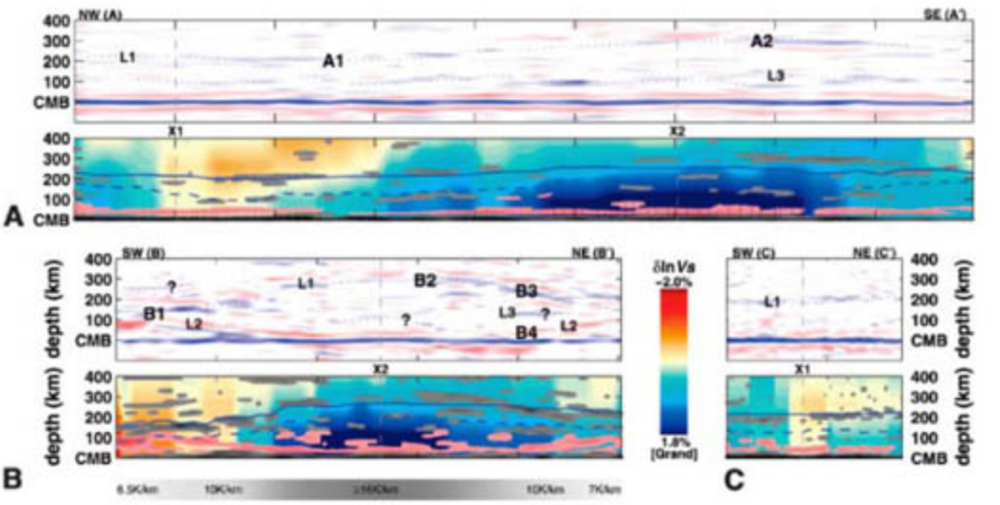

Fig. 3. Reflectivity from inverse scattering, at more than 75% confidence (*18*) (top) and *S*-speed ($d\ln V_S$) from tomography (*19*) (bottom). Scatter images are obtained by interpolation between GRT profiles (Fig. 1B, inset) calculated every 1° (~60 km at CMB) along sections A-A′, B-B′, and C-C′ in Fig. 1. For the frequencies and incidence angles used, the radial resolution is ~10 km. The color scale for tomography is given between B-B′ and C-C′. (**A**) L1, L2, and L3 label the scatter interfaces (thinly dashed). (**B** and **C**) The associated scatterers (visually enhanced) are superimposed on the tomography profiles, with dark gray depicting positive reflections and pink/red negative contrasts. Interface L1 aligns increases of wave speed with increasing depth; L2 delineates a decrease; L3 is more ambiguous but generally coincides with a wave-speed increase. Whereas L1 and L2 are piecewise continuous, L3 has an intermittent, en echelon appearance. The solid (dashed) blue lines in the bottom panels depict the phase transition location predicted by (*21*) (*22*). Points A1 and A2 and points B1 to B4 on L1 and L2 are used for temperature calculations (Fig. 4). The gray scale below B-B′ depicts the lateral variation in temperature gradient along the CMB (for γ_{ppv} = 10 MPa/K) estimated from (*29*). In the central portion of the section, dT/dz cannot be determined directly because the occurrence of the double crossing cannot be resolved.

the latter is (partly) of thermal origin, the GRT images provide direct evidence for a widespread presence of a D″ interface with a positive pressure-temperature relationship.

Sidorin *et al.* (*21*) postulated that a phase transition with Clapeyron slope $\gamma = 6$ MPaK^{-1} marks the top of D″. A recent analysis (*22*) puts the main discontinuity ~95 km deeper (dashed blue line, Fig. 3), but the original prediction (solid blue lines) is quite close to L1. The larger topography on the latter suggests that γ is more than 6 MPaK^{-1}, which is consistent with estimates from mineral physics for the ppv transition (*7*), or that the actual wave-speed variations are larger than inferred tomographically. If, indeed, interface L1 marks the ppv transition, we can estimate in situ mantle temperatures from its topography (Fig. 4). For $\gamma_{ppv} = 10$ MPaK^{-1}, the temperatures at B1 and B2 are ~2000 and ~2900 K, respectively, and the difference between A1 and A2 is ~600 K.

On long wavelengths (1000 to 2000 km), the changes in temperature along L1 reflect the shoaling of the phase boundary toward D″ regions where relatively cool slab debris can be expected. Changes on a scale of ~450 km relate to the margins of these regions and to localized slow regions. Steeper topography is observed locally, for instance at ~800 km along section B-B′, which is close to a steplike jump previously attributed to folding of subducted slab (*23*). Seismic tomography (Fig. 1A) and the above temperature differences both support the presence of slab debris, and slab buckling is indeed likely to occur in this region (*24*). Drawing conclusions from isolated structures can be misleading, however, and partial reconstruction of multiple scatter interfaces can produce ambiguity. Interface L1 aligns the strongest scatterers and is consistent with (*21*), but we cannot rule out that between 0 and 800 km (in section B-B′) it continues southeastward with little topography and that the stronger structure at ~150 km represents interface L3.

Postperovskite lens? The GRT images reveal much structural complexity between the CMB and L1, the presumed top of D″. Particularly intriguing is a wave-speed reduction (producing the negative pulse, L2, in Fig. 1B, lower left) that delineates a large-scale (~2300 km) concave-up interface in the lowermost 100 km or so of the mantle. Because of side lobes of the CMB reflection, L2 cannot be established between 1000 and 2000 km along B-B′, but interfaces that dip toward the seismologically fast central region are resolved on either side of this patch. In this region, (*15*) reported a wave-speed decrease further above CMB and more parallel to the top D″ interface.

Published estimates of CMB temperature T_{cmb} vary from 3750 K to 4800 K (*25*–*27*), and most exceed T_{ppv}. The latter implies that ppv is instable near the CMB and that there is a second crossing of the phase boundary. The back transition (ppv→pv) occurs deeper in colder regions (Fig. 4), thus creating ppv lenses beneath mantle downwellings (*8*, *16*). This transition is hard to detect (*28*), but recent studies provide evidence for it in the lowermost mantle beneath the Pacific (*9*) and the Cocos plate (*22*). In our GRT profiles, the negative pulses are statistically significant (Fig. 1 and fig. S2), and both the sign and the deepening toward regions of presumably lower D″ temperatures is consistent with ppv→pv. The presence of L2 and the anticorrelated topographies of L1 and L2 provide new evidence that ppv-rich lenses do indeed exist. The lens beneath Central America has a width of ~2300 km and a thickness of ~250 km; L1 and L2 merge (near B1) ~125 km above the CMB ($T = 2900$ K; $P = 128$ GPa). Outside this lens, the temperature may be too high for ppv to be stable, except, perhaps, in regions of iron enrichment (*9*).

Mantle temperature near CMB. Whereas the ppv transition constrains temperatures some 150 to 300 km above the CMB, double crossings provide insight into the thermal structure closer to the core (*8*, *9*). We know neither T_{cmb} nor the thickness H and temperature change ΔT_{TBL} across a thermal boundary layer (TBL), but with reasonable assumptions we can estimate T_{cmb} and ΔT_{TBL} by fitting error functions to temperatures at L1 and L2 as a function of H (*29*). H increases from colder to warmer D″ regions. If the CMB is isothermal, and not arbitrarily hot, we obtain stable estimates of T_{cmb} and ΔT_{TBL} for H such that the ppv transition (e.g., at B3) occurs above or near the top of the TBL and the back transition (e.g., at B4) occurs well within it. For $H = 100$ to 200 km and $\gamma_{ppv} = 10$ MPa/K, we infer $T_{cmb} = 3950 \pm 200$ K and $\Delta T_{TBL} = 1600$ to 1400 K (Fig. 4C). These values depend on the Clapeyron slope and, in particular, on the phase-boundary temperature at the CMB; we estimate that $T_{cmb} \approx T_{ppv,cmb} + 290$ K. Our T_{cmb} is lower than, but within error consistent with, the estimate of 4100 K in (*9*).

Despite large uncertainties, T_{cmb} constrains the melting curve of iron in the liquid core because the temperature just below the CMB must exceed the melting temperature of core materials. Experimental and computational estimates of the melting point of pure Fe at CMB pressures span a range from 3200 ± 200 K (*30*) to 4800 ± 200 K (*31*). Minor elements can reduce this by as much as 700 to 1000 K (*27*), but

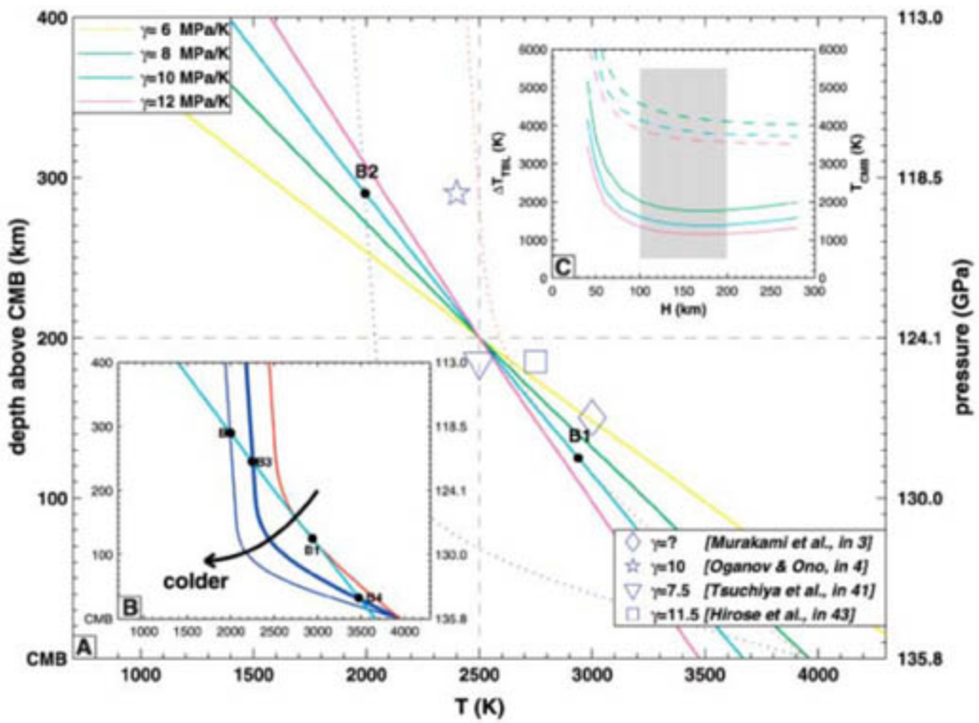

Fig. 4. (**A**) Temperature (*x* axis) versus distance above CMB (*y* axis). As a point of reference for producing absolute temperature and depth (pressure), we assume $P_{ppv} = 124$ GPa and $T_{ppv} = 2500$K, and we consider Clapeyron slopes $\gamma_{ppv} = 6$, 8, 10, and 12 MPa/K. If L1 in Fig. 3 represents the ppv transition, the temperature at points B1 and B2 can be estimated as $\gamma_{ppv} = 10$ MPa/K, $T_{ppv,B2} = 2000$ K, and $T_{ppv,B1} = 2900$ K. Dotted lines depict estimated geotherms through B1 and B2; the shallow part is adiabatic, but toward the CMB the conductive geotherm is described as an error function (the change of adiabat to conductive is not known, however). (**B**) Cold, intermediate, and hot geotherms. As the mantle temperature decreases, a ppv transition occurs at increasing distances above CMB, and a second crossing would occur at decreasing height above CMB. The geotherm through the ppv transition (B3) and the back-transformation (B4) is calculated (*29*) using a thickness of the hypothetical boundary layer, H, of 150 km. (**C**) Mantle temperature, T_{cmb}, at the CMB (dashed lines) and the temperature change, ΔT_{TBL}, across the thermal boundary layer (solid lines) as a function of TBL thickness, H, and for $\gamma_{ppv} = 8$, 10, and 12 MPa/K. Stable estimates are obtained for $H = 100$ to 200 km (gray shading).

experiments reveal that for oxygen and sulfur the effect is small (*32*). If $T_{cmb} = 3950 \pm 200$ K, the melting point in (*31*) may thus be too high.

Core heat flux. To estimate heat flux, we need to know thermal conductivity κ and the temperature gradient dT/dz across the TBL. A lower bound on the latter is given by γ_{ppv}^{-1} (*8*); for $\gamma_{ppv} = 7$ to 10 MPa/K, this implies $dT/dz_{min} = 5.8$ to 8.3 K/km. The gradient must be steeper than γ_{ppv}^{-1} for a double crossing to occur. Our temperature estimates imply gradients of 7 to 16 K/km (Fig. 3B).

Even if we assume that these gradients are reasonably accurate, the regional and, in particular, global heat flux remains subject to considerable uncertainty. First, the region where dT/dz can be estimated does not span a diverse geodynamical environment. We consider the steep gradients as representative of cold D″ areas. Our study region does not include large-scale low wave-speed regions, where higher mantle temperatures and lower gradients are expected. We could speculate that our regional minimum (~7 K/km) is close to the global average, but this would be a lower bound if the anomalously low wave speeds are (in part) due to chemistry [e.g., (*33*)]. Lay *et al.* (*9*) consider effects of iron and estimate the thermal gradient beneath the central Pacific at 8.5 ± 2.5 K/km.

Second, the value of thermal conductivity is debated. The often-used $\kappa = 10$ $Wm^{-1}K^{-1}$ (*25*) would imply a regional variation in heat flux q_{cmb} of 115 ± 45 mWm^{-2}, compared with 85 ± 25 mWm^{-2} below the Pacific (*9*). If one assumes that these regional values represent extremes, a reasonable average flux would be $q_{cmb} \approx 100$ mWm^{-2} (corresponding to a global heat loss across the CMB of ~15 TW). However, κ may be as small as 5 $Wm^{-1}K^{-1}$ (*34*, *35*). Depending on the amount of radiative conduction, the conductive component to the heat loss across the CMB is thus uncertain by (at least) a factor of two ($Q_{cmb} \approx 7.5$ to 15 TW). It is likely, however, that the flux into the base of the mantle exceeds the heat conducted down the core adiabat, which has implications for models of thermal core-mantle coupling, core evolution, and the distribution of heat-producing elements (*36*, *37*).

Other D″ interfaces? Over the entire geographical region studied here, the GRT images suggest the presence of scatterers (L3 in Fig. 3) some 100 km below the presumed top of the D″. Further study is required to establish whether it is the partial detection of a continuous interface (or multiple interfaces) or whether it represents a depth range with intermittent, en echelon scatter zones. The sign of change in elastic properties is not unequivocal because of ambiguity between main pulse and side lobes. Positive and negative changes may both occur, but variations in *S*-wave speed in this depth interval suggest the preponderance of radial increases in wave speed.

Slab folding (*16*, *24*), along with preserved compositional heterogeneities, can perhaps provide the complexity detected here. Alternatively, local changes in temperature or chemical composition [e.g., in iron content (*38*) or partitioning between pv and magnesiowüstite (*39*)] can readily create multiple crossings of the phase boundary. Alternating, irregular ppv and pv lenses (or layers) may be more realistic than a single ppv lens (*40*) and can explain some of the multiple, but intermittent, scatter interfaces. This calls for further investigation by means of joint imaging and geodynamical and petrological modeling.

New Opportunities for Deep-Earth Imaging

The results presented here should be regarded as first steps, but they show the potential of using inverse scattering techniques originally developed to search for hydrocarbon reservoirs for the systematic, high resolution investigation of the lowermost mantle over large regions, including hitherto uncharted D″ territory. Application to Central America allows verification against previous results, but similar high-resolution D″ imaging should be possible elsewhere, for instance, beneath large parts of Eurasia. As we suppose was the case when seismologists pondered over the first reflection profiles of Earth's crust, image quality is not as good everywhere as one would wish, and even first-order observations can be puzzling. However, we expect that refinement of inverse scattering, accounting for increasingly many complexities and using exponentially growing data sets will remove existing ambiguities and provide insight into the structure, dynamics, and evolution of this remote frontier of cross-disciplinary research.

References and Notes

1. M. E. Wysession *et al.*, *Geodynam. Ser. (Am. Geophys. Un.)* **28**, 273 (1998).
2. E. J. Garnero, *Annu. Rev. Earth Planet. Sci.* **28**, 509 (2000).
3. M. Murakami, K. Hirose, K. Kawamura, N. Sata, Y. Ohishi, *Science* **304**, 855 (2004).
4. A. R. Oganov, S. Ono, *Nature* **430**, 445 (2004).
5. S. H. Shim, T. S. Duffy, R. Jeanloz, G. Shen, *Geophys. Res. Lett.* **31**, L10603 (2004).
6. J. Wookey, S. Stackhouse, J.-M. Kendall, J. Brodholt, G. D. Price, *Nature* **438**, 1004 (2005).
7. Relevant here are the pressure P (or depth, z) and temperature T of the ppv transition and the Clapeyron slope γ of the phase boundary in P-T space, all of which have considerable uncertainties. Published values include $P_{ppv} \sim 110$ to 125 GPa, $T_{ppv} \sim 2200$ to 2700 K, and $\gamma_{ppv} \sim 7$ to 11.5 $MPaK^{-1}$ (*4*, *41*–*43*). We convert depth to pressure according to the Preliminary Reference Earth Model (PREM) (*44*).
8. J. W. Hernlund, C. Thomas, P. J. Tackley, *Nature* **434**, 882 (2005).
9. T. Lay, J. Hernlund, E. J. Garnero, M. S. Thorne, *Science* **314**, 1272 (2006).
10. J. R. Cleary, R. A. W. Haddon, *Nature* **240**, 549 (1972).
11. M. A. H. Hedlin, P. M. Shearer, P. S. Earle, *Nature* **387**, 145 (1997).
12. T. Lay, E. J. Garnero, *Geophys. Monogr. Ser.* **150**, 25 (2004).
13. D. V. Helmberger, T. Lay, S. Ni, M. Gurnis, *Proc. Natl. Acad. Sci. U.S.A.* **102**, 17257 (2005).
14. For given impedance contrast, the reflection coefficient R increases with scatter angle, or epicentral distance, in particular toward the critical angle (fig. S1). Wide-angle data can produce strong peaks in the stacks even for weak interfaces, which allows modeling, but radial resolution is diminished because the dependence of travel time on interface position vanishes for near grazing incidence. Near- and postcritical D″ reflections and refractions arrive at ~74° to 85° from the source, but modeling studies often use even narrower distance ranges (e.g., 79° to 82°). With nonuniform source and receiver distributions, narrow distance ranges can imply narrow source-receiver azimuths. The latter may, effectively, turn 3D techniques into 2D probes. We use data in a much larger distance range (43° to 80°, with most data between 50° and 70°); see fig. S3. The inclusion of relatively narrow angle data enhances radial resolution (fig. S1) and allows more complete 3D data coverage.
15. C. Thomas, E. J. Garnero, T. Lay, *J. Geophys. Res.* **109**, B08307 (2004).
16. A. Hutko, T. Lay, E. J. Garnero, J. Revenaugh, *Nature* **441**, 333 (2006).
17. P. Wang, M. V. de Hoop, R. D. van der Hilst, P. Ma, L. Tenorio, *J. Geophys. Res.* **111**, 10.1029/2005JB004241 (2006).
18. P. Ma, P. Wang, L. Tenorio, M. V. de Hoop, R. D. van der Hilst, *J. Geophys. Res.*, Manuscript available at http://quake.mit.edu/hilstgroup/robspage/PapersPDF/2006JB004513R.pdf.
19. S. P. Grand, *Philos. Trans. R. Soc. London A* **360**, 2475 (2002).
20. Upon image construction, we correct for 3D variations in *S*-wave speed (*19*), but the location of the scatterers (discontinuities) could be biased toward (or away from) the CMB in regions where the actual wave speed is higher (or lower) than inferred from tomography. This is the opposite of the observed trend, which suggests that the actual topography (and the Clapeyron slope or temperature variation inferred from it) could be larger than inferred here.
21. I. Sidorin, D. V. Helmberger, M. Gurnis, *Science* **286**, 1326 (1999).
22. D. Sun, T.-R. A. Song, D. Helmberger, *Geophys. Res. Lett.* **33**, L12S07 (2006).
23. Hutko and co-workers (*16*) observe a steplike jump in a north-south section (their A-A') ,whereas we see it best in a southwest-northeast section (B-B'). This is no contradiction; both may sample different (but nearby) parts of a 3D, northwest-southeast trending structure.
24. N. Ribe, E. Stutzmann, Y. Ren, R. D. van der Hilst, *Earth Planet. Sci. Lett.* **254**, 173 (2007).
25. F. Stacey, *Physics of the Earth* (Brookfield, Kenmore, Queensland, Australia, ed. 3, 1992).
26. D. Alfè, M. J. Gillan, G. D. Price, *Earth Planet. Sci. Lett.* **195**, 91 (2002).
27. E. Knittle, R. Jeanloz, *J. Geophys. Res.* **96**, 16169 (1991).
28. C. Flores, T. Lay, *Geophys. Res. Lett.* **32**, 10.1029/2005GL024366 (2005).
29. Absent knowledge about the behavior of the conductive geotherm in this complex thermochemical boundary layer, we use $T(z) = T_{cmb} - \Delta T_{HS}\mathrm{erf}\,(z/H)$, with error function (erf) describing heat diffusion into a half space and ΔT_{HS} the total temperature contrast across the half space. From ΔT_{HS}, we estimate the contrast across the TBL as $\Delta T_{TBL} = \mathrm{erf}(1)\Delta T_{HS} = 0.84\Delta T_{HS}$. For different Clapeyron slopes, we calculate T(B3) and T(B4). For a given diffusion length H, we can then find a unique solution of T_{cmb} and ΔT_{TBL}.
30. R. Boehler, *Nature* **363**, 534 (1993).
31. Q. Williams, R. Jeanloz, J. Bass, B. Svendsen, T. J. Ahrens, *Science* **236**, 181 (1987).
32. R. Boehler, A. Chopelas, A. Zerr, *Chem. Geol.* **120**, 199 (1995).
33. R. D. van der Hilst, H. Kárason, *Science* **283**, 1885 (1999).
34. A. M. Hofmeister, *Science* **283**, 1699 (1999).
35. A. P. van den Berg, E. S. G. Rainey, D. A. Yuen, *Phys. Earth Planet. Inter.* **149**, 259 (2005).
36. J. Bloxham, *Philos. Trans. R. Soc. London A* **358**, 1171 (2000).

37. B. A. Buffett, *Science* **288**, 2007 (2000).
38. W. Mao *et al.*, *Proc. Natl. Acad. Sci. U.S.A.* **101**, 15867 (2004).
39. Y. Kobayashi *et al.*, *Geophys. Res. Lett.* **32**, 10.1029/2005GL023257 (2005).
40. S.-H. Shim, *Am. Geophys. Union Geophys. Monogr.* **160**, 261 (2005).
41. T. Tsuchiya, J. Tsuchiya, K. Umemoto, R. M. Wentzcovitch, *Earth Planet. Sci. Lett.* **224**, 241 (2004).
42. T. Iitaka, K. Hirose, K. Kawamura, M. Murakami, *Nature* **430**, 442 (2004).
43. K. Hirose, R. Sinmyo, N. Sata, Y. Ohishi, *Geophys. Res. Lett.* **33**, L01310 (2006).
44. A. M. Dziewonski, D. L. Anderson, *Phys. Earth Planet. Inter.* **25**, 297 (1981).
45. H. Kárason, R. D. van der Hilst, *J. Geophys. Res.* **106**, 6569 (2001).
46. This research is supported by the Collaboration in Mathematical Geosciences program of the U.S. National Science Foundation. All waveform data were obtained through the Data Management Center of the Incorporate Research Institutions for Seismology. We thank D. Sun (Caltech) for providing their latest ppv model and B. Hager (MIT) and A. van den Berg (Utrecht University) for discussions.

Supporting Online Material
www.sciencemag.org/cgi/content/full/315/5820/1813/DC1
SOM Text
Figs. S1 to S3
References

21 November 2006; accepted 22 February 2007
10.1126/science.1137867

Computational Design of Peptides That Target Transmembrane Helices

Hang Yin,[1]* Joanna S. Slusky,[1]* Bryan W. Berger,[1] Robin S. Walters,[1] Gaston Vilaire,[2] Rustem I. Litvinov,[3] James D. Lear,[1] Gregory A. Caputo,[1] Joel S. Bennett,[2] William F. DeGrado[1,4]†

A variety of methods exist for the design or selection of antibodies and other proteins that recognize the water-soluble regions of proteins; however, companion methods for targeting transmembrane (TM) regions are not available. Here, we describe a method for the computational design of peptides that target TM helices in a sequence-specific manner. To illustrate the method, peptides were designed that specifically recognize the TM helices of two closely related integrins ($\alpha_{IIb}\beta_3$ and $\alpha_v\beta_3$) in micelles, bacterial membranes, and mammalian cells. These data show that sequence-specific recognition of helices in TM proteins can be achieved through optimization of the geometric complementarity of the target-host complex.

Transmembrane (TM) helices play essential roles in biological processes, including signal transduction, ion transmission, and membrane-protein folding. Computational (*1*–*4*) and genetic methods (*5*, *6*) are available to engineer antibody-like molecules that target the water-soluble regions of proteins; however, companion methods to target the TM regions are lacking. The design of TM helices that specifically recognize membrane proteins would advance our understanding of sequence-specific recognition in membranes and simultaneously would provide new approaches to modulate protein-protein interactions in membranes. Here we describe a computational approach, designated computed helical anti-membrane protein (CHAMP), to design peptides that specifically recognize the TM helices of natural proteins (*7*).

Computational design. The design of a CHAMP peptide requires the selection of a backbone geometry for the CHAMP peptide-target complex, followed by computational selection of the CHAMP peptide's amino acid sequence with a side-chain repacking algorithm. To simplify the selection of the backbone geometry, we used the growing database of membrane-protein structures, rather than relying on idealized helical dimers. The majority of the TM helix-helix pairs in TM proteins of known structure fall into a handful of well-defined structural motifs with recognizable sequence signatures (*8*). Thus, it is possible to predict a preferred mode of interaction between a target TM helix and other TM helices from the amino acid sequence alone. Once a preferred mode of interaction has been identified, examples of helix pairs from proteins of known structure can be used as backbone conformations for the design of a desired CHAMP peptide. The next steps are (i) to thread the sequence of the targeted TM helix onto one of the two helices of the selected pair and (ii) to select the amino acid sequence of the CHAMP helix with a side-chain repacking algorithm (*1*–*4*, *9*).

As a stringent test of the CHAMP method, we focused on the recognition of the TM domains of two closely related and extensively studied platelet integrins, $\alpha_{IIb}\beta_3$ and $\alpha_v\beta_3$, as convenient biologically important targets (*10*–*12*). Both the α_{IIb} and α_v TM helices contain a small-X_3-small motif, in which G (*13*) or other small residues (A and S) are spaced four residues apart (*14*) (Fig. 1, B and C). This sequence motif is associated with a high propensity to interact in a tightly packed "parallel GAS_{Right} motif" (*8*) with a right-handed helical crossing angle of ~ 40°. Indeed, site-directed mutagenesis (*15*–*17*) and modeling studies (*15*, *17*, *18*) suggest that the α_{IIb} TM helix binds the β_3 TM helix with this geometry.

Five template backbones were tested in the design of a CHAMP peptide directed against α_{IIb}, and 15 were tested for α_v. The sequences of α_{IIb} and α_v were threaded onto either of the two helices in each template, yielding two different CHAMP peptides per template. A sequence for the opposing CHAMP helix was then selected with a Monte Carlo repacking algorithm that considers different combinations of side chains in low-energy rotamers (*1*–*4*, *9*) [see Supporting Online Material (SOM)]. The rotameric states of the side chains in the target were allowed to vary, as were both the sequence and rotamers of the CHAMP side chains. A simple energy function that is based on a linearly dampened Lennard-Jones potential and a membrane depth–dependent knowledge-based potential (*19*) was then used to select the desired residues. This knowledge-based potential assured that residues with high propensities to occupy the interfacial and fatty acyl region of the bilayer were selected at appropriate positions. The membrane-exposed residues of the CHAMP helix were then randomly selected with a 60% probability of assigning L and a 10% probability of assigning A, I, F, or V.

The TM domains of α_v and α_{IIb} are highly homologous (Fig. 1, B and C), and they both have small-X_3-small motifs. Because a number of other integrin TM helices also contain a small-X_3-small motif, a specific CHAMP peptide must recognize not only this global feature of its target, but also more fine-grained differences in surface topography. In the computed complexes with the lowest energy, the CHAMP sequences designed against α_v and α_{IIb} both have G-X_3-G sequences that create a shallow concavity that is important for recognizing the small-X_3-small sequence on the integrin helices. However, the surrounding sequences differ in response to differences in the sequences of the target (Fig. 1, B and C), thereby providing specificity.

A CHAMP peptide with extensive geometric complementarity to its target (Fig. 1D and fig. S1) was selected based on its energy score, the uniformity of packing of the side chains at the CHAMP-target interface, and the ease of synthesis. [Peptides with multiple strings of β-branched amino acids and sequences with particularly high predictions for amyloid (*20*) were avoided.] The templates for the CHAMP peptide-target complexes were taken from polytopic proteins with no functional or structural relation to integrins, the CHAMP peptide

[1]Department of Biochemistry and Biophysics, School of Medicine, University of Pennsylvania, Philadelphia, PA 19104, USA. [2]Hematology-Oncology Division, Department of Medicine, School of Medicine, University of Pennsylvania, Philadelphia, PA 19104, USA. [3]Department of Cell and Developmental Biology, School of Medicine, University of Pennsylvania, Philadelphia, PA 19104, USA. [4]Department of Chemistry, University of Pennsylvania, Philadelphia, PA 19104, USA.

*These authors contributed equally to this work.
†To whom correspondence should be addressed. E-mail: wdegrado@mail.med.upenn.edu

against α_v (anti-α_v) was taken from the glycerol-3-phosphate transporter (1PW4, residues A64 to A86 and A121 to A141) (*21*), and anti-α_{IIb} was taken from the photosystem I reaction center (1JB0, residues L43 to L65 and L114 to L140) (*22*). The designed peptides and their TM targets (α_{IIb}-TM and α_v-TM) (see SOM) were synthesized with solubility-enhancing groups appended to the C and N termini to facilitate membrane insertion (*23*, *24*). Control peptides, in which the GX_3G motifs were mutated (anti-α_{IIb}mut and anti-$\alpha_v$mut) or scrambled (anti-α_{IIb}scr), were also prepared to study the specificity of the designed sequences (Fig. 1E).

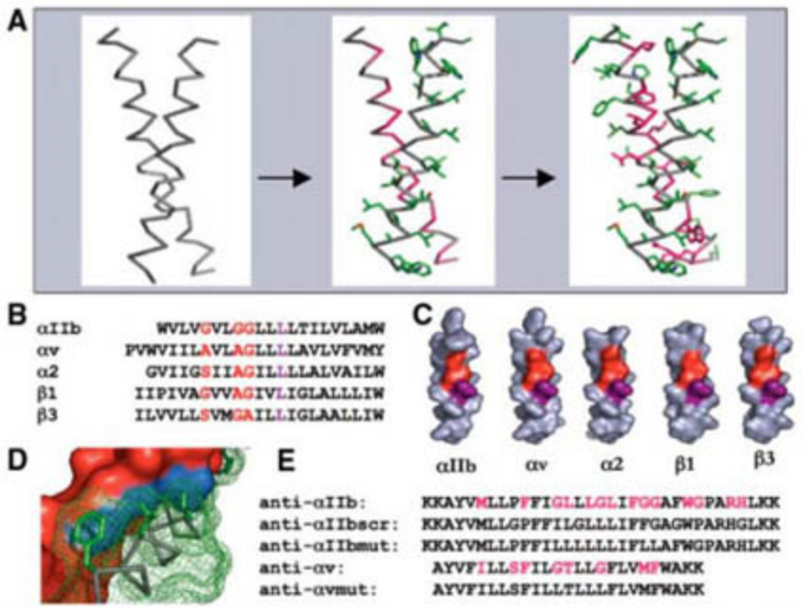

Fig. 1. (**A**) Design of CHAMP peptides. A backbone geometry was selected for the CHAMP-target complex; for α_{IIb}, the template was taken from two interacting helices in a much larger protein, the photosystem I reaction center (*22*). The original sequence was stripped off of the template, and the helices were extended to span the full length of a membrane. The sequence of α_{IIb}-TM was threaded onto the right helix. The 14 positions selected for repacking are pink on the left helix. The final anti-α_{IIb} CHAMP peptide sequence is shown on the left helix with the repacked positions in pink. (**B** and **C**) Human integrin TM targets and TM helices from homologous human integrins used in specificity assays. The sequences (B) are modeled in an idealized helical conformation (C). Common small (G, A, and S) residues are highlighted in red, and a common L on the binding interface is shown in purple. (**D**) Close-up of the predicted tightly packed interface between anti-α_{IIb} and α_{IIb}-TM. α_{IIb}-TM is represented by a red surface with a blue hot spot. The anti-α_{IIb} backbone is depicted in ribbon representation, with key positions designated for computational design shown in green. (**E**) Sequences of CHAMP designs and the control peptides. The residues repacked in the anti-α_{IIb} and anti-α_v peptides are shown in pink. $(Lys)_2$ (*23*) or polyethylene glycol (*24*) was appended to the C and N termini as solubility-enhancing groups.

CHAMP binding in micelles. We used fluorescence resonance energy transfer (FRET) to evaluate the association of anti-α_{IIb} with α_{IIb}-TM in micelles. The titration of 7-hydroxycoumarin–tagged anti-α_{IIb} as a FRET donor, with fluorescein-tagged α_{IIb}-TM as a FRET acceptor, resulted in the quenching of the coumarin emission and the appearance of the fluorescein emission, indicating that the two peptides interacted (Fig. 2A). The apparent dissociation constant (K_d) for the α_{IIb}-TM–anti-α_{IIb} interaction was computed to be 0.32 ± 0.05 μM. The corresponding K_d expressed as a mole fraction (peptide versus detergent) is $3.2 \pm 0.5 \times 10^{-4}$, which is relatively tight when compared with the range of 10^{-2} (for weak associations) to 3×10^{-5} for very strong associations (*25*), measured for TM-peptide associations in a similar micellar environment. Titrations with control peptides showed the specificity of the interaction; there was negligible binding between α_{IIb}-TM and either anti-α_{IIb}mut or α_v-TM (Fig. 2B). Furthermore, titrations with anti-α_v showed that this peptide specifically recognized α_v-TM ($K_d = 1.3 \pm 0.3 \times 10^{-3}$ as a mole fraction), but not α_{IIb}-TM or anti-$\alpha_v$mut (Fig. 2C).

Analytical ultracentrifugation of anti-α_{IIb} and α_{IIb}-TM, as well as anti-α_v and α_v-TM in micelles, indicated that these peptides formed homodimers, as well as heterodimerizing with their respective targets (fig. S2 and table S2). Both CHAMP peptides heterodimerized with

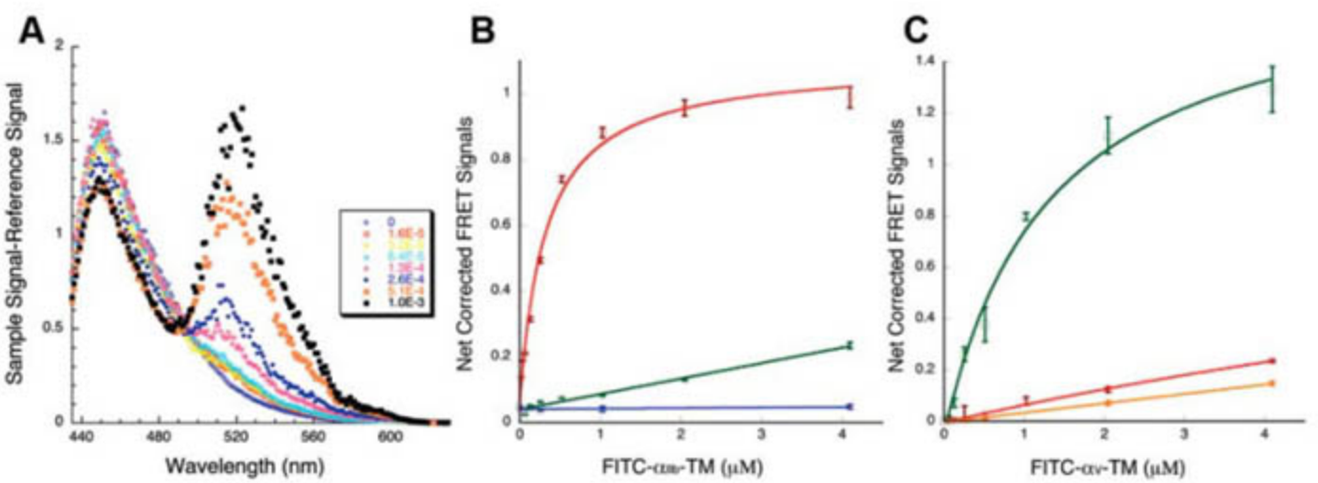

Fig. 2. Affinity and selectivity of CHAMP peptides for their target TM helices. (**A**) Fluorescence emission scans of coumarin-labeled anti-α_{IIb} (64 nM) in the presence of different concentrations of fluorescein isothiocyanate (FITC)–tagged α_{IIb}-TM in 10 mM 4-(2-hydroxyethyl)-1-piperazineethanesulfonic acid (HEPES), pH= 7.5, containing 1.0 mM C14-betaine at 25°C. (Inset) Concentrations as mole fractions. λ_{ex} was set at 415 nm to selectively excite the coumarin. λ_{ex}, excitation wavelength. (**B**) Corrected FRET signals of 64 nM coumarin-labeled anti-α_{IIb} (red), anti-α_v (green), or anti-α_{IIb}mut (blue) in the presence of different concentrations of FITC-tagged α_{IIb}-TM (10 mM HEPES, pH= 7.5, containing 1.0 mM C14-betaine at 25°C). Error bars represent SD of the mean. (**C**) Corrected FRET signals of 64 nM coumarin-labeled anti-α_v (green), anti-α_{IIb} (red), or anti-$\alpha_v$mut (orange) in the presence of different concentrations of FITC-tagged α_v-TM (10 mM HEPES, pH= 7.5, containing 1.0 mM C14-betaine at 25°C). Error bars represent SD of the mean.

their targets at least as strongly as they homodimerized. This behavior is reminiscent of dominant-negative (DN) inhibitors of the helix-loop-helix family of transcription regulators, which engage in both homomeric and heteromeric interactions (*26*).

Dominant-negative TOXCAT. We next evaluated both the affinity and specificity of the CHAMP peptides for their targets when coexpressed in bacterial membranes with a DN-"TOXCAT" assay (Fig. 3). In TOXCAT, a TM sequence of interest is fused to a ToxR protein (TM-ToxR) that binds to the *ctx* promoter as a dimer, which induces expression of chloramphenicol acetyltransferase (CAT) (*27*, *28*). In the DN assay, the TM1-ToxR fusion protein is coexpressed with a second fusion protein (TM2-ToxR*) containing a nonfunctional mutant of the ToxR domain. TM-driven dimerization leads to a ToxR-ToxR* dimer that is unable to bind the *ctx* promoter or to induce CAT synthesis (Fig. 3A). The resulting decrease in CAT activity can be used to monitor the formation of a heterodimeric TM complex. In principle, this assay could be accomplished by adding an exogenous synthetic peptide (*29*); however, it is difficult to assure that different peptides will be similarly inserted into the *Escherichia coli* inner membrane.

The anti-α_{IIb} and anti-α_v peptides both formed homodimers in bacterial membranes (Fig. 3B) with an affinity similar to that of the TM domain of glycophorin A (GpA), which forms tight homodimers in this environment (*27*, *28*). The CAT signal for the anti-α_{IIb}–ToxR construct was attenuated by coexpression of anti-α_{IIb}–ToxR* (Fig. 3B), validating the DN assay. When α_{IIb} was used as the DN partner, the signal from anti-α_{IIb}–ToxR was also strongly attenuated, indicative of heterodimer formation. The magnitude of the decrease in CAT signal due to heterodimerization of anti-α_{IIb} with α_{IIb} TM is particularly notable. The homodimerization of anti-α_{IIb} and GpA (*27*, *28*) are similar in affinity (Fig. 3B, first versus third bar). Thus, because the attenuation of the CAT signal in the DN-TOXCAT assay for an anti-α_{IIb}–anti-α_{IIb} homodimer is similar to that of the anti-α_{IIb}–α_{IIb} TM heterodimer (Fig. 3B, fourth versus fifth bar), the heterodimeric TM complex anti-α_{IIb}–α_{IIb} has similarly strong affinity to that of the anti-α_{IIb} homodimer and therefore also to the GpA homodimer.

The TOXCAT assay also shows that anti-α_{IIb} and anti-α_v are highly specific for their targets versus other integrin TM domains. The TM domains of α_2, α_v, β_1, or β_3 failed to significantly interact with anti-α_{IIb}, despite their high sequence and structural similarity to the α_{IIb} TM (Fig. 1, B and C). Similarly, anti-α_v selectively recognized the α_v TM domain with much greater affinity than the α_2, α_{IIb}, β_1, or β_3 domains.

To probe whether anti-α_{IIb} recognized its target in the intended manner, we measured the effect of mutating residues in anti-α_{IIb} TM to

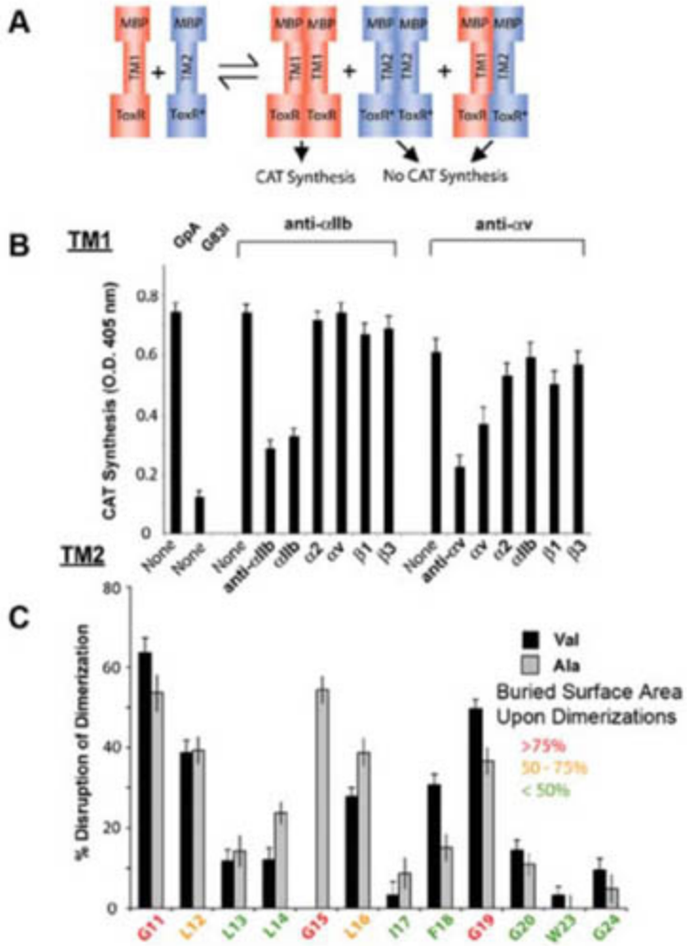

Fig. 3. Specificity of CHAMP sequences in recognizing different integrin TM regions in a bacterial membrane. (**A**) DN-TOXCAT assay. MBP, maltose binding protein. (**B**) Effect on CAT expression of disabled ToxR* fused with the CHAMP sequences or different integrin TM domains. The CAT expression correlates with the homodimerization level of the ToxR receptor fused with anti-α_{IIb} or anti-α_v. Error bars represent SD of the mean. (**C**) Effect of mutations in the anti-α_{IIb} sequence on heterodimerization with α_{IIb}. Black bars represent V substitutions, and gray bars represent A substitutions. Mutations to key residues are highlighted according to their buried surface area upon dimerization (see SOM): >75% buried (red), 50 to 75% buried (orange), and <50% buried (green). The percent disruption of heterodimerization correlates with the predicted amount of area buried upon dimerization, indicating that the anti-α_{IIb} CHAMP peptide recognizes α_{IIb}-TM, as in the designed complex. Error bars represent SD of the mean.

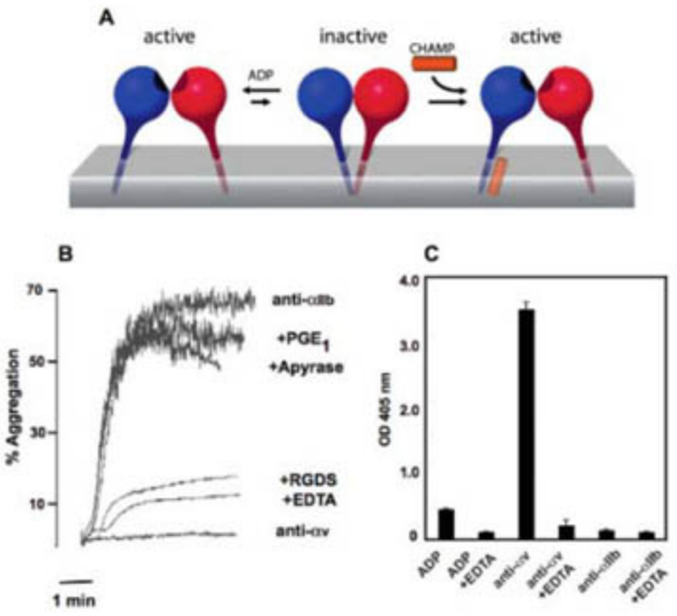

Fig. 4. Anti-α_{IIb} activates $\alpha_{IIb}\beta_3$, and anti-α_v activates $\alpha_v\beta_3$ in human platelets. (**A**) Schematic diagram of integrin regulation. Because the α and β subunit TM domains interact when integrins are inactive, any process that destabilizes this interaction would be expected to allow dissociation of the TM domains with concomitant integrin activation. In platelets, this occurs when the platelets are stimulated by agonists such as ADP. CHAMP peptides destabilize this interaction by blocking the interactions between the TM helices of the α and β subunits. (**B**) Fibrinogen-mediated aggregation of gel-filtered human platelets was measured in a turbidometric aggregometer after the addition of either 0.5 μM anti-α_{IIb} or 10 μM anti-α_v. To differentiate between a direct effect of anti-α_{IIb} on $\alpha_{IIb}\beta_3$ versus anti-α_{IIb}–stimulated signal transduction, anti-α_{IIb}–induced platelet aggregation was also measured in the presence of 2 μM PGE_1, 10 units/ml apyrase, 1 mM RGDS, or 2.5 mM EDTA. (**C**) Platelet adhesion to the wells of microtiter plates coated with osteopontin was measured in the presence of 20 μM ADP, 10 μM anti-α_v, and 2 μM anti-α_{IIb}. The data shown are the mean and SEM of measurements made in triplicate. OD, optical density.

either V or A (Fig. 3C). Mutations to the residues predicted to occur at the helix-helix interface caused disruption of heterodimer formation. Very large effects were observed for buried residues within a 10-residue stretch (residues 11 to 20) spanning the primary interaction site, whereas only minor effects were observed for residues on the non-interacting side of the helix or the more distal sites (residues 23 and 24). Interestingly, the interaction face resembles a "Gly-zipper" (GX_3GX_3G) motif that has recently been shown to mediate intermolecular helix-helix associations in membranes (*30*).

Platelet aggregation and adhesion. To determine whether exogenously added CHAMP peptides recognize their targets in mammalian cells, we first determined whether they were capable of inserting into phospholipid bilayers without perturbing the integrity of the membrane. The addition of anti-α_v or anti-α_{IIb} to phospholipid vesicles led to a large blue shift in the peptide's W fluorescence spectrum, indicative of insertion into the hydrophobic region of bilayers (fig. S3). Furthermore, circular dichroism spectroscopy showed that the vesicle-bound peptides were helical (fig. S4), and attenuated total reflectance–infrared spectroscopy revealed that they adopted a transmembrane orientation, with their helix perpendicular to the bilayer surface (fig. S5). Moreover, anti-α_{IIb} and anti-α_v did not lyse human erythrocyte membranes at the concentrations that were used in the following assays (fig. S6).

Pharmacological studies indicated that the CHAMP peptides interact with their target integrins in mammalian cells. The $\alpha_{IIb}\beta_3$ and $\alpha_v\beta_3$ integrins are heterodimers whose α and β subunits are composed of a large extracellular domain, a TM helix, and a short cytoplasmic domain. In the resting state, the TM helices of their α and β subunits interact (*15–18*) (*18*), whereas they separate when the integrins are activated by mutations or after treatment of cells with pharmacological agonists (*15–18*). Thus, the binding of a CHAMP peptide to the appropriate site on the TM helix of α_{IIb} or α_v should disrupt dimerization with the β_3 TM helix, thereby shifting the conformational equilibrium of the integrin toward its activated state (Fig. 4A). In platelets, $\alpha_{IIb}\beta_3$ is in several-hundred–fold excess over $\alpha_v\beta_3$. Thus, a successful anti-α_v peptide must recognize its target in the presence of a large excess of a closely related integrin, and the anti-α_{IIb} peptide must bind its target without affecting a minor population of $\alpha_v\beta_3$.

The physiological role of $\alpha_{IIb}\beta_3$ is to induce platelet aggregation, which occurs through an interaction with its divalent ligand, the plasma protein fibrinogen. Anti-α_{IIb} rapidly induced platelet aggregation (Fig. 4B) in a dose-dependent manner when added at concentrations from 75 nM to 500 nM (fig. S7). Anti-α_{IIb}–induced aggregation was only minimally affected by the platelet inhibitor prostaglandin E_1 (PGE1) and by the adenosine 5′-diphosphate (ADP) scavenger apyrase, which indicated that it was independent of platelet signal transduction or secreted ADP. Furthermore, anti-α_{IIb}–induced aggregation was inhibited by agents that inhibit the function of $\alpha_{IIb}\beta_3$'s fibrinogen-binding site (Fig. 4B), including EDTA or the peptide RGDS (*10*). In contrast, no platelet aggregation occurred when the platelets were exposed to 10 μM anti-α_v, which demonstrated that this peptide did not activate $\alpha_{IIb}\beta_3$.

The integrin $\alpha_v\beta_3$ mediates the adhesion of platelets to the matrix protein osteopontin, potentially exposed to the circulating blood by rupture of an atherosclerotic plaque. Incubating platelets with anti-α_v induced robust platelet adhesion to osteopontin (Fig. 4C), even in the absence of pharmacological platelet agonists. As expected from the FRET binding curves (Fig. 2C), the potency of anti-α_v in inducing platelet adhesion to osteopontin was lower by a factor of 10 than that of anti-α_{IIb} in inducing platelet aggregation (fig. S9). Anti-α_v–induced adhesion was prevented by agents that inhibit the interaction of $\alpha_v\beta_3$'s extracellular ligand-binding site with osteopontin, including EDTA or the specific RGD-containing $\alpha_v\beta_3$ antagonist XJ735, which confirmed that anti-α_v–induced platelet adhesion to osteopontin is mediated by $\alpha_v\beta_3$. Notably, there was no platelet adhesion to osteopontin when platelets were incubated with anti-α_{IIb} at concentrations that fully activate $\alpha_{IIb}\beta_3$ (Fig. 4C), and anti-α_{IIb}mut and anti-$\alpha_v$mut had negligible effects in activating either integrin. Thus, these experiments indicate that anti-α_v can specifically recognize and activate $\alpha_v\beta_3$ in the presence of a 400-fold excess of $\alpha_{IIb}\beta_3$.

Rupture force spectroscopy. One potential ambiguity with the platelet experiments is that membrane peptides are intrinsically sticky, which could lead to nonspecific interactions that might cloud the interpretation of the results. Furthermore, the TM helices of integrins might engage in a number of homomeric interactions or heteromeric interactions with other membrane proteins (*15–18*), which may cause avidity effects relating to clustering and mutivalent binding. Therefore, to measure the interaction at the single-molecule level, we used laser tweezers–based force spectroscopy to evaluate the activity and selectivity of anti-α_{IIb} and anti-α_v

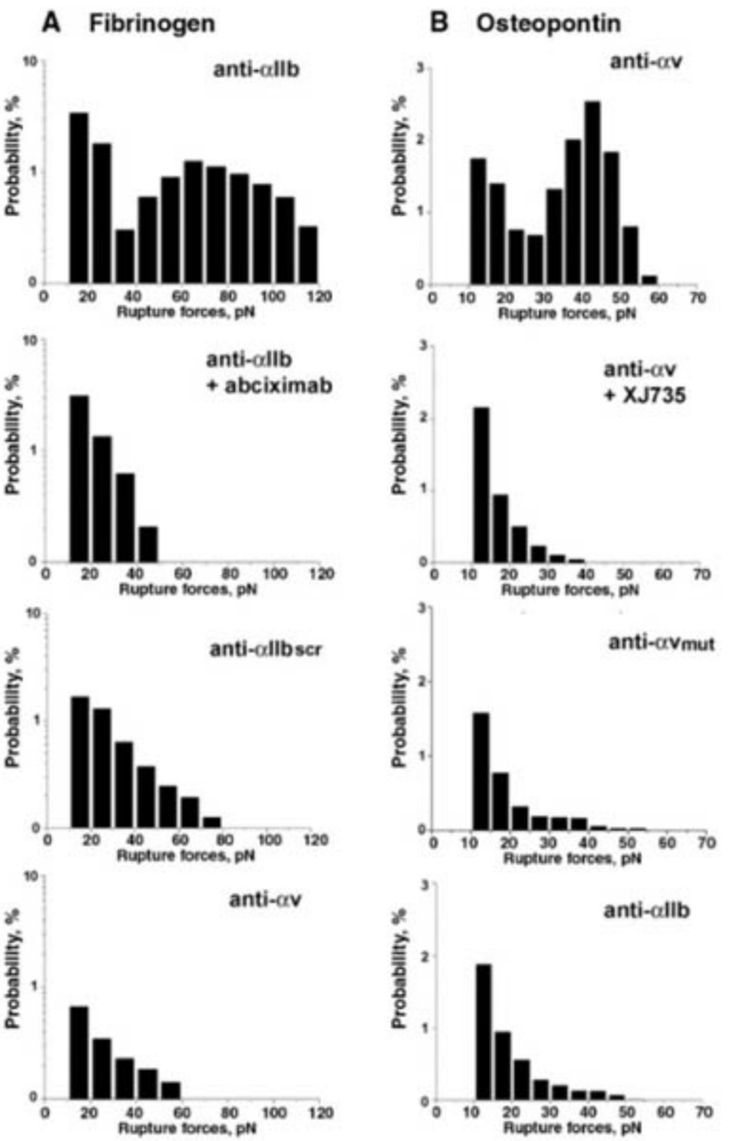

Fig. 5. Rupture force spectroscopy (laser tweezers) was used to measure the effect of anti-α_{IIb} and anti-α_v on platelet $\alpha_{IIb}\beta_3$ and $\alpha_v\beta_3$ at the level of single molecules. The histograms represent the distribution of measured rupture forces between platelets and beads coated with (**A**) fibrinogen, an $\alpha_{IIb}\beta_3$ ligand, or (**B**) osteopontin, an $\alpha_v\beta_3$ ligand. Rupture forces in (A) were measured in the presence of 0.5 μM anti-α_{IIb}, 0.5 μM anti-α_{IIb} and the $\alpha_{IIb}\beta_3$ antagonist abciximab, 0.5 μM anti-α_{IIb}scr, and 10 μM anti-α_v. Rupture forces in (B) were measured in the presence of 10 μM anti-α_v, 10 μM anti-α_v and the $\alpha_v\beta_3$ antagonist XJ735, 10 μM anti-$\alpha_v$mut, and 0.5 μM anti-α_{IIb}.

in platelets. The spectrum of rupture forces required to detach an osteopontin- or fibrinogen-coated bead from a platelet provides a measure of the ability of the CHAMP peptides to activate their target integrin and of the integrin to interact with its appropriate ligand. Histograms of rupture forces collected for a large number of contacts between platelets and ligand-coated beads are shown in Fig. 5. In the absence of CHAMP peptides, the binding probability decreased exponentially with increasing force, indicative of a nonspecific interaction (*31*). However, in the presence of 0.5 μM anti-α_{IIb} (Fig. 5A), a peak is observed at a position similar to that observed when $\alpha_{IIb}\beta_3$ is stimulated by platelet agonists (*31*). The peak was eliminated by addition of the $\alpha_{IIb}\beta_3$-specific antibody, abciximab, which blocks the fibrinogen-binding site on the extracellular domain of $\alpha_{IIb}\beta_3$. Thus, the highly adhesive interaction between platelets and fibrinogen is mediated by activated $\alpha_{IIb}\beta_3$.

Exposing platelets to 10 μM anti-α_v produced a peak of rupture force between platelets and osteopontin-coated beads with a maximum at ~45 pN (Fig. 5B), characteristic of the interaction of $\alpha_v\beta_3$ and osteopontin-coated beads (*32*). This anti-α_v–induced activation was eliminated by the $\alpha_v\beta_3$ antagonist XJ735. There was no peak of specific rupture force between the platelets and the osteopontin-coated beads when the platelets were exposed to concentrations of anti-α_{IIb} that fully activate $\alpha_{IIb}\beta_3$ (Fig. 5B, bottom panel). Demonstrating the specificity of the interaction, anti-α_v failed to induce adhesion to fibrinogen-coated beads (Fig. 5A, bottom panel), and both anti-α_{IIb}scr (Fig. 5A) and anti-$\alpha_v$mut (Fig. 5B) had negligible effects on the activation of either integrin. Thus, by activating specific integrin functions, these experiments confirm that anti-α_{IIb} and anti-α_v can specifically interact with α_{IIb} and α_v in situ in the plasma membrane of platelets.

Discussion. Lateral TM helix-helix associations play essential roles in membrane-protein folding, assembly, and signal transduction (*33*); what defines the specificity for their assembly (*8*)? For TM motifs similar to those studied here, there is only a 3 to 5 kcal/mol energetic difference (a factor of about 100 to 10,000) between a strongly associating TM helix dimer, such as GpA, and the nonspecific dimerization of randomly associating TM helices in micelles (*25*). For this class of helix-helix interaction motifs, nature appears to achieve this modest energetic difference by (i) optimizing the geometric fit (*34*–*36*), electrostatic interactions, and weak C–H···O=C hydrogen bonds (*37*) between the two interacting helices and (ii) positioning the interacting sites on the two helices at precisely the same region of the bilayer. Similar specificity can now be engineered from first principles.

Given that there is only a small energetic difference between randomly associating TM helices and natural high-affinity dimers, it might appear that the design of a CHAMP peptide would require highly accurate computation of the enthalpy and entropy of peptide-peptide and peptide-phospholipid interactions. These calculations would require consideration of computationally challenging interactions, such as interhelical C–H···O=C hydrogen bonds (*37*) and local deviations from ideal helical geometry required to facilitate association of the helices. We largely circumvent the need for such accuracy by using a library of structurally defined helix pairs that are already in local minima with respect to interhelical backbone-backbone interactions and that position side chains for appropriate pairwise interactions. The problem then simplifies to selecting the best backbone from this library for the construction of a CHAMP peptide that maximizes the geometric complementarity between the CHAMP peptide sequence and its target. Although our scoring function for sequence selection is quite simple and we used only a subset of the available helix pairs, the procedure appears to be highly effective. The first two peptides designed with this protocol are described in this paper, whereas a third is described in the SOM. On the basis of this very limited sampling of three peptides, the method has been 100% successful.

The CHAMP design procedure is highly sensitive to the fine-grained topographic differences between the targets, which is consistent with the hypothesis that geometric complementarity is critical for tight and specific recognition. Although the sequences of the TM helices of α_{IIb} and α_v are similar, the sequences of anti-α_{IIb} and anti-α_v differ substantially, resulting in different selectivities. For example, anti-α_{IIb} has a Gly-zipper motif (*30*), which is essential for the recognition of α_{IIb}, whereas anti-α_v has an M rather than the third G in this motif.

It should be possible to extend the CHAMP approach to other TM helix-association motifs, including ones involving polar side chains, which provide a strong driving force for helix-helix association (*33*). In this case, we would search for a helix pair library with structures in which one helix has the polar side chain(s) of interest and the second helix has appropriate side chains to bind it (*38*). Furthermore, the method could be modified to consider multispan bundles, rather than dimers, or to use "negative" design to select for sequences that avoid undesirable interactions; it should be possible to include a scoring function to avoid sequences that are particularly prone to amyloid formation (*20*), or one could computationally screen target CHAMP sequences against undesired targets to minimize off-target binding.

The activity of these CHAMP peptides is consistent with a push-pull mechanism of integrin activation, which postulates that separation of the α and β TM helices is a dominant signal for integrin activation (*15*, *17*, *39*). In this mechanism, integrins are activated by any perturbation that physically pushes the integrin TM helices apart (e.g., mutations that disrupt the α-β TM interface) or that pulls them apart via binding interactions that preferentially stabilize the separated state: CHAMP peptides activate by binding to a site in the α TM helix that physically blocks its interaction with the β TM helix, the binding of talin to the membrane-proximal cytoplasmic domain of the β subunit appears to impede its interactions with the α subunit (*40*), and the homo-oligomerization of the TM domains might activate by competing for heteromeric TM helix-helix associations (*17*).

More generally, CHAMP peptides should provide important reagents to probe the functional consequences of blocking protein-protein interactions in membranes, in a manner similar to the use of antibodies to study water-soluble regions of proteins. Previous investigators have shown that peptides from the TM regions of oligomeric proteins can disrupt the lateral assembly of the native complex (*41*–*43*). However, high concentrations of these TM peptides were required to elicit partial effects. Similarly, we have found that peptides from the TM regions of α_{IIb} and β_3 are substantially weaker activators of $\alpha_{IIb}\beta_3$ activation than anti-α_{IIb} (*44*). It is likely that the affinity and specificity of the CHAMP peptides designed in this work could be further improved by genetic methods used previously for investigating membrane-peptide recognition (*45*), in a process similar to affinity maturation of antibodies. Given the growing appreciation of lateral TM helix associations in membrane-protein folding, assembly, and signal transduction (*33*), CHAMP peptides will provide much needed reagents for probing these processes.

References and Notes

1. T. Kortemme, D. Baker, *Curr. Opin. Chem. Biol.* **8**, 91 (2004).
2. J. M. Shifman, S. L. Mayo, *Proc. Natl. Acad. Sci. U.S.A.* **100**, 13274 (2003).
3. J. Reina *et al.*, *Nat. Struct. Biol.* **9**, 621 (2002).
4. G. Ghirlanda, J. D. Lear, A. Lombardi, W. F. DeGrado, *J. Mol. Biol.* **281**, 379 (1998).
5. H. K. Binz, A. Pluckthun, *Curr. Opin. Biotechnol.* **16**, 459 (2005).
6. G. Winter, *FEBS Lett.* **430**, 92 (1998).
7. Materials and methods are available as supporting material on *Science* Online.
8. R. F. Walters, W. F. DeGrado, *Proc. Natl. Acad. Sci. U.S.A.* **103**, 13658 (2006).
9. J. R. Desjarlais, T. M. Handel, *Protein Sci.* **4**, 2006 (1995).
10. M. A. Arnaout, B. Mahalingam, J. P. Xiong, *Annu. Rev. Cell Dev. Biol.* **21**, 381 (2005).
11. J. S. Bennett, *J. Clin. Invest.* **115**, 3363 (2005).
12. J. Takagi, T. A. Springer, *Immunol. Rev.* **186**, 141 (2002).
13. Single-letter abbreviations for the amino acid residues are as follows: A, Ala; C, Cys; D, Asp; E, Glu; F, Phe; G, Gly; H, His; I, Ile; K, Lys; L, Leu; M, Met; N, Asn; P, Pro; Q, Gln; R, Arg; S, Ser; T, Thr; V, Val; W, Trp; and Y, Tyr.
14. A. Senes, M. Gerstein, D. M. Engelman, *J. Mol. Biol.* **296**, 921 (2000).
15. A. W. Partridge, S. C. Liu, S. Kim, J. U. Bowie, M. H. Ginsberg, *J. Biol. Chem.* **280**, 7294 (2005).
16. B. H. Luo, T. A. Springer, J. Takagi, *PLoS Biol.* **2**, 776 (2004).
17. W. Li *et al.*, *Proc. Natl. Acad. Sci. U.S.A.* **102**, 1424 (2005).

18. K. E. Gottschalk, *Structure* **13**, 703 (2005).
19. A. Senes *et al.*, *J. Mol. Biol.* **366**, 436 (2007).
20. M. Lopez de la Paz, L. Serrano, *Proc. Natl. Acad. Sci. U.S.A.* **101**, 87 (2004).
21. Y. Huang, M. J. Lemieux, J. Song, M. Auer, D. N. Wang, *Science* **301**, 616 (2003).
22. P. Jordan *et al.*, *Nature* **411**, 909 (2001).
23. D. Gerber, N. Sal-Man, Y. Shai, *J. Biol. Chem.* **279**, 21177 (2004).
24. J. M. Harris, N. E. Martin, M. Modi, *Clin. Pharm.* **40**, 539 (2001).
25. A. Z. Ebie, K. G. Fleming, *J. Mol. Biol.* **366**, 517 (2007).
26. R. Fairman *et al.*, *Proc. Natl. Acad. Sci. U.S.A.* **90**, 10429 (1993).
27. W. P. Russ, D. M. Engelman, *Proc. Natl. Acad. Sci. U.S.A.* **96**, 863 (1999).
28. D. Langosch, B. Brosig, H. Kolmar, H. J. Fritz, *J. Mol. Biol.* **263**, 525 (1996).
29. D. Gerber, N. Sal-Man, Y. Shai, *J. Mol. Biol.* **339**, 243 (2004).
30. S. Kim *et al.*, *Proc. Natl. Acad. Sci. U.S.A.* **102**, 14278 (2005).
31. R. I. Litvinov, H. Shuman, J. S. Bennett, J. W. Weisel, *Proc. Natl. Acad. Sci. U.S.A.* **99**, 7426 (2002).
32. R. I. Litvinov, G. Vilaire, H. Shuman, J. S. Bennett, J. W. Weisel, *J. Biol. Chem.* **278**, 51285 (2003).
33. A. Senes, D. E. Engel, W. F. DeGrado, *Curr. Opin. Struct. Biol.* **14**, 465 (2004).
34. K. R. MacKenzie, J. H. Prestegard, D. M. Engelman, *Science* **276**, 131 (1997).
35. D. M. Engelman *et al.*, *FEBS Lett.* **555**, 122 (2003).
36. A. K. Doura, K. G. Fleming, *J. Mol. Biol.* **343**, 1487 (2004).
37. A. Senes, I. Ubarretxena-Belandia, D. M. Engelman, *Proc. Natl. Acad. Sci. U.S.A.* **98**, 9056 (2001).
38. L. Adamian, J. Liang, *Proteins* **47**, 209 (2002).
39. B. H. Luo, C. V. Carman, J. Takagi, T. A. Springer, *Proc. Natl. Acad. Sci. U.S.A.* **102**, 3679 (2005).
40. K. L. Wegener *et al.*, *Cell* **128**, 171 (2007).
41. A. W. Partridge, R. A. Melnyk, D. Yang, J. U. Bowie, C. M. Deber, *J. Biol. Chem.* **278**, 22056 (2003).
42. N. Manolios *et al.*, *Nat. Med.* **3**, 84 (1997).
43. D. Gerber, F. J. Quintana, I. Bloch, I. R. Cohen, Y. Shai, *FASEB J.* **19**, 1190 (2005).
44. H. Yin *et al.*, *J. Biol. Chem.* **281**, 36732 (2006).
45. L. L. Freeman-Cook *et al.*, *J. Mol. Biol.* **338**, 907 (2004).
46. We acknowledge NIH (grants GM60610, HL40387, HL54500, and GM54616) and NSF (grant 050020) for support of this work. We also received training grants from NIH (5T32 CA101968 and 5T32 GM08275) and NSF (DMR03 04531). We thank R. Gorelik for preliminary studies into DN-TOXCAT assays.

Supporting Online Material

www.sciencemag.org/cgi/content/full/315/5820/1817/DC1
Materials and Methods
Figs. S1 to S9
Tables S1 and S2
References

26 October 2006; accepted 16 February 2007
10.1126/science.1136782

REPORTS

Early Optical Polarization of a Gamma-Ray Burst Afterglow

Carole G. Mundell,[1*] Iain A. Steele,[1] Robert J. Smith,[1] Shiho Kobayashi,[1] Andrea Melandri,[1] Cristiano Guidorzi,[1,2,3] Andreja Gomboc,[4] Chris J. Mottram,[1] David Clarke,[5] Alessandro Monfardini,[1,6] David Carter,[1] David Bersier[1]

We report the optical polarization of a gamma-ray burst (GRB) afterglow, obtained 203 seconds after the initial burst of γ-rays from GRB 060418, using a ring polarimeter on the robotic Liverpool Telescope. Our robust (2σ) upper limit on the percentage of polarization, less than 8%, coincides with the fireball deceleration time at the onset of the afterglow. The combination of the rate of decay of the optical brightness and the low polarization at this critical time constrains standard models of GRB ejecta, ruling out the presence of a large-scale ordered magnetic field in the emitting region.

Gamma-ray bursts are the most instantaneously powerful explosions in the universe and represent the most important new astrophysical phenomenon since the discovery of quasars and pulsars. Identified as brief, intense, and unpredictable flashes of high-energy γ-rays on the sky, the most common type of GRB, so-called long bursts, have γ-ray pulses that last longer than 2 s. These are thought to be produced when a massive star reaches the end of its life, its core collapsing to form a black hole and, in the process, ejecting an ultrarelativistic blastwave (*1*, *2*). In many cases, the detected γ-ray flux implies an unphysically high explosion energy if assumed to be emitted isotropically by the source, the so-called energy catastrophe. Instead, focusing the energy into a narrow jet reduces the intrinsic energy output to a canonical $\sim 10^{51}$ erg for most GRBs (*3*).

After the initial burst of γ-rays, the subsequent radiation produced at longer wavelengths (e.g., x-ray, optical, or radio), termed the "afterglow," is generally accepted to be synchrotron radiation whose observed properties are consistent with a focused jet expanding at ultrarelativistic speeds into the interstellar medium. The production of synchrotron radiation requires the presence of a magnetic field, but the origin and role of the magnetic fields in GRB ejecta are a long-standing open issue. In turn, fundamental questions on the driving mechanism of the explosion, in particular, whether the relativistic outflow is dominated by kinetic (baryonic) or magnetic (Poynting flux) energy, remain unanswered (*4*, *5*). The primary challenges in addressing these issues arise because GRBs are short-lived, compact, and lie at vast cosmological distances; our understanding of their physical nature is therefore inferred from the characteristics of their radiation, measured at the earliest possible time when the observed radiation is still sensitive to the properties of the original fireball.

The two main models of collimated relativistic outflows, or jets, that have been proposed are the hydrodynamical and the magnetized jet (*5*). Hydrodynamical jets have no dominant ordered magnetic field but instead produce synchrotron radiation from tangled magnetic fields, concentrated in the thin layer of the expanding shock front, that are generated locally by instabilities in the shock (*6*); the magnetic field does not influence the subsequent evolution of the jet. Models of these jets have been highly successful at reproducing a wide range of observed properties of GRBs (*1*, *2*). A relativistic outflow from a central engine might have a weak ordered or random magnetic field. As long as the magnetic field does not affect the dynamics of the jet, we classify it as a hydrodynamical jet. In contrast, magnetized jets are threaded with strong, globally ordered magnetic fields, which originate at the central source, are advected outward with the expanding flow, and may provide a powerful mechanism for collimating and accelerating the relativistic jet (*7*, *8*). A magnetic driving mechanism is an attractive scenario to account for the prodigious energy outputs and vast accelerations required for GRB ejecta, as well as for overcoming energy-efficiency problems inherent in hydrodynamical models in which internal shocks must convert kinetic energy to radiative energy with sufficient efficiency to produce the observed γ-ray emission and prolonged central engine activity (*9*, *10*).

Observationally, the fading rate of the afterglow emission alone is inadequate as a diagnostic for distinguishing between these theoretical jet models (*11*–*13*); in contrast, the polarization

[1]Astrophysics Research Institute, Liverpool John Moores University, Twelve Quays House, Egerton Wharf, Birkenhead, CH41 1LD, UK. [2]Dipartimento di Fisica, Universitá di Milano-Bicocca, Piazza delle Scienze 3, 20126 Milano, Italy. [3]Istituto Nazionale di Astrofisica-Osservatorio Astronomico di Brera, via Bianchi 46, 23807 Merate (LC), Italy. [4]Faculty of Mathematics and Physics, University of Ljubljana, Jadranska 19, 1000 Ljubljana, Slovenia. [5]Department of Physics and Astronomy, University of Glasgow, Glasgow G12 8QQ, UK. [6]CNRS, Institut Néel, 25 Avenue des Martyrs, 38042 Grenoble, France.

*To whom correspondence should be addressed. E-mail: cgm@astro.livjm.ac.uk

properties are predicted to differ markedly. Observations of the polarization state of GRB afterglow emission therefore offer a diagnostic to eliminate or constrain current models. The testable prediction is that hydrodynamical jets produce a considerable amount of polarization at the geometrical transition phase a few days after the burst, the so-called jet break time when the lateral spreading of the slowing jet produces a characteristic steepening of the light curve, and produce little or no polarization at early times, whereas jets with large-scale globally ordered magnetic fields produce polarization substantially greater than 10% at early times (*12*, *13*) and in some cases as high as ~50% (*13*).

The first detection of polarized optical emission from a GRB afterglow was taken at 0.77 days after the burst of GRB 990510 and, with the exception of GRB 020405 for which an unexplained high degree of optical polarization was measured 1.3 days after the burst (*14*), late-time measurements of optical polarization for other long bursts taken typically at $t \gtrsim 0.2$ day all show consistently low values of $P \sim 1$ to 3%, some of which may be induced by interstellar scattering processes (*15*–*18*). Although these painstaking observations of late-time polarization were vital in confirming the presence of collimated jets in GRBs [e.g., (*15*–*17*)], there was a lack of polarization observations of GRB afterglows in the early phase within the first few minutes, where the predicted properties of magnetized or unmagnetized hydrodynamic jets differ most.

Recent advances in technical efficiency of catching the rapidly fading light from GRBs, driven primarily by the real-time dissemination of accurate localizations of GRBs discovered by the Swift satellite (*19*), have opened a new era in rapid-response follow-up studies of GRBs and their afterglows (*1*, *2*).

GRB 060418 was detected by the Swift satellite at 03:06:08 UT on 18 April 2006 and exhibited a triple-peaked γ-ray light curve with overall duration of ~ 52 s, followed by a small bump at 130 s coincident with a large flare detected in the x-ray light curve and likely associated with ongoing central engine activity (*20*). A localization was communicated automatically to ground-based facilities and triggered robotic follow-up observations at the 2.0-m Liverpool Telescope in La Palma, the Canary Islands. These observations consisted of a 30-s exposure with the RINGO polarimeter (Fig. 1) beginning at 03:09:31 UT or 203 s after the start of the prompt γ-ray emission and contemporaneous with the fading tail of this γ-ray emission, followed by 2 hours of multicolor photometric imaging. We concentrate here on the RINGO measurement.

RINGO uses a rotating polaroid to modulate the incoming beam, followed by corotating deviating optics that transform each star image into a ring that is recorded on the charge-coupled device (CCD) chip. Any polarization signal present in the incoming light is mapped out around the ring in a sin(2θ) pattern. A description of the instrument and the data reduction procedures are given in (*21*). A bright star in the field of view of the GRB (Fig. 1) was used as a check on our data reduction, with multiple measurements made on subsequent nights confirming its measured polarization in the GRB frame of <1%. This value also provides a lower limit to any contribution of polarization that could have been induced into the GRB by galactic interstellar dust. No appreciable polarization signal could be detected from the GRB. To quantify this observation, we carried out a Monte Carlo error analysis in an attempt to recover an artificially induced polarization signal with a noise spectrum identical to that of the GRB data. This gave a firm (2σ) upper limit to the measured polarization of <8% [polarizations of 10%, for example, being easily detectable (*21*)].

The optical and near-infrared light curves of GRB 060418 are smooth and featureless; the infrared (IR) light curves show a smooth rise (decay rate $\alpha \sim 2.7$, where $F \propto t^{\alpha}$) to a broad peak at time $t_{peak} \sim 153$ s (*22*) before fading away with a smooth, unbroken power law with $\alpha \sim -1.2$, identical to the decay rate of the optical light curves and typical of standard fireball models of optical afterglows. In the standard GRB fireball model in which a jet is driven into the surrounding circumburst medium, the early afterglow light is thought to include contributions from both a forward shock, which propagates into the ambient medium, and a reverse shock, which propagates back into the original fireball ejecta (*23*). Forward-shock emission peaks when the fireball decelerates or when the typical synchrotron frequency (ν_m) passes through the observed band. The lack of color change around the peak in the IR light curves of GRB 060418 (*22*) confirms the deceleration interpretation, with ν_m already lying below the optical and IR bands at this time (*22*). The steep temporal rise of the IR light curve ($\alpha \sim 2.7$) is also consistent with theoretical predictions of forward-shock emission before deceleration (*24*).

The RINGO measurement was made close to the time of the peak of the IR light curve at the fireball deceleration time and onset of the afterglow, making the polarization measurement particularly important for testing afterglow predictions from current standard jet models. Our polarization measurement also coincides with the decay phase of the x-ray flare emission. Extrapolating the peak flux density in the x-ray flare at 130 s to optical wavelengths, and assuming a spectral index between optical and x-ray bands of $\beta \sim 1$ ($F_\nu \propto \nu^{-\beta}$), we found that the maximum contribution of the flare to the optical band is negligible, thus ruling out an internal shock origin for the optical emission and confirming that the optical emission represents the afterglow at the time of the RINGO measurement.

Although the optical emission from GRB 060418 was bright at an early time, no dominant optical flash from the reverse shock was detected, similar to other recently studied bright bursts such as GRB 061007 (*25*). The apparent lack of an optical or IR flash is easily explained in the standard fireball model if the typical synchrotron frequency of the forward-shock emission, ν_m, is lower than the observing frequency of the optical (and IR) band, ν_{opt}, at the onset of afterglow, or the peak time t_{peak}. This condition is required also to interpret the IR light-curve peak; otherwise, the rise gradient is expected to be shallower, $t^{1/2}$,

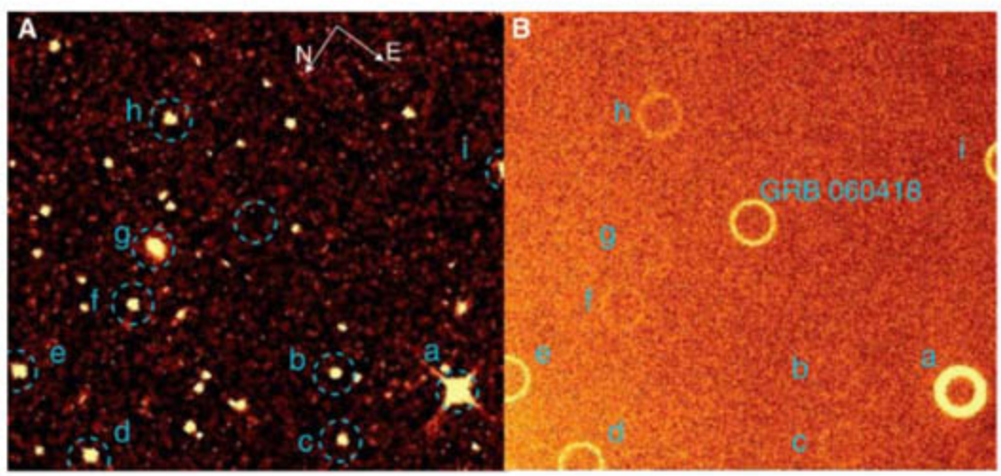

Fig. 1. Direct optical and RINGO polarimeter images of the field containing GRB 060418. The direct R-band image (**A**) is taken from the Digital Sky Survey (DSS) and shows the sky before the GRB occurred. The RINGO image (**B**) consists of a CCD recording of the incoming light from GRB 060418 and other bright sources in the field after the light has been modulated by a rotating polaroid and spread around rings by corotating deviating optics. The objects detected by RINGO are labeled (a) to (i) in both panels and blue dotted rings, corresponding to those in the RINGO image, are shown on the DSS image as a guide. All labeled objects, with the exception of extended object (g), are unresolved point sources and thus produce well-defined rings. The bright star (a) was used for additional calibration as described in the text. The field of view is 4.6 by 4.6 arc min, and the orientation of the field is shown by the white arrows indicating north (N) and east (E).

than observed (*26*). Mundell *et al.* (*25*) suggested that a low value of ν_m may be produced by small microphysics parameters, in particular low ϵ_B, due to small magnetic fields in forward and reverse shock regions. A low typical synchrotron frequency can also result if the fireball is enriched with electron-positron pairs. Nonstandard models of hydrodynamical jets with weak magnetic fields that radiate via inverse Compton emission, rather than synchrotron emission, have also been proposed as a mechanism for suppressing optical flashes. No polarization predictions for nonstandard models exist, so we do not discuss these models further. Instead, we test predictions from standard GRB models of relativistic jets with and without globally ordered magnetic fields that emit synchrotron radiation.

Theoretical models of magnetized jets, with large-scale ordered magnetic fields originating from the central engine, predict high values of polarization at very early times for the prompt γ-ray emission (*12*, *13*). Putative detections of large levels of γ-ray polarization of ~70 to 80% (*27*) and >35% and >50% (*28*) in a small number of GRBs provide support for large-scale ordered magnetic fields in the region of the flow that produces the high-energy prompt emission, but the observational results remain controversial (*29*). The optical emission from the forward shock is also predicted to be highly polarized for these magnetized jets; instabilities in the contact discontinuity at the fireball surface are expected to act as anchors for continuing the ordered magnetic field into the afterglow emission, producing optical polarization as high as 10 to 50% at an early time (*11*–*13*, *30*). The exact level of observed polarization depends on complex details of the degree of mixing between the ordered magnetic field in the ejecta and any tangled component in the shock front. Nevertheless, the key characteristic of emission from jets with large-scale ordered magnetic fields is that the observed polarization does not disappear at very early times (*13*).

Our robust upper limit $P < 8\%$ at the very early time $t \sim 203$ s for GRB 060418 lies below predicted values for reasonable jet properties. In the standard synchrotron shock model, the temporal decay rate of the optical afterglow, α, is related to the underlying power-law distribution of electron energies, or $dn/de = e^{-p}$; for GRB 060418, we derive $p = 2.6$, typical of optical afterglow emission. Theoretical models of a magnetically dominated flow for $p = 2.6$ predict observable polarization of a few tens of percent (*8*), substantially larger than that observed for GRB 060418. Within the limitations of current theoretical models, the low level of polarization observed in GRB 060418 therefore indicates that large-scale ordered magnetic fields are not dominant in the afterglow emission at early times.

Although reverse-shock emission in the form of an optical flash does not dominate the light curves of GRB 060418, in the hydrodynamic jet model more than ~50% of the emitted photons come from the original fireball material (*25*), or reverse-shock region, at the deceleration time when our polarization measurement of GRB 060418 was made. This is because at the peak time, the two shock emissions have the same cooling frequency, and the peak values of νF_ν at the cooling frequency are comparable. The two emissions contribute equally to the total flux at observing frequencies between the cooling frequency and the typical frequency of the forward shock (*24*), as is the case for optical measurements of GRB 060418.

We therefore rule out the presence of a magnetic field with ordered large-scale structure in a hydrodynamic or baryonic jet, in which the energy density of any magnetic field component is comparable to or less than that of the baryonic component, because this would also result in a large amount of polarization at an early time.

Our result is consistent with the theoretical prediction of low or zero polarization for hydrodynamical jets without large-scale ordered magnetic fields when observed at early times (*13*). This is also consistent with the reported lack of linear or circular polarization at radio frequencies for the afterglow of GRB 991216, observed at $t \sim 1$ day after the burst (*31*). Thus, we support models of hydrodynamical jets in which the generation of the magnetic field in the regions responsible for both the prompt and afterglow emission is driven by local processes in the fluid.

References and Notes

1. T. Piran, *Rev. Mod. Phys.* **76**, 1143 (2004).
2. P. Meszaros, *Rep. Prog. Phys.* **69**, 2259 (2006).
3. D. A. Frail *et al.*, *Astrophys. J.* **562**, L55 (2001).
4. T. Piran, *AIP Conf. Proc.* **784**, 164 (2005).
5. M. Lyutikov, *N. J. Phys.* **8**, 119 (2006).
6. A. Gruzinov, E. Waxman, *Astrophys. J.* **511**, 852 (1999).
7. G. Drenkhahn, H. C. Spruit, *Astron. Astrophys.* **391**, 1141 (2002).
8. M. Lyutikov, V. I. Pariev, R. D. Blandford, *Astrophys. J.* **597**, 998 (2003).
9. J. A. Nousek *et al.*, *Astrophys. J.* **642**, 389 (2006).
10. B. Zhang *et al.*, *Astrophys. J.* **642**, 354 (2006).
11. J. Granot, A. Königl, *Astrophys. J.* **594**, L83 (2003).
12. E. M. Rossi, D. Lazzati, J. D. Salmonson, G. Ghisellini, *Mon. Not. R. Astron. Soc.* **354**, 86 (2004).
13. D. Lazzati *et al.*, *Astron. Astrophys.* **422**, 121 (2004).
14. D. Bersier *et al.*, *Astrophys. J.* **583**, L63 (2003).
15. S. Covino *et al.*, *Astron. Astrophys.* **348**, 1 (1999).
16. J. Greiner *et al.*, *Nature* **426**, 157 (2003).
17. S. Covino *et al.*, *Astron. Astrophys.* **392**, 865 (2002).
18. A. J. Barth *et al.*, *Astrophys. J.* **584**, L47 (2003).
19. N. Gehrels *et al.*, *Astrophys. J.* **611**, 1005 (2004).
20. A. D. Falcone *et al.*, *GCN Circ*, 5009 (2006).
21. Materials and methods are available as supporting material on *Science* Online.
22. E. Molinari *et al.*, http://arxiv.org/abs/astro-ph/0612607 (2006).
23. S. Kobayashi, T. Piran, R. Sari, *Astrophys. J.* **513**, 669 (1999).
24. S. Kobayashi, B. Zhang, *Astrophys. J.* **582**, L75 (2003).
25. C. G. Mundell *et al.*, *Astrophys. J.* **660**, 1 (2007).
26. R. Sari, T. Piran, R. Narayan, *Astrophys. J.* **497**, L17 (1998).
27. W. Coburn, S. E. Boggs, *Nature* **423**, 415 (2003).
28. D. R. Willis *et al.*, *Astron. Astrophys.* **439**, 245 (2005).
29. R. E. Rutledge, D. B. Fox, *Mon. Not. R. Astron. Soc.* **350**, 1288 (2004).
30. A. Sagiv, E. Waxman, A. Loeb, *Astrophys. J.* **615**, 366 (2004).
31. J. Granot, G. B. Taylor, *Astrophys. J.* **625**, 263 (2005).

32. We thank S. Covino for useful discussions during the initial stages of the RINGO project. RINGO is a Liverpool Telescope fast-track instrument internally funded by the Astrophysics Research Institute of Liverpool John Moores University. The Liverpool Telescope is operated on the island of La Palma, the Canary Islands, by Liverpool John Moores University at the Observatorio del Roque de los Muchachos of the Instituto de Astrofisica de Canarias. C.G.M. thanks the Royal Society for financial support.

Supporting Online Material

www.sciencemag.org/cgi/content/full/1138484/DC1
Materials and Methods
Figs. S1 to S4
References and Notes

6 December 2006; accepted 2 March 2007
Published online 15 March 2007;
10.1126/science.1138484
Include this information when citing this paper.

Ballistic Electron Microscopy of Individual Molecules

Amin Bannani, Christian Bobisch, Rolf Möller*

We analyzed the transport of ballistic electrons through organic molecules on uniformly flat surfaces of bismuth grown on silicon. For the fullerene C_{60} and for a planar organic molecule (3,4,9,10-perylene-tetracarboxylic acid dianhydride), the signals revealed characteristic submolecular patterns that indicated where ballistic transport was enhanced or attenuated. The transport was associated to specific electronic molecular states. At electron energies of a few electron volts, this "scanning near-field electron transmission microscopy" method could be applied to various adsorbates or thin layers.

Future developments in microelectronics require a reduction in device size, ideally to one molecule, but the power dissipation of the individual element must be reduced accordingly. As demonstrated for silicon-based prototypes (*1*) as well as for carbon nanotubes (*2*), one route to such devices makes use of ballistic electron transistors. In the case of ballistic transport, the flow of electrons is not impeded by scattering at defects, so high speed and minimal energy loss are achieved. Ballistic transport has also been used to image surfaces.

In the scheme for ballistic electron emission microscopy (BEEM) introduced by Bell and Kaiser (*3*, *4*), a thin metal layer on top of a semiconductor is studied. The arrangement allows an evaluation of how the tunneling current is split into a ballistic contribution that reaches the underlying semiconductor and a current of scattered electrons that remains in the metal film. BEEM experiments have primarily focused on studies of the buried interface between the metal and the semiconductor.

An overview of BEEM was given by Narayanamurti *et al.* (*5*), and a theoretical description has been worked out by de Andres *et al.* (*6*). Modifications of the standard BEEM configuration were reported by Rippard *et al.* (*7*), who studied ballistic transport through a metal oxide–metal-semiconductor system. Li *et al.* (*8*) and Troadec *et al.* (*9*) modified the Schottky barrier by inserting an organic film between the metallic layer and the semiconductor.

However, the goal of our experiment is the analysis of the transmission of electrons through objects, such as adsorbates, on top of the metallic layer. Such experiments require an almost perfect preparation of the interface and of the surface of the metal to provide constant detection efficiency. Complementary to scanning tunneling spectroscopy (STS), by which the specific excitation of electronic states (*10*, *11*) or even of a molecular vibration (*12*) may be analyzed, our experiment provides information on the electrons traversing the molecules without encountering significant scattering processes.

An important issue of molecular electronics (*13*) is the nature of the contact between a metallic lead and the molecule. Our experiments correspond to a two-terminal device with two contacts to an individual molecule (*14*, *15*). One of the contacts is given by the supporting surface and may be varied by the preparation to achieve adsorption at a specific site on the surface. The other contact is made by the tunneling tip and may be varied with respect to lateral position relative to the molecule as well as vertical direction from weak tunneling to point contact.

We studied the ballistic transport of electrons through two organic molecules that have been used for molecular electronics: C_{60} (*16*) and the planar organic molecule 3,4,9,10-perylene-tetracarboxylic acid dianhydride (PTCDA) (*17*, *18*). The data reveal the pathways of the ballistic transport through the molecules.

The setup of the experiment is sketched in Fig. 1A. If a thin metallic layer is brought into contact with a semiconductor, a Schottky barrier is formed at the interface (*19*, *20*). The barrier height varies from 0.4 to 1 eV depending on the combination of the metal and the semiconductor (*21*). The adsorbate to be studied is deposited onto the metal layer. Using the tip of a scanning tunneling microscope (STM) (*22*, *23*) at a negative bias voltage relative to the sample, electrons are injected into the sample surface either directly into the metallic layer or via the adsorbates. In the case of ballistic transport, the electrons reach the interface and overcome the barrier if their energy is sufficient and the momentum parallel to the interface is conserved. These conditions create a current, $I_{ballistic}$, that can be measured at a back contact of the semiconductor. We refer to this as the "BEEM current." The majority of the electrons remain in the metallic layer; the BEEM current represents only a very small percentage of the total current of tunneling electrons. Because the feedback of the STM adjusts the distance between tip and sample in such a way that the total tunneling current remains constant, the BEEM current directly yields the relative contribution of the ballistic electrons.

Our method resembles the "projection electron microscopy" introduced by Fink *et al.* (*24*), which uses the field emission of a tip in front of a free-standing sample; the image of the transmitted electrons is detected by a channel plate detector. However, that technique is applicable for free electrons at much higher electron energies, in the range of 20 to 300 eV. In contrast, our experiment relies on tunneling electrons with energies between the Fermi level E_F and the vacuum level; moreover, like STM, it is a near-field technique not limited by diffraction.

The injection and transmission of electrons was studied for two prototype molecules, C_{60} and PTCDA, adsorbed on an atomically flat bismuth film at 130 K. The experiments (including sample preparation) were performed under ultrahigh-vacuum conditions at pressures of $<3 \times 10^{-10}$ mbar. For sample preparation, the Si(100) substrate was flashed to 1500 K to produce a clean (2 × 1) reconstructed surface. About 3 nm of Bi was evaporated on the sample at a low temperature (130 K). The sample was brought to room temperature, and the Bi formed an epitaxial layer that was flat on an atomic scale (*25*). The quality of the surface of both the Si and the Bi surfaces was verified by low-energy electron diffraction (LEED). Finally, about half a monolayer of C_{60} or PTCDA was deposited by thermal evaporation onto the Bi surface at room temperature (*26*).

The interface between the Si and the Bi prepared by the procedure described above was found to be very homogeneous, leading to an almost constant signal of BEEM electrons on the clean metallic surface. The transmission of ballistic electrons was very high relative to other

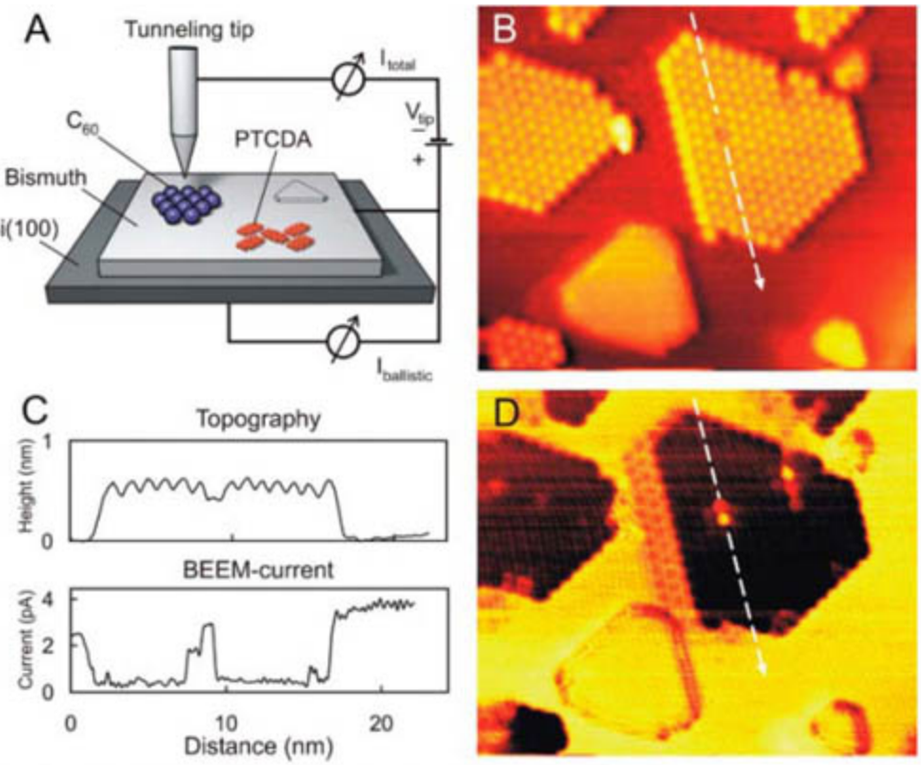

Fig. 1. (**A**) Scheme of the experiment. (**B** to **D**) Topography and BEEM current for C_{60} on Bi(111). The area is 30 nm by 25 nm, and a bias of −1.3 V has been applied to the tip, leading to a total tunneling current of 40 pA; the images show truncated triangular islands of C_{60} [dark in (D)] and bismuth (bright). (B) Topography varying by 0.6 nm from low (dark) to high (bright). (C) Cross sections along the dashed line indicated in (B) and (D); the upper curve displays the height, the lower curve the BEEM current. (D) BEEM current ranging from 0.2 pA (dark) to 4 pA (bright). To the left of the central island of C_{60}, a "ghost image" caused by a double tip can be seen. However, this double tip does not influence the imaging of the island.

Department of Physics, Center of Nano Integration Duisburg-Essen, University of Duisburg-Essen, Lotharstrasse 1, 47048 Duisburg, Germany.

*To whom correspondence should be addressed. E-mail: rolf.moeller@uni.due-de

systems (*3*, *27*) such as gold on silicon. Considering that the injection of tunneling electrons occurred preferentially with a low component of the k vector parallel to the surface, the high transmission may be explained by the good overlap between an electronic state of the Bi that is very close to the $\bar{\Gamma}$-point of the surface Brillouin zone (*28*) and the truncated bulk states of the Si(100) surface. In addition to the data we report, the tunneling current as well as images of the backward scan direction were recorded to verify that artifacts caused by the scan process were negligible.

The topography observed by the STM and the simultaneously measured BEEM signal for the C_{60} molecules are shown in Fig. 1, B and D, respectively. On the flat Bi surface, which appears dark in the topography, triangular islands of Bi formed by one additional double layer of Bi and hexagonally ordered islands of C_{60} can be recognized. The molecules are arranged in a superstructure aligned to the underlying Bi structure and similar to a structure found on Au(111) (*29*). The BEEM current is reduced by a factor of about 8 for the C_{60} layer and shows a faint contrast on the Bi surface that reflects the hexagonal arrangement of the Bi atoms in the (111) surface; this is not visible in the topographic image (see also fig. S1).

We studied the BEEM current as a function of the electron energy, which is given by $E = -eU$, where e is elementary charge and U is applied bias. The spectra for the clean surface (upper curve) and the covered surface (lower curve) are shown in Fig. 2. The onset of the BEEM current above the threshold can be described by a function as a power of $E - E_B$, where E_B is the height of the Schottky barrier (*30*). The dashed curve shows a fit with $I_{ballistic} \propto (E - E_B)^2/E$, yielding a value of 0.58 eV for E_B (*31*). Above 1.1 eV, saturation effects not included in the formula given above lead to deviations from the experimental curve.

The BEEM current through the C_{60} molecules exhibits a more complex dependence on the electron energy. At about 1.5 eV, the signal strongly increases, indicating the opening of an additional channel for the ballistic electrons. A numerical fit to the data displayed in Fig. 2 taking into account a second threshold provides an energy of 1.48 eV for the latter. For the range up to 1.8 eV, an almost perfect fit to the data was obtained; again, saturation was found for higher energies. These results correspond well to the data reported by Yamachika *et al.* (*32*), who analyzed C_{60} on Ag(001) by STS as a function of doping by potassium atoms. For the undoped C_{60}, they found two empty electronic states: the lowest unoccupied molecular orbital (LUMO) at about 0.5 eV and the LUMO+1, the next higher orbital, at 1.6 eV shifting toward a lower energy with increasing doping. Because the first orbital is below the threshold given by the Schottky barrier, only the second orbital will efficiently contribute to ballistic transport.

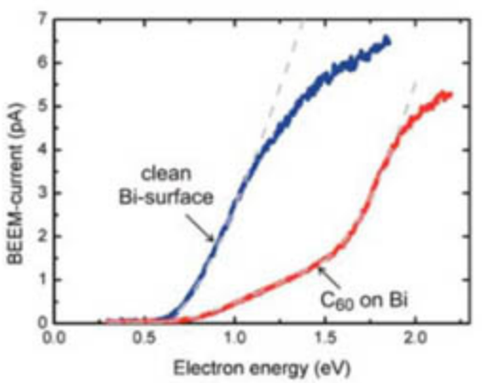

Fig. 2. BEEM current versus electron energy. The blue curve refers to the bare bismuth surface, the red curve to one monolayer of C_{60} on Bi. Each curve was obtained by averaging over 20 spectra at a single position. The dashed gray lines show numerical fits to the data.

The data obtained for a small area near the center of Fig. 1, B and D, is shown in Fig. 3 for E values of 1.3 and 2.1 eV. One molecule appeared somewhat lower in the topography and yielded a rather strong BEEM current. Typically, the effect was not completely localized at one molecule; the neighboring molecules were also slightly affected, as expressed by the "halo" in Fig. 3D. Data recorded at various electron energies revealed that the signal was as strong as for the clean Bi surface over the whole range of energy.

In view of the results discussed for the PTCDA molecule (see below), this observation can be explained by an increased coupling of the electronic states of the particular C_{60} to those of the underlying Bi. This effect is not caused by different adsorption geometries, because the bright appearance of the C_{60} hops back and forth only between the same two molecules in a series of measurements, which implies that the effect is pinned by a localized defect or adsorbate (fig. S4). Hence, we suggest that an impurity (e.g., an alkaline atom) localized on the surface dopes one or the other C_{60} nearby, which shifts the energy of the electronic states of the C_{60} (*32*) and leads to enhanced coupling. The scattering of the electrons injected by the tunneling tip is thereby reduced and the contribution of ballistic electrons increases. This interpretation is supported by a numerical calculation by Ono *et al.*, who analyzed electron transport through undoped and doped C_{60} (*33*).

The images in Fig. 3, C and D, display the BEEM current at an electron energy of 2.1 eV; to improve the visibility of the low signal, Fig. 3D shows the same data as Fig. 3C with enhanced brightness. Each C_{60} molecule exhibits a ring with a slight hexagonal deformation separated by lower-transmission regions. Hence, an increase of BEEM current occurs at the sides of each C_{60} molecule and not between the molecules, as can be clearly seen in Fig. 3D. According to the spectroscopic data discussed above, it can be concluded that this observation is related to the first excited unoccupied electronic state of the C_{60} (LUMO+1).

Although rigorous theoretical consideration requires one to treat the transition from an electron through the tunneling gap, the molecules, the metal layer, and the Schottky barrier as a whole, it is useful to consider the ballistic transport stepwise to understand the observations. The first step is the tunneling process from the metallic tip through the vacuum barrier into the molecule. Neglecting thermal broadening of the Fermi distribution of the electrons, only electrons of the tip with energies ranging from E_F of the sample to eU above E_F contribute to the tunneling current. The molecule does not provide a continuous density of electronic states but provides discrete levels that are broadened by the interaction with the substrate. Tunneling is enabled for those electrons with an energy matching one of these molecular states (e.g., LUMO, LUMO+1, etc.).

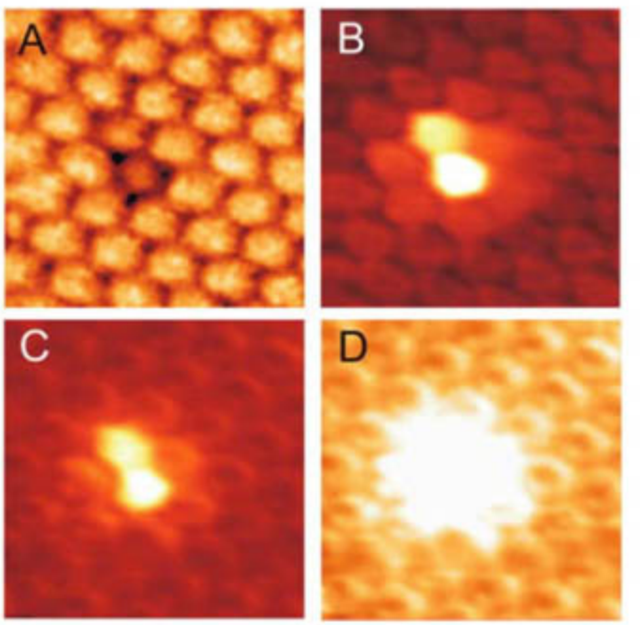

Fig. 3. Topography and BEEM current for a small area of a C_{60} island. The displayed area is about 5 nm by 5 nm; total tunneling current is 40 pA. (**A**) Topography varying by 0.2 nm from low (dark) to high (bright) measured at a bias of −1.3 V applied to the tip. (**B**) BEEM current ranging from 0.2 to 4 pA at a bias of −1.3 V. (**C**) BEEM current ranging from 0.2 to 4 pA at a bias of −2.1 V. (**D**) BEEM current ranging from 0.2 to 1 pA at a bias of −2.1 V. The contrast has been raised to enhance the features at low current.

The second step is given by the intramolecular transport. If inelastic scattering occurs, the energy of the electrons is reduced and the electrons are no longer "ballistic." The third step is the transition from the molecule to the metal layer; the fourth step is the transport within the metal layer. The fifth and last step is the transition across the Schottky barrier between the metal and the semiconductor. It requires that the energy associated with the motion of the electron perpendicular to the interface exceed the Schottky barrier. Furthermore, the component of the wave vector parallel to the surface must match to an empty state of the semiconductor. In contrast to STS, in which only the first step is considered, BEEM takes into account each of these additional steps.

If only the energy filtering of the last step is considered, some resemblance of the BEEM image to data obtained by STS [e.g., for C_{60} (*34*)] is readily understood. The threshold given by the Schottky barrier selects those molecular orbitals with excessive energy, which is LUMO+1 for the C_{60} in the range of interest. However, a close inspection reveals significant differences from the STS data. Most obviously, the minimum of the BEEM current in the center of the C_{60} molecule is not found by STS.

The recent calculation (*33*) for the electron conduction through individual C_{60} molecules bridging two metallic electrodes shows that the current runs along the C-C bonds and that only specific unoccupied molecular orbitals with different symmetries provide the major contribution to the electron transport. They predict the highest density at the sides and the lowest density at the center of the molecule. Both are in good agreement with our observations (e.g., Fig. 3).

To learn more about the transmission of ballistic electrons through molecules, we studied a rather different organic molecule. PTCDA is a planar, almost rectangular molecule. It has significant partial charges due to the strong electronegative anhydride groups at both of the short sides. Figure 4 shows the topography and the BEEM current for a small area around a Bi island that is not covered by PTCDA.

The molecules are arranged in a so-called "herringbone structure" observed for PTCDA on many other metallic substrates (*18*, *35*, *36*). The insets of Fig. 4, A and B, sketch the rectangular unit cell containing two molecules that are rotated by about 90° relative to each other. The displayed data correspond to an electron energy of 1.7 eV. As for C_{60}, a reduction of the BEEM current is observed, ranging from 2% (dark areas) to 35% (bright areas) relative to the uncovered surface. In contrast to the findings for C_{60}, the results do not change significantly as a function of energy in the range between 0.6 and 2.0 eV (fig. S5).

The appearance of the PTCDA molecule completely differs for the observed topography and the map of the measured BEEM current (Fig. 4, D and E). The topographic image is dominated by two maxima located on both sides parallel to the long axis of the molecule. As discussed in (*37*), the maxima can be attributed to the LUMO. Probably because of the semimetallic character of the Bi film, the LUMO remains above E_F, in contrast to a silver substrate, and it is imaged at a negative tip bias. However, the major contribution to the BEEM current occurred in one longish area centered on top of the long axis. As pointed out in (*37*), this feature corresponds to the LUMO+1 state, which has a significant coupling to the bulk states of the substrates. Close inspection of the BEEM signal (e.g., in the line scan of Fig. 4F) reveals an important difference with respect to the STS images of the LUMO+1. The maximum of the BEEM signal is not at the center of the perylene core but at the anhydride groups. Hence, we can conclude that the electron transport through the molecule or the transition to the Bi substrate works best at these positions. The latter is suggested by x-ray diffraction measurements showing that for a silver substrate, the four oxygen atoms at the corners bend downward toward the substrate (*38*, *39*) and increase the coupling to the bulk.

The presented variation of STM-BEEM allows the analysis of electronic transport through a thin layer of adsorbates in great detail. If the Schottky contact supporting this layer is prepared homogeneously, it provides a detector for ballistic electrons with an almost constant efficiency as a function of the lateral position. The setup represents a "scanning near-field transmission electron microscope" operating at electron energies ranging from 0.5 to 3 eV and capable of submolecular resolution for a monolayer of

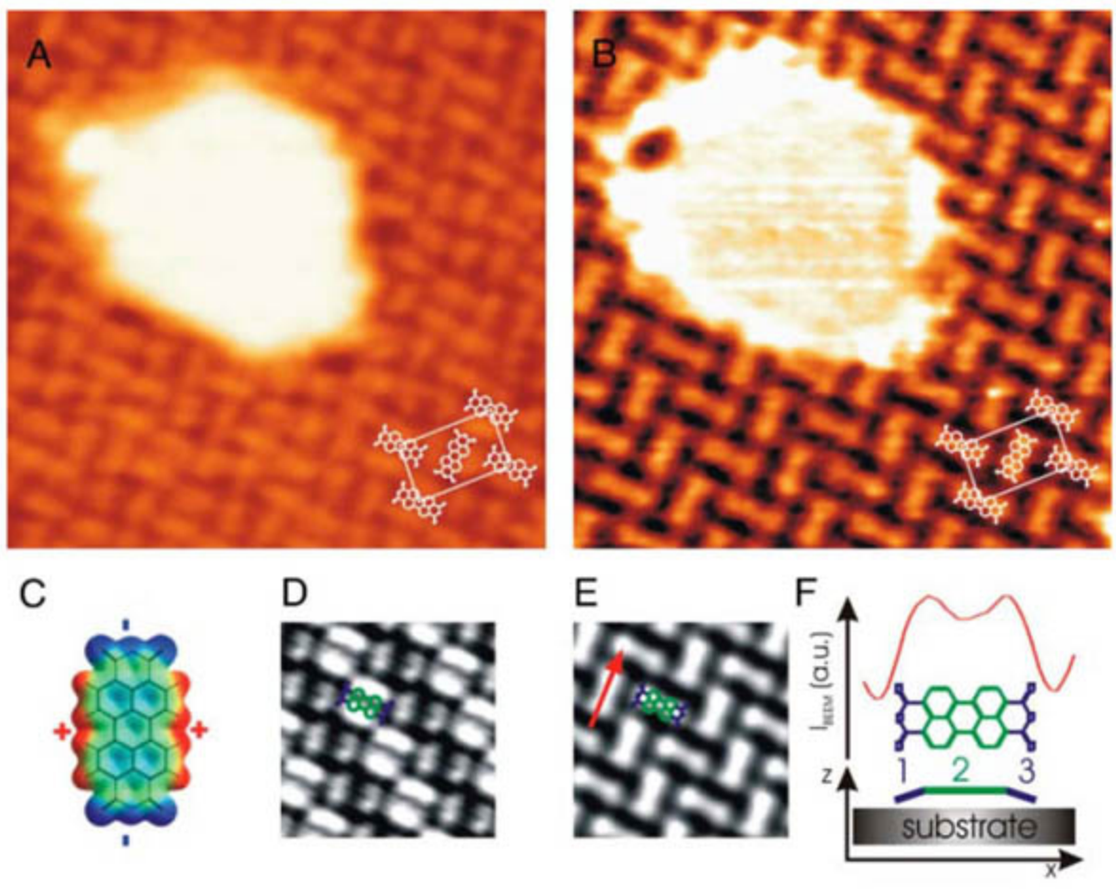

Fig. 4. Topography and BEEM current for a small area covered by PTCDA molecules. The displayed area is about 9.3 nm by 9.3 nm; total tunneling current is 40 pA with a bias of −1.7 V applied to the tip. (**A**) Topography of a bismuth island surrounded by a PTCDA domain arranged in a herringbone structure. (**B**) BEEM current ranging from 0.2 to 5.4 pA. (**C**) Partial charge distribution of the PTCDA molecule and structure model. (**D**) Detailed view of the PTCDA topography averaged over the unit cell. (**E**) Averaged BEEM current of the PTCDA structure in (B). (**F**) Line scan showing slight maxima at the position of the anhydride groups.

adsorbates. Specific paths for the ballistic transport of electrons through the molecules could be identified for C_{60} and PTCDA. They result from tunneling into the LUMO+1 electronic state followed by intramolecular transport and coupling to the bulk states of the underlying metal.

References and Notes

1. G. Timp *et al.*, *IEDM Tech. Digest*, 55 (1999).
2. A. Javey, J. Guo, Q. Wang, M. Lundstrom, H. Dai, *Nature* **424**, 654 (2003).
3. W. J. Kaiser, L. D. Bell, *Phys. Rev. Lett.* **60**, 1406 (1988).
4. L. D. Bell, W. J. Kaiser, *Phys. Rev. Lett.* **61**, 2368 (1988).
5. V. Narayanamurti, M. Kozhevnikov, *Phys. Rep.* **349**, 447 (2001).
6. P. L. de Andres, F. J. Garcia-Vidal, K. Reuter, F. Flores, *Prog. Surf. Sci.* **66**, 3 (2001).
7. W. H. Rippard, A. C. Perrella, R. A. Buhrman, *Appl. Phys. Lett.* **78**, 1601 (2001).
8. W. Li *et al.*, *J. Chem. Phys. B* **109**, 6252 (2005).
9. C. Troadec *et al.*, *Nanotechnology* **15**, 1818 (2004).
10. R. M. Feenstra, J. A. Stroscio, J. Tersoff, A. P. Fein, *Phys. Rev. Lett.* **58**, 1192 (1987).
11. R. J. Hamers, R. M. Tromp, J. E. Demuth, *Phys. Rev. Lett.* **56**, 1972 (1986).
12. B. C. Stipe, M. A. Rezaei, W. Ho, *Science* **280**, 1732 (1998).
13. C. Joachim, M. A. Ratner, *Proc. Natl. Acad. Sci. U.S.A.* **102**, 8801 (2005).
14. A. Nitzan, M. A. Ratner, *Science* **300**, 1384 (2003).
15. J. Park *et al.*, *Nature* **417**, 722 (2002).
16. H. W. Kroto, J. R. Heath, S. C. O'Brien, R. F. Curl, R. E. Smalley, *Nature* **318**, 162 (1985).
17. S. R. Forrest, *Chem. Rev.* **97**, 1793 (1997).
18. K. Glöckler *et al.*, *Surf. Sci.* **405**, 1 (1998).
19. W. Schottky, *Z. Phys.* **113**, 367 (1939).
20. F. Braun, *Pogg. Ann. Phys.* **153**, 556 (1874).
21. W. Mönch, *Electronic Properties of Semiconductor Interfaces* (Springer-Verlag, Berlin, ed. 43, 2004).
22. G. Binnig, H. Rohrer, Ch. Gerber, E. Weibel, *Appl. Phys. Lett.* **40**, 178 (1982).
23. G. Binnig, H. Rohrer, Ch. Gerber, E. Weibel, *Phys. Rev. Lett.* **50**, 120 (1983).
24. H. W. Fink, H. Schmid, H. J. Kreuzer, A. Wierzbicki, *Phys. Rev. Lett.* **67**, 1543 (1991).
25. C. Bobisch, A. Bannani, M. Matena, R. Möller, *Nanotechnology* **18**, 055606 (2007).
26. The experiments were performed at a sample temperature of 130 K with the use of a commercial instrument (Nanoprobe; Omicron, Taunusstein, Germany) that was modified for the requirements of the experiment. The instrument provides three STM units that can be operated independently. Atomic resolution [e.g., on Bi(111)] can be obtained with each tip. For our experiment, one of the additional STM tips was used to gently contact the metallic bismuth layer. To conduct BEEM, we chose tunneling currents between 10 and 50 pA as a compromise between the threshold for damaging the molecular layer and a reasonable signal-to-noise ratio for the current of ballistic electrons. At a tunneling current of 50 pA, the BEEM current typically amounted to 4 pA on the clean bismuth surface, 0.5 pA for most of the C_{60} molecules, and 3 pA for the PTCDA molecules.
27. H. Sirringhaus, E. Y. Lee, H. von Känel, *Phys. Rev. Lett.* **73**, 577 (1994).
28. C. R. Ast, H. Höchst, *Phys. Rev. B* **67**, 113102 (2003).
29. E. I. Altman, R. J. Colton, *Phys. Rev. B* **48**, 18244 (1993).
30. M. Prietsch, *Phys. Rep.* **253**, 163 (1995).
31. As discussed in several publications (*3–6*, *30*), for a constant distance between tip and sample, a good description is given by $I_{ballistic} \propto (E - E_B)^2$. However, in the experiment, the total tunneling current is kept constant and the distance increases as the bias is increased. Assuming a linear dependence between the tunneling current and the bias voltage, this can be corrected by dividing by the bias voltage (or electron energy).
32. R. Yamachika, M. Grobis, A. Wachowiak, M. F. Crommie, *Science* **304**, 281 (2004); published online 11 March 2004 (10.1126/science.1095069).
33. T. Ono, K. Hirose, *Phys. Rev. Lett.* **98**, 026804 (2007).
34. C. Rogero, J. I. Pascual, J. Gómez-Herrero, A. M. Baró, *J. Chem. Phys.* **116**, 832 (2002).
35. I. Chizhov, A. Kahn, G. Scoles, *J. Cryst. Growth* **208**, 449 (2000).
36. E. Umbach, M. Sokolowski, R. Fink, *Appl. Phys. A* **63**, 565 (1996).
37. R. Temirov, S. Soubatch, A. Luican, F. S. Tautz, *Nature* **444**, 350 (2006).
38. A. Hauschild *et al.*, *Phys. Rev. Lett.* **94**, 036106 (2005).
39. A. Hauschild *et al.*, *Phys. Rev. Lett.* **95**, 209602 (2005).

40. We thank H. Nienhaus and A. Lorke for fruitful discussions. Supported by the German Research Council within Sonderforschungsbereich 616, "Energy Dissipation at Surfaces."

Supporting Online Material

www.sciencemag.org/cgi/content/full/315/5820/1824/DC1
Figs. S1 to S5

11 December 2006; accepted 21 February 2007
10.1126/science.1138668

Role of Solvent-Host Interactions That Lead to Very Large Swelling of Hybrid Frameworks

C. Serre,[1]* C. Mellot-Draznieks,[1,2] S. Surblé,[1] N. Audebrand,[3] Y. Filinchuk,[4] G. Férey[1]

An unusually large expansion upon solvent adsorption occurs without apparent bond breaking in the network of a series of isoreticular chromium(III) or iron(III) diarboxylates labeled MIL-88A to D [dicarbox = fumarate (88A); terephthalate (1,4-BDC) (88B); 2,6-naphthalenedicarboxylate (2,6-NDC) (88C); and 4-4′-biphenyldicarboxylate (4-4′-BPDC) (88D)]. This reversible "breathing" motion was analyzed in terms of cell dimensions (extent of breathing), movements within the framework (mechanism of transformation), and the interactions between the guests and the skeleton. In situ techniques show that these flexible solids are highly selective absorbents and that this selectivity is strongly dependent on the nature of the organic linker.

Crystalline solids are normally quite rigid, but a reversible feature of some large-pore, hybrid, inorganic-organic crystalline solids is an unexpected swelling under external stimuli (such as pressure, temperature, light, or gas or solvent adsorption), sometimes with large magnitude (~5 Å) (*1*, *2*) in the variation of cell parameters. Such large volume variations suggest that these solids might have useful applications because of their selective adsorption, increased storage, and facile delivery (*3*, *4*).

The flexibility of hybrid organic-inorganic porous frameworks that enables these volume changes is governed by their host-guest interactions. Kitagawa (*3*, *5*) recently classified the different known behaviors of flexibility into six classes according to these interactions and the dimensions of the inorganic subnetwork, with the highest "breathing" amplitude so far being 40% (*2*). However, most of the studies reported have been limited to the structures of the frameworks at the initial and final stages of breathing but have not revealed the geometric changes and locations of the guests during the swelling that would provide insight into the mechanism of breathing. These necessary structural data are not always easy to obtain, because the swelling often breaks the crystals into powders, which are sometimes poorly crystallized.

We recently overcame these limitations by implementing a strategy based on a combination of targeted chemistry that controls the nature of the inorganic building block (*6*) and computer simulation (*7*). The structure of hybrid frameworks with giant cells [~380,000 $Å^3$ (*8*) and ~700,000 $Å^3$ (*9*)] can be determined for powdered samples by means of a direct space-computational strategy, by pushing the limits of conventional ab initio structure-determination methods of nonmolecular solids from synchrotron data. Moreover, when the crystal structure of a parent hybrid framework is known, lattice energy minimizations can be used to anticipate the series of related crystal structures experimentally obtained with linkers of greater size, with a simple ligand-replacement strategy in which the observed cell parameters of the series are used as target values. The simulations then provide the most likely atomic coordinates for the new framework (*10*), which may be directly used for further Rietveld refinements. The same combined approach was used successfully in the case study of the atypical iron(III) fumarate

[1]Institut Lavoisier, (UMR-CNRS 8180), Université de Versailles, 45 Avenue des Etats-Unis, 78035 Versailles Cedex, France. [2]Royal Institution of Great Britain, 21 Albemarle Street, London W1S 4BS, UK. [3]Sciences Chimiques de Rennes (UMR-CNRS 6226), Université de Rennes 1, Avenue du Général Leclerc, 35042 Rennes Cedex, France. [4]Swiss Norwegian Beamlines (SNBL) at the European Synchrotron Radiation Facility (ESRF), rue Jules Horowitz, 38043 Grenoble, France.

*To whom correspondence should be addressed. E-mail: serre@chimie.uvsq.fr

MIL-88A and allowed the elucidation of its structural transformations after adsorptions (*11*). In that system, a reversible expansion of ~85% was observed between the dehydrated and hydrated forms of MIL-88A, whereas other polar solvents (CH_3OH, C_2H_5OH, and C_4H_9OH) yielded intermediate variations in cell volume. Simulations provided an atomic-scale description of the structural changes involved in flexibility, yielding framework models for each host-guest system. The case study of MIL-88A illustrated how a flexible framework may adsorb a wide range of organic molecules or gases by simply adapting its framework structure. It also revealed to us that further exploration of this kind of framework was needed, together with a deeper understanding of the mechanisms at play.

We applied a similar strategy that combines observed cell parameters and lattice-energy minimizations for the analysis of the unusually large swelling without the apparent breaking of any chemical bond, in a series of isoreticular chromium(III) or iron(III) dicarboxylates formulated $[M_3^{III}O(H_2O)_2X(dicarbox)_3]$•guest (*10*) (M = Fe, Cr; X = F, Cl, acetate) and labeled MIL-88A to D (MIL standing for Materials of Institut Lavoisier) [dicarbox = fumarate (88A); terephthalate (1,4-BDC) (88B); 2,6-naphthalenedicarboxylate (2,6-NDC) (88C); and 4-4′-biphenyldicarboxylate (4-4′-BPDC) (88D)] (*10*). We characterized the breathing motion in three ways: (i) by the unit cell dimensions for the extent of swelling, (ii) by the movements within the framework for the mechanics of transformation, and (iii) from the guests and their interactions with the skeleton, which are the source of the movements. Below, we discuss the effect of swelling on the adsorption properties of different solvents.

The MIL-88 structure type is hexagonal (space group *P*-62*c* or $P6_3/mmc$) (*6*) and is built up from the connection of trimers of iron(III) or chromium(III) octahedra that share a μ_3-O oxygen with dicarboxylates (Fig. 1) in such a way that two types of cavities exist: tunnels along [001] and bipyramidal cages with trimers at the vertices. The height of the bipyramid corresponds to the *c* cell parameter, whereas *a* corresponds to the distance between two trimers in the equatorial plane. In a general way, the as-synthesized form (hereafter noted *as*) can accept solvents with a noticeable and continuous increase of the unit cell volume, one that maintains the same space group, to give the open form (hereafter noted as op) (figs. S1 to S4). Further desolvation through heating provides the desolvated form (hereafter noted as dry) while retaining the space group. During the reversible transformations, the Bragg peaks of the x-ray diffraction (XRD) powder patterns exhibit drastic but continuous displacements that are characteristic of a very large breathing effect and allow the refinement of the cell parameters of the different solids.

The data collection on the three powdered forms of each member of the series in its open form was performed at the European Synchrotron Radiation Facility (ESRF). Starting from the structures of the *as* forms, the application of our strategy (*8*) provided the starting atomic coordinates of the atoms of the hybrid framework for further Rietveld refinements (table S1 and figs. S5 to S7) (*12*).

The unit cell parameters (Fig. 2) increase almost linearly with the length of the linker, but, for each member, whereas the *c* parameter decreases by several angströms from the dry to the open form, the *a* axis drastically increases. The breathing phenomenon is anisotropic. The consequences for cell volume are spectacular, with a V_{op}/V_{dry} ratio (V_{op}, cell volume of the open form; V_{dry}, cell volume of the dried solid) that varies from 1.85 for the MIL-88A form to 3.3 for the MIL-88D form, which is considerably larger than the magnitude of breathing observed so far for hybrid solids (ratio ≤1.4). Such volume increases, between two- and threefold during insertion of guests, imply a reversible coordinated atomic movement of >10 Å, without any apparent bond breaking. For the sake of comparison, the similar ratio for lungs is only 1.4; furthermore, some polymers can expand to a comparable extent, but these materials are amorphous, whereas the MIL-88 solids stay crystalline, despite an anisotropic peak broadening, during all of the adsorption and desorption process. An interesting feature of the expansion is the lack of variation of the *a* parameter across the entire series of the dry form, which corresponds to the distance between trimers on each (001) plane. This *a* parameter remains almost constant within one estimated standard deviation, whatever the length of the linker. This indicates that, in the dry form, the building blocks are closely packed in the (001) plane, which excludes any further contraction. Thus, the interior of the bipyramid is not accessible to the guests, unlike the tunnels, which remain accessible even in the dry state. The initial stage of solvation will likely occur within the tunnels. Moreover, as already shown with MIL-88A (*11*), hydrophilic inorganic parts of constant thickness 2.9 Å alternate in these tunnels with hydrophobic organic groups whose thickness

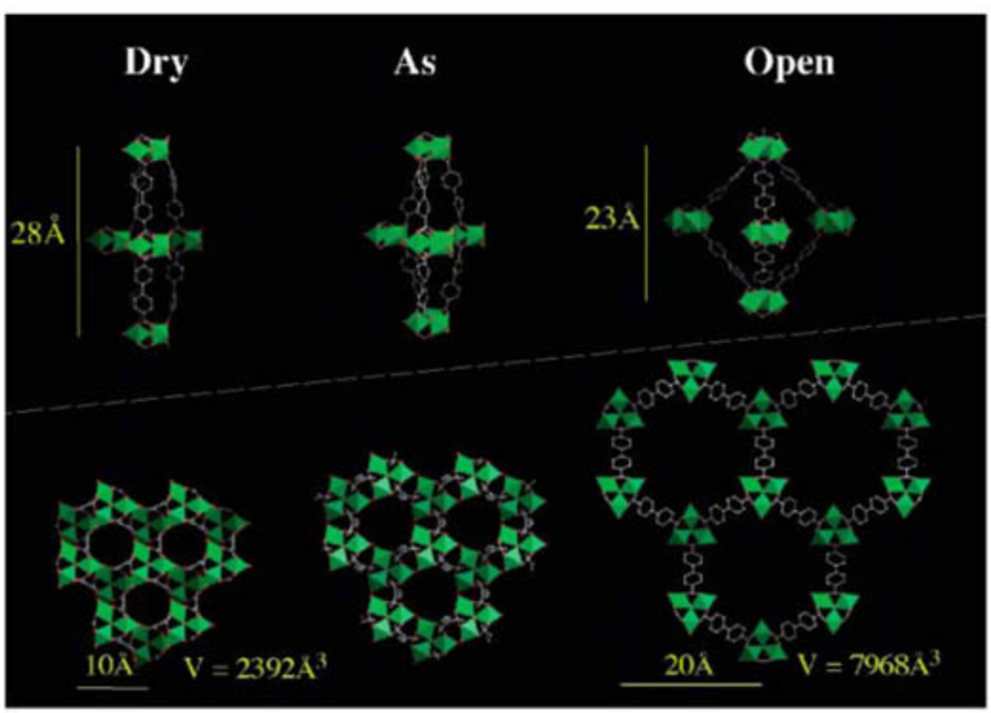

Fig. 1. (**Top**) Perspective view of the evolution of the bipyramidal cage of MIL-88D during the chemical (as → open) and thermal treatments (open → dry). (**Bottom**) Correlative evolution of the structure seen along [001]. Chromium octahedra, carbon, and oxygen atoms are green, red, and gray, respectively.

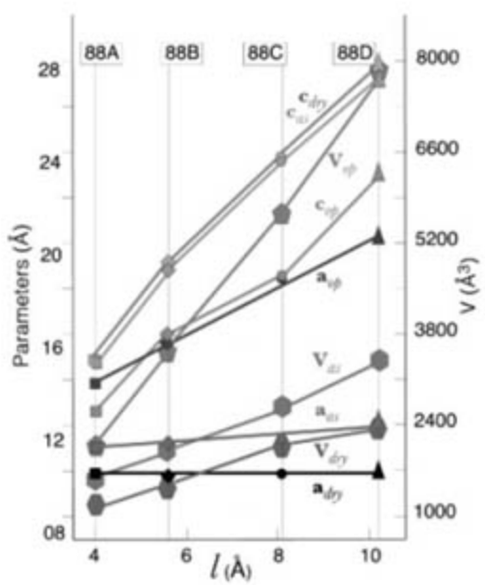

Fig. 2. Evolution of cell parameters and volumes of MIL-88 A through D in their different states (as synthesized, open, and dry) as a function of the length of the linker.

depends on the length of the linker (Fig. 1). This observation will help the explanation below of the different behaviors during resolvation.

What common characteristics of the frameworks allow such a reversible swelling? All of them exhibit, first, a continuous rotation of the trimers around [001] by a maximum of 30° during the transformation (Fig. 1). The O-O axis of the carboxylate functions acts as a "knee cap" (Fig. 3), around which the trimer and the phenyl rings can change their respective angular orientations, and allows rotations of the moieties that accommodate the constraints and minimize the lattice energy (see legend of Fig. 3 for details). This "mechanical" process, allowed by both the directivity of the covalent bonds of the linker and the lack of directivity of the metal-oxygen ionic bonds of the inorganic clusters, explains the softness of the transformations induced by host-guest interactions.

Once the swelling of the MIL-88 solids was rationally explained, we focused on how these interactions affect the selectivity of the adsorption process. The MIL-88 solids were soaked with various polar and nonpolar liquids. The breathing behavior is selective. Indeed, the pore opening strongly depends on the nature of the solvent, as shown in Fig. 4 by the XRD patterns of MIL-88C after immersion in various liquids. Depending on the chemical nature of the solvent, three degrees of pore opening are evidenced (Fig. 4 and Table 1): (i) small polar molecules (water and methanol) and apolar solvents (hexane and toluene) induced a small swelling magnitude, between 6 and 8% in volume; (ii) more hydrophobic but still polar liquids [butanol, dimethylcarbonate, dimethylformamide (DMF), and dimethylsulfoxide] generate a larger pore opening (15 to 60%), whereas (iii) pyridine and diethylformamide (DEF) completely open the structure, with a resulting huge increase in cell volume of about 165 to 170% (Table 1).

The reason for such dissimilarities in the magnitude of opening must be found in the characteristics of the tunnels and from the nature of the guest and its associated interactions. Indeed, we already noted above that hydrophilic inorganic parts of constant thickness 2.9 Å (free aperture 3.7 Å for MIL-88C) alternate in the tunnels with hydrophobic organic parts (free aperture 3.2 Å), the thickness of which depends on the length of the linker. Thus, several types of interactions are possible in MIL-88C: (i) Similar to those with MIL-88A (*10*, *11*), small polar liquids may interact with the inorganic trimers of metal(III) octahedra (coordination of the metal, hydrogen bond interactions). (ii) Weak interactions are expected with the organic linker, such as van der Waals, π-π, and CH-π interactions. Nonpolar liquids interact only with the linker, and the presence of some coordinated terminal water molecules in the trimers does not favor their adsorption into the framework. More hydrophobic polar liquids interact preferentially with the organic parts of the tunnels [as proved by the structure of MIL-88C filled by pyridine (fig. S8)] and increase the number of CH-π interactions, which explains why butanol is more adsorbed than methanol or ethanol. For the same reason, DMF and DEF generate a larger pore opening in MIL-88C. More surprising, however, is the very large difference in pore opening magnitude observed for MIL-88C when 2,6-dimethyl pyridine (lutidine) (V_{op}/V_{dry} = 107 to 108%) is used instead of pyridine (V_{op}/V_{dry} = 265 to 270%). Pyridine is well known for its ability to interact strongly with polar moieties or to coordinate the metals and to interact with aromatic rings from the naphthalene linker through π-π interactions; in the case of the 2,6-dimethyl pyridine, the steric hindrance of the methyl groups considerably weakens such interactions and thus drastically decreases its adsorption by the porous framework. These features illustrate the competition during the adsorption process between the inorganic and the organic parts of the tunnel for attracting the guest molecules depending on their nature and steric hindrance.

However, MIL-88C presents differences from the other members of the MIL-88 series that relate to the orientation of the phenyl rings in MIL-88C, which are orthogonal to those

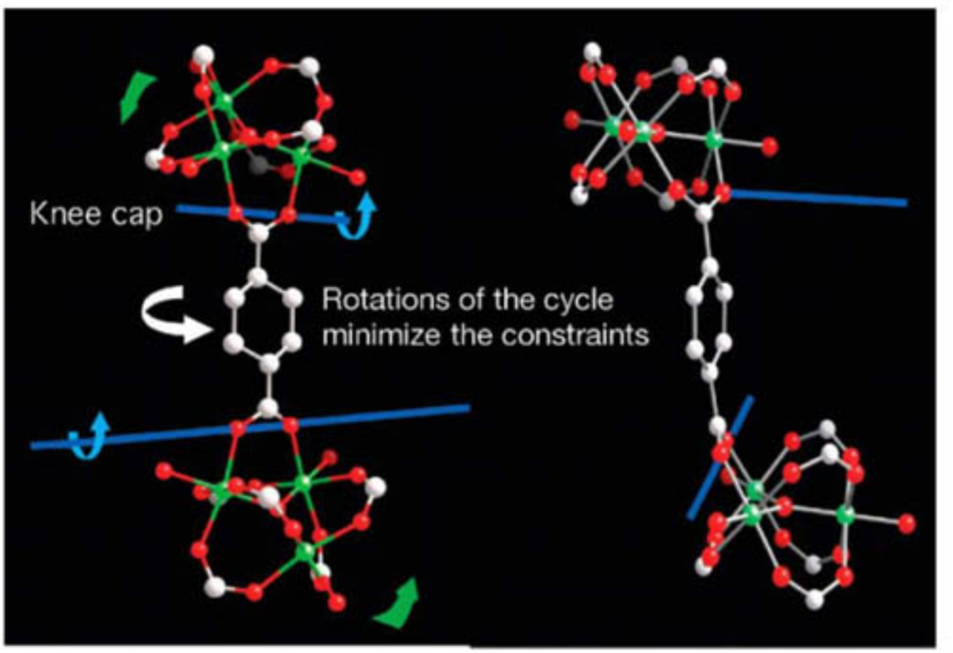

Fig. 3. Part of the structure of the cage in MIL-88B, which corresponds to one edge of the trigonal bipyramid. It illustrates the framework displacements during breathing, which occur around the knee cap O-O axis [blue line and sense of rotation (blue arrow)] of the carboxylates. This allows the rotation around this axis of the whole trimeric units (green arrows). The free rotations of the phenyl ring and of the trimers around the OOC-COO axis only relax the constraints and minimize the lattice energy during the transformation. Chromium, carbon, and oxygen atoms are green, red, and white, respectively.

Fig. 4. Evolution of the XRD patterns for MIL-88C in various solvents at room temperature (arbitrary units).

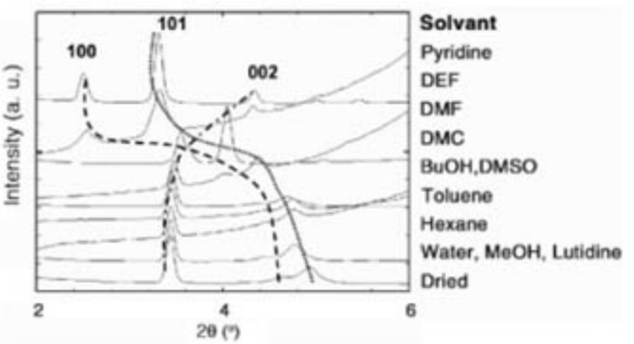

Table 1. Cell volumes and the breathing amplitudes for MIL-88C at its largest expansion relative to the dry form (2120 Å^3).

Solvent	Cell volume	
	Initial (Å^3)	V_{op}/V_{dry} (%)
Pyridine	5695	270
DEF	5600	265
DMF	3415	160
DMC	2775	130
BuOH, DMSO	2435	115
Toluene	2295	108
Hexane	2285	108
Water, MeOH, lutidine	2270	107

of MIL-88B and MIL-88D (fig. S9). Unlike MIL-88C, the plane of the rings in the other members points toward the interior of the tunnel and leaves less room for adsorption, especially for MIL-88D. When starting from the dried form, the pore opening remains rather weak (<20%) when the solid is dispersed at room temperature in a liquid, despite the importance of the organic linker (fig. S10). Alternatively, the use of the as-synthesized form of MIL-88D leads to an almost MIL-88B–like adsorption behavior (figs. S11 and S12); with adsorption of different liquids, the magnitude of pore opening depends, once more, on the nature of the guest. Besides the specific interactions between solvent molecules and the framework, a geometrical threshold exists for an adsorption in the tunnels. Moreover, this threshold is thermally activated, because at 150°C, dispersion of MIL-88D in pyridine leads to its total opening (fig. S13). The same behavior is observed for MIL-88C in its dried state. Dispersed in DMF at room temperature, it exhibited a 60% pore opening, whereas the same experiment performed at 150°C showed a total opening (170%) (fig. S14). However, thermodynamically, if there is a thermal effect related to the pore opening of the framework, it is masked by that of solvation, which occurs simultaneously.

We can briefly discuss the kinetics of adsorption. From our experiments, it seems that the kinetics of breathing is distinctive for each MIL-88–solvent association. For example, MIL-88A and MIL-88B breathe within a few seconds in the presence of ethanol, whereas it takes several days for MIL-88B to open its pores completely in the presence of water or nitrobenzene (figs. S15 and S16). Similarly, MIL-88C opens rapidly with pyridine (<1 min) but slowly with DEF (hours).

Finally, it is not known whether there is a phase transition when a solvent is adsorbed. The nets are topologically invariant and are not reconstructed between the different forms. In this sense, if there is a transition, it might be only a displacement, but even in this case, most of the structural transitions are associated with a change in symmetry and, therefore, in the XRD patterns. Here, the space group remains the same (*P*-62*c* or $P6_3/mmc$), and the patterns show a continuous evolution (figs. S17 to S20). Thus, this breathing phenomenon is reversible for each solid and without any apparent loss of crystallinity, even if anisotropic peak broadening is observed with drying for the (hk0) Bragg reflections while (001) peaks retain their initial width. However, the anisotropy disappears with wetting, and both (hk0) and (001) reflections recover the same peak width, which also rules out the appearance of an impurity or a structural change during the breathing phenomenon. At first glance, the peak broadening with drying could be due to some disorder (residual molecules of solvent) in the (*ab*) plane.

The cyclability of the breathing phenomenon has not been addressed so far. However, we have observed by XRD that the pore opening still occurs with no apparent loss of crystallinity after a few desolvation-solvation cycles (fig. S17 to S20). Further investigations will be needed in order to understand both the energetics and the cyclability of this breathing phenomenon.

References and Notes

1. K. Barthelet, J. Marrot, D. Riou, G. Férey, *Angew. Chem. Int. Ed.* **41**, 281 (2002).
2. C. Serre *et al.*, *J. Am. Chem. Soc.* **124**, 13519 (2002).
3. S. Kitagawa, K. Uemura, *Chem. Soc. Rev.* **34**, 109 (2005).
4. A. J. Fletcher, K. Thomas, M. Rosseinsky, *J. Solid State Chem.* **178**, 2491 (2005).
5. K. Uemura, R. Matsuda, S. Kitagawa, *J. Solid State Chem.* **178**, 2420 (2005).
6. C. Serre, F. Millange, S. Surblé, G. Férey, *Angew. Chem. Int. Ed.* **43**, 6285 (2004).
7. C. Mellot-Draznieks, J. Dutour, G. Férey, *Angew. Chem. Int. Ed.* **43**, 6290 (2004).
8. G. Férey *et al.*, *Angew. Chem. Int. Ed.* **43**, 6296 (2004).
9. G. Férey *et al.*, *Science* **309**, 2040 (2005).
10. S. Surblé, C. Serre, C. Mellot-Draznieks, F. Millange, G. Férey, *Chem. Commun.* **2006**, 284 (2006).
11. C. Mellot-Draznieks *et al.*, *J. Am. Chem. Soc.* **127**, 16273 (2005).
12. Supplementary data and figures are available on *Science* Online.

13. We are indebted to the ESRF in Grenoble for providing beamtime and for the help of the staff during and after the experiments. F. Millange and G. Marsolier are also acknowledged for their help in collecting XRD patterns. CNRS is acknowledged for financial support. Coordinates of MIL-88A to D deduced from computer simulation (dry, open forms) as well as the experimental structures of the open forms of MIL-88A to D (with solvents) have been deposited with ICSD data bank, deposition numbers CSD 417746, 417747, 417748, 417749, 417750, 417751, 417752, 417753, 417756, 417757, 417758, and 417759.

Supporting Online Material

www.sciencemag.org/cgi/content/full/315/5820/1828/DC1
Materials and Methods
Figs. S1 to S20
Table S1
References

27 November 2006; accepted 21 February 2007
10.1126/science.1137975

Plastic Deformation Recovery in Freestanding Nanocrystalline Aluminum and Gold Thin Films

Jagannathan Rajagopalan, Jong H. Han, M. Taher A. Saif*

In nanocrystalline metals, lack of intragranular dislocation sources leads to plastic deformation mechanisms that substantially differ from those in coarse-grained metals. However, irrespective of grain size, plastic deformation is considered irrecoverable. We show experimentally that plastically deformed nanocrystalline aluminum and gold films with grain sizes of 65 nanometers and 50 nanometers, respectively, recovered a substantial fraction (50 to 100%) of plastic strain after unloading. This recovery was time dependent and was expedited at higher temperatures. Furthermore, the stress-strain characteristics during the next loading remained almost unchanged when strain recovery was complete. These observations in two dissimilar face-centered cubic metals suggest that strain recovery might be characteristic of other metals with similar grain sizes and crystalline packing.

In coarse-grained metals, dislocation-mediated processes govern plastic deformation, with the dislocations generated by intragranular sources. Dislocations propagating in intersecting slip planes can interact with each other and, in the process, form new dislocations that are immobile. These immobile dislocations obstruct the passage of other slip dislocations through these planes and harden the crystal, a phenomenon commonly referred to as work hardening (*1*).

Nanocrystalline metals, where the grain size is typically less than 100 nm, are expected to behave differently because the grain size is smaller than the characteristic length scales associated with nucleation and propagation of dislocations (*2*–*4*). Experiments (*5*, *6*) indicate that intragranular dislocation sources like the Frank-Read source cease to operate in nanocrystalline metals, although in situ transmission electron microscopy (TEM) observations of tensile deformation have shown dislocation activity, especially near crack tips (*7*). The lack of dislocation sources results in high strength and reduced plasticity in these materials (*8*, *9*), although recent experiments (*10*) indicated that stress-assisted grain growth during deformation can lead to enhanced ductility. Atomistic simulations suggest that dislocations nucleated at grain boundaries (GBs) carry out plastic deformation in the nanocrystalline regime; once nucleated, these dislocations travel across the grains and are eventually absorbed in the opposite GB (*11*–*13*). Atomistic simulations and experiments also suggest that, at very small grain sizes (~10 nm), GB sliding and migration become the dominant deformation mechanisms and cause a reduction in strength (*14*–*17*).

Although the behavior of nanocrystalline metals during deformation has been investigated, their postdeformation behavior has received little

Department of Mechanical Science and Engineering, University of Illinois at Urbana-Champaign, Urbana, IL 61801, USA.

*To whom correspondence should be addressed. E-mail: saif@uiuc.edu

attention. We report an unexpected recovery of plastic deformation in sputter-deposited freestanding aluminum and gold films after unloading. Six aluminum specimens from two different wafers (batches) and two gold specimens from a single wafer were tested for this study, all of which showed plastic deformation recovery. The aluminum films were 200 nm thick, 50 to 60 μm wide, and 300 to 360 μm long; whereas the gold films were 200 nm thick, 12 to 20 μm wide, and 185 μm long. TEM observations and cross-sectional scanning electron microscopy (SEM) studies revealed an average grain size of 65 nm for the aluminum films. TEM observations, x-ray diffraction analysis, and cross-sectional SEM studies of the gold films revealed a strong [111] texture along the film growth direction and a mean grain size of 50 nm. The aluminum films typically had two to three grains along the film thickness (aspect ratio of 1 to 1.5), whereas the gold films had three to four grains (aspect ratio of 1 to 1.3). The specimens were macroscopically stress-free during the strain recovery, and the aluminum specimens showed strain recovery even at room temperature (RT), with the recovery rate increasing with increasing annealing temperature.

The freestanding aluminum and gold specimens were cofabricated with a microelectromechanical system–based tensile testing chip capable of measuring stress and strain simultaneously. This tensile testing chip is similar to the microtensile stage described in (*18*); the only difference is that the films in this case are deposited on Si and not SiO_2. The chip is loaded by a piezo actuator that has a displacement resolution of 0.02 μm, and the entire setup is placed in a scanning electron microscope for testing (*19*). The strain and stress resolution were 0.005% and 10 MPa, respectively, for measurements on the aluminum specimens. For the gold specimens, the corresponding values were 0.01% and 1.5 MPa.

We measured the stress-strain curves (Fig. 1) for a series of deformation recovery experiments performed on an aluminum specimen (specimen A). For all the experiments, the loading was performed at RT, and the annealing time was 7 min, except where indicated otherwise. The temperature fluctuation during annealing was less than ±2°C for all the results reported. In the first experiment (curve I), the specimen was deformed to 1.38% strain, inducing a plastic strain (ε_p) of 0.65%. During loading, the specimen started yielding around 330 MPa, where a marked reduction in the stress-strain slope (compared with 70 GPa in the elastic region) was seen. The specimen also showed strain hardening after yielding, as indicated by a positive, although reduced, postyielding slope. The stress-strain characteristics seemed to be time independent, because no stress relaxation or creep was seen when the piezo voltage was held constant for 5-min periods at various points during loading. This time independence was observed during all the subsequent loadings as well. However, fast relaxation processes, if any, could have gone undetected if they were occurring on time scales much shorter than our loading strain rate ($\sim 1 \times 10^{-4}$ s^{-1}). The strain rate was obtained by observing the displacement of the sample ends directly (by using strain-sensing gauges, labeled G1 and G2 in fig. S1).

After rapid unloading (strain rate $\sim 1 \times 10^{-3}$ s^{-1}), the specimen was annealed at 100°C for 15 min, which produced no noticeable recovery. The specimen was then annealed at 240°C for 7 min, during which time it recovered 0.33% strain ($\sim 0.5\varepsilon_p$). Annealing at 240°C for a further 20 min did not produce any additional recovery. In the second experiment (curve II), a plastic strain of 0.33% was induced so that the accumulated plastic strain was the same as after the first deformation. During loading, the stress-strain characteristics were almost identical to those of the first deformation, and the specimen recovered the entire additional plastic strain on annealing at 220°C.

Curve III shows the third loading and recovery (recoverable plastic strain ε_{pr} = 0.52%) upon annealing at 205°C. Although the yield point remained unchanged, the specimen showed larger postyielding hardening as well as a larger fraction of recoverable plastic strain ($\varepsilon_{pr}/\varepsilon_p \sim 0.7$) compared with the first experiment, which points to a link between work hardening and plastic deformation recovery. Further annealing at 240°C did not produce any additional recovery. The fourth and fifth experiments were performed to assess the temperature dependence of strain recovery; the annealing temperatures were 120°C and 60°C, respectively. Curves IV and V show that the recovery at 120°C is substantially larger (ε_{pr} = 0.4%) compared with that at 60°C (ε_{pr} = 0.24%), even though the ε_p is almost identical ($\varepsilon_p \sim 0.4\%$). During the sixth experiment (curve VI), the specimen showed notable residual work hardening as the yield stress increased to 395 MPa from 330 MPa. Moreover, a strain of 1% induced a plastic strain of only 0.23%, whereas in previous experiments the plastic strain was ~0.3%. The specimen was then left at RT for 19 hours, during which time it recovered 0.25% strain. When the specimen was loaded from this point, the deformation path was similar to curve VI, confirming the presence of residual hardening in the absence of full recovery of ε_{pr}. Upon annealing at 48°C, the specimen recovered 0.23% strain. In these experiments, the stress-strain measurements were done at fairly large increments of strain, because the stress-strain behavior of similar aluminum films had been well characterized in previous studies (*20*, *21*). TEM observations of the specimen after deformation and annealing at 240°C did not reveal any noticeable change in the grain size compared to the as-fabricated state (fig. S2). The findings presented were certified by similar experiments on other aluminum specimens.

To verify whether plastic strain recovery occurs in other face-centered cubic (fcc) metals, we performed similar experiments (*19*) on gold films synthesized by using the same technique. The gold specimens, like the aluminum specimens, showed no stress relaxation or creep during loading in any of the experiments. Figure 2 shows the strain recovery measurements on one of the gold specimens. In the first experiment, the specimen was deformed to 1.28% strain, leading to a plastic strain of 0.7%. During loading, the specimen started yielding at around 70 MPa and showed substantial postyielding hardening. After unloading, the specimen showed no strain recovery when annealed at 100°C for 10 min but recovered 0.35% strain ($0.5\varepsilon_p$) after annealing at 210°C for 5 min. Further annealing at 210°C did not result in any additional recovery. When the specimen was loaded again, the stress-strain characteristics were very similar to the first loading. TEM observations showed no grain growth during either deformation or annealing.

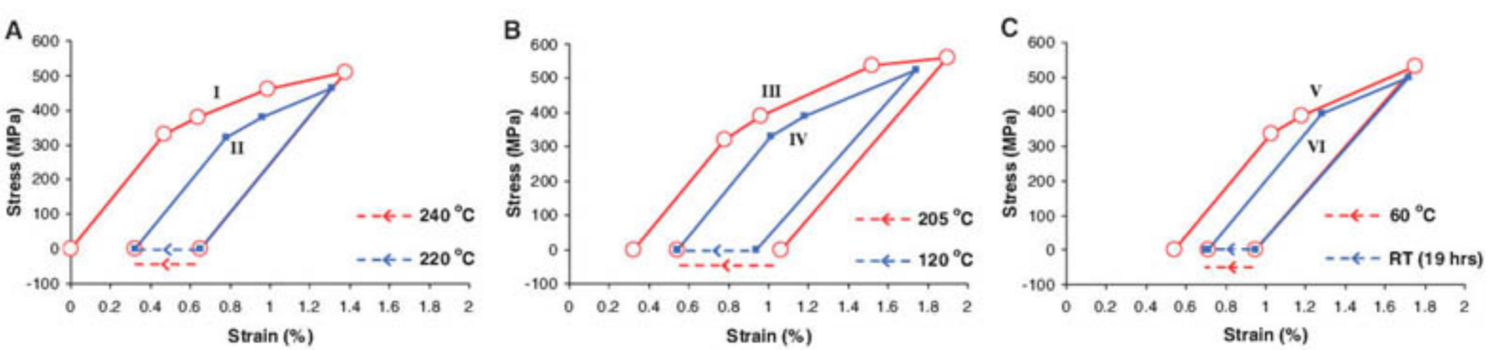

Fig. 1. (**A** to **C**) Stress-strain curves for deformation recovery experiments on specimen A (aluminum). A fraction of the plastic strain is recoverable, and, once that strain is recovered, the specimen shows no residual hardening during the next loading. When recovery is incomplete (curve V), an increase in yield stress is seen during the next loading (curve VI). The dashed arrows indicate strain recovery at different annealing temperatures.

In a thermally activated process, one would expect to see a substantial drop in the rate with a reduction in temperature. But in the aluminum specimen (specimen A), annealing at 60°C and 48°C produced very similar amounts of strain recovery, whereas the recovery at 120°C was substantially higher. This suggests that a fraction of strain recovery, possibly involving higher activation energy processes, is accessible only at high temperatures (>100°C) within the 7-min annealing time. To test this hypothesis, we annealed a similar aluminum specimen (specimen B) at 240°C a priori and then deformed it to a plastic strain of 0.55%. We then observed the time dependence of recovery at different annealing temperatures (Fig. 3). The results indicate that a fraction of RT recovery (~40%) occurs very quickly, within a time period of about 400 s, whereas processes that are much slower (time constant ~ 10^5 s) dictate the rest of the recovery. Also, increasing the temperature leads to sharp spurts in recovery that saturate in a short period of time. These observations suggest that the recovery process is governed by a distribution of activation energies and that higher temperatures help to overcome larger activation barriers faster.

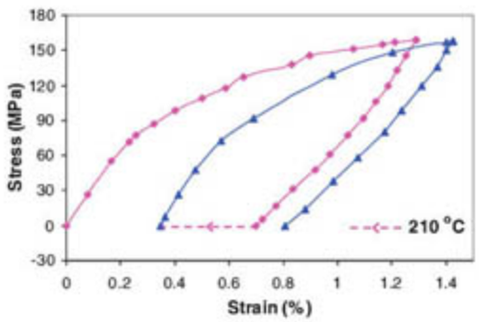

Fig. 2. Stress-strain curves for deformation recovery experiments performed on a gold specimen. This specimen also showed substantial (50%) plastic strain recovery and no residual hardening during the next loading.

Because both the aluminum and gold films were sputter-deposited and had similar grain sizes, we performed the same experiment on two sputter-deposited aluminum films of similar thickness (215 nm) but with a much larger average grain size (180 nm) to check whether the strain recovery is restricted to certain range of grain sizes. These films were also annealed a priori at 240°C and then deformed to a plastic strain of 0.55%. However, these films showed no deformation recovery even when annealed at 220°C for 30 min. This observation and the fact that similarly synthesized aluminum films, but with much smaller grain sizes (10 to 20 nm), show very little plasticity during deformation (*22*) suggest that the strain recovery is restricted to a small range of grain sizes. We noted, however, that the large-grained (180 nm) aluminum films had a columnar grain structure, unlike the films that showed recovery, which could have also caused them to behave differently.

The experimental results reveal that the deformation recovery is time dependent and that the process is thermally activated. Because the specimens are macroscopically stress-free when the recovery occurs, it is likely that this process is driven by residual internal stresses caused, perhaps, by inhomogeneous deformation during loading. Figure 4A shows an energy landscape that could govern the loading and unloading processes. During the initial stages of loading, all the grains deform elastically, leading to homogeneous elastic deformation strain (ε_e). After a critical stress (the macroscopic yield point) is reached, some relatively larger or favorably oriented grains start deforming plastically, whereas others still accommodate the strain elastically. This leads to increased compliance and hence a reduced but positive stress-strain slope. During this phase, plastic deformation proceeds with the overcoming of local energy barriers. However, due to the inhomogeneous nature of the deformation, internal stresses build up in the specimen. As the external stress is increased, even relatively smaller or unfavorably oriented grains start deforming plastically, eventually leading to homogeneous plastic deformation with near-zero stress-strain slope. The plastic strain in the specimen hence is composed of permanent plastic strain (ε_{pp}), resulting from homogeneous deformation (no internal stress buildup), and recoverable plastic strain (ε_{pr}), which occurs during inhomogeneous deformation.

On unloading, ε_e is instantaneously recoverable, whereas ε_{pp} is completely irrecoverable. ε_{pr} recovers over time, driven by the reduction in internal residual stresses. Because this process involves the overcoming of local energy barriers, it exhibits temperature dependence as well. It is quite likely that the apparent strain hardening seen during loading in our experiments on both

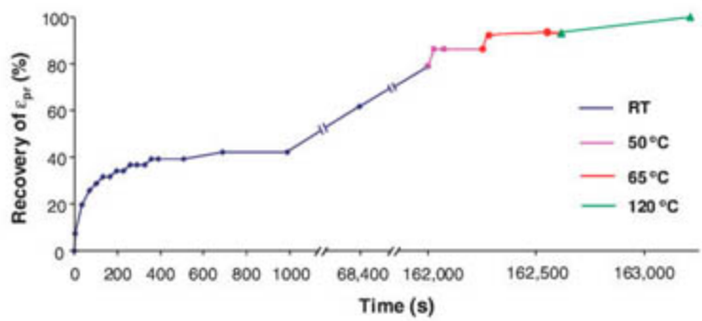

Fig. 3. Time evolution of strain recovery at different annealing temperatures for specimen B (aluminum). About 40% of strain recovery at RT happens within 400 s, whereas the rest of the recovery takes much longer time. The sharp spurts in recovery after increasing the temperature saturate in a short period of time. These characteristics of the strain recovery indicate that it is thermally activated and that it may involve a distribution of activation energies.

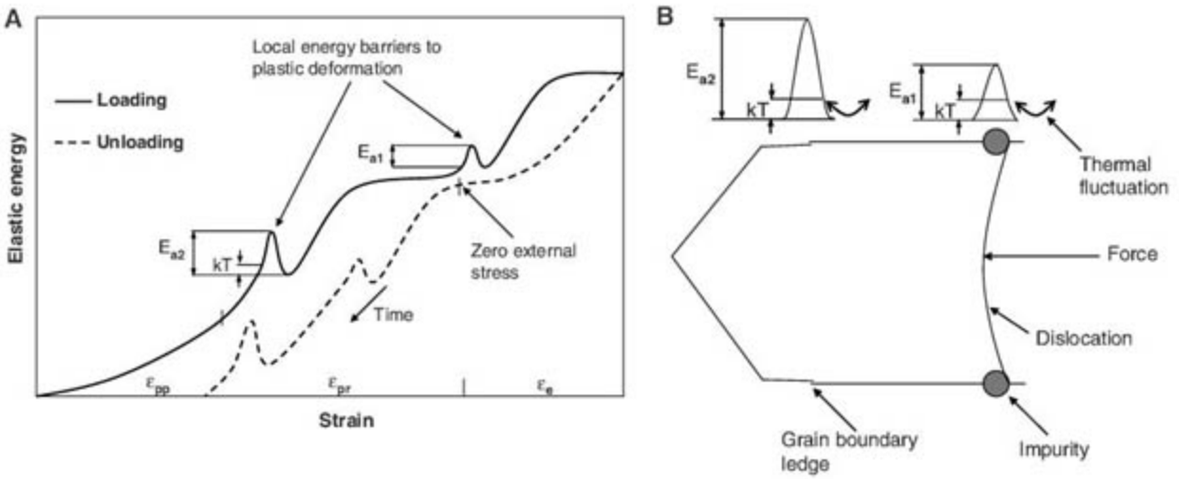

Fig. 4. (**A**) Energy landscape for loading and unloading. During loading, the strain is composed of homogenous elastic strain (ε_e), permanent plastic strain (ε_{pp}), and recoverable plastic strain (ε_{pr}). On unloading, ε_e is instantaneously recoverable, and ε_{pp} is completely irrecoverable, whereas ε_{pr} recovers over time. ε_e, ε_{pr}, and ε_{pp} shown are for the unloading process. (**B**) Dynamics of dislocation glide. The dislocation is pinned at the ends by GB defects that act as barriers to its propagation during both loading and unloading. Depinning occurs through local atomic rearrangements arising from thermal fluctuations and leads to further propagation. During loading, the dislocation experiences a force due to the external applied stress, whereas after unloading the force arises from residual internal stresses caused by inhomogeneous deformation.

aluminum and gold is a result of inhomogeneous deformation that encompasses ε_{pr}. It would also explain why larger strain hardening leads to a larger fraction of recoverable strain, as seen during the third experiment on the aluminum sample (Fig. 1B, curve III). In the figure, ε_{pr} and ε_{pp} are shown separately for the loading process merely to enhance clarity; these processes can occur simultaneously.

A process that can lead to this kind of strain recovery can be visualized as follows. Consider a dislocation that has moved into the grain interior because of applied stress (Fig. 4B). The dislocation is pinned at the ends by GB defects that act as barriers to its propagation during both loading and unloading. During loading, the large external stress along with the thermal fluctuations allows the dislocation to overcome the barriers quickly. At a given stress, once a barrier is overcome, the dislocation attains equilibrium, because further propagation would involve an "uphill ride," that is, an increase in energy due to the positive slope of the energy landscape. During strain recovery after unloading, the residual internal stresses drive the dislocation back to the GB where it originated. But, unlike loading, the reverse motion of the dislocation involves a "downhill ride" along the energy landscape, and hence it continues to move backward through thermally assisted depinning until all the residual stresses are eliminated.

Atomistic simulations (*23*) have shown that GB ledges, which act as pinning points, could hinder dislocation propagation and that depinning occurs through thermal activation, leading to further propagation. Some experimental studies (*24*, *25*) have also provided indirect evidence for such a mechanism. It is quite conceivable that such dislocation pinning and thermally activated depinning is responsible for the temperature dependence of recovery rate seen in our experiments, where, apart from GB ledges, impurities present in the GBs could also act as pinning points. To assess the impurity levels in the samples, we examined them in as-fabricated as well as annealed condition by using Auger electron spectroscopy. Both the as-fabricated and annealed aluminum films (fig. S3) showed similar impurity levels, with a fairly large nitrogen content (~4.5%) and smaller amounts of carbon and oxygen (<1% each). Similarly, there was no major difference in the impurity contents of as-fabricated and annealed gold samples, but both of them had much less nitrogen content (<0.5%) compared with the aluminum films. In assessing the possibility of impurities acting as pinning points, it is worth noting that, although specimen A did not show any noticeable recovery at 100°C during the first experiment, it recovered even at 48°C, after it had undergone annealing at 240°C. This enhancement of recovery rate could be due to the reduction in pinning sites caused by redistribution of GB impurities during high temperature annealing.

The process described in Fig. 4B is just one possible strain recovery mechanism. One can visualize such thermally assisted strain recovery for plastic deformation resulting from other processes, like diffusion-assisted GB sliding and grain rotation. For example, it has been shown that an internal stress field with cracklike singular stresses can develop when GB diffusion is blocked by an obstacle in a thin film (*26*–*29*). Hence, if diffusivity is not uniform in all GBs in a thin film, either because of presence of impurities or because of inherent variations in the structure of GBs, deformation will result in heterogeneous GB diffusion. Such diffusion can cause severe internal stresses to develop during loading that can serve as driving force for plastic strain recovery.

Although there have been no previous reports of substantial (50 to 100%) plastic strain recovery in nanocrystalline materials, investigations on bulk nanocrystalline Ni (*30*, *31*) have revealed that x-ray peak broadening due to inhomogeneous strain during loading is reversible upon unloading at RT but not at 180 K and that the additional broadening at 180 K disappears on warming to RT. Furthermore, time-dependent recovery of root mean square strain (*32*) and existence of small negative creep (~2% of total plastic strain) during strain dip tests (*24*) have also been reported for bulk nanocrystalline Ni. These results, along with our observation of thermally activated strain recovery in thin films, suggest that there is a substantial thermal component and an element of reversibility in plastic deformation of nanocrystalline fcc metals, in both bulk and thin film form.

Although both gold and aluminum are free metals, some of their properties, such as stacking fault energy (30 mJ m^{-2} for gold, 120 mJ m^{-2} for aluminum), differ substantially. Furthermore, the gold films tested in this study differ from aluminum films in the following aspects: (i) absence of native oxide layer on the surface, (ii) presence of strong [111] texture along the film growth direction, and (iii) smaller impurity content. Despite these differences, they show similar strain recovery characteristics, which suggests that grain size dictates strain recovery. Hence, it is reasonable to expect similar behavior in other fcc metals if they have similar grain sizes.

The experimental observations suggest that strain recovery results from the combined effect of a small mean grain size and inhomogeneities in the microstructure (variations in the size and orientation of individual grains and structure of GBs); the small grain size precludes intragranular dislocation sources, whereas variations in the microstructure lead to plastic deformation (through dislocations originating from GBs) in relatively larger grains and elastic accommodation in smaller grains. Upon unloading, this results in inhomogeneous residual internal stresses, which drive the strain recovery. Hence, in exploring plastic deformation of nanocrystalline metals, it might be necessary to consider not only the average size of the microstructure but also the inherent variations.

References and Notes

1. A. H. Cottrell, *Dislocations and Plastic Flow in Crystals* (Oxford Univ. Press, Oxford, 1953).
2. E. Arzt, *Acta Mater.* **46**, 5611 (1998).
3. S. P. Baker, *Mater. Sci. Eng. A* **319-321**, 16 (2001).
4. J. R. Weertman, in *Nanostructured Materials: Processing, Properties, and Applications*, C. C. Koch, Ed. (William Andrews, Norwich, NY, 2002).
5. M. Legros, B. R. Elliot, M. N. Rittner, J. R. Weertman, K. J. Hemker, *Philos. Mag. A* **80**, 1017 (2000).
6. M. A. Haque, M. T. A. Saif, *J. Mater. Res.* **20**, 1769 (2005).
7. K. S. Kumar, S. Suresh, M. F. Chisholm, J. A. Horton, P. Wang, *Acta Mater.* **51**, 387 (2003).
8. M. A. Haque, M. T. A. Saif, *Sens. Actuators A* **97-98**, 239 (2002).
9. Y. M. Wang *et al.*, *Scr. Mater.* **48**, 1581 (2003).
10. D. S. Gianola *et al.*, *Acta Mater.* **54**, 2253 (2006).
11. V. Yamakov, D. Wolf, S. R. Phillpot, A. K. Mukherjee, H. Gleiter, *Nat. Mater.* **1**, 45 (2002).
12. J. Schiøtz, K. W. Jacobsen, *Science* **301**, 1357 (2003).
13. H. Van Swygenhoven, P. M. Derlet, A. Hasnaoui, *Phys. Rev. B* **66**, 024101 (2002).
14. J. Schiøtz, F. D. Tolla, K. W. Jacobsen, *Nature* **391**, 561 (1998).
15. V. Yamakov, D. Wolf, S. R. Phillpot, A. K. Mukherjee, H. Gleiter, *Nat. Mater.* **3**, 43 (2004).
16. H. Conrad, J. Narayan, *Appl. Phy. Lett.* **81**, 2241 (2002).
17. K. J. Van Vliet, S. Tsikata, S. Suresh, *Appl. Phy. Lett.* **83**, 1441 (2003).
18. J. H. Han, M. T. A. Saif, *Rev. Sci. Instrum.* **77**, 045102 (2006).
19. Materials and methods are available as supporting material on *Science Online*.
20. M. A. Haque, M. T. A. Saif, *Acta Mater.* **51**, 3053 (2003).
21. M. A. Haque, M. T. A. Saif, *Proc. Natl. Acad. Sci. U.S.A.* **101**, 6335 (2004).
22. M. A. Haque, M. T. A. Saif, *Scr. Mater.* **47**, 863 (2002).
23. H. Van Swygenhoven, P. M. Derlet, A. G. Froseth, *Acta Mater.* **54**, 1975 (2006).
24. S. Van Petegem, S. Brandstetter, H. Van Swygenhoven, J.-L. Martin, *Appl. Phy. Lett.* **89**, 073102 (2006).
25. Y. M. Wang, A. V. Hamza, E. Ma, *Acta Mater.* **54**, 2715 (2006).
26. H. Gao, L. Zhang, W. D. Nix, C. V. Thompson, E. Artz, *Acta Mater.* **47**, 2865 (1999).
27. D. Weiss, H. Gao, E. Arzt, *Acta Mater.* **49**, 2395 (2001).
28. M. J. Buehler, A. Hartmaier, H. Gao, *J. Mech. Phys. Solids* **51**, 2105 (2003).
29. A. Hartmaier, M. J. Buehler, H. Gao, *Mater. Sci. Eng. A* **400–401**, 260 (2005).
30. Z. Budrovic, H. Van Swygenhoven, P. M. Derlet, S. Van Petegem, B. Schmitt, *Science* **304**, 273 (2004).
31. S. Brandstetter *et al.*, *Appl. Phy. Lett.* **87**, 231910 (2005).
32. S. Brandstetter *et al.*, *Adv. Mater.* **18**, 1545 (2006).

33. Supported by NSF grants ECS 05-24675 and ECS 03-04243 and Air Force Office of Scientific Research grant USAF-5212-STI-SC-0004. The x-ray diffraction and Auger spectroscopy measurements were carried out in the Center for Microanalysis of Materials, University of Illinois (UIUC), which is partially supported by the U.S. Department of Energy under grant DEFG02-91-ER45439. The tensile testing stage was fabricated in the Micro-Miniature Systems Laboratory and the Micro-Nano Technology Laboratory at UIUC. Experiments were performed in the environmental SEM at the Beckman Institute at UIUC. We thank W. D. Nix (Stanford University), F. Spaepen (Harvard University), and G. Dehm (Erich Schmid Institute of Materials Science) for valuable discussions.

Supporting Online Material

www.sciencemag.org/cgi/content/full/315/5820/1831/DC1
Materials and Methods
Figs. S1 to S3

14 November 2006; accepted 26 February 2007
10.1126/science.1137580

Discovery of Till Deposition at the Grounding Line of Whillans Ice Stream

Sridhar Anandakrishnan,[1]* Ginny A. Catania,[2] Richard B. Alley,[1] Huw J. Horgan[1]

We report on the discovery of a grounding-line sedimentary wedge ("till delta") deposited by Whillans Ice Stream, West Antarctica. Our observation is that grounding-line deposition serves to thicken the ice and stabilize the position of the grounding line. The ice thickness at the grounding line is greater than that of floating ice in hydrostatic equilibrium. Thus, the grounding line will tend to remain in the same location despite changes in sea level (until sea level rises enough to overcome the excess thickness that is due to the wedge). Further, our observation demonstrates the occurrence of rapid subglacial erosion, sediment transport by distributed subglacial till deformation, and grounding-line sedimentation, which have important implications for ice dynamics, numerical modeling of ice flow, and interpretation of the sedimentation record.

Subglacial sediment deformation and transport is an integral part of the glacial system, affecting or controlling both short-term (*1*) and long-term (*2*) glacier fluctuations through changes in the basal speed of the glaciers. Extensive data sets on sediment transport are available for many modern mountain glaciers (*3*), allowing assessment of the effects of sediment on ice dynamics. However, knowledge of sediment fluxes from modern ice sheets remains much sketchier. We demonstrate that rapid sedimentation has been occurring at the grounding line of a modern Antarctic ice stream, and, in a companion paper (*4*), we show that this sedimentation plays an important role in ice-sheet stability. The large sediment fluxes implied by our observations point to distributed deformation over a considerable thickness of subglacial till and thus to a deformation rate that increases with a low power of the basal shear stress.

We conducted radar surveys from the floating Ross Ice Shelf onto the grounded ice of Whillans Ice Stream as part of a larger study of the behavior of the West Antarctic Ice Sheet. We used a pulsed-radar and a resistively loaded dipole antenna, with a center frequency of 2 MHz as the source, and a similar antenna and a storage oscilloscope for receiving the return energy [see (*5*) for details on the instrument]. Figure 1 is a radargram along the line "ab" (whose location is shown on the inset map of the region); ice flow is from right (kilometer 25) to left (kilometer 0) (with a smaller component of flow out of the page). The main features apparent in the radargram are the strong basal echo and, between kilometer 25 and kilometer 17, a strong second echo indicating the base of a subglacial wedge.

Numerous basal crevasses are apparent in the radargram (hyperbolic arrivals associated with the line diffractors of the crevasse shoulders), downflow of the grounding line at kilometer 12. We determine the grounding-line location from the drop in ice surface elevation z_s (10 m over a short distance of 3 km) and the coincident slight decrease in ice thickness h_i (Fig. 2); the ice-thickness change is insufficient to explain most of the surface drop. This "surface ramp" marks a change in bed slope and a marked increase in basal crevasses. In addition, Global Positioning System (GPS) and strand-crack observations (*6*) are consistent with our interpretation of the grounding line.

We infer that the subglacial wedge continues downstream of kilometer 17 to the grounding line at kilometer 12. The abrupt termination of radar returns from the base of the subglacial wedge (at kilometer 17) is likely a consequence of seawater infiltration beneath the ice from the upglacier-most basal crevasse at kilometer 17. As sketched in Fig. 3, the observed basal crevasses on our line may be extensions of features opened by tidal flexure of floating ice where the grounding line is embayed nearby; relatively dense seawater injected along such a crevasse during opening would subsequently drain downglacier along the ice-wedge interface above the fresher pore waters of the wedge. The skin depth for seawater is on the order of 10^{-3} m (*7*), so even a thin layer would effectively mask deeper reflectors (*8*). Thus, we suggest that the subglacial wedge is present between kilometer 17 and kilometer 12.

Converting the radar basal-echo time to h_i [using a velocity $c_i = 168$ m μs^{-1} (*9*)] and subtracting h_i from z_s (determined by differential GPS measurements), we calculate bed elevation z_b (Fig. 2). The bed rises gradually along the wedge and the grounding zone before dropping abruptly (7 m over 2 km, from kilometer 14 to kilometer 12) at the grounding line. The bed drop is coincident with the rapid drop in z_s ("surface ramp") of 10 m.

To characterize the properties of the wedge, we measure both the polarity of the echo and the return power P_r (in dB) [defined as $P_r = 10 \log_{10}\left(1/(t_2 - t_1)\int_{t_1}^{t_2} |f(t)|^2 dt\right)$, where t is time, $f(t)$ is the echo amplitude, and $(t_2 - t_1)$ is the duration of the echo, which is very similar to a three-humped Ricker wavelet (*10*)] for its top and bottom.

The basal echo is of reversed polarity along the whole line, which indicates that the permittivity of the subglacial material is greater than

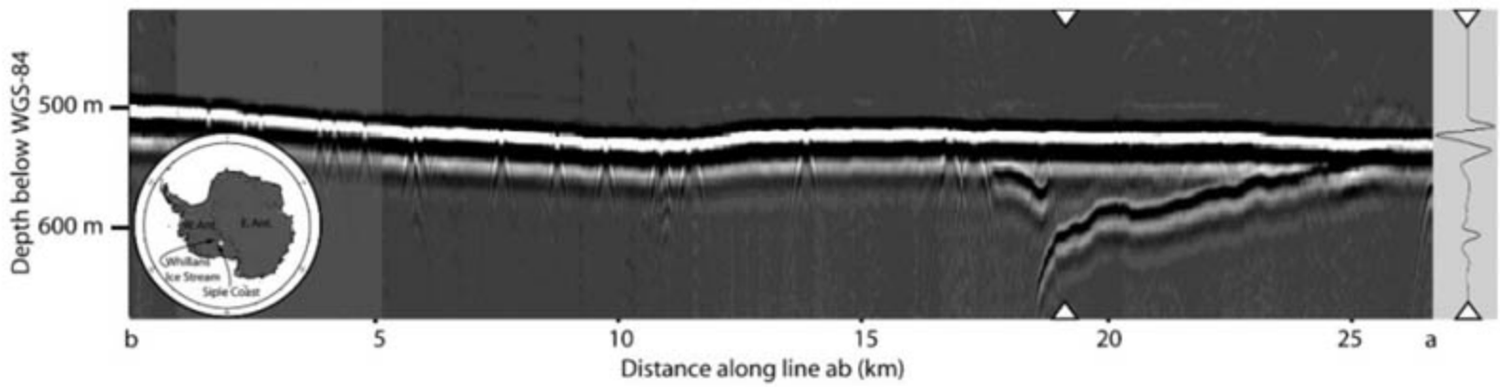

Fig. 1. Radargram along line ab from grounded ice (**right**) to floating ice (**left**). Abscissa is distance in kilometers from the farthest downstream position; ordinate is depth below the WGS-84 geoid. Flow is from right to left on the radargram (with a component out of the page) and from northeast to southwest on the map (**inset**) showing the study region. The map of Antarctica is oriented with the Greenwich meridian directed upward, and the location of Whillans Ice Stream is indicated by the white dot. On the right of the radargram, a single radar trace (from the location marked with triangles on the radargram) is plotted to illustrate the Ricker-wavelet–like form of the ice-bottom reflection and the phase change of the reflection at the wedge bottom.

[1]Department of Geosciences, Pennsylvania State University, University Park, PA 16802, USA. [2]Institute for Geophysics, University of Texas at Austin, Austin, TX 78758, USA.

*To whom correspondence should be addressed. E-mail: sak@essc.psu.edu

that of ice (for ice, we use a permittivity value of $\varepsilon_i = 3.2$). The echo from the base of wedge, however, is of normal polarity, which shows that the permittivity of the material beneath the wedge is lower than that of the wedge.

The reflection off the base of the wedge is about 12 dB less than that off the top of the wedge (Fig. 4). The difference in bed return power ΔP_r varies almost linearly with wedge thickness. Fitting a straight line to the data results in $\Delta P_r = -6.7\Delta t - 7.2$, where Δt is the two-way travel time through the wedge. Assuming that the power loss at the base of the wedge is independent of distance along the wedge, we find that the attenuation within the wedge is -6.7 ± 4 dB μs^{-1} and that the power loss at the base is -7.2 ± 2 dB (where the uncertainties correspond to one SD).

We reject the hypothesis that the wedge consists of free water because the hydrologic potential $H = \rho_w g z_b + \rho_i g(z_s - z_b)$ decreases notably along the wedge (where ρ_i and ρ_w are ice and water densities, respectively, and g is gravitational acceleration). For a water body that is this large [i.e., many ice thicknesses along flow and at least a few ice thicknesses across flow (*11*)], the hydrologic potential would be constant. In addition, both salt water and groundwater have high electrical conductivity that would lead to a much greater attenuation than that observed. We reject the hypothesis that the wedge is basal accretion ice because of the large absolute reflection coefficient at the top of the wedge (*12*), which is only slightly lower than the reflection from the ice shelf. Finally, we reject the possibility that this feature is an artifact such as sideswipe (*13*), because the reflection polarity is opposite to that of the primary bed reflection; sideswipe would have the same polarity as the bed.

In Table 1, we estimate the attenuation for sediments with varying porosity. We include fresh water and seawater for reference. We also calculate the reflection coefficient for the assumed wedge fill over a rock with $\varepsilon' = 6.6$, where ε' is the real part of the electrical permittivity [the "unfrozen bedrock" case of Peters *et al.* (*14*)].

The measured attenuation data, ΔP_r, are best explained by a wedge fill consisting of an unfrozen till layer with low-electrical-conductivity (almost fresh) water in the pores. We cannot distinguish between low- and high-porosity sediment with this technique, but borehole measurements farther upstream on this glacier have found that porosity $\phi \approx 45\%$ (*15*, *16*). For the case of a sedimentary fill, the radar wave speed is $c = c_0/\sqrt{\varepsilon'} = 70$ m μs^{-1} for $\varepsilon' = 18$ (unfrozen till; Table 1), and the maximum thickness of the wedge is 31 m (where $c_0 = 300$ m μs^{-1} is the speed of light in a vacuum). The imaged volume of the wedge is on the order of 10^5 m^3 per unit width, with perhaps a similar volume obscured by seawater downglacier of kilometer 17, including material inferred beyond the grounding line. The grounding-line position has probably been stable near the present position for a millennium (*17*). Hence, deposition of the wedge has resulted from a sediment flux on the order of 10^2 m^3 m^{-1} a^{-1}.

The wedge that we observe matches closely, in size, shape, and setting, with the numerous wedges on the floor of the Ross Sea beyond the Ross Ice Shelf (*18*, *19*). Those wedges were deposited at the edge of the continental shelf at the Last glacial maximum and during retreat across the continental shelf. Those relict wedges are typically tens of kilometers long and tens of meters high. The wedges occur in troughs that were occupied by ice-age extensions of the modern ice streams, with a trough-mouth wedge and one to three retreat wedges along each trough. (No information is available on the possible occurrence of additional retreat wedges beneath the floating Ross Ice Shelf.) Available sampling indicates that the wedges in the Ross Sea are composed of diamicton, which can be distinguished from water-washed sub–ice-shelf sediments (*20*), and that "Grounding-zone wedges contain the sediment that was transported within the subglacial deforming till layer" (*19*).

Megascale glacial lineations on the upglacier sides of the Ross Sea wedges show that ice streaming persisted during deposition and that the wedges exerted drag on the flowing ice. The wedges sit on the Ross Sea Unconformity that eroded during glacial advance and thus were deposited during the glacial maximum (shelf-edge) and retreat of the ice. Any wedges associated with the glacial advance or with earlier glacial cycles have been extensively modified or removed and no longer preserve their topo-

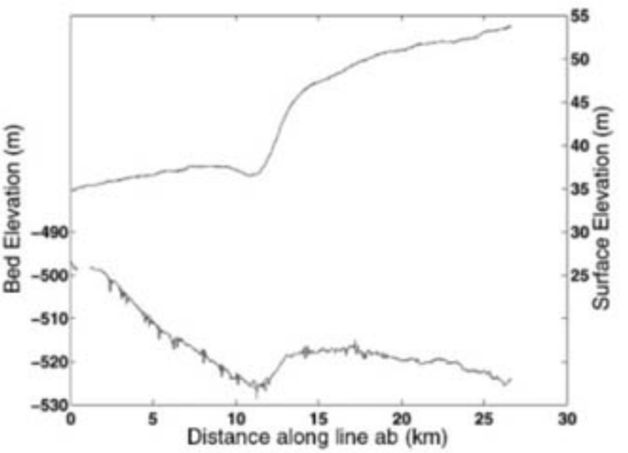

Fig. 2. Surface elevation z_s (upper curve) and bed elevation z_b (lower curve) along line ab. Note that the two elevation scales are different and that there is a discontinuity between them. Abscissa is the same as in Fig. 1.

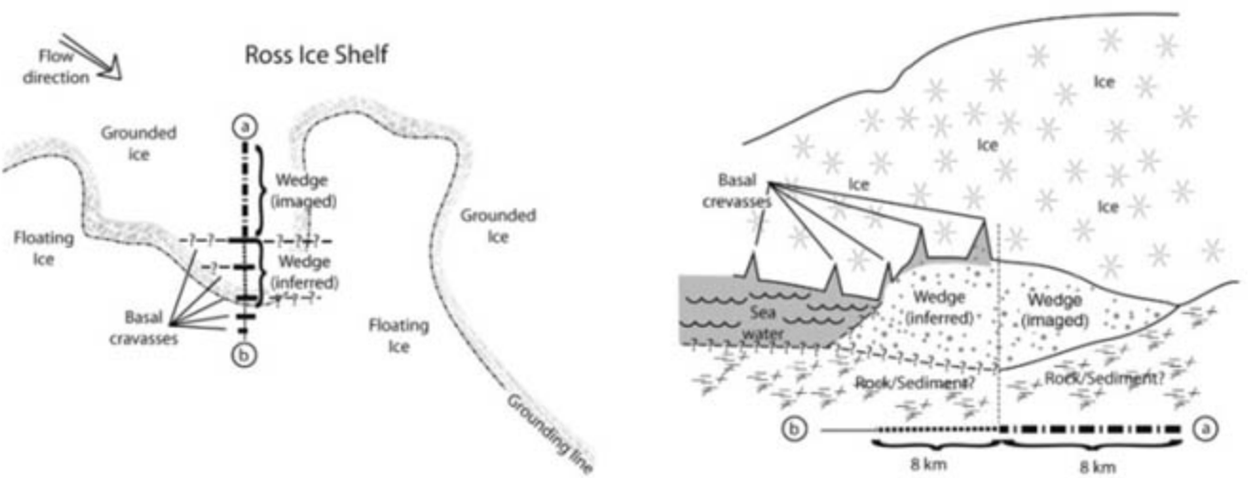

Fig. 3. Cartoon illustrating the subglacial wedge. (**Left**) Map view of the region showing the radar line crossing the grounding line from grounded ice to floating ice. (**Right**) Cross section along the radar line. The wedge is well-imaged for part of its length, but ends abruptly when basal crevasses begin to appear. We suggest that the wedge continues beyond the apparent termination but can only speculate on its extent (illustrated by question marks).

graphic form. Similarly, upglacier of our field site, prograding beds are observed that are likely to have originated from an earlier grounding-line wedge but are without preserved topographic expression (*21*).

Our modern observations, together with the observations of deglacial features, provide several insights to ice-sheet flow and the coupled sedimentary system. The modern grounding line, just beyond the crest of its wedge, occurs where the bed falls away rather than where the ice thins enough to allow its flotation over a nearly horizontal bed. The ice just upglacier of the grounding line is substantially thicker than that needed to allow flotation, owing to the restraint from friction with the wedge. We show in a companion paper (*4*) that this is a necessary result of sub–ice-shelf sedimentation and serves to stabilize the grounding-line position. This phenomenon also allows deposition of a discrete wedge rather than the spreading of deposits more uniformly over a broader area.

The implied sedimentation rate for the modern wedge requires long-term erosion rates beneath Whillans Ice Stream and its catchment of just over 0.1 mm a^{-1}, substantially smaller than those for actively eroding mountain glaciers but still notable as compared to many subaerial situations (*22*, *23*). Erosion is likely concentrated in restricted places where basal melting occurs over poorly consolidated sedimentary substrates. Erosion in these regions then would be sufficiently rapid to matter to ice-sheet evolution over multiple ice-age cycles.

The sediment flux implied by our observations likely points to transport dominated by distributed deformation over a considerable thickness (tens of centimeters or more) of subglacial till, averaged over the past millennium. Steady-state meltwater fluxes for the West Antarctic Ice Sheet are incapable of transporting such large quantities of sediment. Dilute debris likely exists in a basal ice layer ~10 m thick, frozen onto the base of the ice stream (*15*) from a through-going water system. Debris concentrations are poorly known in this layer but are probably on the order of 3% or less, based on limiting values reported in (*24*) for presumably comparable ice beneath the neighboring Kamb Ice Stream. The grounding-zone melt rate in this area has been estimated as ~0.05 m a^{-1} (*25*), based on modeling that assumed deeper water than what is locally present, which likely overestimates the heat transport and melt rate. The modeled melt rate would give an estimated sediment flux to the wedge (from the melting off of the debris in the ice) that is nearly an order of magnitude too small to explain our observed deposit.

Existence of subglacial till deformation is supported by two observations beneath West Antarctic ice streams (*15*, *26*) that suggest a flux of sediment on the order of 150 m^3 m^{-1} a^{-1}, though with considerable scatter in the results. Our observation is consistent with these measurements. Finally, the depth of deformation in subglacial till may provide insight to the "flow law" relating strain rate to stress in the material. Sustained high stress is expected to collapse deformation to a surface (*27*). Considerations of measured profiles of sediment properties with depth indicate that the deformation surface would be at or very close to the base of the ice, where ice velocity would be largely decoupled from the stress supported on the basal sediment (Coulomb-plastic behavior) (*27*). However, processes perhaps linked to dilatancy and the non-steady response to tidal forcing can allow more-distributed deformation and strain rate increasing as a low power of stress (*27*, *28*). Hence, the deposit that we observe and the older deposits on the Ross Sea floor point to subglacial till deformation distributed across a considerable depth and thus to a low stress exponent in the sediment flow law.

Our observations overall show that the ice-sheet flow and sedimentary processes indicated by very-short-term measurements under ice streams (*15*), and by geological observations of deglaciated regions (*19*), have continued over intermediate times. The sediment transport is intimately linked to the lubrication allowing ice-stream persistence. The sediment deposition serves to stabilize the grounding line, which has numerous implications (*4*).

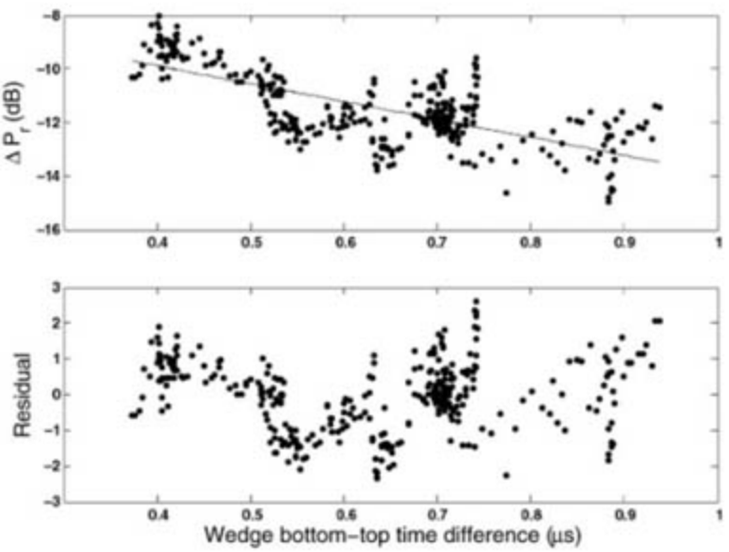

Fig. 4. (**Top**) ΔP_r between the top and bottom of the subglacial wedge plotted against Δt. A linear fit through the points is shown. (**Bottom**) Plot of the residuals between the data and the fit.

Table 1. Calculated attenuations [$\exp(-2\pi\Delta t f \tan\delta)$ in dB μs^{-1} for radar frequency f = 2 MHz, where $\tan\delta$ is the complex part of the electrical permittivity and is related to absorption] and reflectivity at the base of different wedge fill materials. fw, fresh water; gw, groundwater. The complex permittivity is given by $\varepsilon = \varepsilon'(1 - i\tan\delta)$, where i is the square root of −1; we determine ε' and $\tan\delta$ from equations 24 and 25 of (*29*). This range encompasses reasonable glacial till values (indicated by the "a" superscript in the $\tan\delta$ column). We assume that the material below the wedge is unfrozen bedrock with $\varepsilon' = 6.6$.

Wedge fill	Permittivity ε'	$\tan\delta$	Attenuation (dB μs^{-1})	Reflectivity (dB)
Unfrozen till (45% fw)	30	0.01 to 0.1[a]	−1 to −5	−10
Unfrozen till (25% fw)	18	0.01 to 0.1[a]	−1 to −5	−10
Unfrozen till (15% fw)	12	0.01 to 0.1[a]	−1 to −5	−9
Unfrozen till (40% gw)	18	0.82	−89	−6
Fresh water	80	0.002	−1	−2.5
Groundwater	80	1.4	−152	−2.5
Seawater	77	11.3	10^3	−2.6

References and Notes

1. M. F. Meier, A. Post, *J. Geophys. Res.* **99**, 9051 (1987).
2. P. Clark, D. Pollard, *Paleoceanography* **13**, 1 (1998).
3. B. Hallet, L. Hunter, J. Bogen, *Global Planet. Change* **12**, 213 (1996).
4. R. B. Alley, S. Anandakrishnan, T. K. Dupont, B. R. Parizek, D. Pollard, *Science* **315**, 1838 (2007); published online 1 March 2007 (10.1126/science.1138396).
5. A. Gades, thesis, University of Washington (1998).
6. H. J. Horgan, S. Anandakrishnan, *Geophys. Res. Lett.* **33**, L18502 (2006).
7. S. Shabtaie, C. R. Bentley, *J. Geophys. Res.* **92**, 1311 (1987).
8. The alternative explanation for termination of the wedge (i.e., it is cut by bedrock raised along a near-vertical fault plane striking across our line) is geologically unlikely considering the dominant trend of structures in the region, which are controlled by north-south extension.
9. V. V. Bogorodsky, C. R. Bentley, P. E. Gudmandsen, *Radioglaciology* (Reidel, Dordrecht, Netherlands, 1985).
10. R. E. Sheriff, L. P. Geldart, *Exploration Seismology* (Cambridge Univ. Press, Cambridge, ed. 2, 1995).
11. No transverse radar lines crossed this feature. However, our longitudinal line was placed with no a priori knowledge of the feature, making it unlikely that this is a narrow feature that we found by chance.
12. T. Murray *et al.*, *J. Geophys. Res.* **105**, 13491 (2000).

13. P. M. Tucker, H. J. Yorston, *Pitfalls in Seismic Interpretation*, J. C. Hollister, Ed. (Society of Exploration Geophysicists, Tulsa, OK, 1973).
14. L. E. Peters *et al.*, *J. Geophys. Res.* **111**, B01302 (2006).
15. B. Kamb, *The West Antarctic Ice Sheet: Behavior and Environment*, R. B. Alley, R. A. Bindschadler, Eds. (American Geophysical Union, Washington, DC, 2001), pp. 157–200.
16. The phase of the reflection from the base of the till is diagnostic of porosity, with reflection phase angles ranging from 70° to 120° for porosity ϕ from 45 to 15%, respectively. However, our instrument was not phase sensitive; future work with a phase-sensitive radar or with seismic experiments would determine this property.
17. H. Conway, B. L. Hall, G. H. Denton, *Science* **286**, 280 (1999).
18. S. Shipp, J. B. Anderson, E. W. Domack, *Geol. Soc. Am. Bull.* **111**, 1486 (1999).
19. A. B. Mosola, J. B. Anderson, *Quat. Sci. Rev.* **25**, 2177 (2006).
20. E. Domack, E. Jacobson, S. Shipp, J. Anderson, *Geol. Soc. Am. Bull.* **111**, 1517 (1999).
21. D. Blankenship, S. Rooney, R. Alley, C. Bentley, *Ann. Glaciol.* **12**, 200 (1989).
22. B. Hallet, L. Hunter, J. Bogen, *Global Planet. Change* **12**, 213 (1996).
23. Similar or somewhat larger sediment fluxes are indicated by the geometry and likely time for deposition of the grounding-zone wedges described by Mosola and Anderson (*19*), which is consistent with the ice sheet having expanded over easily eroded, poorly consolidated sediments of the Ross Sea.
24. P. Christoffersen, S. Tulaczyk, F. D. Carsey, A. E. Behar, *J. Geophys. Res.* **111**, F01017 (2006).
25. D. M. Holland, S. S. Jacobs, A. Jenkins, *Antarct. Sci.* **15**, 13 (2003).
26. H. Engelhardt, W. B. Kamb, *J. Glaciol.* **44**, 223 (1998).
27. N. R. Iverson, T. S. Hooyer, R. W. Baker, *J. Glaciol.* **44**, 634 (1998).
28. R. B. Alley, *Deformation of Glacial Materials*, A. J. Maltman, B. Hubbard, M. J. Hambrey, Eds. (Special Publication 176, Geological Society of London, 2000), pp. 171–179.
29. P. N. Sen, C. Scala, M. H. Cohen, *Geophysics* **46**, 781 (1981).
30. We thank D. Voigt, I. Joughin, P. Winberry, L. Peters, B. Bindschadler, and P. Burkett for their help; and University Navstar Consortium (UNAVCO), Raytheon Polar Services, and Kenn Borek Air for logistical support. Partial support was provided by NSF through grant numbers 0229629, 0226535, 0424589, 0440447, 0440899, 0447235, 0531211, and 0539578, and by the Gary Comer Science and Education Foundation.

Supporting Online Material

www.sciencemag.org/cgi/content/full/1138393/DC1
Fig. S1

4 December 2006; accepted 21 February 2007
Published online 1 March 2007;
10.1126/science.1138393
Include this information when citing this paper.

Effect of Sedimentation on Ice-Sheet Grounding-Line Stability

Richard B. Alley,[1]* Sridhar Anandakrishnan,[1] Todd K. Dupont,[1,2]
Byron R. Parizek,[1,3] David Pollard[1]

Sedimentation filling space beneath ice shelves helps to stabilize ice sheets against grounding-line retreat in response to a rise in relative sea level of at least several meters. Recent Antarctic changes thus cannot be attributed to sea-level rise, strengthening earlier interpretations that warming has driven ice-sheet mass loss. Large sea-level rise, such as the ≈100-meter rise at the end of the last ice age, may overwhelm the stabilizing feedback from sedimentation, but smaller sea-level changes are unlikely to have synchronized the behavior of ice sheets in the past.

Ice sheets both cause and respond to sea-level changes. Large, rapid ice-sheet fluctuations have occurred in the past (*1*) and may recur, but the relative importance of different causes remains uncertain. Here we show that sedimentation beneath ice shelves at grounding lines (where ice begins to float) provides substantial stability against ice-sheet advance or retreat during sea-level changes of up to a few meters or more. Such forcing from sea-level change occurs on the same time scale as does sedimentary stabilization, pointing to other environmental controls as being especially important to ice sheets.

In 1905, R. F. Scott reported evidence of the geologically recent shrinkage of the Antarctic Ice Sheet, despite persistently cold conditions (*2*). Scott suggested that more snowfall in a warmer past explained the larger ice sheet at that time. Subsequent evidence showing the (near)synchrony of northern and southern ice retreat after the last ice age and that Antarctica had experienced larger ice sheets when the southern climate was colder and drier disproved Scott's hypothesis.

Many workers (*3*) instead came to accept Penck's argument that sea-level rise from the melting of northern ice sheets had driven the Antarctic ice to retreat (*4*). Ice-sheet synchronization by smaller sea-level changes linked to Heinrich events or other millennial events has also been frequently proposed (*1*). However, simple sea-level control is inconsistent with sparse data indicating that, after an initial retreat from the outer shelf (*5*), additional Antarctic shrinkage was delayed until near the end of the northern-driven deglacial sea-level rise (*6*). Sea-level control is also inconsistent with the observed slowing of Antarctic ice-stream motion in response to rising tide (*7*, *8*).

Sedimentary stabilization of nonfloating tidewater glaciers is well known (*9*): Tall, steep-sided sediment bodies deposited between ice and water reduce iceberg calving. Ice flowing from large ice sheets more typically forms floating ice shelves, with sediment being deposited beneath the gradually sloping ice-shelf base. Our model results and the observations of (*10*) show that such sedimentation also serves to stabilize the grounding line and thus to prevent ice-sheet shrinkage in response to a small (≤≈10 m) sea-level rise. Penck's hypothesis (*4*) may still be valid for ice-sheet response to a larger sea-level rise (≈100 m); however, our results, together with recent evidence that ice shelves respond sensitively to ocean temperature changes and quickly propagate the response inland (*11*), point to the greater importance of other environmental variables, especially sub–ice-shelf temperature.

Going from the grounded West Antarctic Ice Sheet to the floating Ross Ice Shelf, the upper surface typically drops ≈10 to 25 m in a ramp extending over a few kilometers, which is much steeper than the slope upglacier or downglacier (*12*). Where data are available, this surface-elevation drop is not caused by thinning of the ice, as might occur from strong basal melting near the grounding line, nor from the effects of basal crevassing or near-surface density changes (*12*). Instead, the surface-elevation ramp results mainly from a corresponding ramp in basal topography. Thus, the onset of flotation is not caused primarily by a downglacier thinning of ice to the flotation criterion, but more by a downglacier drop in the elevation of the glacier bed. This contributes to the observed stability of the grounding-line position over many decades (*12*) and to the ice-stream slowdown in response to rising tide (*7*, *8*).

Available data indicate that the topographic step in the glacier bed was formed by the recent deposition of primarily subglacially transported sediment. As shown in (*10*), a sediment wedge occurs just upglacier of the grounding line of Whillans Ice Stream, and this wedge is remarkably similar to the numerous till-dominated deposits formed at the grounding line of the extended ice sheet during its retreat from the continental-shelf edge as the last ice age ended (*13*). Observations are available from beneath the grounded portions of two active ice streams (Whillans and Bindschadler) feeding the Ross Ice Shelf, and both showed deformation of soft tills (*14*); although the deformation is probably discontinuous in space and time (*14*), notable sediment transport results. The geology near the grounding zone of the Ross Ice Shelf has not been mapped in detail, but available data indicate that the ice flows along fault-controlled basins containing poorly consolidated Tertiary and perhaps Quaternary sediments (*15*). It is highly unlikely that the sedimentary

[1]Department of Geosciences and Earth and Environmental Systems Institute, Pennsylvania State University, University Park, PA 16802, USA. [2]Department of Earth and Environmental Sciences, University of Illinois at Chicago, Chicago, IL 60607, USA. [3]Department of Physics, The College of New Jersey, Ewing, NJ 08628, USA.

*To whom correspondence should be addressed. E-mail: rba6@psu.edu

deposit discovered by Anandakrishnan *et al.* (*10*) is a localized feature and that the topographic step is caused by an unknown transverse geologic structure extending across the entire Ross Ice Shelf, except where surveyed by Anandakrishnan *et al.* (*10*). Instead, sedimentary control of most or all of the grounding line is highly likely, with the available data supporting wedge formation within the troughs of modern and past ice streams (*13*).

Using three different ice-flow models [labeled Dt (Dupont), Pk (Parizek), and Pd (Pollard) for their lead developers (*11*, *16*, *17*)] including longitudinal as well as basal shear stresses, we have assessed the effect of sub–ice-shelf sedimentation on an ice-stream/ice-shelf system. The models were run for a coupled ice-stream/ice-shelf configuration approximating Whillans Ice Stream and the adjacent Ross Ice Shelf across the grounding-zone wedge. In some runs, ice-shelf buttressing was prescribed, offsetting much of the spreading tendency at the grounding line. After reaching a steady state with a flat bed, the model ice-stream/ice-shelf system was perturbed by instantaneously adding a wedge of sediment similar to the 31-m-high wedge observed by Anandakrishnan *et al.* (*10*), with the same basal friction as beneath the preexisting ice stream (*18*). The evolution to a new steady state was assessed while the geometry of the sediment wedge was held constant. The response of steady-state configurations to instantaneous sea-level change was simulated with and without grounding-zone wedges.

The frictional drag from increased ice/sediment contact with the addition of the wedge slows and thickens the ice above, which in turn causes the geometric effect of the wedge to become important and to further restrict the ice flow (Fig. 1). The resulting grounding-line advance beyond the crest of the wedge causes flotation to occur where the bed falls away, matching observations at the modern grounding line, whereas without the wedge, flotation occurs where the ice thins sufficiently.

In all of our models, sea-level rise in the absence of a wedge causes the grounding line to retreat from its initial position because the reduction in basal friction from the flotation of previously grounded ice is more important than the increase in back pressure from the deeper water. The wedge causes the ice above the wedge crest to thicken to well above the flotation level; small instantaneous sea-level rise then causes very small grounding-line retreat to a new position that still lies beyond the crest of the wedge and well beyond the no-wedge position. Larger sea-level rise (≈5 m or more) causes the ice to float free of the wedge and to reach the same steady state as in the no-wedge case (Figs. 1 and 2).

Larger wedges have greater ice thickness above flotation levels at the wedge crest and so require larger sea-level rise to force the grounding line upglacier of the wedge crest. However, as shown in Fig. 3, the dependence of the resistance on the wedge height or length is steeper for smaller wedges than for larger ones. Furthermore, if the wedge volume grows at a constant rate, the wedge height and length will increase more rapidly at first and more slowly later. Both effects combine to produce a more rapid increase in resistance at early stages of growth than at later stages (*19*).

Stiffer wedges (those with greater frictional resistance for a given basal velocity) also require larger sea-level rise to force the grounding line upglacier of the wedge crest (Fig. 2). We expect that at least portions of a wedge will often be stiffer than the surrounding no-wedge regions. The steepened ice/air surface slope that develops in response to friction from a wedge (Figs. 1 and 4) will steepen the subglacial hydrologic-potential gradient and speed the flow of subglacial water, reducing water storage and pressure and thus reducing the lubrication of ice motion by sliding or till deformation (*20*). Consideration of our numerical experiments with stiffer wedges and of the additional stabilizing effect that would occur from sedimentation during sea-level rise at ordinary rates suggests to us that a sea-level rise of >≈10 m may be required to force retreat from the wedge deposited beneath Whillans Ice Stream over the past millennium or so (*10*).

Additional simulations of grounding-line/wedge interactions reveal a rich range of behavior

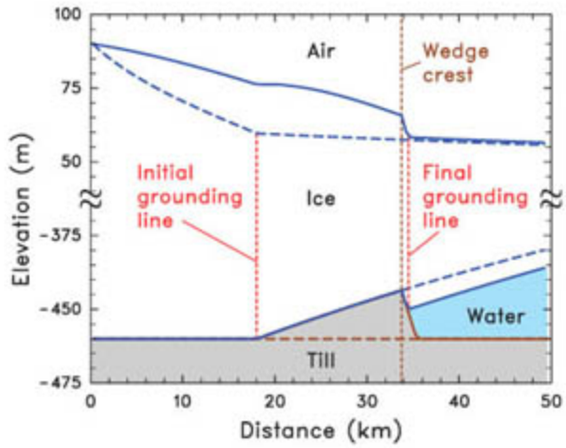

Fig. 1. Effect of grounding-line deposition (Pd model). Dashed lines show the steady ice-stream profile in the absence of a grounding-line wedge, and solid lines show the wedge and the corresponding steady ice-stream profile. The wedge causes the ice to thicken, the grounding line to advance past the wedge crest, and an inflection point to form in the upper surface at the upglacier end of the wedge, which might serve to increase water storage there.

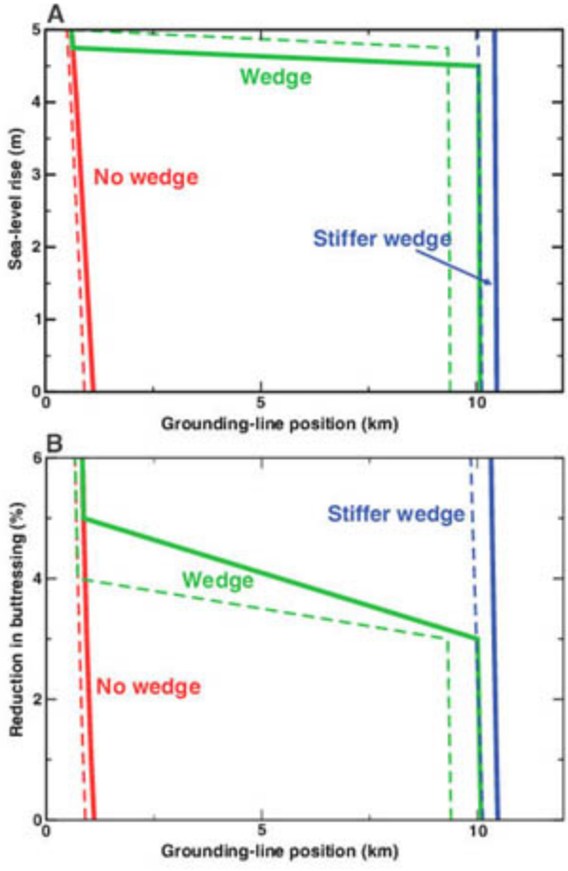

Fig. 2. Grounding-line stability in the Pk (solid lines) and Dt (dashed lines) models. Ice flows from left to right. In the absence of a wedge, the grounding line is at 1.1 km on this scale. The Pk and Dt experiments are not identical because of effects of the underlying model physics on the ice-shelf and wedge geometry, but the experiments are roughly comparable, and the results are clearly qualitatively identical and quantitatively similar. The ability of the grounding line to retreat is greatly limited by the constant-thickness boundary condition at the upglacier (left) end of the model domain; additional experiments with the same boundary condition applied farther away from the grounding line show much greater sensitivity to perturbations when the grounding line is upglacier of the wedge, and they emphasize the stabilizing influence of the wedge. (**A**) Response to sea-level rise. Adding the wedge moves the grounding line to 10.1 km, and increasing the stiffness of the wedge (the frictional resistance for a specified sliding velocity) by an order of magnitude moves the grounding line to 10.5 km. Sea-level rise causes retreat in all cases. However, the wedge causes the grounding-line retreat to be small up to some limit, beyond which the behavior is identical to the no-wedge case. The stiffer wedge requires a higher sea-level rise to reach that limit. (**B**) Response to a reduction in buttressing. Initial buttressing opposes 69% of the spreading tendency of the ice shelf at the grounding line. A 6% reduction means that buttressing opposes 0.94 × 69% = 65% of the spreading tendency. A reduction of ≈25% is required to cause retreat from the stiffer wedge.

(Fig. 4). Steady grounding-line positions on the upglacier side of a wedge were not simulated, consistent with the theory that such solutions are unstable (*21*). Migration of the grounding line across an otherwise horizontal bed is strongly influenced by any wedges encountered (*22*). The advance of the grounding line to a wedge crest is accelerated, but advance beyond the wedge crest slows relative to the no-wedge case. Similarly, the grounding line lingers on the downglacier side of a wedge during retreat and then races off of the upglacier edge. Under some circumstances, an advancing ice shelf has a more gradual basal slope than the upglacier side of a wedge, causing ice to bridge across water and ground on the wedge top, with the possibility of trapping water subglacially if the transverse geometry is favorable (*23*).

Our models show that the thickening of overlying ice in response to sedimentation stabilizes the grounding-line position against sea-level rise or buttressing reduction, and we infer that the extra thickness will tend to stabilize against any other environmental perturbation. Even a few centuries of sedimentation typically should provide stability against sudden sea-level rise from an outburst flood or surge of plausible-magnitude from another ice sheet, so sea-level change that is sufficiently large to control grounding-line positions will typically occur through noncatastrophic processes at usual rates (on the order of 1 cm/year or less) over several hundred to thousands of years. An ice-thickness change of ≈1.1 m has the same effect on grounding-line flotation as does a sea-level rise of 1 m, but this effect can be achieved more rapidly through sustained changes in snowfall or temperature. (Although slight warming causes very little surface melting in cold places, such as Whillans Ice Stream, a 1°C change can increase the surface melt rate by many tens of centimeters per year in warmer regions, such as some south-Greenland outlet glaciers.)

Changes in ice-shelf buttressing may be especially effective in overcoming the stabilizing effect of grounding-line sedimentation. As shown in Fig. 2, a 5% reduction in buttressing has about the same influence on the grounding line as does a 5-m rise in sea level for our reference case. A 5-m sea-level rise requires 500 years at the typical rate of the last deglaciation and 2500 years at 20th-century rates. Under some circumstances, a 5% decrease in buttressing will be achieved by an ≈5% decrease in the ice-shelf area generating side drag (*24*, *25*). Because the basal melt rate of ice shelves is observed to increase with water temperature by ~10 m $year^{-1}$ $°C^{-1}$ (*26*), even a fairly subtle perturbation in water temperature can cause a change of >5% in buttressing over years or decades. As an extreme example, a much larger change occurred in a few weeks during 2002 for the Larsen B Ice Shelf (*27*).

Grounding-zone sedimentation appears to be widespread to ubiquitous under major ice streams that control ice sheets (*28*, *29*). Any near-stillstand of a grounding line (from an encounter with a preexisting basal high or narrowing of a trough or from time changes in basal lubrication, ice-shelf melting, or other environmental conditions) will be stabilized by sedimentation, except under special circumstances. In turn, because of spatial variability in sedimentation rates and physiographic variations between ice-stream troughs, any grounding-line retreats that are forced by sea-level rise are likely to be asynchronous for different ice sheets or different sectors of a large ice sheet.

Penck's hypothesis that Northern Hemisphere ice-sheet melting drove Antarctic ice-sheet retreat at the end of the ice age (*4*) may be accurate [also see (*30*)], with the delay in Antarctic retreat after the onset of sea-level rise being linked to sedimentary dynamics. Although our results indicate that sea-level changes of a few meters are unlikely to substantially affect ice-sheet behavior, 100-m changes should have considerable effects. However, sea level may exert the primary control on the ice sheet only if there is multimillennial stability in the other variables that affect ice sheets more quickly, such as water temperature under ice shelves. Because oceanic temperature probably changed with the deglaciation, perhaps linked to the return of North Atlantic Deep Water to the Southern Ocean (*31*), we consider it possible that ice-shelf changes contributed to or even dominated grounding-line retreat in some sectors of the ice sheet. Regardless, our results show that synchronous behavior of ice sheets with active sedimentary systems on millennial time scales is unlikely to indicate ice-sheet teleconnections via sea level and instead probably indicates common climatic forcing, which demonstrably can have very large and rapid effects on ice sheets.

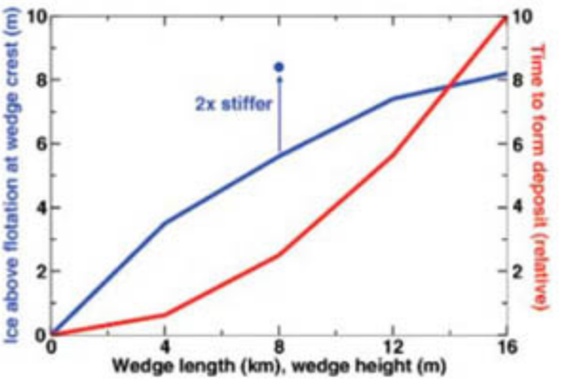

Fig. 3. Effect of wedge height on resistance to grounding-line retreat (blue) and on the time required for wedge deposition (red) in the Pd model. In this case, simulations were run for wedges having an upglacier slope of 0.001, a downglacier slope of 0.01, and heights of 0, 4, 8, 12, and 16 m with corresponding lengths of 0, 4, 8, 12, and 16 km, respectively. The thickness of ice above the wedge crest, which provides the resistance to grounding-line retreat, increases with wedge size; however, the increase in ice height above the flotation level is slower than the increase in wedge height, so earlier increments of wedge growth are more effective at stabilizing the grounding line, especially as successive height increments take longer to form if the sediment supply is constant. (The time depends on the sediment flux and so is plotted in relative units.) In comparison, the effect of doubling the stiffness of an 8-km wedge is also indicated. Similar experiments in the Dt model yield comparable trends but somewhat smaller height above the flotation level.

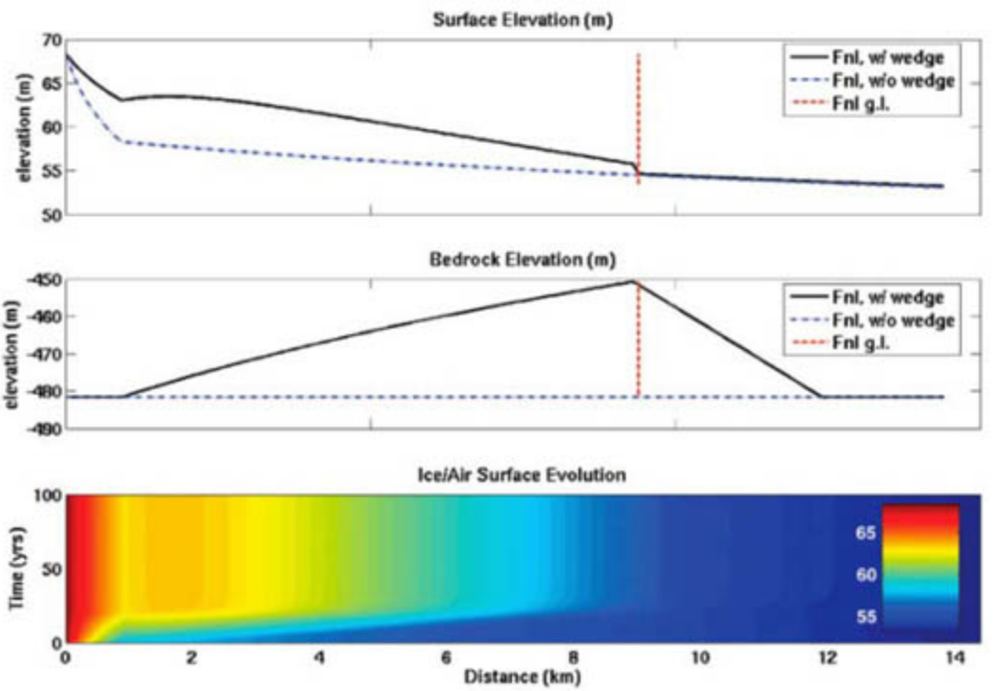

Fig. 4. Time-dependent response to instantaneous insertion of a wedge (Dt model). The final (Fnl.) geometries of the surface and bed are shown at the top, and the ice/air surface elevation (in meters) as a function of time and distance is color-coded. Ice thickness was held constant at the upglacier end (0 km, left). Most of the response to the insertion of the wedge was completed in ≈20 years.

References and Notes

1. M. Elliot *et al.*, *Paleoceanography* **13**, 433 (1998).
2. R. F. Scott, *Geogr. J.* **25**, 353 (1905).
3. J. T. Hollin, *J. Glaciol.* **32**, 173 (1962).
4. A. Penck, *Sitzungsber. Preuss. Akad. Wiss. Berlin Phys.-Math. Kl.* **6**, 76 (1928).
5. J. B. Anderson, S. S. Shipp, A. L. Lowe, J. S. Wellner, A. B. Mosola, *Quat. Sci. Rev.* **21**, 49 (2002).
6. H. Conway, B. L. Hall, G. H. Denton, A. M. Gades, E. D. Waddington, *Science* **286**, 280 (1999).
7. S. Anandakrishnan, D. E. Voigt, R. B. Alley, M. A. King, *Geophys. Res. Lett.* **30**, 1361 (2003).
8. The increase in pressure opposing ice flow from the rising tide is more important than the decrease in basal friction as the rising tide floats ice off of its bed, contrary to the expectation of the simplest model, in which the spreading tendency of grounded (nonfloating) ice is restrained by basal friction. If the forcing and the resulting slowdown were sustained, thickening and grounding-line advance would result from the sea-level rise.
9. M. Meier, A. Post, *J. Geophys. Res.* **92**, 9051 (1987).
10. S. Anandakrishnan, G. A. Catania, R. B. Alley, H. J. Horgan, *Science* **315**, 1835 (2007); published online 1 March 2007 (10.1126/science.1138393).
11. T. K. Dupont, R. B. Alley, *Geophys. Res. Lett.* **32**, L04503 (2005).
12. H. J. Horgan, S. Anandakrishnan, *Geophys. Res. Lett.* **33**, L18502 (2006).
13. A. B. Mosola, J. B. Anderson, *Quat. Sci. Rev* **25**, 2177 (2006).
14. B. Kamb, in *The West Antarctic Ice Sheet: Behavior and Environment*, R. B. Alley, R. A. Bindschadler, Eds. (American Geophysical Union, Washington, DC, 2001), pp. 157–199.
15. S. T. Rooney, D. D. Blankenship, R. B. Alley, C. R. Bentley, in *Geological Evolution of Antarctica*, M. R. A. Thomson, J. A. Crame, J. W. Thompson, Eds. (Cambridge Univ. Press, Cambridge, 1991), pp. 261–265.
16. B. R. Parizek, R. B. Alley, *Global Planet. Change* **42**, 265 (2004).
17. Materials and methods are available as supporting material on *Science* Online.
18. A sediment wedge with a rise of 31 m over 8 km and then a fall of 31 m over 3.2 km is typical of the reference experiment; however, because the sediment was added beneath an equilibrated ice shelf and the different models give slightly different equilibrium shelves, the sediment wedges differ somewhat between the models.
19. To good approximation, for a sediment deposit of maximum height h filling a sub–ice-shelf cavity of constant angle θ, relative to the horizontal bed, and with constant angle of repose ϕ, the sediment volume per unit of width is $V = (\cot\theta + \cot\phi)h^2/2$, and the volume increment dV to thicken by dh increases linearly with the wedge thickness as $dV = (\cot\theta + \cot\phi)hdh$.
20. G. K. C. Clarke, *Annu. Rev. Earth Planet. Sci.* **33**, 247 (2005).
21. J. Weertman, *J. Glaciol.* **13**, 3 (1974).
22. Bedrock bumps have the same effect as soft-sediment wedges and are much more likely to be encountered by a retreating grounding line than are sediment wedges. As shown in (*12*), soft-sediment wedges are formed at the grounding line during retreat and may be encountered on readvance, but they are unlikely to survive being overrun by advancing ice, so as to exist beneath grounded ice to influence grounding-line retreat.
23. R. B. Alley *et al.*, *Geomorphology* **75**, 76 (2006).
24. T. K. Dupont, R. B. Alley, *Geophys. Res. Lett.* **33**, L09503 (2006).
25. For sufficiently extensive ice shelves, a 5% decrease in buttressing will require a >5% decrease in the side-drag area.
26. E. Rignot, S. S. Jacobs, *Science* **296**, 2020 (2002).
27. T. A. Scambos, J. A. Bohlander, C. A. Shuman, P. Skvarca, *Geophys. Res. Lett.* **31**, L18402 (2004).
28. J. A. Dowdeswell, A. Elverhoi, *Mar. Geol.* **188**, 3 (2002).
29. J. S. Wellner, D. C. Heroy, J. B. Anderson, *Geomorphology* **75**, 157 (2006).
30. P. Huybrechts, *Quat. Sci. Rev.* **21**, 203 (2002).
31. J. F. Adkins, K. McIntyre, D. R. Schrag, *Science* **298**, 1769 (2002).

32. We thank J. Anderson, H. Horgan, S. Jacobs, D. Voigt, P. Burkett, and other colleagues. Partial funding was provided by NSF through grants (including 0424589, 0440447, 0440899, 0531211, 0447235, and 0539578) and by the Gary Comer Science and Education Foundation

Supporting Online Material

www.sciencemag.org/cgi/content/full/1138396/DC1
Materials and Methods
References and Notes

4 December 2006; accepted 21 February 2007
Published online 1 March 2007;
10.1126/science.1138396
Include this information when citing this paper.

Permissive and Instructive Anterior Patterning Rely on mRNA Localization in the Wasp Embryo

Ava E. Brent, Gozde Yucel, Stephen Small, Claude Desplan*

The long-germ mode of embryogenesis, in which segments arise simultaneously along the anterior-posterior axis, has evolved several times in different lineages of the holometabolous, or fully metamorphosing, insects. *Drosophila*'s long-germ fate map is established largely by the activity of the dipteran-specific Bicoid (Bcd) morphogen gradient, which operates both instructively and permissively to accomplish anterior patterning. By contrast, all nondipteran long-germ insects must achieve anterior patterning independently of *bcd*. We show that *bcd*'s permissive function is mimicked in the wasp by a maternal repression system in which anterior localization of the wasp ortholog of *giant* represses anterior expression of the trunk gap genes so that head and thorax can properly form.

The highly conserved segmented insect body plan is achieved by great flexibility in developmental mechanisms. In the ancestral short-germ mode of embryogenesis, head and thorax arise from the egg's posterior, and abdominal segments emerge progressively from a posterior growth zone. By contrast, in the more derived long-germ mode, all segments form simultaneously in a syncytial environment, with head and thorax at the egg's anterior. Long-germ development has evolved several times in different holometabolous insect lineages (*1*), including the Diptera, of which the most extensively studied member is *Drosophila melanogaster* (*Dm*). A morphogen gradient of Bicoid (Bcd) protein, formed by translation from a maternal, anteriorly localized mRNA source, establishes the *Drosophila* body plan. Embryos derived from *bcd* mutant mothers lack head, thorax, and some abdominal segments (*2*, *3*).

Despite its critical role in patterning the *Drosophila* long-germ embryo, *bcd* is distinctive to the higher Diptera (*4*). Thus, all other insects, including long-germ nondipterans, must employ a *bcd*-independent mechanism to accomplish segmentation. To identify such a mechanism, we investigated anterior patterning in the hymenopteran parasitoid wasp, *Nasonia vitripennis* (*Nv*) (*5*). The embryonic fate map of this independently evolved (*6*) long-germ insect is essentially identical to that of *Drosophila*, except that it is formed in the absence of *bcd*. We previously showed that in the early *Nasonia* embryo, *bcd*'s morphogenetic activity is performed by *orthodenticle1* (*Nv-otd1*), the ortholog of the *Drosophila bcd* target gene, *Dm-otd* (*5*). Although strictly zygotic in *Drosophila*, *Nv-otd1* mRNA is maternally provided and localized to both oocyte poles, resulting in bipolar protein gradients. The anterior *Nv-otd1* gradient regulates expression of zygotic head and thoracic gap genes, including the *Nasonia* orthologs of the *bcd* targets, *giant* (*gt*), and *hunchback* (*hb*) (*5*).

In addition to instructively activating the genes that pattern the head and thorax, *bcd* also functions permissively in *Drosophila* to indirectly repress posteriorly acting genes, such as the trunk gap genes, that would otherwise inhibit anterior development (*7*). We show here that *Nasonia* accomplishes this task by further employing maternal mRNA localization to position a repressor of trunk development at the anterior, thereby allowing formation of the head and thorax.

In the *Drosophila* embryo, the gap gene *Krüppel* (*Dm-Kr*) is expressed in a broad central stripe (Fig. 1A) and is required for formation of thoracic segment 1 (T1) through abdominal segment 5 (A5) (*8*). The positioning of *Kr* and, hence, of the trunk, is established by *bcd* and the terminal system; in embryos derived from *bcd* mutant mothers, the *Dm-Kr* domain broadens and shifts anteriorly (Fig. 1B) (*7*, *9*). *bcd*'s zygotic targets, *Dm-hb* and *Dm-gt*, mediate this regulation; in single *Dm-hb* (*7*, *9*) or *Dm-gt* mutant embryos (Fig. 1C), *Dm-Kr* shows slight anterior expansion (*10*), and in embryos mutant for both, *Dm-Kr*'s anterior shift is comparable to that seen from loss of *bcd* alone (*11*). However,

New York University, Department of Biology, Center for Developmental Genetics, 100 Washington Square East, New York, NY 10003, USA.

*To whom correspondence should be addressed. E-mail: cd38@nyu.edu

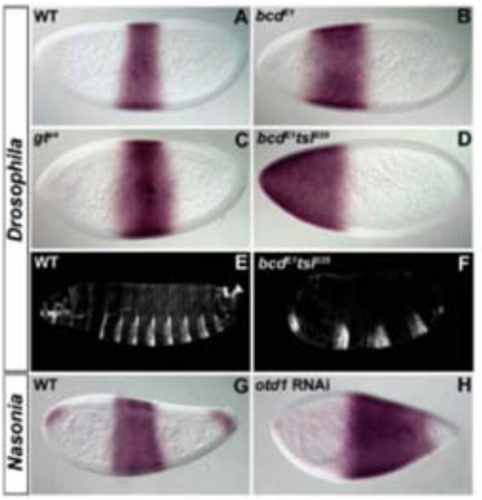

Fig. 1. Regulation of *Kr* in *Drosophila* and *Nasonia*. *Dm-Kr* expression in embryos that are wild-type (**A**), lacking *Dm-bcd* (**B**), mutant for *Dm-gt* (**C**), or lacking *Dm-bcd* and *Dm-tsl* (**D**). (**E**) Wild-type or (**F**) *Dm-bcd;tsl* cuticle. Cellular blastoderm expression of *Nv-Kr* in wild-type embryos (**G**) or after *Nv-otd1* RNAi (**H**).

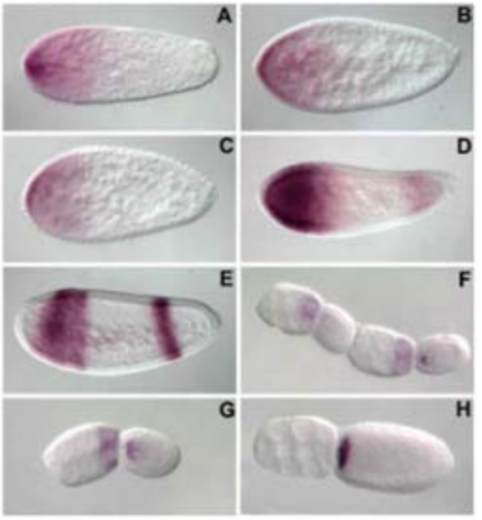

Fig. 2. Expression of maternal and zygotic *Nv-gt* during *Nasonia* oogenesis and embryogenesis. Maternal *Nv-gt* mRNA in freshly laid embryos (**A**), during pole cell formation (**B**), and in the syncytial blastoderm (**C**). Zygotic *Nv-gt* expression at onset of cellularization (**D**) and in the cellular blastoderm (**E**). Maternal anterior localization during oocyte development (**F** to **H**).

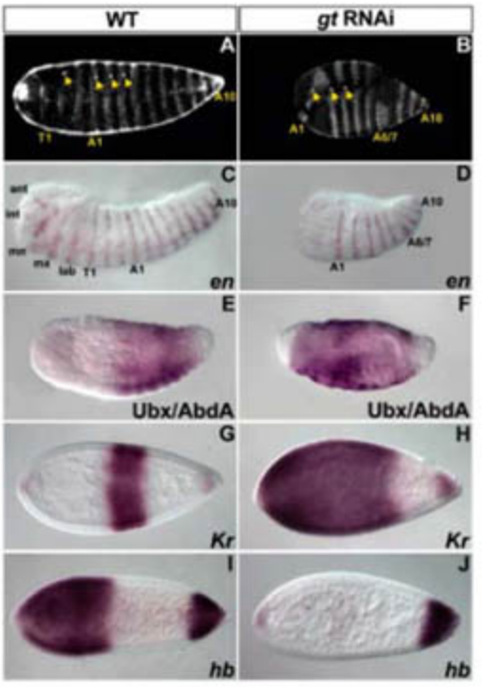

Fig. 3. Knockdown of *Nv-gt* in *Nasonia* results in anterior deletions. Wild-type (**A**) and *Nv-gt* RNAi (**B**) cuticles. Yellow arrows indicate spiracles on T2, A1 to A3. Expression of *Nv-en* (**C** and **D**), *Nv-Kr* (**G** and **H**), and *Nv-hb$_{zyg}$* (**I** and **J**) in wild-type [(C), (G), and (I)] and *Nv-gt* RNAi [(D), (H), and (J)] embryos. Ubx/AbdA protein expression in wild-type (**E**) and *Nv-gt* RNAi (**F**) embryos.

Dm-Kr does not reach the anterior tip of the embryo because of additional repression by the terminal system; in embryos lacking *bcd* and *torsolike* (*Dm-tsl*), *Dm-Kr* expands throughout the anterior (Fig. 1D), resulting in embryos with as few as four abdominal segments (Fig. 1, E and F) (*7*).

To determine how the *Nasonia* embryo's trunk is positioned, we isolated the *Nasonia* ortholog of *Kr* and found that it was expressed in a central gap–like domain (Fig. 1G). To confirm that *Nv-Kr* was acting as a gap gene, we knocked down *Nv-Kr* using parental RNA interference (RNAi) (*5*, *12*) and observed a gap phenotype: loss of T3 and A1 to A4. We hypothesized that because *Nv-otd1* performs other *bcd* functions, the *otd1* anterior morphogenetic gradient might be functioning to position *Nv-Kr*. However, after *Nv-otd1* RNAi, we found that although *Nv-Kr* expanded posteriorly, the anterior boundary was unaffected (Fig. 1H).

We next asked whether one of *bcd*'s zygotic gap gene targets could be implicated in *Nv-Kr* anterior boundary formation. Our analysis of *Nv-gt* revealed an essential role in repressing *Nv-Kr*. In *Drosophila*, *Dm-gt* is expressed in two regions, a posterior stripe and a *bcd*-activated anterior domain (*13*). *Nv-gt* expression in cellularized embryos was similar (Fig. 2E); however, we found *Nv-gt* expressed maternally at earlier stages. In freshly laid embryos, *Nv-gt* mRNA occupied a broad anterior gradient, with highest levels at the anterior pole (Fig. 2A). This domain persisted through pole cell formation (Fig. 2B) and syncytial blastoderm stages (Fig. 2C), intensifying at the onset of cellularization simultaneously with the appearance of a posterior cap, marking commencement of zygotic expression (Fig. 2D). During cellularization, *Nv-gt* expression resolved into zygotic anterior and posterior gap domains (Fig. 2E), which are regulated by *Nv-otd1* (*5*). To confirm that the early *Nv-gt* expression we had observed was maternal, we examined egg chambers and detected *Nv-gt* in the nurse cells and in the oocyte, where it accumulated around the nucleus (Fig. 2F). In mature oocytes, *Nv-gt* was localized to the anterior pole (Fig. 2G), ultimately assuming a tight anterior localization pattern (Fig. 2H).

Having established that *Nv-gt* is maternally provided and anteriorly localized, we used RNAi to determine its role during segmentation. Knockdown of *Nv-gt* resulted in unhatched larvae, all arrested with the same phenotype: complete loss of head and thoracic (T1-T3) segments (Fig. 3, A and B). In addition, A6 and A7 showed fusions and deletions due to loss of posterior zygotic *Nv-gt* (Fig. 3B). Anterior defects were also visible at earlier stages in knockdown embryos; analysis of *engrailed* (*Nv-en*) revealed anterior truncations (Fig. 3, C and D), whereas Ultrabithorax/AbdominalA (Ubx/AbdA) expression showed that all remaining tissue was abdominal (Fig. 3, E and F). The *Nv-gt* RNAi anterior phenotype was more severe than that of *Dm-gt* null mutations, in which anterior defects are limited to loss of labial and labral structures (*13*). By contrast, knockdown of *Nv-gt* resembled the all-abdominal phenotype observed in *Drosophila* embryos lacking both *bcd* and *Dm-tsl* (Fig. 1F).

In *Drosophila*, it has been shown that *Dm-gt* and *Dm-Kr* mutually repress each other, a relationship that defines the embryo's center (*10*, *11*). To determine whether *Nv-gt* also regulates *Nv-Kr*, we examined *Nv-Kr* expression in *Nv-gt* RNAi embryos and found dramatic expansion of *Nv-Kr* to the anterior pole (Fig. 3, G and H), indicating a major role for *Nv-gt* in setting the *Nv-Kr* anterior boundary. Moreover, loss of zygotic *Nv-gt* alone did not result in anterior *Nv-Kr* expansion. As noted earlier, the anterior *Nv-Kr* border was unaffected by *Nv-otd1* RNAi (Fig. 1H), whereas zygotic *Nv-gt* was eliminated (*5*). Thus, maternal *Nv-gt* appears to be the main repressor of *Nv-Kr*, mimicking both *bcd* and the terminal system in *Drosophila*.

The absence of head and thorax after *Nv-gt* RNAi was also similar to the phenotype of the *Nasonia* zygotic *hb* mutant *headless* (*14*). To investigate this correlation, we examined zygotic *Nv-hb* expression after *Nv-gt* RNAi and observed loss of the anterior *Nv-hb* domain (Fig. 3, I and J), suggesting that the anterior deletions seen in *Nv-gt* RNAi embryos were caused by loss of zygotic *Nv-hb*. Our observations generated two models for *Nv-gt* function: Either maternally localized *Nv-gt* activates expression of anterior zygotic *Nv-hb* (Fig. 4A), or *Nv-gt* negatively regulates a *hb*-repressor (Fig. 4A). Because *Dm*-Gt principally acts as a repressor (*15*), we favored the second model, hypothesizing that *Nv-Kr* might be the *hb*-repressor (Fig. 4A). In support of this model, we observed that the anterior and posterior zygotic *Nv-hb* domains expanded toward the center in *Nv-Kr* RNAi embryos (Figs. 3I and 4C). This double-repressor model for head and thorax patterning circumscribes maternally localized *Nv-gt* function solely to the repression of *Nv-Kr*.

To test this model, we asked whether expansion of *Nv-Kr* into the developing head and thoracic region causes deletion of those segments. If so, we would expect to see anterior patterning restored in embryos lacking *Nv-gt* and *Nv-Kr*. As a control for double RNAi, we examined embryos from females knocked down for

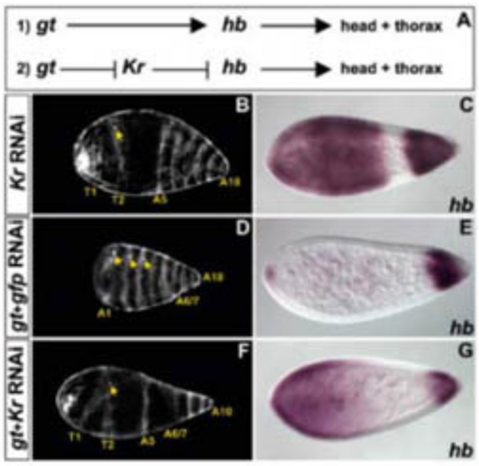

Fig. 4. Repression of *Nv-Kr* by maternal *Nv-gt* is required for head and thorax formation in *Nasonia*. (**A**) Two models for maternal *Nv-gt* function. Cuticular analysis (**B**, **D**, and **F**) and *Nv-hb*$_{zyg}$ expression (**C**, **E**, and **G**) after knockdown for *Nv-Kr* [(B) and (C)], *Nv-gt+gfp* [(D) and (E)], and *Nv-gt+Kr* [(F) and (G)].

Nv-gt and *green fluorescent protein* (*gfp*) and observed the expected *Nv-gt* phenotype: deletion of head and thorax, as well as loss of anterior *Nv-hb* expression (Fig. 4, D and E). Knockdown of *Nv-gt* and *Nv-Kr* yielded striking results. In 92% of examined embryos, the head and thorax (T1/T2) were restored (Fig. 4F), and the resulting cuticular phenotypes were essentially identical to those after *Nv-Kr* RNAi alone (Fig. 4B). Consistent with rescued head and thorax development, anterior zygotic *Nv-hb* was also restored, although not to wild-type levels (Fig. 4G). Nonetheless, the amount of *Nv-hb* present in *Nv-gt+Kr* RNAi embryos was sufficient to direct head and thorax development, demonstrating that *Nv-Kr* expansion impedes anterior patterning and that maternally localized *Nv-gt* confines *Nv-Kr* to the embryo's center. Thus, whereas in *Drosophila*, *bcd*-activated *Dm-gt* plays only a moderate role in positioning *Nv-Kr* (Fig. 1C), in *Nasonia*, maternal *Nv-gt* is sufficient to perform this function. This distinction led us to consider whether *Dm-gt*'s role in *Drosophila* would be enhanced if the *Drosophila* embryo were reengineered to develop like *Nasonia*—with *Dm-gt* maternally provided and anteriorly localized. We found that, whereas *Dm-gt* was sufficient to repress *Dm-Kr* anteriorly in the absence of *bcd* (fig. S1B), head and thoracic structures were not rescued (fig. S1C)—an unsurprising result given that, in addition to permitting anterior development by regulating *Kr*-repressing gap genes, *bcd* also functions instructively to activate genes required for head and thorax formation. In *Nasonia*, by contrast, the instructive and permissive anterior patterning functions are discrete. Head- and thorax-specific genes are triggered by an instructive anterior determinant, maternal *Nv-otd1*, which is localized independently of the permissively acting maternal repression system, *Nv-gt*.

A comparison of the molecular mechanisms employed by two independently evolved (*6*) long-germ insects not only uncovers those features essential to this developmental mode but also sheds light on how the *bcd*-dependent anterior patterning program might have evolved. Through analysis of the regulation of the trunk gap gene *Kr* in *Drosophila* and *Nasonia*, we have been able to demonstrate that anterior repression of *Kr* is essential for head and thorax formation and is a common feature of long-germ patterning. Both insects accomplish this task through maternal, anteriorly localized factors that either indirectly (*Drosophila*) or directly (*Nasonia*) repress *Kr* and, hence, trunk fates. In *Drosophila*, the terminal system and *bcd* regulate expression of gap genes, including *Dm-gt*, that repress *Dm-Kr*. *Nasonia*'s *bcd*-independent long-germ embryos must solve the same problem, but they employ a maternally localized repression system in which maternal *Nv-gt* is localized to the oocyte's anterior, where it represses *Nv-Kr*. In the dipteran lineage, whereas *gt* retained the ability to repress *Kr*, maternal regulation of *Kr*'s position was taken over by two novel features—*bcd*, a specific dipteran innovation, and the terminal pathway, which, although present ancestrally, appears to function less extensively in the anterior of non-dipteran insects (*16*, *17*). In addition to activating anterior patterning genes such as *otd* and *hb*, *bcd* also acquired regulation of *gt*, which became a strictly zygotic gene with a reduced role in repressing *Kr*. Our findings thus identify two independent mechanisms for long-germ anterior patterning—one using two maternally localized genes, *otd1* and *gt*, that respectively activate anterior zygotic patterning genes and repress trunk fates, and a second using *bcd* for these same functions, thereby demoting *otd* and *gt* to zygotic gap genes. Interestingly, it appears that long-germ embryos use RNA localization for a number of different developmental processes (*5*, *18*, *19*). By contrast, in short-germ insects, although some localized RNAs have been identified, there is as yet no evidence of their contribution to anterior-posterior patterning (*20*). mRNA localization indeed appears to be an important component of long-germ embryogenesis, perhaps even playing a role in the transition from the ancestral short-germ to the derived long-germ fate.

References and Notes

1. G. K. Davis, N. H. Patel, *Annu. Rev. Entomol.* **47**, 669 (2002).
2. T. Berleth *et al.*, *EMBO J.* **7**, 1749 (1988).
3. W. Driever, C. Nusslein-Volhard, *Cell* **54**, 83 (1988).
4. J. Lynch, C. Desplan, *Curr. Biol.* **13**, R557 (2003).
5. J. A. Lynch, A. E. Brent, D. S. Leaf, M. A. Pultz, C. Desplan, *Nature* **439**, 728 (2006).
6. J. Savard *et al.*, *Genome Res.* **16**, 1334 (2006).
7. G. Struhl, P. Johnston, P. A. Lawrence, *Cell* **69**, 237 (1992).
8. A. Preiss, U. B. Rosenberg, A. Kienlin, E. Seifert, H. Jackle, *Nature* **313**, 27 (1985).
9. M. Hulskamp, C. Pfeifle, D. Tautz, *Nature* **346**, 577 (1990).
10. X. Wu, R. Vakani, S. Small, *Development* **125**, 3765 (1998).
11. R. Kraut, M. Levine, *Development* **111**, 611 (1991).
12. J. A. Lynch, C. Desplan, *Nat. Protocols* **1**, 486 (2006).
13. R. Kraut, M. Levine, *Development* **111**, 601 (1991).
14. M. A. Pultz *et al.*, *Development* **132**, 3705 (2005).
15. G. F. Hewitt *et al.*, *Development* **126**, 1201 (1999).
16. J. A. Lynch, E. C. Olesnicky, C. Desplan, *Dev. Genes Evol.* **216**, 493 (2006).
17. R. Schroder, C. Eckert, C. Wolff, D. Tautz, *Proc. Natl. Acad. Sci. U.S.A.* **97**, 6591 (2000).
18. E. C. Olesnicky *et al.*, *Development* **133**, 3973 (2006).
19. A. Bashirullah, R. L. Cooperstock, H. D. Lipshitz, *Annu. Rev. Biochem.* **67**, 335 (1998).
20. G. Bucher, L. Farzana, S. J. Brown, M. Klingler, *Evol. Dev.* **7**, 142 (2005).
21. The authors wish to thank members of the Desplan and Small laboratories for support and advice. This project was supported by NIH grants GM64864, awarded to C.D., and GM51946, awarded to S.S. A.E.B is a Damon Runyon Fellow, supported by the Damon Runyon Cancer Research Foundation (DRG-1870-05).

Supporting Online Material

www.sciencemag.org/cgi/content/full/315/5820/1841/DC1
Materials and Methods
SOM Text
Fig. S1
References

13 November 2006; accepted 7 March 2007
10.1126/science.1137528

Emergent Biogeography of Microbial Communities in a Model Ocean

Michael J. Follows,[1]* Stephanie Dutkiewicz,[1] Scott Grant,[1,2] Sallie W. Chisholm[3]

A marine ecosystem model seeded with many phytoplankton types, whose physiological traits were randomly assigned from ranges defined by field and laboratory data, generated an emergent community structure and biogeography consistent with observed global phytoplankton distributions. The modeled organisms included types analogous to the marine cyanobacterium *Prochlorococcus*. Their emergent global distributions and physiological properties simultaneously correspond to observations. This flexible representation of community structure can be used to explore relations between ecosystems, biogeochemical cycles, and climate change.

A significant challenge in understanding the changing earth system is to quantify and model the role of ocean ecosystems in the global carbon cycle. The structure of microbial communities in the surface ocean is known to regulate important biogeochemical pathways, including the efficiency of export of organic carbon to the deep ocean. Although there is extraordinary diversity in the oceans, the biomass of local microbial communities at

any location is typically dominated by a smaller subset of strains. Their relative fitness and ecosystem community structure are regulated by a variety of factors, including physical conditions, dispersal, predation, competition for resources, and the variability of the environment (*1*–*3*). Models reflecting this conceptual view have been examined in idealized ecological settings (*4*) and have been applied to studies of terrestrial ecosystems (*5*). We have used this approach in a marine ecosystem model that embraces the diversity of microbes and their genomic underpinnings, a model in which microbial community structure "emerges" from a wider set of possibilities and, thus, mimics aspects of the process of natural selection. The system is flexible enough to respond to changing ocean environments and can be used to interpret the structure and development of marine microbial communities and to reveal critical links between marine ecosystem structure, global biogeochemical cycles, and climate change.

Recent ocean models have begun to resolve community structure by the explicit representation of three or four classes, or functional groups, of phytoplankton (*6*–*9*), but significant challenges remain (*10*, *11*). First, the specification of functional groups and diversity of the model ecosystem is subjective and somewhat arbitrary. Second, it is difficult to evaluate the parameters controlling such models because quantitative, physiological information from laboratory cultures is extremely limited. Third, observations of microbial community structure with which to evaluate global-scale models are still relatively sparse. Finally, model ecosystem structures optimized to reflect today's ocean may not be sufficiently dynamic to adapt appropriately to a changing climate where radical shifts in community structure might be possible.

To circumvent some of these difficulties, we formulated a marine ecosystem model that represents a large number of potentially viable phytoplankton types whose physiological characteristics were determined stochastically. The initialized organism types interacted with one another and their environment, evolving into a sustainable ecosystem where community structure and diversity were not imposed, but were emergent properties.

The ecosystem model consisted of a set of coupled prognostic equations (eqs. S1 to S5), with idealized representations of the transformations of inorganic and organic forms of phosphorus, nitrogen, iron, and silica. Many tens of phytoplankton types (here, 78) were initialized in each simulation, each type distinguished by its physiological capabilities and the values of coefficients that control the rates and sensitivities of metabolic processes. These were provided by random drawing from broad ranges guided by laboratory and field studies (table S1). We focused these choices on light, temperature, and nutrient requirements (fig. S1), the niche dimensions for phytoplankton thought to be most important in regulating growth. To facilitate a test of the approach, we also specifically addressed functions that differentiate *Prochlorococcus* spp. from other phytoplankton, including their small size and inability to assimilate nitrate. Other functions could be emphasized depending on the aim of the study. Ecological trade-offs were imposed through highly simplified allometric constraints [see supporting online material (SOM)]. To reflect the extra energetic expense of using nitrate, relative to other inorganic nitrogen sources, we allowed the maximum growth rate to increase slightly when nitrate was not the major nitrogen source (*12*). Organisms incapable of utilizing nitrate were given a slightly lower nutrient half-saturation. We explicitly represented predation by two classes of grazer and, for the action of heterotrophic microbes, we used a simple remineralization rate (SOM).

A global ocean circulation model constrained by observations (*13*) provided flow fields and mixing coefficients that transport all biological and chemical tracers. All phytoplankton types were initialized with identical distributions of biomass, and the model was integrated forward for 10 years, over which time a repeating annual cycle in ecosystem structure emerged. We repeated the integration 10 times, each time with a different random selection of phytoplankton physiologies, forming an ensemble of 10 members. Although each ensemble member produced a unique emergent ecosystem, the broad-scale patterns of productivity, community structure, and biogeography were robust across all 10. Global patterns of open-ocean biomass (Fig. 1A), primary production, and nutrients (fig. S3) were qualitatively consistent with in situ and remote observations. The ensemble mean globally integrated, annual primary production was 44 gigatons C per year, with a standard deviation of less than 5%. This small standard deviation suggested that sufficient phytoplankton "types" were initialized for consistent emergent solutions and also reflects the large-scale regulation by the physical transport of nutrients.

After an initial adjustment, the biomass of some phytoplankton types fell below the threshold of numerical noise, and these types were assumed to have become "extinct." In all ensemble members, about 20 phytoplankton types accounted for almost all of the total global biomass (fig. S2). We classified the phytoplankton types into four broad functional groups, each a

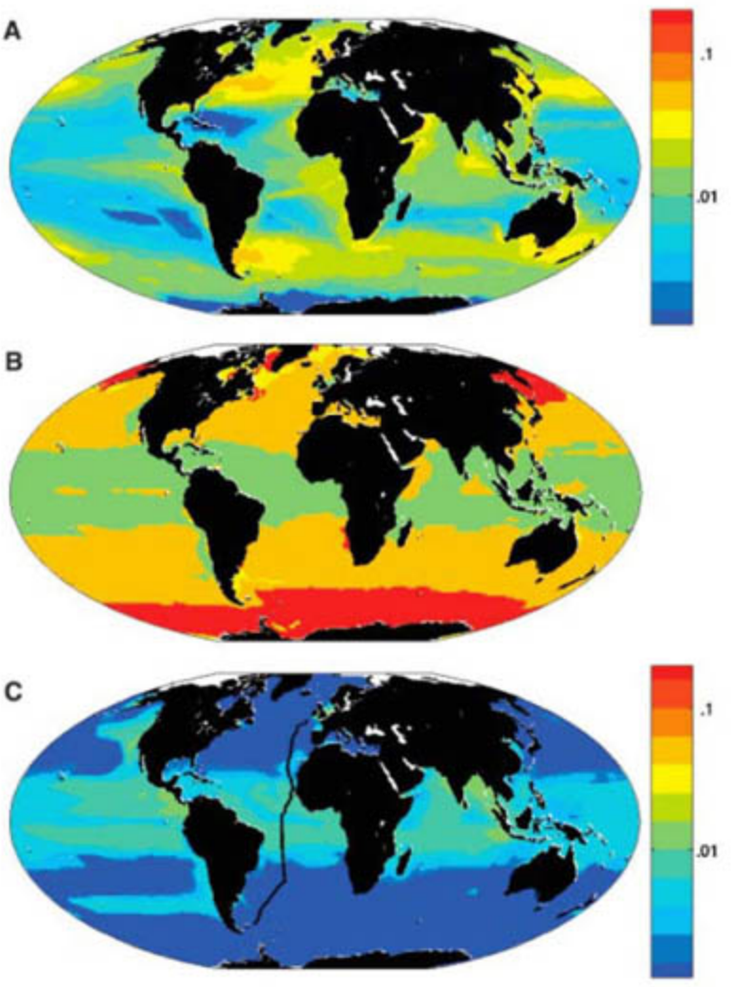

Fig. 1. Annual mean biomass and biogeography from single integration. (**A**) Total phytoplankton biomass (μM P, 0 to 50 m average). (**B**) Emergent biogeography: Modeled photo-autotrophs were categorized into four functional groups; color coding is according to group locally dominating annual mean biomass. Green, analogs of *Prochlorococcus*; orange, other small photo-autotrophs; red, diatoms; and yellow, other large phytoplankton. (**C**) Total biomass of *Prochlorococcus* analogs (μM P, 0 to 50 m average). Black line indicates the track of AMT13.

[1]Department of Earth, Atmospheric and Planetary Sciences, Massachusetts Institute of Technology, 54-1514 MIT, Cambridge, MA 02139, USA. [2]Department of Oceanography, University of Hawaii, 1000 Pope Road, Honolulu, HI 96822, USA. [3]Departments of Civil and Environmental Engineering and Biology, Massachusetts Institute of Technology, 48-419 MIT, Cambridge, MA 02139, USA

*To whom correspondence should be addressed. E-mail: mick@mit.edu

composite of several types, according to aspects of their physiology: (i) diatom analogs—large phytoplankton that require silica, (ii) other large eukaryotes, (iii) *Prochlorococcus* analogs—small phytoplankton that cannot assimilate nitrate, and (iv) other small photo-autotrophs. The large-scale biogeography of the emergent phytoplankton community was plausible with respect to observations (Fig. 1B) and consistent among the 10 ensemble members. The model successfully captured the domination of annual biomass by large phytoplankton in subpolar upwelling regions, where both light and macronutrients are seasonally plentiful. The subtropical oceans were dominated by small phytoplankton functional types (*14*). Large areas of the tropics and subtropics were dominated by several *Prochlorococcus* analogs (Fig. 1C), also in accord with observations (*15*, *16*). Along the cruise track of Atlantic Meridional Transect 13 (AMT13), total *Prochlorococcus* abundance (the sum of all *Prochlorococcus* analogs) qualitatively and quantitatively reflected the major features of the observed distribution with highest abundances in the most oligotrophic (nutrient-depleted) waters (*15*, *17*) (Fig. 2, A to D).

Real-world *Prochlorococcus* exhibit genetic diversity, which leads to differences in light and temperature sensitivities (*17*–*20*), as well as nitrogen assimilation abilities (*21*). The strains, or ecotypes, of *Prochlorococcus* exhibit distinct patterns of abundance along ocean gradients (*15*, *17*), and observations on AMT13 (*17*) (Fig. 2, E, G, I, and K) provide an ideal test for the stochastic modeling strategy: Do the emergent model analogs of *Prochlorococcus* reflect the geographic distributions, relative abundances, and physiological properties of their real-world counterparts?

Of the *Prochlorococcus* analogs initialized in each model solution, between three and six variants persisted with significant abundances (fig. S4). We grouped the analogs by defining three "model ecotypes" based only on distinct geographic habitats, without regard to physiology, which had a qualitative resemblance to the observed distributions of ecotypes along AMT13. In any ensemble member, more than one emergent *Prochlorococcus* analog may fall into a particular model-ecotype classification, and some were ambiguous. Model ecotype *m-e1* (Fig. 2F) was defined to include emergent analogs with significant biomass in the upper 25 m along the transect between 15°N and 15°S, qualitatively corresponding to the habitat of real-world ecotype eMIT9312 (Fig. 2E). Model ecotype *m-e2* (Fig. 2H) included analogs that had significant biomass in surface waters polewards of 15° but low biomass within 15° of the equator, broadly reflecting eMED4 (Fig. 2G). Finally, model ecotype *m-e3* (Fig. 2J) was defined to include analogs that had a subsurface maximum biomass, in common with eMIT9313 and eNATL2A (Fig. 2, I and K). The observed widespread distribution of deep maxima with low abundance associated with eMIT9313 and eNATL2A was not clearly reflected in the model analogs. This might be explained by the tendency toward unrealistically complete competitive exclusion typical in ecosystem models (*22*, *23*), precluding persistent populations at low abundance. There is a deep, high biomass layer in the model made up of other, nitrate-consuming, small phytoplankton. This may partially reflect a contribution from nitrate-utilizing *Prochlorococcus*, which have recently been inferred from ocean observations (*24*), but which have not yet been seen in culture.

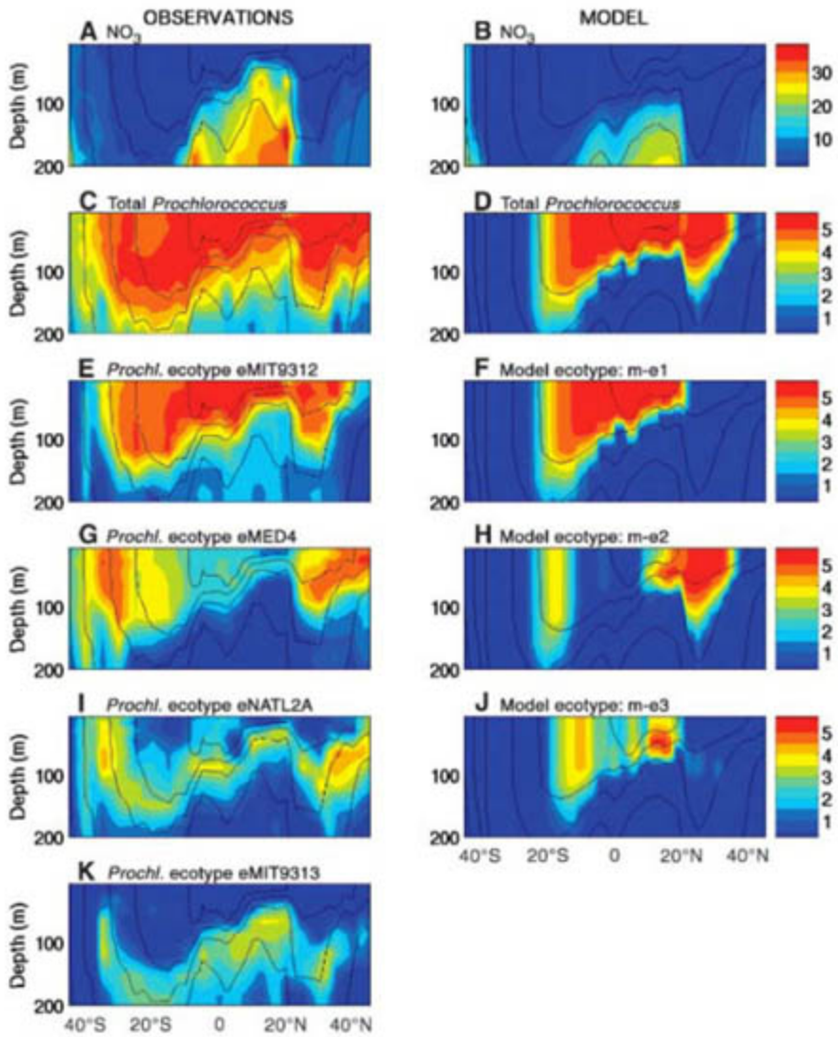

Fig. 2. Observed and modeled properties along the AMT13 cruise track. Left column shows observations (*17*), right column shows results from a single model integration. (**A** and **B**) Nitrate (μmol kg^{-1}); (**C** and **D**) total *Prochlorococcus* abundance [log (cells ml^{-1})]. (**E**, **G**, **I**, and **K**) Distributions of the four most abundant *Prochlorococcus* ecotypes [log (cells ml^{-1})] ranked vertically. (**F**, **H**, and **J**) The three emergent model ecotypes ranked vertically by abundance. Model *Prochlorococcus* biomass was converted to cell density assuming a quota of 1 fg P $cell^{-1}$ (*27*). Black lines indicate isotherms.

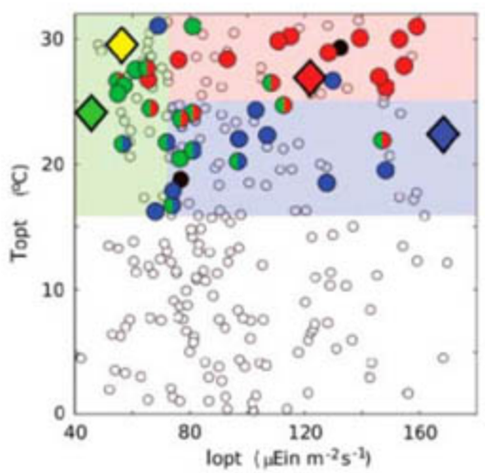

Fig. 3. Optimum temperature and light intensity for growth, T_{opt} and I_{opt}, of all initialized *Prochlorococcus* analogs (all circles) from the ensemble of 10 model integrations. Large circles indicate the analogs that exceeded a total biomass of 10^6 mol P along AMT13 in the 10th year. Colors indicate classification into model ecotypes (see main text): Red circles, *m-e1*; blue circles, *m-e2*; green circles, *m-e3*. Mixed-color and solid black circles denote ambiguity in model-ecotype classification. Bold diamonds indicate real-world *Prochlorococcus* ecotypes (red, eMIT9312; blue, eMED4; green, eNATL2A; and yellow, eMIT9313).

Within each ensemble member, emergent model ecotypes typically followed the abundance ranking of their geographically identified real-world counterparts (Fig. 2 and fig. S4): Model ecotypes *m-e1* and *m-e2* ranked first and second (compare these with eMIT9312 and eMED4, respectively), with *m-e3* consistently at lower abundances (compare this with ecotypes eNATL2A and eMIT9313).

There is a simultaneous correspondence between the physiological characteristics of emergent, modeled ecotypes and cultured representatives of the wild population. Each cultured strain of *Prochlorococcus* and the emergent model ecotypes from all 10 ensemble members were characterized by an optimal temperature (T_{opt}) and photon flux (I_{opt}) for growth, the temperature or light intensity at which growth rates are greatest if all other limitations are set aside (fig. S1). Potentially viable *Prochlorococcus* analogs were seeded in the model over wide ranges of optimal temperature and photon fluxes (all circles, Fig. 3), but those that maintained significant abundances along the AMT transect (solid large circles, Fig. 3) were all characterized by $T_{opt} > 15$°C. This is consistent with the observations of *Prochlorococcus* in warmer waters and with the warm T_{opt} of cultured strains (*17*). Our model indicates that the oligotrophic conditions confined *Prochlorococcus* analogs to warmer waters and selected for warm T_{opt}, an emergent "adaptation" driven by other environmental factors. In the cooler waters of the model, nutrients are typically abundant, and so larger phytoplankton, with higher intrinsic maximum growth rates, have an advantage. In the highly oligotrophic (typically warmer) regions, the *Prochlorococcus* analogs' lower half-saturation (consistent with their very small size) is advantageous.

Across the ensemble of 10 integrations, the geographically defined model ecotypes were clustered in optimal temperature and light parameter space (Fig. 3): Model ecotype *m-e1* (red circles) generally occupied the warmest area of parameter space over a broad, upper range of optimal photon fluxes; *m-e2* (blue circles) generally had a lower T_{opt} but a similar range of I_{opt}. This is consistent with their surface-oriented habitats and latitudinal (or temperature) separation. In contrast, *m-e3* (green circles) occupied a wider range of T_{opt} but only in the region of lowest I_{opt}, consistent with its expression of subsurface maxima. Although there were exceptions, the clustering of geographically defined model ecotypes in physiological parameter space indicated that robust ecological controls were operating across the 10 integrations. The physiological characteristics (T_{opt}, I_{opt}) of real-world ecotypes (colored diamonds, Fig. 3) are notably consistent with the grouping of their model counterparts. This correspondence was not imposed, but emerged as a feature of the model solution.

Significantly, there was simultaneous consistency between the geographical habitat, rank abundance, and physiological specialization of the emergent *Prochlorococcus* model ecotypes and their real-world counterparts. These parallels indicate that the stochastic, self-organizing representation of marine ecosystems reflects real-world processes and is suitable for application in ecological and biogeochemical studies. This approach circumvents some of the obstacles facing most current ocean ecosystem models, such as the a priori imposition of low diversity, the prescription of dominant functional types, and the difficulty of specifying the physiological rate coefficients that define them. This function-based approach can naturally evolve to exploit the growing body of genomic and metagenomic data mapping the oceans in terms of genes and their encoded physiological functionality (*25*, *26*). Finally, because the ecosystem structure and function are, by design, emergent and not tightly prescribed, this modeling approach is ideally suited for studies of the relations between marine ecosystems, evolution, biogeochemical cycles, and past and future climate change.

References and Notes

1. D. Tilman, *Ecology* **58**, 338 (1977).
2. R. Margalef, *Perspectives in Ecological Theory* (Univ. of Chicago Press, Chicago, 1968).
3. C. Pedrós-Alió, *Trends Microbiol.* **14**, 257 (2006).
4. S. L. Pimm, J. H. Lawton, *Nature* **268**, 329 (1977).
5. A. Kleidon, H. A. Mooney, *Glob. Change Biol.* **6**, 507 (2000).
6. J. K. Moore, S. Doney, J. Kleyplas, D. Glover, I. Fung, *Deep-Sea Res. II* **49**, 403 (2001).
7. W. W. Gregg, P. Ginoux, P. S. Schopf, N. W. Casey, *Deep-Sea Res. II* **50**, 3143 (2003).
8. E. Litchman, C. A. Klausmeier, J. R. Miller, O. M. Schofield, P. G. Falkowski, *Biogeosciences* **3**, 585 (2006).
9. C. LeQuere *et al.*, *Glob. Change Biol.* **11**, 2016 (2006).
10. T. R. Anderson, *J. Plankton Res.* **27**, 1073 (2005).
11. R. R. Hood *et al.*, *Deep-Sea Res. II* **53**, 459 (2006).
12. P. A. Thompson *et al.*, *Limnol. Oceanogr.* **34**, 1014 (1989).
13. C. Wunsch, P. Heimbach, *Physica D* 10.1016/j.physd.2006.09.040 (2006).
14. Y. Dandonneau, Y. Montel, J. Blanchot, J. Giraudeau, J. Neveux, *Deep-Sea Res. I* **53**, 689 (2006).
15. M. V. Zubkov, M. A. Sleigh, P. H. Burkill, R. J. G. Leakey, *Prog. Oceanogr.* **45**, 369 (2000).
16. H. A. Bouman *et al.*, *Science* **312**, 918 (2006).
17. Z. I. Johnson *et al.*, *Science* **311**, 1737 (2006).
18. L. R. Moore, G. Rocap, S. W. Chisholm, *Nature* **393**, 464 (1998).
19. G. Rocap *et al.*, *Nature* **424**, 1042 (2003).
20. L. R. Moore, S. W. Chisholm, *Limnol. Oceanogr.* **44**, 628 (1999).
21. L. R. Moore, A. F. Post, G. Rocap, S. W. Chisholm, *Limnol. Oceanogr.* **47**, 989 (2002).
22. G. E. Hutchinson, *Am. Nat.* **95**, 137 (1961).
23. R. A. Armstrong, R. McGehee, *Am. Nat.* **115**, 151 (1980).
24. M. W. Lomas, F. Lipschultz, *Limnol. Oceanogr.* **51**, 2453 (2006).
25. J. C. Venter *et al.*, *Science* **304**, 66 (2004).
26. E. F. DeLong *et al.*, *Science* **311**, 496 (2006).
27. S. Bertilsson, O. Berglund, D. M. Karl, S. W. Chisholm, *Limnol. Oceanogr.* **48**, 1721 (2003).

28. Thanks to J. Marshall, R. Williams, P. Falkowski, J. Cullen, and J. Bragg for inspiration and encouragement. Thanks also to M. Coleman, R. Hood, and three anonymous reviewers for stimulating comments on the manuscript; to C. Hill for computing guidance; and to P. Heimbach, C. Wunsch, and the ECCO group for ocean circulation state estimates. We are grateful for funding from the PARADIGM consortium of the National Ocean Partnership Program, NSF (M.J.F., S.D.), NSF, DOE (S.W.C.), and the Gordon and Betty Moore Foundation (S.W.C., M.J.F.). M.J.F. is also grateful for the MIT Global Habitat Longevity Award. We acknowledge the Atlantic Meridional Transect consortium (NER/O/S/2001/00680), which enabled the biogeographical observations first published in (*17*) (AMT contribution no. 107).

Supporting Online Material

www.sciencemag.org/cgi/content/full/315/5820/1843/DC1
Materials and Methods
SOM Text
Figs. S1 to S4
Table S1
References and Notes

7 December 2006; accepted 5 March 2007
10.1126/science.1138544

Cascading Effects of the Loss of Apex Predatory Sharks from a Coastal Ocean

Ransom A. Myers,[1] Julia K. Baum,[1]* Travis D. Shepherd,[1] Sean P. Powers,[2] Charles H. Peterson[3]*

Impacts of chronic overfishing are evident in population depletions worldwide, yet indirect ecosystem effects induced by predator removal from oceanic food webs remain unpredictable. As abundances of all 11 great sharks that consume other elasmobranchs (rays, skates, and small sharks) fell over the past 35 years, 12 of 14 of these prey species increased in coastal northwest Atlantic ecosystems. Effects of this community restructuring have cascaded downward from the cownose ray, whose enhanced predation on its bay scallop prey was sufficient to terminate a century-long scallop fishery. Analogous top-down effects may be a predictable consequence of eliminating entire functional groups of predators.

Ecological impacts of eliminating top predators can be far-reaching (*1*) and include release of mesopredator prey populations from predatory control (*2*) and induction of subsequent cascades of indirect trophic interactions (*3*–*5*). In the oceans, fishing has dispropor-

tionately reduced abundances of apex predators (*6*, *7*), eliciting concern about their conservation and the indirect effects that might ensue from their removal. Despite a rich ecological literature on trophic cascades, consequences of removing oceanic apex predators remain uncertain (*8*–*11*). Although some have argued that in complex marine food webs with many interacting species top-down effects may attenuate (*10*, *11*), fundamental constraints on studying oceanic food webs and apex predators may alternatively hinder detection of such effects. We met this challenge by using a unique compilation of time series data and predator exclusion experiments to investigate ecosystem consequences of functionally eliminating apex predatory sharks.

Exploitation of large (>2 m) sharks has intensified worldwide in recent decades, driven by an upsurge in demand for shark fins and meat (*12*) and in bycatch in many fisheries. Data to assess direct impacts of exploitation on the great sharks are limited but consistently indicate that they have been driven to low levels (*12*–*14*). Whether functional elimination of great sharks also induces indirect ecosystem effects, however, is an open question (*14*).

We hypothesized that weakened top-down control by all elasmobranch-consuming sharks could increase abundances of their elasmobranch prey (rays, skates, and small sharks) and that the enhanced predation by these mesopredators might cascade to lower trophic levels. Because mesopredatory elasmobranchs are relatively large, even as juveniles, and are thus consumed almost exclusively by great sharks (*15*), we inferred that these prey would be the most likely affected. Moreover, interannual variability in elasmobranch populations is minimal because of their low reproductive rates, such that changes effected by predator removal should be detectable in time series data. We tested these hypotheses for 1970–2005 on the United States' eastern seaboard between Cape Cod, Massachusetts (41.5°N) and Cape Canaveral, Florida (28°N).

For each elasmobranch, we modeled population trends in each of several data sets and also in a meta-analysis to yield synthetic estimates of rates of change (*15*). We first assembled all available species-specific data from scientific research surveys that began before 1990 and used standardized methodology. Seventeen surveys, which together cover the eastern U.S. coast (fig. S1), met these criteria (tables S2 and S3; mean time span = 28 years). Trends in relative abundance of each elasmobranch were estimated by fitting generalized linear models (GLMs, table S4) to each survey in which the species appeared in at least 3 years. Because not all great sharks were sampled in surveys and because the U.S. pelagic longline fishery covers a much greater proportion of the sharks' northwest Atlantic ranges, trends for these species also were estimated from this fishery's observer and logbook data [by fitting generalized linear mixed models and GLMs, respectively (*15*)].

The eastern seaboard's longest continuous shark-targeted survey (UNC), conducted annually since 1972 off North Carolina, demonstrates sufficiently large declines in great sharks to imply their likely functional elimination. Declines in seven species range from 87% for sandbar sharks (*Carcharhinus plumbeus*); 93% for blacktip sharks (*C. limbatus*); up to 97% for tiger sharks (*Galeocerdo cuvier*); 98% for scalloped hammerheads (*Sphyrna lewini*); and 99% or more for bull (*C. leucas*), dusky (*C. obscurus*), and smooth hammerhead (*S. zygaena*) sharks (Fig. 1 and table S5). Because this survey is

[1]Department of Biology, Dalhousie University, 1355 Oxford Street, Halifax, NS B3H 4J1, Canada. [2]Department of Marine Sciences, University of South Alabama, and Dauphin Island Sea Lab, 101 Bienville Boulevard, Dauphin Island, AL 36528, USA. [3]Institute of Marine Sciences, University of North Carolina (UNC) at Chapel Hill, Morehead City, NC 28557, USA.

*To whom correspondence should be addressed. E-mail: baum@mscs.dal.ca (J.K.B.); cpeters@email.unc.edu (C.H.P.)

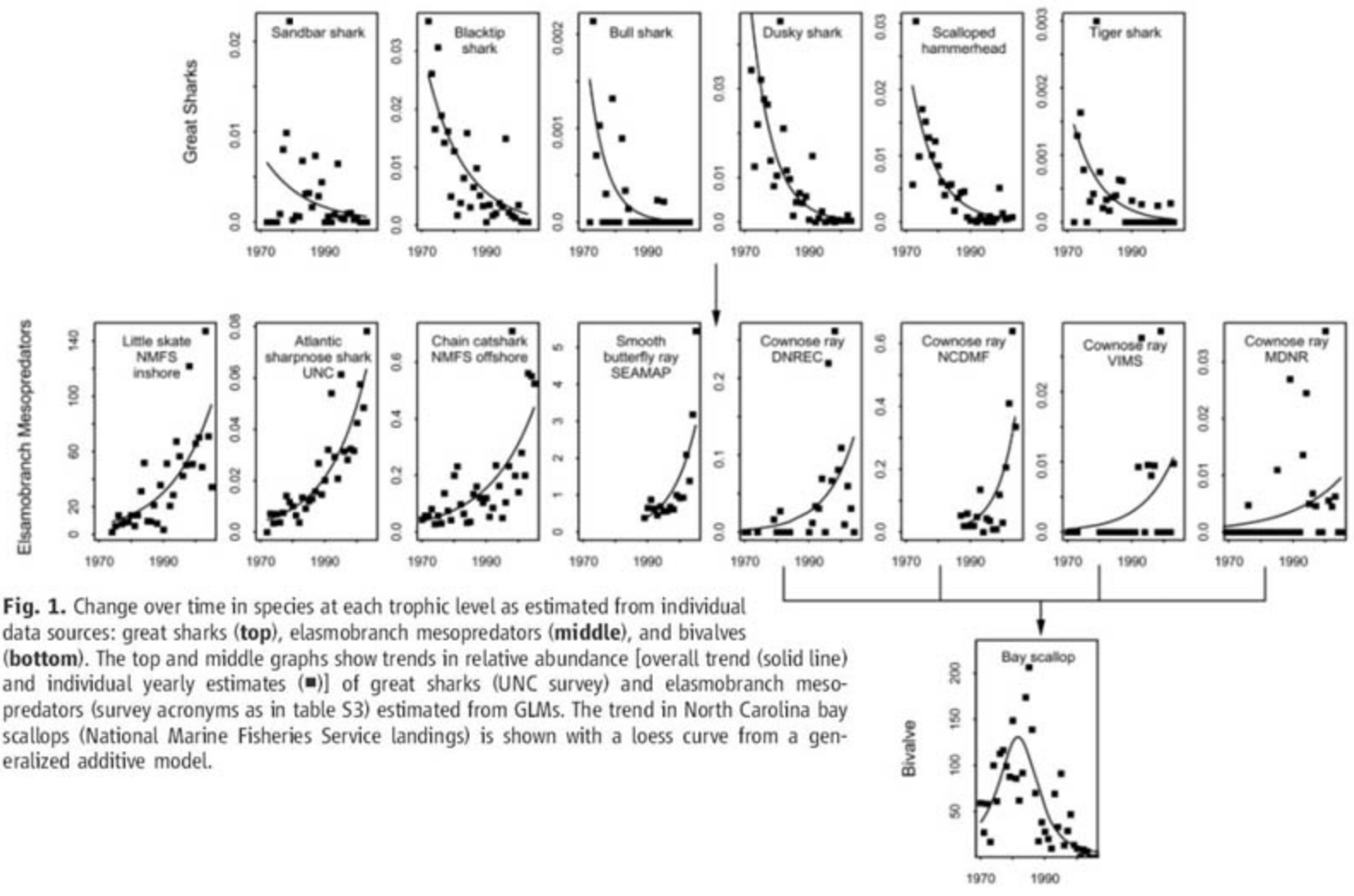

Fig. 1. Change over time in species at each trophic level as estimated from individual data sources: great sharks (**top**), elasmobranch mesopredators (**middle**), and bivalves (**bottom**). The top and middle graphs show trends in relative abundance [overall trend (solid line) and individual yearly estimates (■)] of great sharks (UNC survey) and elasmobranch mesopredators (survey acronyms as in table S3) estimated from GLMs. The trend in North Carolina bay scallops (National Marine Fisheries Service landings) is shown with a loess curve from a generalized additive model.

situated where it intercepts sharks on their seasonal migrations, these trends in abundance may be indicative of coastwide population changes. The UNC survey also showed the loss of the largest individuals, with declines in mean lengths of blacktip, bull, dusky, sandbar, and tiger sharks of 17 to 47% (fig. S3), suggesting that overexploitation has left few mature individuals in these populations. The remaining four elasmobranch-consuming great sharks were caught too rarely to detect trends from this survey. Two of those, great white (*Carcharodon carcharias*) and sand tiger (*Carcharias taurus*) sharks, were each caught only once and early in the UNC survey (in 1974 and 1978, respectively). The only survey that has caught enough sand tigers to note a trend targets sharks in Chesapeake Bay and suggests a decline of over 99% between 1974 and 2004 (*15*, *16*).

Consistent with the UNC survey, all but one of the other six significant survey trends indicate decreasing great shark abundances (table S5). The only significant increase is for juvenile hammerheads from a single survey and consequently may reflect recently increased survival after losses of their only predators, larger apex predatory sharks. Accordingly, meta-analytic results portray a consistent pattern of declines in great sharks (Fig. 2A).

Fisheries data from the past 2 decades help confirm losses of elasmobranch-consuming great sharks (Fig. 2A). Logbook data show declines between 1986 and 2000 ranging from 40% in makos [predominantly shortfin mako (*Isurus oxyrinchus*)] to 89% in hammerheads [scalloped, great (*S. mokarran*), and smooth] (*13*) (table S5). Trend estimates from observer data collected between 1992 and 2005 differ from logbook data for tiger sharks (after a decline, this species may have recently increased) but are concordant for all other species: Makos declined moderately (38%), whereas large coastals (genus *Carcharhinus*, including dusky, sandbar, blacktip, and bull) and hammerheads declined by 67% and 76%, respectively (table S5).

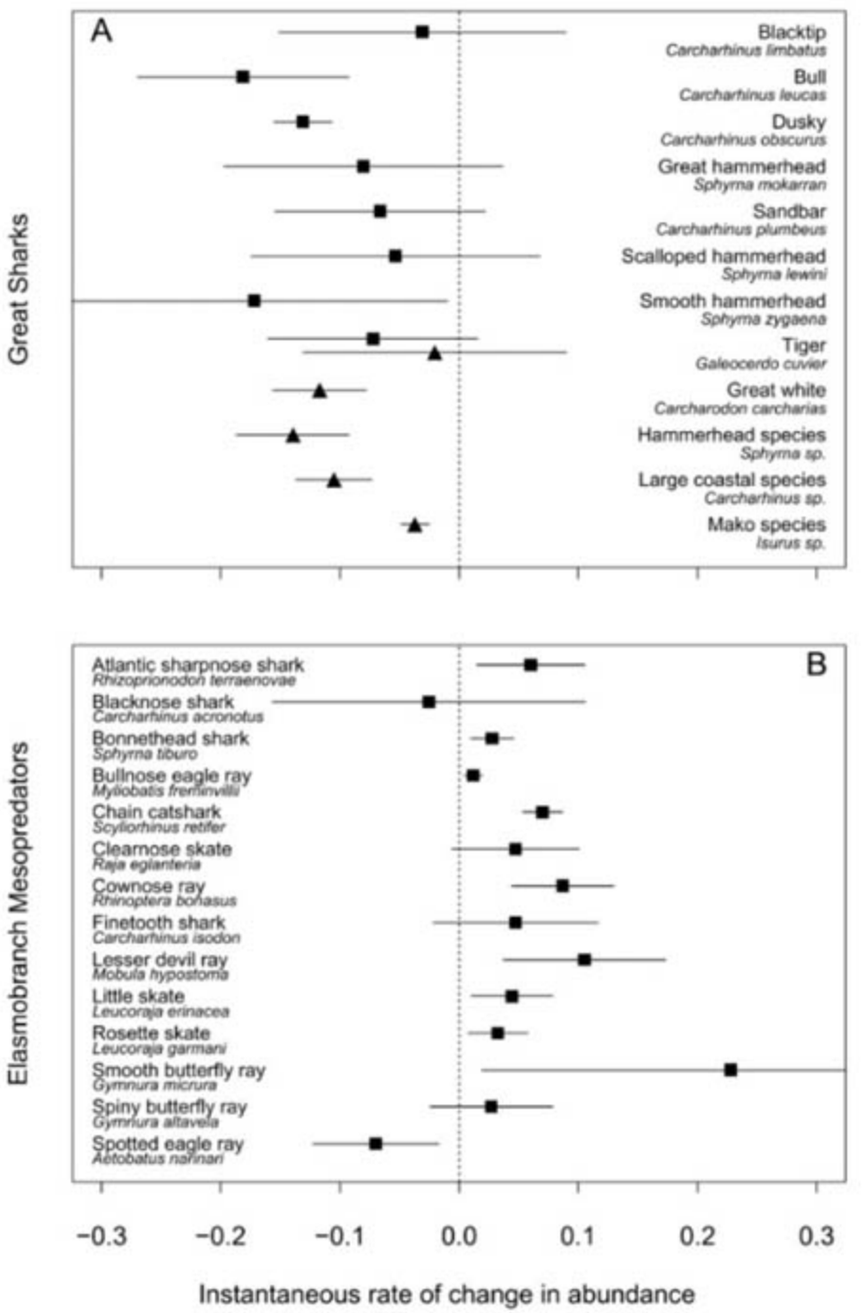

Fig. 2. Instantaneous rates of change in relative abundance (±95% confidence intervals) for (**A**) great sharks and (**B**) elasmobranch mesopredators, as estimated by random-effects meta-analyses of research survey (■) and fisheries (▲) data.

Concurrent with reductions in great sharks, their mesopredatory elasmobranch prey have increased along the eastern seaboard. This group of 14 rays, skates, and small sharks is taxonomically diverse (seven families) and includes demersal and pelagic species from estuaries and the inshore coast to the continental shelf and slope. Individual surveys indicate that little skate (*Leucoraja erinacea*), Atlantic sharpnose shark (*Rhizoprionodon terraenovae*), chain catshark (*Scyliorhinus retifer*), and smooth butterfly ray (*Gymnura altavela*) populations may have each increased by about an order of magnitude (Fig. 1). Overall, meta-analyses of research survey data reveal increases over the past 16 to 35 years for 12 of the species, with estimated mean instantaneous rates of increase ranging from 0.012 for bullnose eagle ray (*Myliobatis freminvillii*) to 0.228 for smooth butterfly ray (Fig. 2B).

Most conspicuous (*17*) among the increasing mesopredators is the cownose ray (*Rhinoptera bonasus*). Six of seven surveys covering the U.S. Atlantic population's range (southeast Florida to Raritan Bay, New Jersey, with recent expansion to Long Island, New York) show significant increases (Fig. 1 and table S5). Together, these rates of change (mean = 0.087, 95% confidence interval 0.021 to 0.127) (Fig. 2B) indicate an order-of-magnitude increase in cownose rays coastwide since the mid-1970s and, when combined with earlier population estimates from aerial surveys in Chesapeake Bay (*18*), suggest that there may now be over 40 million rays in the population. When considered with its known late maturity and low fecundity, this high population growth rate would make the cownose ray anomalous among fishes in its combination of life-history traits (*15*). Only if its natural mortality rate were substantially greater than at present would the life history conform, implying that higher predation by great sharks prevailed in the past and possible reduction in bycatch is insufficient to explain the ascent of this ray.

Collectively, the hyperabundant cownose ray population consumes a large quantity of bivalves, implying a high potential for trophic cascades. Cownose rays migrate southward in autumn from northerly estuaries to overwinter-

ing grounds on the Florida shelf (*19*), often entering bays and sounds en route. Their diet consists largely of bay scallops (*Argopecten irradians*), soft-shell clams (*Mya arenaria*), hard clams (*Mercenaria mercenaria*), oysters (*Crassostrea virginica*), and several smaller, noncommercial bivalves (*18*, *20*). Annual bivalve demand within the Chesapeake Bay, based on our abundance estimate, individual daily consumption rates of ~210 g shell-free wet weight (*15*), and 100-day occupancy each year, may approach 840,000 metric tons. In comparison, the 2003 commercial bivalve harvest in Virginia and Maryland totaled only 300 metric tons, substantially lower than historic landings (*15*).

A second link in an apparent trophic cascade has emerged over the past 2 decades as the cownose ray population grew coastwide (Figs. 1 and 3). Field sampling in 1983 and 1984 before and after ray presence during late-summer migration showed no impacts of ray predation on bay scallops (Fig. 3A) (*21*). Analogous recent sampling, confirmed by controlled ray-exclusion experiments using stockades, demonstrates that since 1996 migrating cownose rays have caused almost complete scallop mortality by early fall (Fig. 3A) (*22*) at every site with initial adult scallop densities above a threshold for intensive ray foraging (~2 m^{-2}, Fig. 3, B and C). Bay scallop abundance declined much less inside cownose ray exclosures than on unprotected grounds (Fig. 3A) and, in the absence of scallop emigration, numbers inside stockades would probably have remained nearly constant (*22*). Unlike the fishery harvest, which occurs after, ray predation occurs before spawning of this annual species (*23*). By 2004, ray predation had terminated North Carolina's century-old bay scallop fishery because too few scallops survived into fall to sustain fishing and a consequent Allee effect (apparently induced at adult densities below ~1 to 2 m^{-2}) limited reproductive success (*23*). The fishery has remained closed through 2007 (Fig. 1) because of low recruitment and continued ray predation on any high-density patch of scallops. Having depleted the more readily targeted epibiotic bay scallops, it is reasonable to expect future expansion of cownose ray foraging on infaunal bivalves, with associated uprooting of seagrass and thus loss of nursery habitat (*20*, *24*).

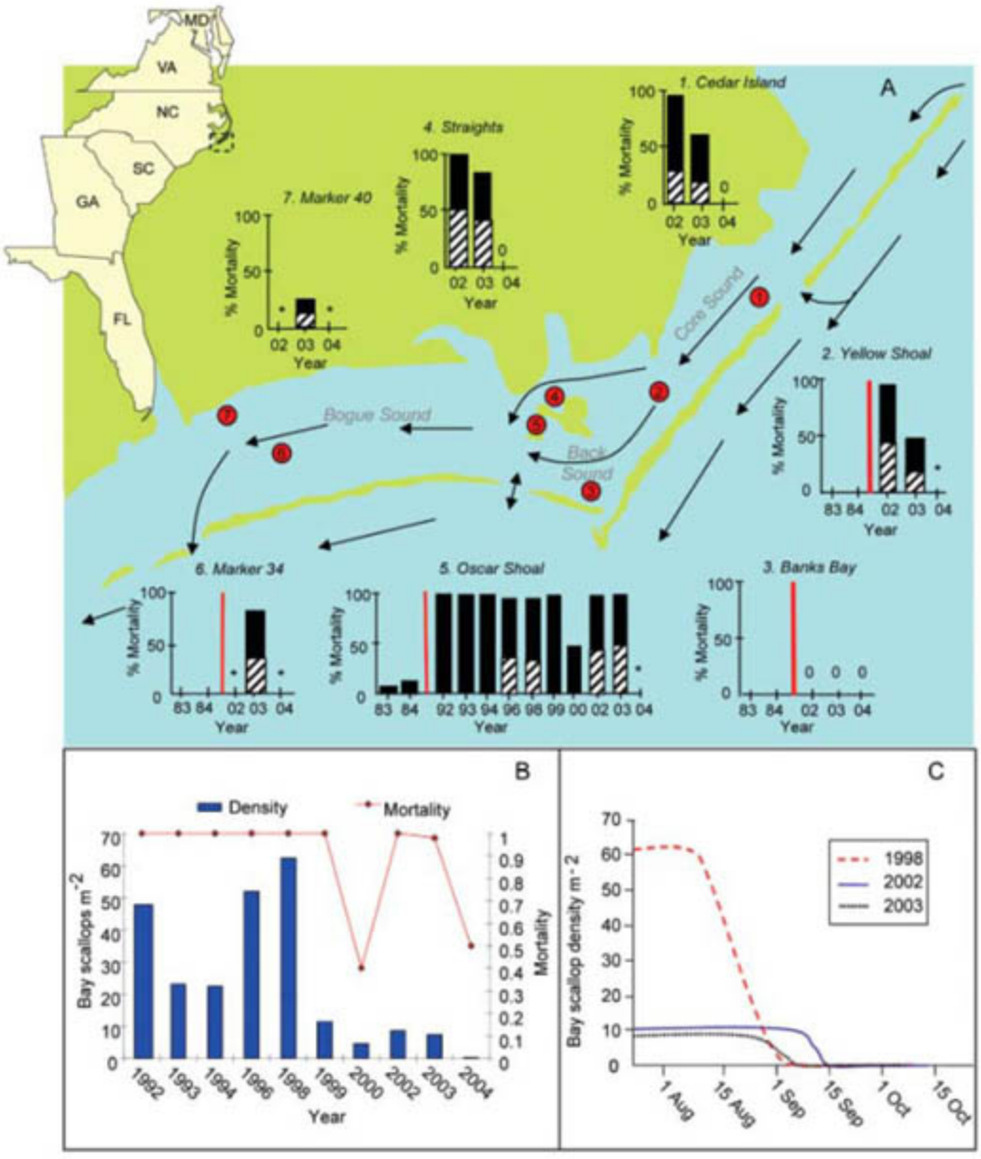

Fig. 3. (**A**) Map of southeastern United States indicating the study location (inset) and North Carolina bay scallop monitoring sites. Total mortality (black bars) compares August (pre–cownose ray migration) to late September and October (postmigration) densities. Low scallop densities before ray migration are indicated by asterisks (<1 to 2 m^{-2}) or zeroes (0 m^{-2}). Hatched bars represent mortality within experimental stockades that exclude rays (performed in a subset of years). Scallops were free to emigrate from stockades. Arrows denote direction of ray migration. (**B**) Mean scallop density measured in midsummer and mortality from early summer to early fall at Oscar Shoal for 10 years. (**C**) Scallop density trends at Oscar Shoal, based on 12 weekly surveys in 1998 and 8 in 2002 and 2003.

Increased predation by cownose rays also may now inhibit recovery of hard clams, soft-shell clams, and oysters (*17*), compounding the effects of overexploitation, disease, habitat destruction, and pollution, which have depressed these species (*7*). Landings data for these bivalves and bay scallops from within the cownose ray's range show them falling without substantial recovery (fig. S2) as the rays increased, despite active shellfish enhancement and habitat restoration. In contrast, areas beyond the ray's northernmost limit show examples of stable or increasing bivalve landings (fig. S2).

Analogous elasmobranch community inversions and trophic cascades are probably occurring in other coastal oceans. Studies in the northeast Atlantic Ocean have shown increasing abundances of several mesopredatory elasmobranchs despite substantial exploitation (*25*, *26*). In Japan's Ariake Sound in the northwest Pacific Ocean, where exploitation of apex predatory sharks is probably intense, wild stocks and cultured populations of multiple shellfish species are now decimated annually by expanding numbers of another elasmobranch mesopredator, the longheaded eagle ray (*Aetobatus flagellum*) (*27*). Many other prey depletions may be going unrecognized because little monitoring and research exists for noncommercial marine species.

Our study provides evidence for an oceanic ecosystem transformation that is most parsimoniously explained by the functional elimination of apex predators, the great sharks, instead of assuming numerous coincidental increases in their mesopredatory prey. Consequences of this region-wide proliferation of rays, skates, and smaller sharks have cascaded down the food web through cownose rays to bay scallops and possibly other bivalves. This cascade potentially could extend to seagrass habitat, exacerbating stresses on already highly degraded coastal

benthic systems. Thus, like the classic killer whale–sea otter–urchin–kelp trophic cascade (*5*), eliminating great sharks carries risks of broader ecosystem degradation. Prevailing theory suggests that community-level trophic cascades arise only in simple food webs lacking functional redundancy (*4*, *10*), but we propose that top-down effects must be widely expected whenever entire functional groups of predators are depressed, as can occur with industrial fisheries. Illuminating the operation of indirect species interactions within marine and other environments brightens the future for development of what is now so widely sought, ecosystem-based management to achieve sustainability of natural living resources.

References and Notes

1. J. E. Duffy, *Oikos* **99**, 201 (2002).
2. K. R. Crooks, M. E. Soulé, *Nature* **400**, 563 (1999).
3. R. T. Paine, *J. Anim. Ecol.* **49**, 667 (1980).
4. M. L. Pace, J. G. Cole, S. R. Carpenter, J. F. Kitchell, *Trends Ecol. Evol.* **14**, 483 (1999).
5. J. A. Estes, M. T. Tinker, T. M. Williams, D. F. Doak, *Science* **282**, 473 (1998).
6. D. Pauly, V. Christensen, J. Dalsgaard, R. Froese, F. Torres Jr., *Science* **279**, 860 (1998).
7. J. B. C. Jackson *et al.*, *Science* **293**, 629 (2001).
8. J. Bascompte, C. J. Melián, E. Sala, *Proc. Natl. Acad. Sci. U.S.A.* **102**, 5443 (2005).
9. K. T. Frank, B. Petrie, J. S. Choi, W. C. Leggett, *Science* **308**, 1621 (2005).
10. D. R. Strong, *Ecology* **73**, 747 (1992).
11. S. Jennings, M. J. Kaiser, *Adv. Mar. Biol.* **34**, 201 (1998).
12. S. L. Fowler *et al.*, Eds., *Sharks, Rays and Chimaeras: The Status of the Chondrichthyan Fishes* (Shark Specialist Group, Species Survival Commission, World Conservation Union, Cambridge, 2005).
13. J. K. Baum *et al.*, *Science* **299**, 389 (2003).
14. J. D. Stevens, R. Bonfil, N. K. Dulvy, P. A. Walker, *ICES J. Mar. Sci.* **57**, 476 (2000).
15. Species information and detailed methods are available on *Science* Online.
16. D. H. Ha, thesis, College of William and Mary, Gloucester Point, VA (2006).
17. D. A. Fahrenthold, *Washington Post*, www.washingtonpost.com/wp-dyn/articles/A29969-2004Aug24.html (25 August 2004).
18. R. A. Blaylock, *Estuaries* **16**, 255 (1993).
19. D. S. Grusha, thesis, College of William and Mary, Gloucester Point, VA (2005).
20. J. W. Smith, J. V. Merriner, *Estuaries* **8**, 305 (1985).
21. C. H. Peterson, H. C. Summerson, S. R. Fegley, R. C. Prescott, *J. Exp. Mar. Biol. Ecol.* **127**, 121 (1989).
22. C. H. Peterson, F. J. Fodrie, H. C. Summerson, S. P. Powers, *Oecologia* **129**, 349 (2001).
23. C. H. Peterson, H. C. Summerson, R. A. Luettich Jr., *Mar. Ecol. Prog. Ser.* **132**, 93 (1996).
24. R. J. Orth, *Chesapeake Sci.* **16**, 205 (1975).
25. N. K. Dulvy, J. D. Metcalfe, J. Glanville, M. G. Pawson, J. D. Reynolds, *Conserv. Biol.* **14**, 283 (2000).
26. S. I. Rogers, J. R. Ellis, *ICES J. Mar. Sci.* **57**, 866 (2000).
27. A. Yamaguchi, I. Kawahara, S. Ito, *Environ. Biol. Fish.* **74**, 229 (2005).

28. We thank J. Boylan, J. Collie, E. Durell, D. Gaskill, J. Hoey, W. Hogarth, D. Kahn, J. Kraeuter, R. Lipcius, M. McDuff, P. Rago, D. Ricard, R. Seitz, D. Simpson, F. Schwartz, J. Smith, G. Ulrich, K. West, and the North Carolina Division of Marine Fisheries (NCDMF) for sharing data. North Carolina biological data were provided at the authors' request by the NCDMF. Analyses of these data and conclusions drawn there from are those of the authors and do not necessarily represent the views of NCDMF. We also thank D. Gaskill for assistance conducting the field research and the UNC Institute of Marine Sciences for providing support to conduct the longline shark survey. V. Garcia, J. Hoenig, H. Lotze, L. Lucifora, A. Sugden, J. Valentine, B. Worm, and the referees provided helpful comments on the manuscript. We acknowledge funding from Pew Institute for Ocean Science, Sloan Census of Marine Life, Natural Sciences and Engineering Research Council of Canada, Killam Trusts, NC Fisheries Resource Grants Program, NC Sea Grant, and NSF.

Supporting Online Material

www.sciencemag.org/cgi/content/full/315/5820/1846/DC1
Materials and Methods
SOM Text
Figs. S1 to S3
Tables S1 to S5

11 December 2006; accepted 5 March 2007
10.1126/science.1138657

Protein Composition of Catalytically Active Human Telomerase from Immortal Cells

Scott B. Cohen,[1] Mark E. Graham,[2] George O. Lovrecz,[3] Nicolai Bache,[4] Phillip J. Robinson,[2] Roger R. Reddel[1]*

Telomerase is a ribonucleoprotein enzyme complex that adds 5′-TTAGGG-3′ repeats onto the ends of human chromosomes, providing a telomere maintenance mechanism for ~90% of human cancers. We have purified human telomerase ~10^8-fold, with the final elution dependent on the enzyme's ability to catalyze nucleotide addition onto a DNA oligonucleotide of telomeric sequence, thereby providing specificity for catalytically active telomerase. Mass spectrometric sequencing of the protein components and molecular size determination indicated an enzyme composition of two molecules each of telomerase reverse transcriptase, telomerase RNA, and dyskerin.

Telomeres, repetitive nucleoprotein structures at the ends of linear chromosomes (*1*), shorten during each cycle of cell division (*2*), providing a counting mechanism to limit the number of times a cell can divide (*3*). Many cancer cells escape limits on proliferation by activating the ribonucleoprotein enzyme telomerase to catalyze the synthesis of telomeric repeats (*4*). The protein component, human telomerase reverse transcriptase (hTERT), contains conserved catalytic reverse transcriptase motifs (*5*, *6*), and the human telomerase RNA component (hTR) (*7*) directs the addition of deoxynucleotide triphosphates (dNTPs) by means of an internal template complementary to the telomeric repeat sequence TTAGGG.

Telomerase has previously been purified only from the ciliate *Euplotes aediculatus* as a complex of TERT, RNA, and associated protein p43 (*8*). At least 32 distinct proteins have been proposed to associate with human telomerase (table S1). Size measurements of human telomerase have indicated a complex larger than expected for a composition of one hTERT (127 kD) and one hTR (153 kD) (*9*, *10*) but smaller than the sum of all proposed protein associations (~2.6 MD). Nonetheless, the precise composition of the active enzyme complex within the cell has remained undefined.

We measured the size of the active human telomerase complex in a panel of immortal cell lines (MCF-7, A2182, HCT-116, TE-85, HT-1080, and HEK-293, derived from cancers of the breast, lung, colon, bone, and connective tissue, and from embryonic kidney cells, respectively). Quantification of telomerase was performed with a direct (non–polymerase chain reaction) primer-extension activity assay (fig. S1). Whole-cell lysates (*11*) from all cell lines exhibited a similar sedimentation profile, with ≥60% of total activity eluting in fractions 9 and 10 (Fig. 1, A to C). Thyroglobulin (669 kD) peaked in fraction 9 (Fig. 1B), indicating that telomerase exists as an enzyme complex of ~650 to 670 kD.

We developed a purification scheme that achieved ~10^8-fold enrichment of active telomerase in three steps (*11*). The first step was immunoaffinity purification with a sheep polyclonal antibody generated against the peptide antigen ARPAEEATSLEGALSGTRH (hTERT amino acids 276 to 294). HEK-293 lysate was incu-

[1]Cancer Research Unit, Children's Medical Research Institute, 214 Hawkesbury Road, Westmead NSW 2145, Australia. [2]Cell Signalling Unit, Children's Medical Research Institute, 214 Hawkesbury Road, Westmead NSW 2145, Australia. [3]Fermentation Lab, Commonwealth Scientific and Industrial Research Organisation, Molecular and Health Technologies, 343 Royal Parade, Parkville VIC 3052, Australia. [4]Department of Biochemistry and Molecular Biology, University of Southern Denmark, Campusvej 55, 5230 Odense M, Denmark.

*To whom correspondence should be addressed. E-mail: rreddel@cmri.usyd.edu.au

bated with antibody, and the antibody-enzyme complex was immobilized onto protein G agarose beads. Excess antigenic peptide was added to the resuspended immunoprecipitate to allow dissociation of the enzyme from immobilized antibody into solution (Fig. 1D, lane 1). Immunopurified telomerase displayed excellent stability (Fig. 1D, lane 2), allowing the purification to be continued at room temperature.

The specificity of the second and third steps is provided by thermodynamic and kinetic properties of the telomerase enzyme. The dissociation rate of the telomeric DNA substrate primer 5′-(TTAGGG)$_3$-3′ from human telomerase is known to be very slow ($t_{1/2} \geq 10$ hours) (*12*). We exploited this stable binding between enzyme and substrate to develop a substrate-directed affinity purification. The synthetic DNA 5′-Biotin-CTAGACCTGTCATCA(TTAGGG)$_3$-3′ was immobilized onto neutravidin beads, providing the affinity reagent.

Immunopurified telomerase from the first step was precleared with unmodified neutravidin beads and 5′-CTAGACCTGTCATCA-3′; loss of telomerase activity was negligible (Fig. 1D, lane 3). The precleared solution was then treated with (TTAGGG)$_3$-modified beads to capture telomerase. This affinity purification consistently proceeded to >90% yield, as evidenced by the low level of telomerase activity remaining in solution (Fig. 1D, lane 4). Activity from the captured enzyme was detected by suspending the beads in assay buffer (dNTPs), resulting in extension of the immobilized DNA substrate (fig. S2).

The stable binding between telomerase and immobilized DNA primer ($t_{1/2} \geq 10$ hours) required that we develop a rapid elution procedure specifically for catalytically active enzyme complexes under mild conditions. We exploited a distinctive relationship between human telomerase and DNA primer: K_d and k_{off} between enzyme and primer change as a function of the nucleotide at the 3′ end (*12*). A primer ending in GGG, such as 5′-(TTAGGG)$_3$-3′, affords the most stable binding interaction; primers ending in TTA display the weakest binding between enzyme and primer, with dissociation occurring in minutes. An active enzyme immobilized onto 5′-(TTAGGG)$_3$-3′, in the presence of only deoxythymidine triphosphate (dTTP) and deoxyadenosine triphosphate (dATP), should catalyze the addition of TTA, thereby transforming a stable enzyme-substrate complex ($t_{1/2} \geq 10$ hours) into a relatively unstable complex ($t_{1/2} <$ 5 min), promoting rapid elution (Fig. 2A).

To demonstrate activity-dependent elution, (TTAGGG)$_3$-modified beads bearing telomerase were divided into two suspensions. Excess free 5′-(TTAGGG)$_3$-3′ was added to trap the enzyme in solution phase after dissociation. One suspension was left as a control to follow dissociation from DNA with GGG at the 3′-end; to the other was added dTTP and dATP. Samples of each suspension were removed over time, and the solution phase was separated from beads to measure the amount of dissociated telomerase (Fig. 2, B and C). The presence of dTTP and dATP promoted a dramatic increase in the rate of enzyme dissociation (control, $k <$ 0.002 min^{-1}; +dTTP/dATP, $k = 0.25 \pm 0.05$ min^{-1}). At 10 min, the selectivity for activity-dependent elution is >50:1 (Fig. 2C). Such strong dependence on dTTP/dATP provides exquisite specificity in the final elution and illustrates an elegant structure-activity relationship of human telomerase: Transformation to a less stable enzyme-substrate complex as nucleotide addition approaches the end of the template facilitates efficient translocation.

For the purification, the (TTAGGG)$_3$ beads bearing telomerase were suspended in buffer containing free (TTAGGG)$_3$ for 1 hour as a further washing step, during which time just 4 to 5% of telomerase had dissociated (Fig. 1D, lane 5). The beads were suspended in buffer containing free (TTAGGG)$_3$ for 10 min; this "control elution," with <1% activity, was collected for mass spectrometry. Finally, the beads were suspended in buffer containing free (TTAGGG)$_3$ and dTTP/dATP, and the product solution was collected after 10 min to provide purified telomerase (Fig. 1D, lane 6).

Purified telomerase was assessed for size and yield. The sedimentation profile of purified telomerase was conserved relative to that of the crude lysate (Fig. 3, A and B). Yield of telomerase was determined by Northern blot analysis against hTR, with gel-purified in vitro transcribed hTR as a quantitation standard (fig. S3). From 50 fmol HEK-293 cells (~100 g), we obtained ~250 to 300 fmol purified telomerase (5 to 6 molecules per cell, ~100 ng). These data were used to determine the cellular abundance of telomerase, factoring in the percent yield of purification, for which an upper limit is estimated at ≤30% [immunopurification, ≤60%;

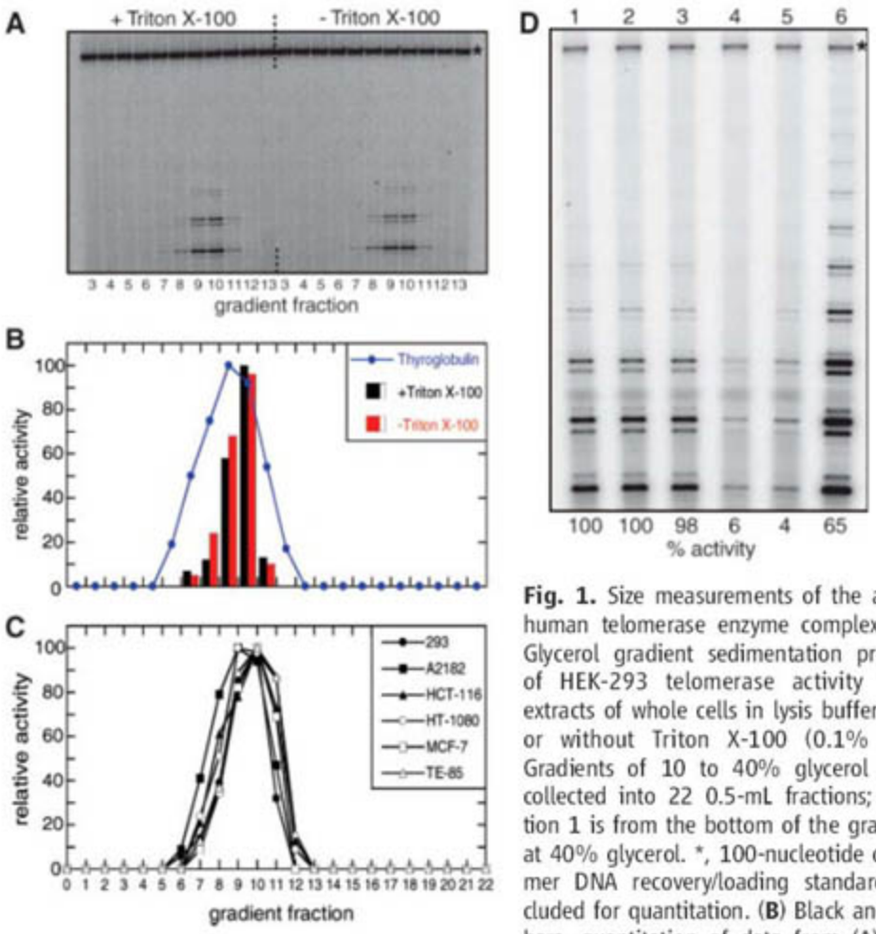

Fig. 1. Size measurements of the active human telomerase enzyme complex. (**A**) Glycerol gradient sedimentation profiles of HEK-293 telomerase activity from extracts of whole cells in lysis buffer with or without Triton X-100 (0.1% v/v). Gradients of 10 to 40% glycerol were collected into 22 0.5-mL fractions; fraction 1 is from the bottom of the gradient at 40% glycerol. *, 100-nucleotide oligomer DNA recovery/loading standard included for quantitation. (**B**) Black and red bars, quantitation of data from (A); the lane with the highest activity is arbitrarily given a value of 100. Blue line, sedimentation profile of thyroglobulin (669 kD). (**C**) Glycerol gradient sedimentation profiles of telomerase activity for all cell lines examined. (**D**) Tracking HEK-293 telomerase activity through the purification. Lane 1, immunoaffinity-purified telomerase (defined as 100%; subsequent yields are quantified relative to lane 1). Lane 2, immunoaffinity-purified telomerase after incubation at room temperature for 5 hours. Lane 3, immunoaffinity-purified telomerase after preclearing with unmodified neutravidin beads. Lane 4, telomerase left in solution after treatment with (TTAGGG)$_3$-modified neutravidin beads. Lane 5, telomerase eluted in 1 hour from (TTAGGG)$_3$ beads in the absence of dTTP/dATP. Lane 6, telomerase eluted in 10 min from (TTAGGG)$_3$ beads in the presence of dTTP/dATP. The volumes of the samples represented in lanes 5 and 6 are reduced by factors of 5 and 10, respectively, relative to those in lanes 1 to 4.

$(TTAGGG)_3$ immobilization, ≤90%; +dNTP elution, ≤60%]. This corresponds to a lower limit of ~20 telomerase molecules per HEK-293 cell. Allowing for error in these analyses, and given the variability of telomerase levels in different cell subpopulations (*13*), we conclude that an average HEK-293 cell has ~20 to 50 molecules of telomerase. The data also indicate a purification factor of ~10^8 (~100 ng telomerase from 100 g cells, adjusted for ≤30% yield) (*11*).

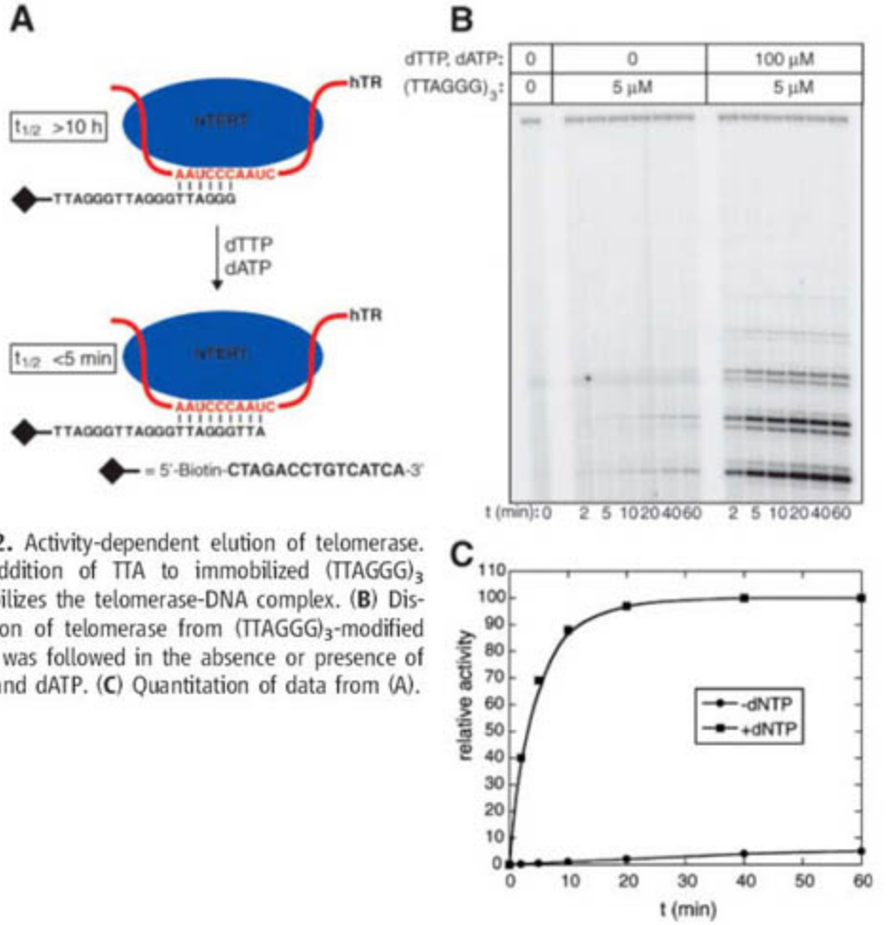

Fig. 2. Activity-dependent elution of telomerase. (**A**) Addition of TTA to immobilized $(TTAGGG)_3$ destabilizes the telomerase-DNA complex. (**B**) Dissociation of telomerase from $(TTAGGG)_3$-modified beads was followed in the absence or presence of dTTP and dATP. (**C**) Quantitation of data from (A).

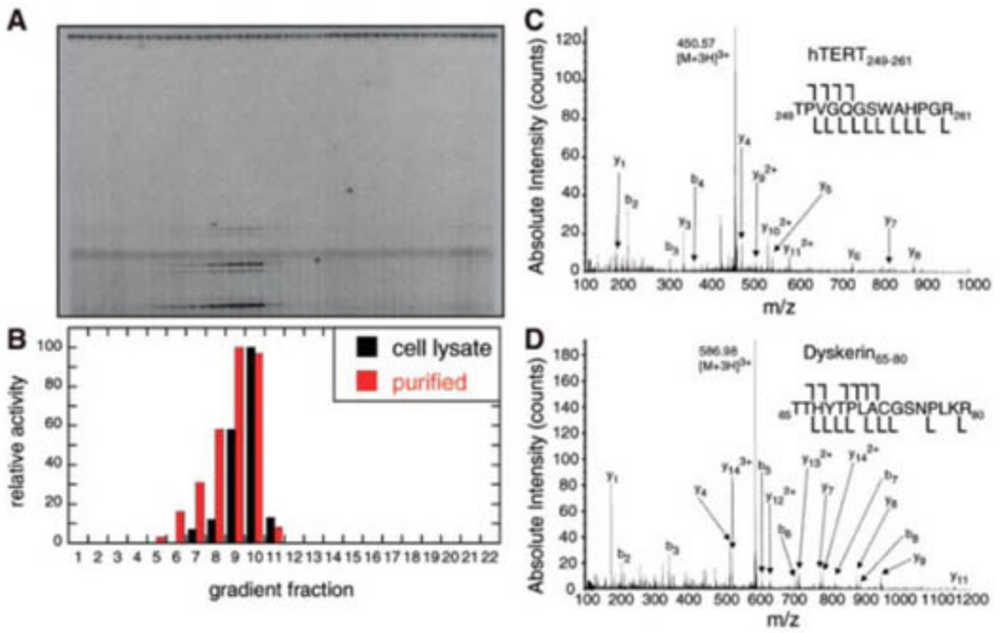

Fig. 3. Characterization of the purified HEK-293 telomerase enzyme complex. (**A**) Glycerol gradient sedimentation profile of telomerase activity from purified HEK-293 telomerase. (**B**) Elution profile of purified enzyme [data from (A)] was compared with that of whole cell lysate (data from Fig. 1B). (**C**) MS/MS spectrum for hTERT amino acids 249 to 261: TPVGQGSWAHPGR. (**D**) MS/MS spectrum for dyskerin amino acids 65 to 80: TTHYTPLACGSNPLKR.

Purified telomerase was digested with trypsin in solution, and the resulting peptides were captured on cation exchange resin at pH 4 to remove buffers, nucleic acid, and detergent (*11*). The peptide products were eluted and analyzed by nano–liquid chromatography–tandem mass spectrometry (nanoLC-MS/MS). Protein identification from peptide sequencing was performed on three independent purifications, each from 100 g HEK-293 cells. The 10-min control elution, containing only $(TTAGGG)_3$ and essentially devoid of telomerase activity, was analyzed in parallel with the dTTP/dATP-dependent elution of telomerase. Comparison of these samples identified proteins dependent on the presence of dTTP/dATP and telomerase activity. In the control sample, typically 6 to 8 proteins were observed at low levels in each run, 5 of which were observed consistently: tubulin, actin, Y-box, heterogeneous nuclear ribonucleoprotein (hnRNP) A1, and hnRNP M. These proteins represent background and result from nonspecific adhesion inherent in protein purification. In the telomerase sample, in addition to the background proteins tubulin and actin, two new proteins were consistently observed: hTERT and dyskerin (Fig. 3, C and D, figs. S4 and S5, and Table 1). Only hTERT and dyskerin were specifically enriched in the active telomerase fraction.

We conclude that the active human telomerase enzyme complex is composed solely of two protein components, hTERT and dyskerin, and the RNA component hTR. Dyskerin is a putative pseudouridine synthase within the class of H/ACA box ribonucleoproteins (*14*). The H/ACA sequence motif is present in hTR (*15*). A relationship between telomere length, telomerase, and dyskerin has been documented in dyskeratosis congenita, a syndrome characterized by reduced proliferative capacity attributed to telomerase deficiency. Mutations in dyskerin resulted in poor telomere maintenance and lower telomerase activity, and the evidence supported an association of dyskerin with telomerase (*16*). It is noteworthy that mutations in hTERT (*17*), hTR (*18*), and dyskerin (*16*), the three components of the active telomerase enzyme complex, are the only known genes whose mutation has been shown to cause dyskeratosis congenita.

The combined mass of hTERT (127 kD), hTR (153 kD), and dyskerin (57 kD) make up about half the observed size (650 to 670 kD). There is considerable evidence from in vitro reconstitution studies that telomerase exists as a dimer (*9*, *19*, *20*). We propose that human telomerase exists as a complex of two molecules each of hTERT, hTR, and dyskerin. It should be emphasized that the purification is specific for catalytically active enzyme complexes and therefore represents a restricted view of the overall biology of telomerase. Other proteins reported

Table 1. hTERT and human dyskerin peptides sequenced by nanoLC-MS/MS (*21*).

hTERT	Dyskerin
$_{202}$AWNHSVR$_{208}$	$_{292}$LLTSHKR$_{297}$
$_{1085}$HRVTYVPLLGSLR$_{1097}$	$_{378}$KWGLGPK$_{384}$
$_{143}$RVGDDVLVHLLAR$_{155}$	$_{400}$HGKPTDSTPATWK$_{412}$
$_{249}$TPVGQGSWAHPGR$_{261}$	$_{144}$SQQSAGKEYVGIVR$_{157}$
$_{552}$RSPGVGCVPAAEHR$_{535}$	$_{65}$TTHYTPLACGSNPLKR$_{80}$
$_{866}$LVDDFLLVTPHLTHAK$_{881}$	$_{394}$QGLLDKHGKPTDSTPATWK$_{412}$
$_{246}$PERTPVGQGSWAHPGR$_{261}$	$_{19}$KSLPEEDVAEIQHAEEFLIKPESK$_{42}$
$_{672}$RPGLLGASVLGLDDIHR$_{688}$	
$_{276}$ARPAEEATSLEGALSGTR$_{293}$	
$_{670}$ARRPGLLGASVLGLDDIHR$_{688}$	
$_{240}$RGAAPEPERTPVGQGSWAHPGR$_{261}$	

to associate with telomerase (table S1) may be involved in its biogenesis, trafficking, recruitment to the telomere, and degradation. However, from the analyses described here, it can be concluded that these proteins are not required for nucleotide addition, nor do they constitute integral components of the catalytically active enzyme complex.

References and Notes

1. R. K. Moyzis *et al.*, *Proc. Natl. Acad. Sci. U.S.A.* **85**, 6622 (1988).
2. C. B. Harley, A. B. Futcher, C. W. Greider, *Nature* **345**, 458 (1990).
3. A. M. Olovnikov, *J. Theor. Biol.* **41**, 181 (1973).
4. C. W. Greider, E. H. Blackburn, *Cell* **43**, 405 (1985).
5. J. Lingner *et al.*, *Science* **276**, 561 (1997).
6. T. M. Nakamura *et al.*, *Science* **277**, 955 (1997).
7. J. Feng *et al.*, *Science* **269**, 1236 (1995).
8. J. Lingner, T. R. Cech, *Proc. Natl. Acad. Sci. U.S.A.* **93**, 10712 (1996).
9. C. Wenz *et al.*, *EMBO J.* **20**, 3526 (2001).
10. G. Schnapp, H. Rodi, W. J. Rettig, A. Schnapp, K. Damm, *Nucleic Acids Res.* **26**, 3311 (1998).
11. Materials and methods are available as supporting material on *Science* Online.
12. G. Wallweber, S. Gryaznov, K. Pongracz, R. Pruzan, *Biochemistry* **42**, 589 (2003).
13. T. M. Bryan, A. Englezou, M. A. Dunham, R. R. Reddel, *Exp. Cell Res.* **239**, 370 (1998).
14. N. S. Heiss *et al.*, *Nat. Genet.* **19**, 32 (1998).
15. J. R. Mitchell, J. Cheng, K. Collins, *Mol. Cell. Biol.* **19**, 567 (1999).
16. J. R. Mitchell, E. Wood, K. Collins, *Nature* **402**, 551 (1999).
17. M. Armanios *et al.*, *Proc. Natl. Acad. Sci. U.S.A.* **102**, 15960 (2005).
18. T. Vulliamy *et al.*, *Nature* **413**, 432 (2001).
19. T. L. Beattie, W. Zhou, M. O. Robinson, L. Harrington, *Mol. Cell. Biol.* **21**, 6151 (2001).
20. K. Arai *et al.*, *J. Biol. Chem.* **277**, 8538 (2002).
21. Single-letter abbreviations for the amino acid residues are as follows: A, Ala; C, Cys; D, Asp; E, Glu; F, Phe; G, Gly; H, His; I, Ile; K, Lys; L, Leu; M, Met; N, Asn; P, Pro; Q, Gln; R, Arg; S, Ser; T, Thr; V, Val; W, Trp; and Y, Tyr.

22. We thank the laboratory of T. Bryan (Cell Biology Unit, Children's Medical Research Institute) for assistance with telomerase methods and L. Cheong, L. Lu, and T. Phan (Commonwealth Scientific and Industrial Research Organisation) for fermentation support. This research was supported by the Carcinogenesis Fellowship of the Cancer Council of New South Wales and by the National Health and Medical Research Council of Australia. The accession numbers for hTERT and human dyskerin are O14746 and CAA11970, respectively.

Supporting Online Material

www.sciencemag.org/cgi/content/full/315/5820/1850/DC1
Materials and Methods
Figs. S1 to S5
References

8 December 2006; accepted 27 February 2007
10.1126/science.1138596

Regulation of Hepatic Stellate Cell Differentiation by the Neurotrophin Receptor p75^{NTR}

Melissa A. Passino, Ryan A. Adams, Shoana L. Sikorski, Katerina Akassoglou*

Differentiation of hepatic stellate cells (HSCs) to extracellular matrix– and growth factor–producing cells supports liver regeneration through promotion of hepatocyte proliferation. We show that the neurotrophin receptor p75^{NTR}, a tumor necrosis factor receptor superfamily member expressed in HSCs after fibrotic and cirrhotic liver injury in humans, is a regulator of liver repair. In mice, depletion of p75^{NTR} exacerbated liver pathology and inhibited hepatocyte proliferation in vivo. *p75$^{NTR-/-}$* HSCs failed to differentiate to myofibroblasts and did not support hepatocyte proliferation. Moreover, inhibition of p75^{NTR} signaling to the small guanosine triphosphatase Rho resulted in impaired HSC differentiation. Our results identify signaling from p75^{NTR} to Rho as a mechanism for the regulation of HSC differentiation to regeneration-promoting cells that support hepatocyte proliferation in the diseased liver.

Liver regeneration driven by hepatocyte proliferation is necessary for tissue repair and survival after acute liver injury, liver transplantation, and chronic hepatic disease, such as liver fibrosis and cirrhosis (*1*). Induction of hepatocyte proliferation depends on cross-talk between hepatocytes and nonparenchymal liver cells, such as hepatic stellate cells (HSCs) (*1*). At sites of injury, HSCs differentiate to myofibroblasts and secrete extracellular matrix (ECM) and growth factors that support hepatocyte proliferation (*2*). Although HSC differentiation is considered a central process for the induction of liver regeneration, the molecular mechanisms that regulate the transition to repair-supporting cells in the liver remain poorly understood. Expression of p75^{NTR} is increased in HSCs in the cirrhotic liver in humans and in animal models (*3*, *4*). p75^{NTR} is expressed in the nervous system during development or after injury (*5*), and it has been primarily studied as a regulator of survival and apoptosis in neurons and glia cells (*6*). p75^{NTR} is also widely expressed in nonneuronal tissues (*7*). However, the biological importance of the injury-induced, nonneuronal expression of p75^{NTR} remains enigmatic.

To address the role of p75^{NTR} in liver disease in vivo, we crossed mice deficient for p75^{NTR} with plasminogen-deficient (*plg$^{-/-}$*) mice (*8*) that spontaneously develop liver disease (*9*, *10*). At 5 weeks of age, *plg$^{-/-}$p75$^{NTR-/-}$* mice were smaller than littermate controls (fig. S1A). *plg$^{-/-}$* mice have a median survival time of 6 months (*10*). By contrast, *plg$^{-/-}$p75$^{NTR-/-}$* mice had a median survival time of 2.5 months (Fig. 1A). *plg$^{-/-}$p75$^{NTR-/-}$* mice showed prominent liver lesions as early as 10 weeks of age (fig. S1B), with large necrotic areas (Fig. 1B) not observed in either wild-type (WT) or 10-week-old *plg$^{-/-}$* control littermates. Overall, these results suggest that p75^{NTR} plays a protective role in liver disease.

We hypothesized that p75^{NTR} might regulate the progression of liver disease via altering the pathophysiological characteristics of HSCs. WT control mice expressed low amounts of p75^{NTR},

Department of Pharmacology, University of California, San Diego (UCSD), La Jolla, CA 92093–0636, USA.

*To whom correspondence should be addressed. E-mail: akass@ucsd.edu

whereas livers of $plg^{-/-}$ mice expressed more $p75^{NTR}$ (Fig. 2A), which colocalized with the HSC marker desmin (Fig. 2B). Gene expression of both α-smooth muscle actin (*αSMA*) and collagen I (*col1α1*), which are expressed by HSCs after differentiation to myofibroblasts (*11*), was significantly reduced in the livers of $plg^{-/-}p75^{NTR-/-}$ mice compared with that in the livers of $plg^{-/-}$ mice (Fig. 2C). Total numbers of HSCs were similar between $plg^{-/-}$ and $plg^{-/-}p75^{NTR-/-}$ mice (fig. S6C). Examination of fibrin deposition, which is the causative agent for liver disease in the $plg^{-/-}$ mouse (*10*), showed no differences between $plg^{-/-}$ and $plg^{-/-}p75^{NTR-/-}$ mice (fig. S2). Overall, these results suggest that $p75^{NTR}$ regulates liver pathology by inducing HSC activation.

To examine whether $p75^{NTR}$ might directly regulate HSC differentiation to myofibroblasts, we assessed the ability of primary HSCs isolated from $p75^{NTR-/-}$ mice to differentiate in vitro. WT HSCs undergo activation within 2 weeks in culture, and $p75^{NTR}$ expression positively correlates with HSC activation (*4*). After 3 weeks in culture, WT HSCs exhibited morphologic features of activated myofibroblasts, whereas $p75^{NTR-/-}$ HSCs were mostly in a quiescent state (Fig. 3A). $p75^{NTR-/-}$ HSCs showed significantly reduced differentiation (fig. S3A) and reduction in protein expression of αSMA and collagen I (fig. S3B), as well as reduced gene expression of both *col1α1* and transforming growth factor β–1 (*TGFβ-1*) (fig. S3C), compared with those of WT HSCs. Lentiviral short hairpin RNA–mediated knockdown of $p75^{NTR}$ in WT HSCs decreased cell differentiation compared with control (fig. S4, $P < 0.009$). Adenoviral delivery of $p75^{NTR}$ (*12*) in $p75^{NTR-/-}$ HSCs restored differentiation (Fig. 3B).

The effects of $p75^{NTR}$ on HSC differentiation occurred in the absence of exogenous neurotrophin ligands. $p75^{NTR}$ contributes to several signaling pathways and biological functions, not only following neurotrophin binding but also independently of neurotrophins (*5*, *13*–*15*). In the absence of neurotrophins, $p75^{NTR}$ or the intracellular domain (ICD) of $p75^{NTR}$ alone can induce apoptosis (*16*, *17*) and activation of phosphatidylinositol 3-kinase (*12*) and Rho (*18*). Moreover, $p75^{NTR}$ may act in combination with other receptors, such as Nogo receptor, to mediate biological effects (*5*, *14*, *19*). Neutralization of neurotrophins either by antibody to nerve growth factor (NGF), neurotrophin scavenger Fc-$p75^{NTR}$, or brain-derived neurotrophic factor (BDNF) scavenger Fc-TrkB, or inhibition of the other neurotrophin receptor, Trk, had no effect on HSC differentiation (fig. S5). Adenoviral delivery of the ICD of $p75^{NTR}$ restored differentiation of the $p75^{NTR-/-}$ HSCs to an extent similar to that of full-length (FL) $p75^{NTR}$ (Fig. 3B). Prior studies have shown a 1.5-fold increase in HSC apoptosis after exposure to exogenous NGF (*4*), which we confirmed (fig. S6A). Our differentiation experiments (Fig. 3 and figs. S3 to S5 and S7) were done in the absence of exogenous NGF, and WT and $p75^{NTR-/-}$ HSCs showed no difference in apoptosis (fig. S6A), suggesting that apoptosis cannot account for the differences observed in HSC differentiation. HSCs do not show apoptosis in 10-week-old $plg^{-/-}$ mice, whereas apoptosis in the livers of $plg^{-/-}p75^{NTR-/-}$ mice was exclusive to hepatocytes (fig. S6B). These results confirm data from human liver fibrotic disease showing that HSC apoptosis occurs primarily at late stages of liver disease (*20*) and that differentiated HSCs are resistant to apoptosis (*21*). The number of total desmin-positive HSCs was similar in adult WT and $p75^{NTR-/-}$ mice, suggesting that $p75^{NTR}$ does not affect the developmental differentiation or the total number of HSCs (fig. S6C).

The signal transduction mechanisms that promote and control HSC differentiation into myofibroblasts remain elusive. Rho is implicated in regulating myofibroblast morphology through reorganization of the actin cytoskeleton (*22*). A signaling relationship between $p75^{NTR}$ and Rho is well documented in the nervous system, where $p75^{NTR}$-mediated Rho signaling is involved in the regulation of neurite outgrowth (*23*). Because either $p75^{NTR}$ in the absence of ligand or the ICD of $p75^{NTR}$ alone can activate Rho through a direct interaction (*18*) and because Rho is involved in promoting the myofibroblastic state of HSCs (*22*), we examined whether $p75^{NTR}$ promoted HSC activation through Rho. Unlike in WT HSCs, expression of phospho-cofilin, a marker for Rho activation (*24*), was undetectable in $p75^{NTR-/-}$ HSCs (Fig. 3C). Adenoviral delivery of constitutively activated Rho (*25*) restored differentiation in $p75^{NTR-/-}$ HSCs (Fig. 3D). WT HSCs treated with TAT-Pep5, which is a cell-permeable peptide inhibitor that specifically blocks the activation of Rho through $p75^{NTR}$ (*23*), showed undifferentiated morphology (Fig. 3E), reduced immunostaining of phospho-cofilin (fig. S7A), and decreased gene expression of *col1α1* and *TGFβ-1* (fig. S7B), similar to the features of $p75^{NTR-/-}$ HSCs. Taken together, these results suggest that $p75^{NTR}$ signaling through Rho promotes HSC differentiation to myofibroblasts.

Because cross-talk of HSCs with hepatocytes drives hepatocyte proliferation and liver repair

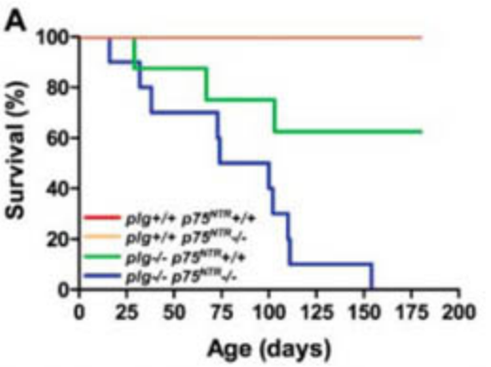

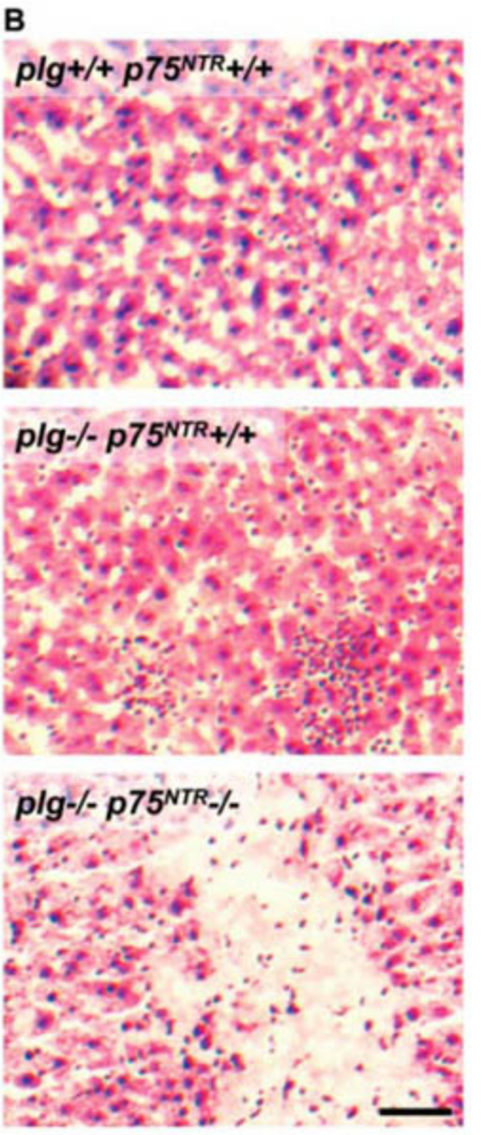

Fig. 1. Exacerbated mortality and liver pathology caused by $p75^{NTR}$ deficiency. (**A**) Survival of $plg^{+/+}p75^{NTR+/+}$ ($n = 35$), $plg^{+/+}p75^{NTR-/-}$ ($n = 11$), $plg^{-/-}p75^{NTR+/+}$ ($n = 8$), and $plg^{-/-}p75^{NTR-/-}$ ($n = 10$) mice. Because both $plg^{+/+}p75^{NTR+/+}$ and $plg^{+/+}p75^{NTR-/-}$ mice exhibited 100% survival, the curves overlap and appear as a single line. (**B**) Hematoxylin stain of representative liver sections of 10-week-old $plg^{+/+}p75^{NTR+/+}$ (top), $plg^{-/-}p75^{NTR+/+}$ (middle), and $plg^{-/-}p75^{NTR-/-}$ (bottom) mice. Scale bar indicates 56 μm.

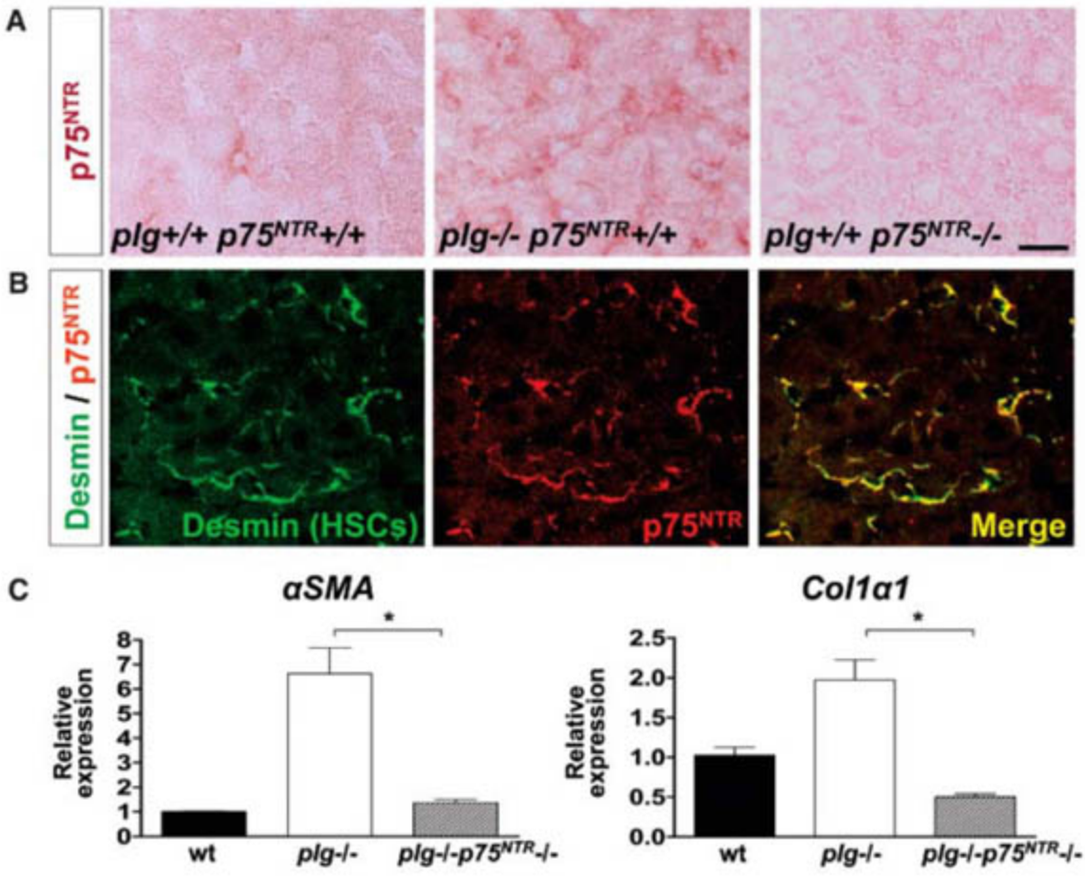

Fig. 2. Inhibited HSC activation after loss of $p75^{NTR}$. (**A**) Immunochemical detection of $p75^{NTR}$ (dark red) in livers of 10-week-old $plg^{+/+}p75^{NTR+/+}$ (left), $plg^{-/-}p75^{NTR+/+}$ (middle), and $plg^{+/+}p75^{NTR-/-}$ (right; negative control) mice. Immunoreactive cells show spindle morphology and perihepatocyte localization characteristic of HSCs. (**B**) Confocal double immunofluorescence in $plg^{-/-}$ liver shows colocalization (yellow) of the HSC marker desmin (green) with $p75^{NTR}$ (red). (**C**) Analysis of markers of HSC activation in whole liver. *αSMA* and *col1α1* gene expression was examined in 4-week-old mice (n = 3 mice per genotype) by real-time polymerase chain reaction (PCR) analysis performed in duplicates. Bar graphs represent means ± SEM [$^*P < 0.001$ by one-way analysis of variance (ANOVA)]. Scale bar shown can be applied to all images and represents 19 μm in (A) and 25 μm in (B).

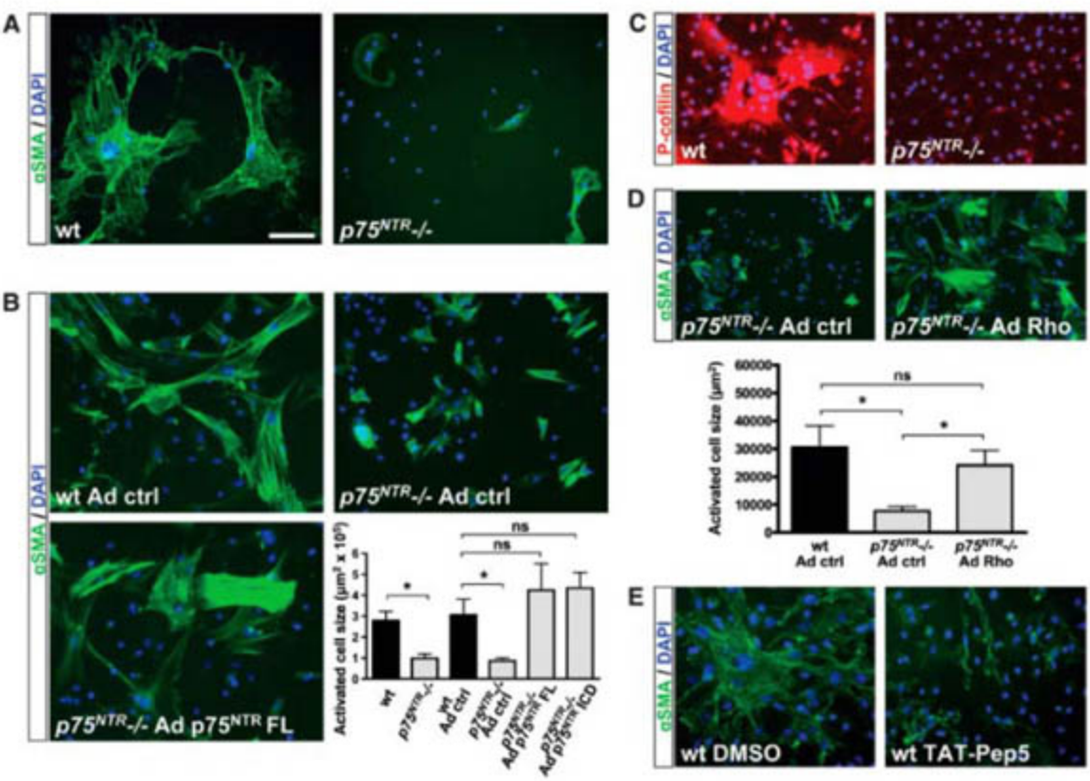

Fig. 3. Role of Rho in $p75^{NTR}$-promoted HSC activation. (**A**) αSMA immunostaining (green) of activated WT and $p75^{NTR-/-}$ HSCs after 21 days in culture. Wt HSCs are characterized by wide, spread-out morphology and large round nuclei. $p75^{NTR-/-}$ HSCs are unable to differentiate, and the few cells that showed immunostaining for αSMA are arrested at an intermediate stage of differentiation, characterized by small size and shrunken morphology. Nuclei are stained with 4′,6′-diamidino-2-phenylindole (DAPI) (blue). Representative images from seven independent experiments are shown. (**B**) Adenoviral delivery of FL or ICD $p75^{NTR}$. Freshly isolated WT and $p75^{NTR-/-}$ HSCs were transduced on day 2 with adenovirus. αSMA immunostaining (green) was performed on day 7. Nuclei were stained with DAPI (blue). Activated cell size was quantitated by determining the area of αSMA-positive cells in three independent experiments performed in duplicates. Adenoviral empty vector was used as control (Ad ctrl). Bar graphs represent means ± SEM ($^*P < 0.05$ and ns, not significant, by one-way ANOVA). (**C**) Detection of phosphorylated cofilin (P-cofilin), a marker indicative of Rho activation, by immunostaining (red) in WT and $p75^{NTR-/-}$ HSCs after 21 days in culture. Nuclei are stained with DAPI (blue). (**D**) Adenoviral delivery of constitutively active Rho. HSC transduction and analysis of activated cell size was done as described in (B). Bar graphs represent means ± SEM ($^*P < 0.05$ and ns, not significant, by one-way ANOVA). (**E**) Specific blocking of $p75^{NTR}$-mediated Rho activation. Representative images of αSMA immunostaining (green) of freshly isolated WT HSCs after a 7-day treatment with either vehicle [dimethyl sulfoxide (DMSO)] or TAT-Pep5. TAT-Pep5 is a fused peptide of the amino-terminal protein transduction domain (11 amino acids) from the human immunodeficiency virus protein TAT with Pep5, which is a peptide inhibitor of the activation of Rho by $p75^{NTR}$. Nuclei are stained with DAPI (blue). Scale bar shown can be applied to all images and represents 93 μm in (A), 79 μm in (B), 93 μm in (C), 105 μm in (D), and 32 μm in (E).

(*1*, *2*, *26*), we examined whether $p75^{NTR}$ could regulate hepatocyte proliferation. $plg^{-/-}$ mice showed an increased number of proliferating hepatocytes [126.6 ± 3.9 (SEM), Fig. 4A] when compared with WT mice [95.2 ± 3.7 (SEM)], suggestive of the regenerative response in the liver after injury. By contrast, $plg^{-/-}p75^{NTR-/-}$ mice displayed significantly decreased cell proliferation [74.2 ± 9.1 (SEM)] compared with $plg^{-/-}$ mice (Fig. 4A, $P < 0.001$). One of the key mediators in promoting hepatocyte proliferation is hepatocyte growth factor (HGF) (*1*). Whole-liver homogenates from $plg^{-/-}p75^{NTR-/-}$ mice showed only one-third of the amount of HGF protein detected in $plg^{-/-}$ livers (Fig. 4B). HSCs are a major source of HGF in the liver (*27*, *28*); thus, the reduction in HGF in the $plg^{-/-}p75^{NTR-/-}$ mouse is in accordance with the defective HSC activation observed after genetic loss of $p75^{NTR}$ both in vivo (Fig. 2C) and in vitro (Fig. 3). In co-culture (*26*), hepatocytes in culture with $p75^{NTR-/-}$ HSCs exhibited a 30% decrease in proliferation compared with those incubated with WT HSCs (Fig. 4C, $P < 0.05$). Proliferation was largely restored when HGF was added to the culture medium (Fig. 4C). Taken together, these results suggest that $p75^{NTR}$ expression by HSCs is necessary for their differentiation to repair-supporting, HGF-secreting cells, which in turn can promote hepatocyte proliferation.

HSC differentiation is a hallmark of fibrotic liver disease of different etiologies, such as hepatitis and chronic alcohol consumption (*20*). Initiation of HSC differentiation results in secretion of HGF and synthesis of ECM, which are critical mediators for the restoration of normal liver structure, hepatocyte proliferation, and liver regeneration (*1*). However, perpetuation of HSC activation to a myofibroblastic state leads to excessive collagen and ECM deposition, which results in liver fibrosis. Therefore, sustained differentiation of HSCs is considered a target for the treatment of liver fibrosis (*11*). At late stages of liver disease, resolution of fibrosis depends on HSC apoptosis (*20*). Our study showed that $p75^{NTR}$ induces HSC differentiation and demonstrated that the mild in vitro effect of NGF on HSC apoptosis (*4*, *29*) is mediated by $p75^{NTR}$. These results suggest that in liver injury $p75^{NTR}$ might function both as a regulator of HSC differentiation and, depending on the bioavailability of neurotrophins, might also participate together with other apoptotic mediators in orchestrating the resolution of fibrosis. Identification of $p75^{NTR}$ as a molecular link between HSC activation and hepatocyte proliferation could provide a therapeutic target for manipulating the stages of HSC activation during the progression of chronic liver disease.

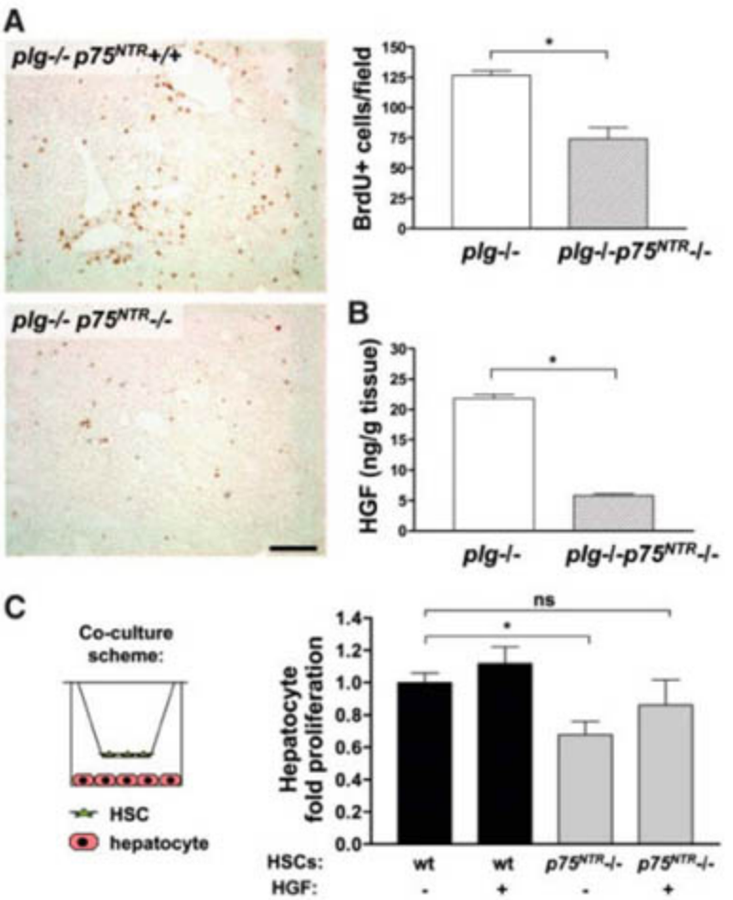

Fig. 4. $p75^{NTR}$-dependent promotion of hepatocyte proliferation through regulation of HGF secretion by HSCs. (**A**) Liver cell proliferation in $plg^{-/-}p75^{NTR+/+}$ and $plg^{-/-}p75^{NTR-/-}$ mice. Ten-week-old mice were injected intraperitoneally with bromodeoxyuridine (BrdU) (100 mg/kg) daily for 3 days. Proliferating cells were visualized by immunochemical detection of BrdU. Liver cell proliferation was quantified by counting the number of BrdU+ cells per field (field corresponds to 1.5 mm^2) (top right). Graph represents mean ± SEM ($n = 5$ per genotype, $^*P < 0.001$ by unpaired Student's t test). Scale bar, 198 μm. (**B**) HGF in the livers of $plg^{-/-}$ and $plg^{-/-}p75^{NTR-/-}$ mice as quantified by enzyme-linked immunosorbent assay. Graph represents mean ± SEM ($n = 8$ for $plg^{-/-}$ and $n = 5$ for $plg^{-/-}p75^{NTR-/-}$, $^*P < 0.0001$ by unpaired Student's t test). (**C**) Culture of primary hepatocytes with WT and $p75^{NTR-/-}$ HSCs. Hepatocytes were plated in the bottom of the well and incubated with HSCs grown on inserts placed within the well. Hepatocytes were cultured with WT or $p75^{NTR-/-}$ HSCs (day 7 to 21, passage 2 to 4), with or without HGF (50 ng/ml). After 2 days, hepatocyte proliferation was assessed by [^{3}H]thymidine incorporation (right). All data are mean ± SEM from four independent experiments performed in duplicates ($^*P < 0.05$ and ns, not significant, by one-way ANOVA).

References and Notes

1. R. Taub, *Nat. Rev. Mol. Cell Biol.* **5**, 836 (2004).
2. C. Balabaud, P. Bioulac-Sage, A. Desmouliere, *J. Hepatol.* **40**, 1023 (2004).
3. D. Cassiman, C. Denef, V. J. Desmet, T. Roskams, *Hepatology* **33**, 148 (2001).
4. N. Trim *et al.*, *Am. J. Pathol.* **156**, 1235 (2000).
5. M. V. Chao, *Nat. Rev. Neurosci.* **4**, 299 (2003).
6. G. Dechant, Y. A. Barde, *Nat. Neurosci.* **5**, 1131 (2002).
7. C. Lomen-Hoerth, E. M. Shooter, *J. Neurochem.* **64**, 1780 (1995).
8. Materials and methods are available on *Science* Online.
9. V. L. Ng *et al.*, *J. Hepatol.* **35**, 781 (2001).
10. T. H. Bugge *et al.*, *Cell* **87**, 709 (1996).
11. R. Bataller, D. A. Brenner, *Semin. Liver Dis.* **21**, 437 (2001).
12. P. P. Roux, A. L. Bhakar, T. E. Kennedy, P. A. Barker, *J. Biol. Chem.* **276**, 23097 (2001).
13. N. Zampieri, M. V. Chao, *Biochem. Soc. Trans.* **34**, 607 (2006).
14. P. A. Barker, *Neuron* **42**, 529 (2004).
15. K. K. Teng, B. L. Hempstead, *Cell. Mol. Life Sci.* **61**, 35 (2004).
16. S. Rabizadeh *et al.*, *Science* **261**, 345 (1993).
17. M. Majdan *et al.*, *J. Neurosci.* **17**, 6988 (1997).
18. T. Yamashita, K. L. Tucker, Y. A. Barde, *Neuron* **24**, 585 (1999).
19. L. F. Reichardt, *Philos. Trans. R. Soc. London Ser. B* **361**, 1545 (2006).
20. T. Kisseleva, D. A. Brenner, *J. Gastroenterol. Hepatol.* **21** (suppl. 3), S84 (2006).
21. E. Novo *et al.*, *Gut* **55**, 1174 (2006).
22. M. Kato *et al.*, *J. Hepatol.* **31**, 91 (1999).
23. T. Yamashita, M. Tohyama, *Nat. Neurosci.* **6**, 461 (2003).
24. M. Maekawa *et al.*, *Science* **285**, 895 (1999).
25. M. Hoshijima, V. P. Sah, Y. Wang, K. R. Chien, J. H. Brown, *J. Biol. Chem.* **273**, 7725 (1998).
26. N. Uyama *et al.*, *J. Hepatol.* **36**, 590 (2002).
27. Z. Hu, R. P. Evarts, K. Fujio, E. R. Marsden, S. S. Thorgeirsson, *Am. J. Pathol.* **142**, 1823 (1993).
28. J. J. Maher, *J. Clin. Investig.* **91**, 2244 (1993).
29. F. Oakley *et al.*, *Am. J. Pathol.* **163**, 1849 (2003).

30. We thank P. Barker and M. V. Chao for providing us with the $p75^{NTR}$ adenoviral vectors and the $p75^{NTR}$ antibodies, respectively, invaluable discussions, and critical reading of the manuscript; J. Heller Brown for the constitutive active adenoviral Rho vector; J. Han and T. Nuriel for technical assistance; members of P. Insel's lab for assistance with real-time polymerase chain reaction (PCR) and αSMA immunostaining protocol; W. Naugler for primary hepatocyte culture protocols; R. Rippe for HSC culture protocols; and K. Barrett for critical reading of the manuscript. Supported by NIH/National Institute of Neurological Disorders and Stroke (NINDS) grant P30-NS047101 to the UCSD Neuroscience Microscopy Shared Facility, NIH training grant 5T32-GM07752 to M.A.P., and NIH/NINDS grant NS051470 to K.A.

Supporting Online Material

www.sciencemag.org/cgi/content/full/315/5820/1853/DC1
Materials and Methods
Figs. S1 to S7
References

15 November 2006; accepted 28 February 2007
10.1126/science.1137603

CREB-Binding Protein Modulates Repeat Instability in a *Drosophila* Model for PolyQ Disease

Joonil Jung[1] and Nancy Bonini[1,2]*

Although expansion of trinucleotide repeats accounts for over 30 human diseases, mechanisms of repeat instability remain poorly understood. We show that a *Drosophila* model for the CAG/polyglutamine (polyQ) disease spinocerebellar ataxia type 3 recapitulates key features of human CAG-repeat instability, including large repeat changes and strong expansion bias. Instability is dramatically enhanced by transcription and modulated by nuclear excision repair and a regulator of DNA repair adenosine 3′,5′-monophosphate (cAMP) response element–binding protein (CREB)–binding protein—a histone acetyltransferase (HAT) whose decreased activity contributes to polyQ disease. Pharmacological treatment to normalize acetylation suppressed instability. Thus, toxic consequences of pathogenic polyQ protein may include enhancing repeat instability.

Expansion of repeat sequences causes more than 30 human diseases, including the CAG-repeat polyQ diseases spinocerebellar ataxia type 3 (SCA3) and Huntington's disease (HD), as well as noncoding repeat expansion diseases like the CGG 5′ untranslated region (5′UTR)–repeat disease fragile X syndrome (*1*, *2*). Although the repeats are normally polymorphic in size, disease occurs only when the number of repeats expands beyond a critical threshold characteristic for each disease. Repeat instability also underlines anticipation, as expanded repeats have a strong tendency to further expand, causing the disease to occur earlier with greater severity in successive generations.

To better understand mechanisms of instability, we determined whether *Drosophila* displays intergenerational repeat instability in a CAG-repeat model of human SCA3. Transgenes retaining at least some native genomic context surrounding the CAG repeat manifest instability, as for the Httexon1 transgenic mouse (*3*). The SCA3tr-Q78 transgene in our fly model (*4*) is derived from exon 10 of the human SCA3 gene and contains two polymorphic nucleotides linked to the majority of high-normal and expanded repeat alleles in patients (*5*), which suggests that it may contain genomic elements important for instability.

The rate of repeat instability was initially determined in three independent transgenic lines, following a nine-generation protocol (fig. S1). These studies showed that CAG repeats were stable with only minimal repeat changes (Fig. 1, A and D) (*6*). However, most human trinucleotide-repeat genes, including *SCA3*, are expressed in germ cells, where dramatic instability occurs (*7*). In *Escherichia coli* and mouse, transcription may play a role (*8*). Therefore, we then expressed the SCA3 transgenes in germ cells using a *nos-GAL4* driver line (fig. S2). With germline transcription, all lines now bore a striking percentage of progeny with altered repeat lengths (Fig. 1, B and D). Different transgenic lines showed different degrees of instability, which was not correlated with the level of transgene expression (Fig. 1, D and E). This highlights a potential influence of the genomic context of the transgenic insertion site per se in modulating the degree of instability, as noted in HD and muscular dystrophy models (*9*).

Although all transgenic lines showed instability with transcription (Fig. 1 and fig. S3A), we focused on line 2 for detailed mechanistic studies, confirming all key findings with at

[1]Department of Biology, University of Pennsylvania, Philadelphia, PA 19104, USA. [2]Howard Hughes Medical Institute, University of Pennsylvania, Philadelphia, PA 19104, USA.

*To whom correspondence should be addressed. E-mail: nbonini@sas.upenn.edu

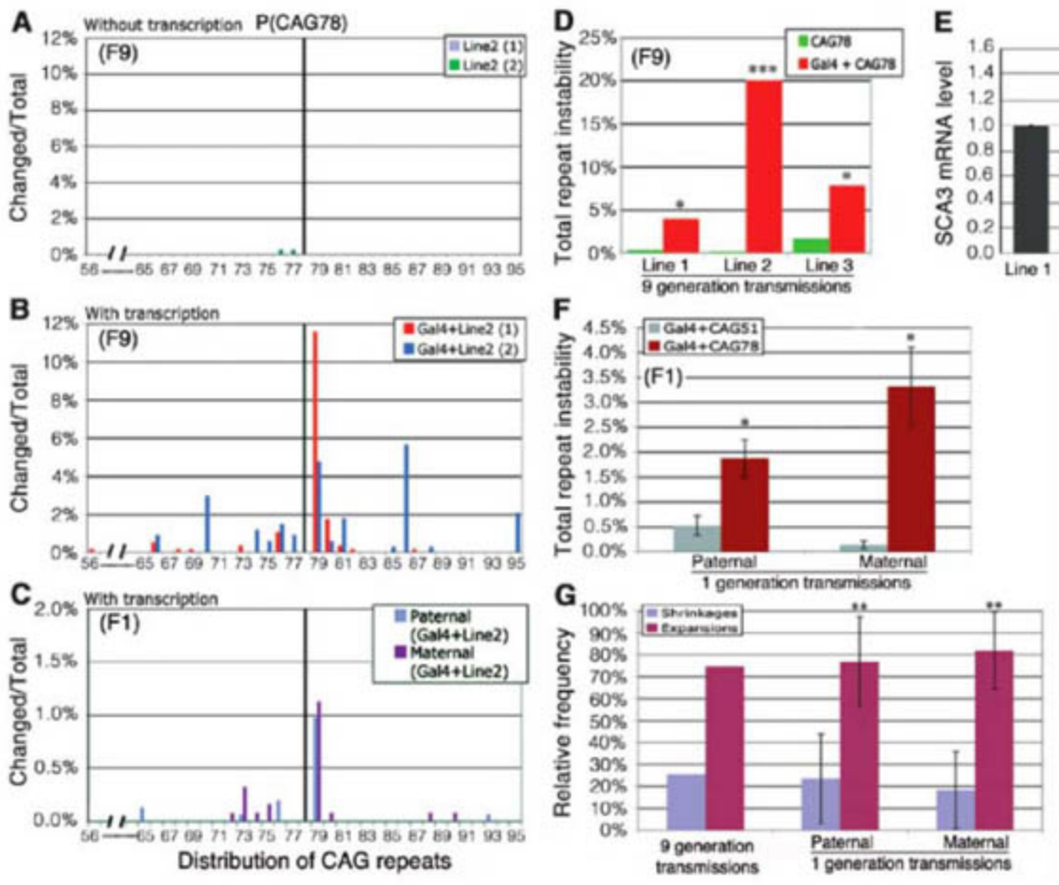

Fig. 1. CAG-repeat instability in an SCA3 model mimics human CAG-repeat instability. (A, B, and D) Germline transcription with *nos-GAL4* (Gal4) significantly enhanced instability in nine-generation studies (chi-square test, $*P < 0.05$, $***P < 0.0001$). (**A** and **B**) CAG-repeat distribution among F_9 progeny of line 2. Parental repeat is labeled P(CAG78). (**C**) CAG-repeat instability in single-generation studies. (**D** and **E**) Similar levels of SCA3 mRNA were present, but repeat instability was significantly different between lines 1 and 2. (chi-square test, $P < 10^{-6}$). (**F**) CAG51 (27 repeat shrinkage of line 2) showed a significantly lower rate of instability than the original CAG78 allele [Student's t test, $*P < 0.05$; mean ± SEM; $n = 3$ (CAG51) or 4 (CAG78)]. (**G**) Expansion bias was observed in repeat instability of line 2 (Student's t test, $**P < 0.01$; mean ± SD; $n = 2$ (F_9), 6 (F_1, paternal transmission), or 5 (F_1, maternal transmissions).

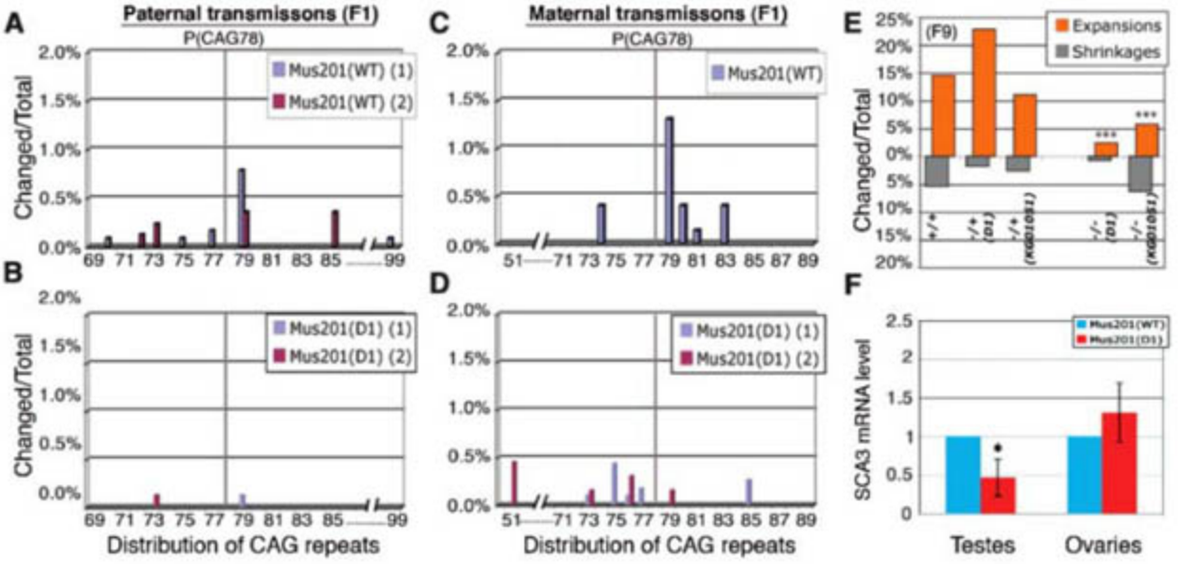

Fig. 2. Suppression of CAG-repeat expansions with loss of NER and/or TCR. (**A** and **B**) Compared with the control, *mus201*^{D1} flies showed a significantly reduced overall rate of instability in paternal transmission (Student's *t* test, $P = 0.01$). (**C** and **D**) In maternal transmission, expansions were selectively reduced with *mus201*^{D1} (Fisher's exact test, $P < 0.001$). Repeat shrinkages were unaffected. (**E**) CAG-repeat expansions were suppressed in nine-generation studies, tested with two independent alleles *mus201*^{D1} and *mus201*^{KG01051} (Fisher's exact test, $^{***}P < 0.001$). (**F**) SCA3 expression level was not affected in ovaries, but was reduced in testes (Student's *t* test, $^{*}P < 0.05$; mean ± SD; $n = 3$).

least one additional line and/or distinct disease transgene. For line 2, whereas small repeat changes involving one to three repeat expansions made up the majority of events (58% of changes), large repeat expansions and shrinkages involving ≥10 CAG repeats were also frequent (10%; Fig. 1B). Moreover, the wide range of repeat size variation (56 to 95 CAG repeats, reflecting shrinkages of 22 repeat units to expansions of 17) was similar to the range of CAG-repeat sizes seen in SCA3 patients (*10*).

In single-generation studies, the repeats also showed little instability without transcription, but strong instability upon germline transcription (Fig. 1C). Of note, changes involving ≥10 repeat expansions or shrinkages were seen. This suggests a mechanism(s) in vivo that generates long repeat changes in single or a few molecular events. Additionally, we observed length-dependent increases in the rate of instability, as are seen in mammals (Fig. 1F) (*11*). We also observed an ~3:1 bias for repeat expansions (Fig. 1G). This is similar to what is observed in humans, although expansion bias is primarily observed in paternal transmissions. In mammals, the prolonged period of meiotic arrest during oogenesis is thought to play a role in maternal repeat shrinkages (*12*, *13*); lack of such an arrest during *Drosophila* oogenesis may explain the expansion bias in maternal transmission. Thus, the SCA3 fly model with germline transcription displays several key features of CAG-repeat instability that are seen in human SCA3 patients.

Expanded trinucleotide repeats form unusual DNA structures in vitro, such as hairpins and slipped strands (*14*). These may attract DNA repair proteins and trigger repair responses leading to repeat instability in vivo (*15*, *16*). The strong relation between repeat instability and transcription in the fly raised the possibility that DNA repair mechanisms—transcription-coupled repair (TCR) in particular—may be involved (*17*). The fly Mus201 protein is an ortholog of human Rad2/XPG, and loss of Mus201 function leads to complete loss of nucleotide excision repair (NER) and/or TCR in flies. We therefore examined the effect of eliminating TCR on repeat instability.

In the *mus201*^{D1} (a null mutant) background, we observed a dramatic reduction in instability. Control flies showed the typical 1 to 3% instability with strong bias for repeat expansions (Fig. 2, A and C). However, with loss of Mus201 function, repeat expansions were suppressed in both maternal and paternal transmissions (Fig. 2, B and D), as well as in nine-generation studies (Fig. 2E). SCA3 mRNA levels were reduced in the testes, which suggested a dependence on the TCR pathway for transgene expression, but were not reduced in ovaries (Fig. 2F). This indicates a specific effect

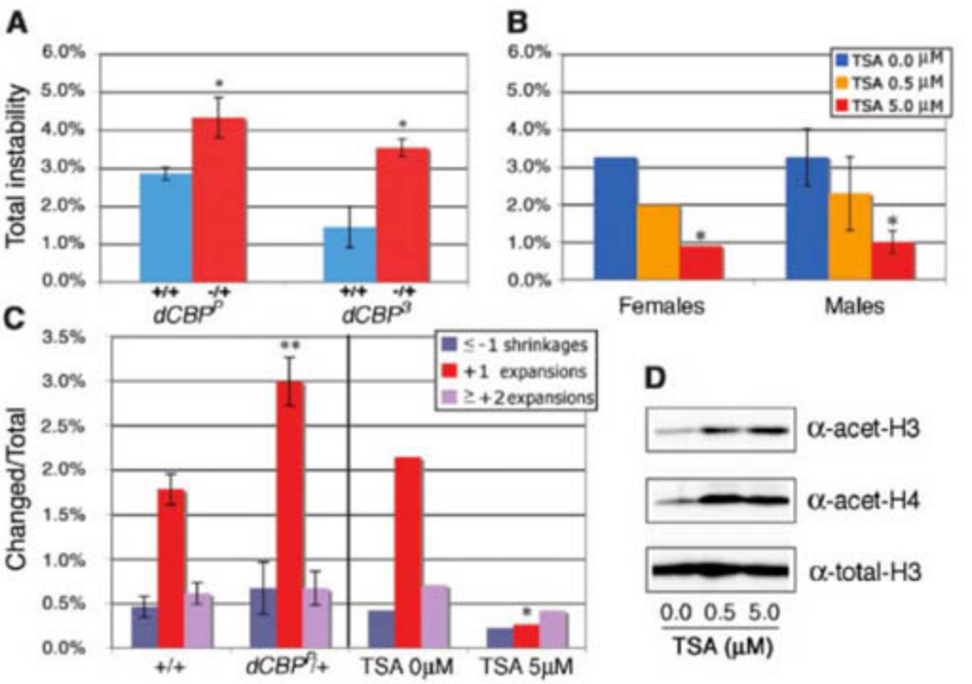

Fig. 3. dCBP and the HDAC inhibitor TSA modulate repeat instability. (**A**) Significant increase in repeat instability was observed in *dCBP* mutants (Student's *t* test, $^{*}P < 0.05$; $n = 3$). Fly genotypes: *dCBP*^{P}/*FM7c* with CAG78/CAG78 (left) and *dCBP*^{3}/+ with CAG78/CAG46 (right). (**B**) Treatment of flies bearing CAG78/CAG78 with TSA suppressed instability [Student's *t* test, $^{*}P < 0.05$; $n = 2$ (females) or 3 (males)]. (**C**) Decrease in dCBP (*dCBP*^{P}/+) preferentially increased +1 expansions (two-way ANOVA Bonferroni post test, $^{**}P < 0.01$), whereas TSA treatment (5 µM) had the opposite effect (Fisher's exact test, $^{*}P < 0.05$). All values, means ± SEM. (**D**) TSA-treated flies had increased levels of acetylated histones H3 and H4.

of Mus201 activity on repeat instability in females. Effects of NER have been reported in *Escherichia coli* and cell lines with conflicting results; our findings indicate that Mus201/TCR modulates CAG-repeat expansions during germline transmissions in vivo. This potentially contributes to the genetic "anticipation" phenomenon prevalent in human patients.

In polyQ diseases, expanded CAG repeats are translated into pathogenic polyQ tracts to form nuclear inclusions. Key regulators of DNA repair, such as adenosine 3′,5′-monophosphate (cAMP) response element–binding protein (CREB)–binding protein (CBP) (*18*, *19*), are found in polyQ inclusions, which leads to a reduction in soluble CBP levels (*20*, *21*). Soluble pathogenic polyQ protein may also increase degradation of CBP (*22*), as well as inhibit CBP/p300 histone acetyltransferase (HAT) activity through direct binding (*23*). We therefore tested whether decreased CBP levels could alter DNA repair activity in flies. Decreasing *Drosophila* CBP (*dCBP*) gene dosage significantly modified the survival rate of methyl methanesulfonate–treated larvae (a measure of DNA repair) (fig. S4). This raised the possibility that pathogenic polyQ protein may indirectly enhance CAG-repeat instability in polyQ disease by inhibiting CBP functions important for DNA repair.

To test this, we determined whether loss of dCBP enhanced repeat instability. Because dCBP is essential, heterozygous flies were tested. Such partial loss of CBP function may reflect well the typical prolonged disease situation, as severe CBP depletion causes cytotoxic cell loss. We examined two different alleles of *dCBP*: $dCBP^{P}$, a hypomorphic allele, and $dCBP^{3}$, a null microdeletion. Both alleles enhance polyQ toxicity in heterozygous animals in *Drosophila* (*24*). The effects of the $dCBP^{P}$ allele were examined on CAG78/CAG78 flies; however, the $dCBP^{3}$ allele was deleterious in that background, so instability was examined with CAG78 in trans to a less toxic CAG46 allele (CAG78/CAG46). CAG78/CAG78 control flies showed an instability rate of 2.85 ± 0.17%; the CAG78/CAG46 flies showed a reduced rate, with the CAG78 repeat showing 1.45 ± 0.54% instability (Fig. 3A). In both situations, however, a significant increase in instability of the CAG78 repeat was observed [4.33 ± 0.53% ($dCBP^{P}$) and 3.35 ± 0.23% ($dCBP^{3}$)] (Fig. 3A). Similar increases in instability were confirmed in independent transgenic lines (fig. S3A). Although we did not observe an obvious change in the overall pattern of histone H3 or H4 acetylation in ovaries of mutant flies, localized decreases in acetylation of histones or other protein targets may occur. Significant changes in SCA3 transgene expression were not observed (fig. S5A). We further tested the role of CBP on repeat instability by up-regulating *dCBP* in males using an overexpression allele $dCBP^{EP1179}$; this resulted in a reduced rate of instability (fig. S3B).

The inhibitory effect of pathogenic polyQ proteins on CBP is thought to be due to loss of its HAT activity. Treating flies or mouse models of polyQ disease with histone deacetylase (HDAC) inhibitors to normalize acetylation levels protects against polyQ protein pathogenesis (*25*). Our data indicated that HDAC inhibitors may also protect against the increased rate of repeat instability. We therefore treated flies expressing the pathogenic polyQ protein in germ cells with an HDAC inhibitor trichostatin A (TSA), and measured repeat instability.

Placebo-treated flies showed normal instability [3.26 ± 0.29% and 3.26 ± 0.76% for maternal and paternal transmissions, respectively] (Fig. 3B). In contrast, there was a sharp drop in rate of instability of flies fed TSA. With 5 μM TSA, CAG-repeat instability decreased to 0.90 ± 0.02% and 1.00 ± 0.29% for maternal and paternal transmissions, respectively (Fig. 3B). TSA treatment increased the level of acetylated histones in flies (Fig. 3D), and SCA3 transcription was not affected (fig. S5B). Although TSA is known to affect multiple pathways in vivo, analysis of the pattern of repeat changes by TSA suggested that reduced instability was, at least in part, due to compensation for decreased dCBP and/or HAT activity, as both *dCBP* gene changes and TSA treatment preferentially modulated +1 repeat changes relative to other events (Fig. 3C).

Several lines of evidence suggested that the features we characterized for repeat instability of SCA3 transgenes may have broader implications. For example, the majority of triplet-repeat disease genes are expressed in germ cells, and a number of polyQ proteins (Huntingtin, androgen receptor, ataxin-7, and ataxin-3) interact with or inhibit CBP or other HAT proteins (*26*). Therefore, to extend these findings, we examined the effects of transcription and the contribution of CBP to HD models; we also examined instability in a model for fragile X CGG premutation expansions, an unstable noncoding trinucleotide repeat (*27*). As with SCA3, we found a consistent enhancement of repeat instability with germline transcription for both HD and CGG models (fig. S6). We also tested the role of CBP on HD. As with SCA3tr-Q78, reducing the level of *dCBP* ($dCBP^{P}$/+) enhanced repeat instability of an HD Httexon1Q93 transgene (fig. S7). Thus, features of repeat instability, including transcriptional dependence, may be fundamental aspects of trinucleotide instability displayed in multiple disease models.

These studies reveal that *Drosophila* recapitulates several central features of human CAG-repeat instability, including the wide range of repeat changes and strong bias for expansions. Moreover, germline transcription along with NER and/or TCR dramatically enhanced instability. A consequence of polyQ gene expression in germ cells is that polyQ protein pathology—namely, inhibition of CBP activity via sequestration or inhibitory interactions—may further enhance repeat instability. In HD, dramatic expansion of CAG repeats occurs not only intergenerationally, but also somatically, in affected brain regions, which develop striking inclusions containing CBP (*28*, *29*). Known modifiers like Msh2 modulate CAG-repeat instability similarly in both the germline and somatic tissues, which suggests that our findings with germline instability may be applicable to somatic instability.

Trinucleotide-repeat instability has been viewed largely as a matter of DNA metabolism; however, our data suggest that repeat instability may be influenced by aspects of polyQ protein toxicity; thus, treatments to curb polyQ protein pathology may also be effective means to help clamp repeat instability. Among these, HDAC inhibitors are in clinical trials (*30*).

References and Notes

1. J. R. Gatchel, H. Y. Zoghbi, *Nat. Rev. Genet.* **6**, 743 (2005).
2. C. E. Pearson, K. N. Edamura, J. D. Cleary, *Nat. Rev. Genet.* **6**, 729 (2005).
3. L. Mangiarini *et al.*, *Nat. Genet.* **15**, 197 (1997).
4. J. M. Warrick *et al.*, *Cell* **93**, 939 (1998).
5. P. Maciel *et al.*, *Eur. J. Hum. Genet.* **7**, 147 (1999).
6. S. M. Jackson *et al.*, *Gene* **347**, 35 (2005).
7. Y. Kawaguchi *et al.*, *Nat. Genet.* **8**, 221 (1994).
8. F. Tanaka *et al.*, *Am. J. Hum. Genet.* **65**, 966 (1999).
9. Y. Zhang, D. G. Monckton, M. J. Siciliano, T. H. Connor, M. L. Meistrich, *Hum. Mol. Genet.* **11**, 791 (2002).
10. Y. Takiyama *et al.*, *Hum. Mol. Genet.* **6**, 1063 (1997).
11. V. C. Wheeler *et al.*, *Hum. Mol. Genet.* **8**, 115 (1999).
12. T. Sato *et al.*, *Hum. Mol. Genet.* **8**, 99 (1999).
13. M. D. Kaytor, E. N. Burright, L. A. Duvick, H. Y. Zoghbi, H. T. Orr, *Hum. Mol. Genet.* **6**, 2135 (1997).
14. R. D. Wells, R. Dere, M. L. Hebert, M. Napierala, L. S. Son, *Nucleic Acids Res.* **33**, 3785 (2005).
15. K. Manley, T. L. Shirley, L. Flaherty, A. Messer, *Nat. Genet.* **23**, 471 (1999).
16. C. Savouret *et al.*, *EMBO J.* **22**, 2264 (2003).
17. Y. Lin, V. Dion, J. H. Wilson, *Nat. Struct. Mol. Biol.* **13**, 179 (2006).
18. S. Hasan, M. O. Hottiger, *J. Mol. Med.* **80**, 463 (2002).
19. M. Tini *et al.*, *Mol. Cell* **9**, 265 (2002).
20. F. C. Nucifora Jr. *et al.*, *Science* **291**, 2423 (2001).
21. Y. Chai, J. Shao, V. M. Miller, A. Williams, H. L. Paulson, *Proc. Natl. Acad. Sci. U.S.A.* **99**, 9310 (2002).
22. H. Jiang, F. C. Nucifora Jr., C. A. Ross, D. B. DeFranco, *Hum. Mol. Genet.* **12**, 1 (2003).
23. G. Schaffar *et al.*, *Mol. Cell* **15**, 95 (2004).
24. J. P. Taylor *et al.*, *Genes Dev.* **17**, 1463 (2003).
25. J. S. Steffan *et al.*, *Nature* **413**, 739 (2001).
26. L. Bodai, J. Pallos, L. M. Thompson, J. L. Marsh, *Curr. Med. Chem.* **10**, 2577 (2003).
27. P. Jin *et al.*, *Neuron* **39**, 739 (2003).
28. L. Kennedy *et al.*, *Hum. Mol. Genet.* **12**, 3359 (2003).
29. M. DiFiglia *et al.*, *Science* **277**, 1990 (1997).
30. J. Marx, *Science* **310**, 43 (2005).

31. We thank R. Pittman, H. Paulson, A. Cashmore, D. Lessing, L. Li, M. Watson for comments; S. DiNardo, L. Thompson, L. Goldstein, and P. Jin for reagents; and K. Xu and X. Teng for technical assistance. Supported by grants from the Hereditary Disease Foundation (to J.J.), the Packard Foundation, and NINDS (to N.M.B.). N.M.B. is an investigator of the Howard Hughes Medical Institute.

Supporting Online Material

www.sciencemag.org/cgi/content/full/1139517/DC1
Materials and Methods
Figs. S1 to S7
References

4 January 2007; accepted 9 February 2007
Published online 1 March 2007;
10.1126/science.1139517
Include this information when citing this paper.

Top-Down Versus Bottom-Up Control of Attention in the Prefrontal and Posterior Parietal Cortices

Timothy J. Buschman and Earl K. Miller*

Attention can be focused volitionally by "top-down" signals derived from task demands and automatically by "bottom-up" signals from salient stimuli. The frontal and parietal cortices are involved, but their neural activity has not been directly compared. Therefore, we recorded from them simultaneously in monkeys. Prefrontal neurons reflected the target location first during top-down attention, whereas parietal neurons signaled it earlier during bottom-up attention. Synchrony between frontal and parietal areas was stronger in lower frequencies during top-down attention and in higher frequencies during bottom-up attention. This result indicates that top-down and bottom-up signals arise from the frontal and sensory cortex, respectively, and different modes of attention may emphasize synchrony at different frequencies.

Volitional shifts of attention are thought to depend on "top-down" signals derived from knowledge about the current task (e.g., finding your lost keys), whereas the automatic "bottom-up" capture of attention is driven by properties inherent in stimuli—that is, by salience (e.g., a flashing fire alarm) (*1*–*3*). Imaging and neurophysiological studies have found neural correlates of both types in the frontal and posterior parietal cortices (*1*, *2*, *4*–*6*), but their respective contributions are not clear; they have largely been studied in separate experiments, rendering comparisons difficult and obscuring timing differences that could give clues to information flow (*7*).

We therefore recorded from multiple electrodes simultaneously implanted in the frontal and parietal cortices as monkeys (*Macaca mulatta*) found a visual target under two conditions (Fig. 1A). The target was randomly located in an array of four stimuli, with conditions differing in how the distractors related to the target. In "pop-out," the distractors were identical and differed from the target along two dimensions (color and orientation), so the target's salience automatically drew attention to it (*1*–*3*). During "search," each distractor independently differed from the target. Because the target matched some of the distractors in each dimension, it was not salient and had to be sought using only its remembered appearance (*1*–*3*). The monkeys showed the behavioral hallmarks of bottom-up versus top-down attention. Psychophysical testing showed a shallower increase in reaction time with more distractors during pop-out than during search (6 ms per item for pop-out, 22 ms per item for search; $P < 0.001$, t test of least-squares linear regression). During recording, when three distractors were always presented, the monkeys' reaction time was significantly longer and more variable for search than for pop-out (Fig. 1B).

We focused on the lateral intraparietal area (LIP) in the parietal cortex and the lateral prefrontal cortex (LPFC) and frontal eye fields (FEF) in the frontal cortex (*1*, *2*, *4*–*6*, *8*–*11*). For each recording session, we implanted up to 50 electrodes (25 in frontal and 25 in parietal cortex). We recorded the activity of 802 neurons over 24 sessions (*12*).

We determined when each neuron first "found" (reflected) the target location by computing when the amount of information in its firing rate about target location first reached significance (*13*). The data for each trial were grouped by condition (pop-out or search) and by target location, thus factoring out information about target features. The top row of Fig. 2 shows the distribution of these times relative to the start of the saccade. During pop-out, there was a bimodal distribution (Fig. 2A). For each area, there was a population of neurons that first found the target well before the saccade (i.e., shortly after visual array onset) and a separate population that found the target after the saccade. The early population consisted of 35% of all target location–selective LIP neurons (24/68), 51% of selective LPFC neurons (40/78), and 31% of selective FEF neurons (17/54). There were clear differences in timing: LIP neurons found the target first, followed by LPFC neurons and then FEF neurons. Fits of bimodal Gaussians (Fig. 2A) indicated that the early population of LIP neurons was centered at 162 ms before the saccade [95% confidence interval (CI), 200 to 124 ms], followed by the early populations in LPFC and FEF, 77 ms (95% CI, 84 to 70 ms) and 40 ms (95% CI, 56 to 23 ms) before the saccade, respectively (LIP < PFC, $P < 10^{-25}$; LIP < FEF, $P = 6 \times 10^{-8}$; PFC < FEF,

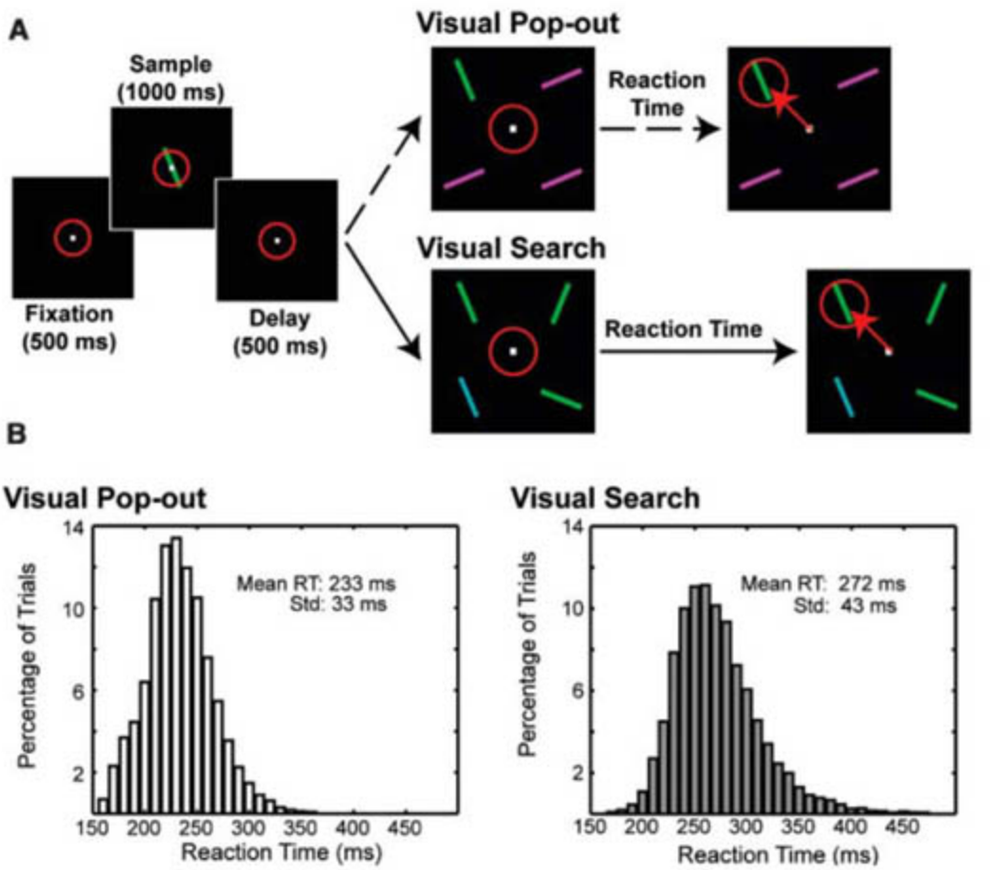

Fig. 1. (**A**) Behavioral task comparing visual search and pop-out. Red circle indicates eye position. (**B**) Histogram of reaction times (RTs) during search and pop-out tasks across all recording sessions for one target and three distractors. Average RTs for search (272 ms) and pop-out (233 ms) differed significantly ($P < 10^{-5}$, t test). The variance in RT also differed significantly (SDs of 43 ms for search and 33 ms for pop-out, $P < 10^{-5}$, χ^2 test).

Picower Institute for Learning and Memory, RIKEN-MIT Neuroscience Research Center, and Department of Brain and Cognitive Science, Massachusetts Institute of Technology, Cambridge, MA 02139, USA.

*To whom correspondence should be addressed. E-mail: ekmiller@mit.edu

$P = 6 \times 10^{-5}$; t test) (*12*). The distribution of the neurons that found the target after the saccade was overlapping in all three areas and centered about 100 ms after saccade (Fig. 2A).

The same ordering was seen in the cumulative distributions of these data (Fig. 2C) (*14*). LIP, LPFC, and FEF neurons began finding the target 170 ms, 120 ms, and 35 ms before saccade, respectively (LIP < PFC, $P = 0.05$; LIP < FEF, $P = 0.009$; PFC < FEF, $P = 0.002$; randomization test) (*12*). One-quarter of the selective LIP neurons (17/68) began encoding the target location before the LPFC population first carried significant information. This is more than expected by chance ($P = 2 \times 10^{-5}$, tested against binomial distribution). When aligning trials on visual array onset instead of saccade, we found similar results (*12*).

In the search task, neurons began finding the target later than in pop-out, just before the saccade, and in the reverse order: The frontal areas (LPFC and FEF) showed selectivity first, followed by LIP (Fig. 2, B and D). About one-third of all selective neurons in FEF and LPFC began to reflect the target location before the saccade (19/60 and 21/70, respectively), whereas only 14% (8/58) of selective LIP cells did so. This is greater than expected by chance for FEF and LPFC, but not for LIP ($P = 8 \times 10^{-5}$, $P = 4 \times 10^{-5}$, and $P = 0.41$, respectively, tested against binomial distribution). The cumulative distributions in Fig. 2D show that target location information reached significance in the FEF and LPFC at 50 and 40 ms before the saccade, respectively, followed by LIP (LPFC and FEF were earlier than LIP, $P = 0.027$ and $P = 0.006$, respectively; randomization test) (*12*). Whereas during pop-out, the LIP neurons found the target first (and well before the saccade); during search, target location information in LIP did not reach significance until 32 ms after the saccade. As with pop-out, similar results were observed when trials were aligned on visual array onset (*12*).

Synchrony of neural activity may increase the effectiveness of connections between brain areas and enhance the representation of attended stimuli (*15*–*19*). To investigate this, we quantified the degree of synchrony between local field potentials (LFPs) in the parietal and frontal cortices. Synchrony was measured between all pairs of simultaneously recorded electrodes that had at least one neuron selective for target location (282 pairs). The degree of synchrony was captured in the coherence statistic, a measure of the co-spectrum between two signals, normalized for the power (*20*). Significance was determined by randomization tests (*12*). Because similar results were found between LIP and LPFC and between LIP and FEF, we combined data from the LPFC and FEF.

During both search and pop-out, there was an increase in coherence between LIP and frontal cortex in a middle (22 to 34 Hz) and upper (35 to 55 Hz) frequency band (Fig. 3) that peaked during the perisaccadic period (i.e., around the time of the attention shift) (Fig. 4A). The increase in coherence for each frequency band differed between bottom-up and top-down (Fig. 4A). This was highlighted by subtracting coherence during pop-out from coherence during search. Figure 4B shows a greater increase in middle-frequency (22 to 34 Hz) coherence between LIP and frontal cortex during top-down search than during bottom-up pop-out. By contrast, the increase in upper-

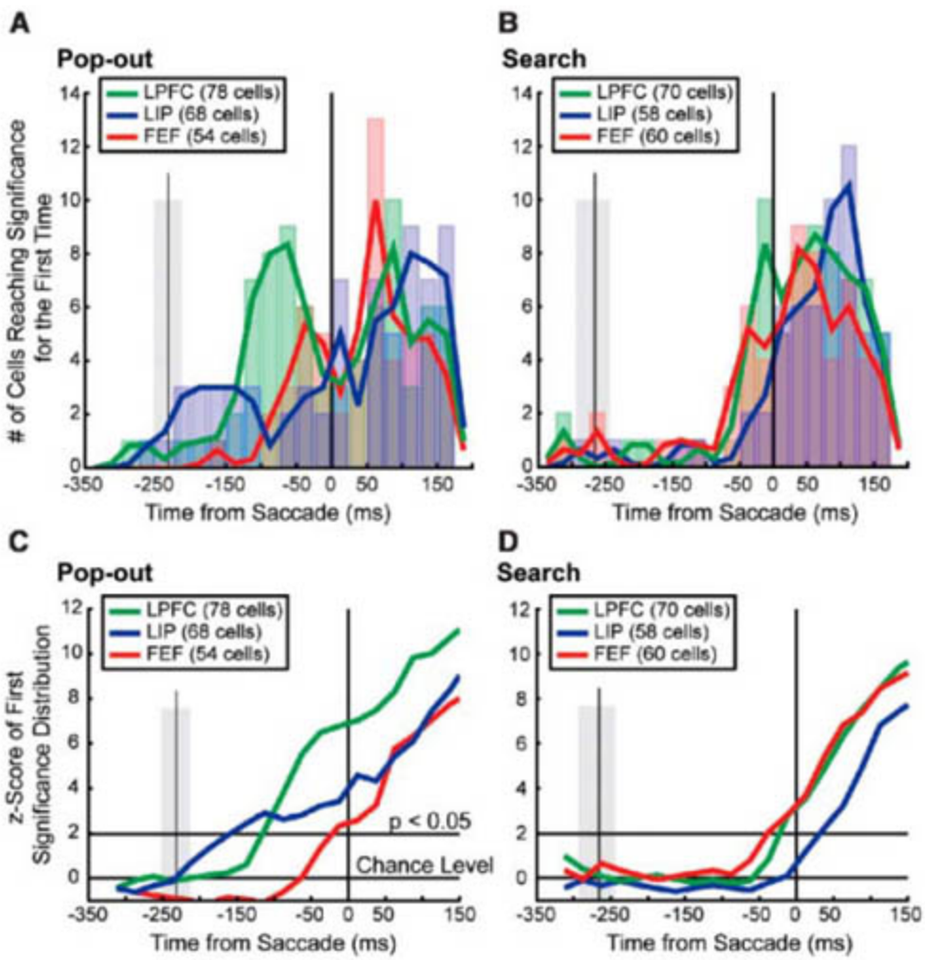

Fig. 2. Timing of target location selectivity during pop-out (left column) and search (right column). Significance was determined through randomization tests (*12*). (**A** and **B**) Distribution of times at which neurons first began to carry significant information about the target location, relative to the saccade. Vertical black line indicates saccade; gray shaded regions indicate mean (±1 SD) of distribution of visual array onset. (**C** and **D**) Normalized cumulative sums of the histograms shown in (A) and (B), respectively. A z-score for the observed distribution was calculated through randomization tests and was corrected for multiple comparisons (*12*).

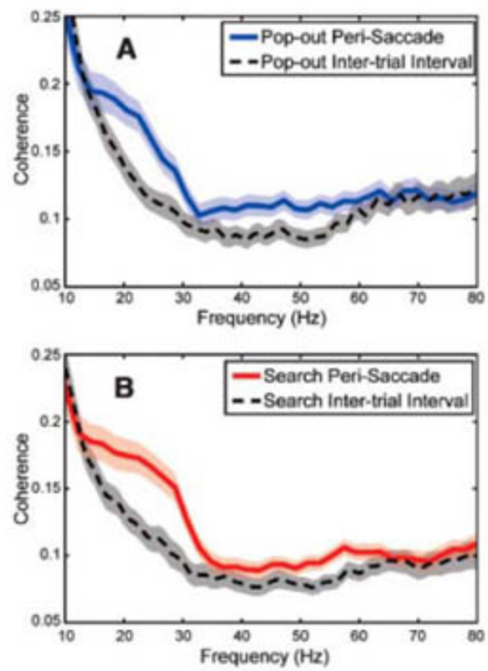

Fig. 3. LFP coherence between LIP and frontal cortex (LPFC and FEF) across frequencies for (**A**) pop-out and (**B**) search tasks. Coherence was calculated around the time of the attention shift (in a perisaccadic period, beginning 150 ms before saccade to 50 ms afterward) and compared to a baseline, an intertrial interval (ITI) epoch (a 200-ms window starting 500 ms before trial onset). Shaded regions are 95% confidence intervals around average coherence. Frequencies below 10 Hz are not meaningful (and are not shown) because of the relatively short time epochs used.

frequency (35 to 55 Hz) coherence was greater during pop-out than during search. Thus, bottom-up and top-down attention may rely on different frequency bands of coherence between the frontal and parietal cortex.

The source of top-down signals has largely been inferred from indirect evidence such as patterns of anatomical connections (*7*). In the case of visual attention, previous research has shown its neural correlates throughout the cortex, with control attributed to parietofrontal networks (*1*, *2*, *5*). Our results suggest that within this network, fast, bottom-up target selection occurs first in LIP, whereas longer-latency top-down selection occurs first in the frontal cortex. This supports the hypothesis that parietal neurons form "saliency maps" for bottom-up selection (*21*–*23*) as well as studies showing that stimulation of the frontal cortex causes attention-like effects in the extrastriate cortex (*24*). It also fits with attenuation of top-down effects in the posterior cortex after PFC damage (*25*–*27*). Although both the frontal and parietal cortex are involved in attention, our results illustrate that bottom-up signals appear first in LIP and top-down signals appear first in the frontal cortex.

Localized synchrony of activity within a brain area may help resolve competition for attentional selection (*18*, *19*), and interareal synchrony may aid in long-range communication between areas (*15*–*17*). Our results suggest that the flow of top-down and bottom-up information is aided by coherence emphasizing different frequency bands. Lower-frequency bands are more robust to spike timing delays and thus may be better suited for longer-range coupling between multiple, distant areas (*28*–*30*). The increase in low-frequency synchrony during search could reflect a "broadcast" of top-down signals on a larger anatomical scale. Synchrony at higher-frequency bands might support the local interactions needed to enhance stimulus representations (*28*–*30*). The emphasis of higher-frequency synchrony during pop-out could reflect local enhancement of stimulus representations that are passed forward from parietal to frontal cortex. This suggests that the brain may emphasize coherence at different frequency bands for the dynamic modulation of interareal connections, which in turn engages the network best suited for the current task.

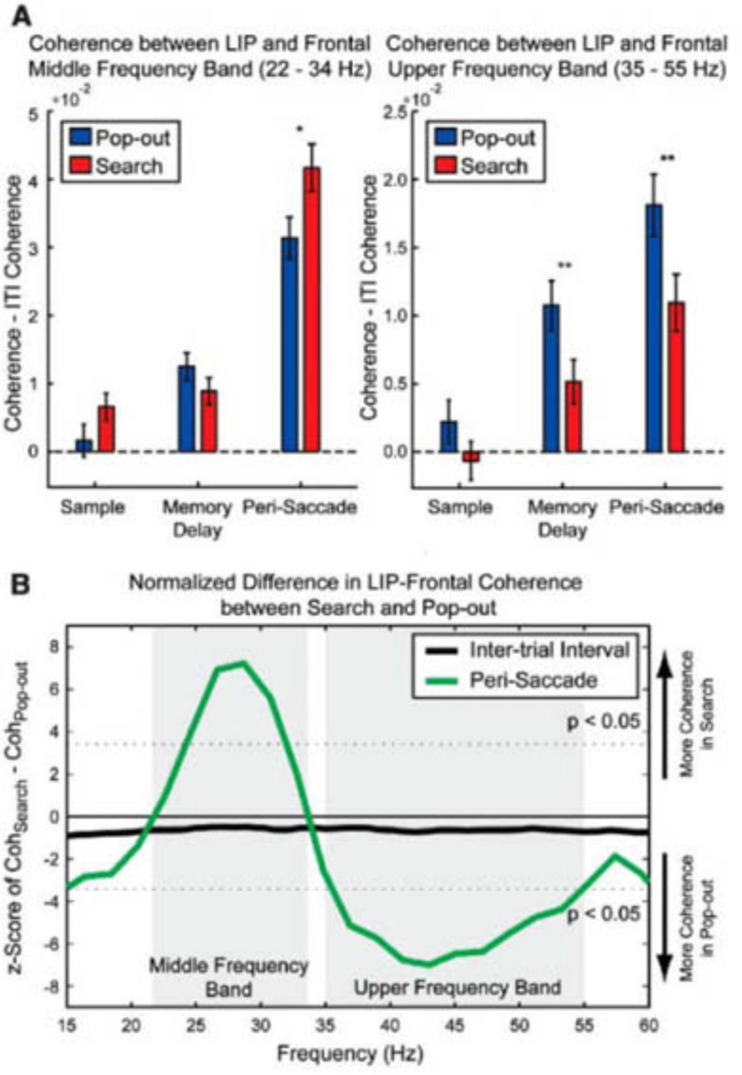

Fig. 4. (**A**) Level of coherence for pop-out and search during the middle (left, 22 to 34 Hz) and upper (right, 35 to 55 Hz) frequency bands in different trial epochs. $^{*}P < 0.05$, $^{**}P < 0.01$ (*t* test). (**B**) Differences in LFP coherence between LIP and frontal cortex during pop-out and search for the perisaccadic period (green) and ITI (black). Pop-out coherence was subtracted from search coherence (Fig. 3). Dashed lines indicate significance levels ($P < 0.05$, corrected for multiple comparisons). Differences above the upper dashed line indicate significantly more coherence during search than during pop-out; differences below the lower dashed line denote significantly more coherence during pop-out than during search.

References and Notes

1. R. Desimone, J. Duncan, *Annu. Rev. Neurosci.* **18**, 193 (1995).
2. S. Kastner, L. Ungerleider, *Annu. Rev. Neurosci.* **23**, 315 (2000).
3. A. M. Treisman, G. Gelade, *Cognit. Psychol.* **12**, 97 (1980).
4. M. Corbetta, G. L. Shulman, *Nat. Rev. Neurosci.* **3**, 201 (2002).
5. J. H. Reynolds, L. Chelazzi, *Annu. Rev. Neurosci.* **27**, 611 (2004).
6. J. D. Schall, *Philos. Trans. R. Soc. London Ser. B* **357**, 1073 (2002).
7. B. T. Miller, M. D'Esposito, *Neuron* **48**, 535 (2005).
8. G. J. Blatt, R. A. Andersen, G. R. Stoner, *J. Comp. Neurol.* **299**, 421 (1990).
9. E. K. Miller, J. D. Cohen, *Annu. Rev. Neurosci.* **24**, 167 (2001).
10. G. B. Stanton, C. J. Bruce, M. E. Goldberg, *J. Comp. Neurol.* **353**, 291 (1995).
11. S. Ferraina, M. Pare, R. H. Wurtz, *J. Neurophysiol.* **87**, 845 (2002).
12. See supporting material on *Science* Online.
13. A sliding window of 25 ms was stepped every 25 ms. Significance was determined by constructing a null distribution through randomization tests (*12*). A neuron was said to first indicate the target location when significant at $P = 0.05$ for two bins in a row.
14. The cumulative distribution is the cumulative sum of the histogram of when each cell first carried significant information about the target location (Fig. 2, top row). The cumulative sum was then normalized for the number of significant cells expected at each point in time by chance. This procedure corrected for multiple comparisons and determined when an area carried information about the target location, allowing us to infer the order of selectivity. See (*12*) for details.
15. A. M. Aertsen, G. L. Gerstein, M. K. Habib, G. Palm, *J. Neurophysiol.* **61**, 900 (1989).
16. E. Salinas, T. J. Sejnowski, *Nat. Rev. Neurosci.* **2**, 539 (2001).
17. P. Fries, *Trends Cognit. Sci.* **9**, 474 (2005).
18. P. Fries, J. H. Reynolds, A. E. Rorie, R. Desimone, *Science* **291**, 1560 (2001).
19. N. P. Bichot, A. F. Rossi, R. Desimone, *Science* **308**, 529 (2005).
20. M. R. Jarvis, P. P. Mitra, *Neural Comput.* **13**, 717 (2001).
21. J. W. Bisley, M. E. Goldberg, *Science* **299**, 81 (2003).
22. C. Constantinidis, M. A. Steinmetz, *J. Neurosci.* **25**, 233 (2005).
23. L. Itti, C. Koch, *Nat. Rev. Neurosci.* **2**, 194 (2001).
24. T. Moore, M. Fallah, *Proc. Natl. Acad. Sci. U.S.A.* **98**, 1273 (2001).
25. H. Tomita, M. Ohbayashi, K. Nakahara, I. Hasegawa, Y. Miyashita, *Nature* **401**, 699 (1999).
26. M. Eglin, L. C. Robertson, R. T. Knight, *Cereb. Cortex* **1**, 262 (1991).
27. L. L. Chao, R. T. Knight, *Cereb. Cortex* **7**, 63 (1997).
28. A. K. Engel, P. Fries, W. Singer, *Nat. Rev. Neurosci.* **2**, 704 (2001).
29. A. von Stein, J. Samthein, *Int. J. Psychophysiol.* **38**, 301 (2000).
30. N. Kopell, G. B. Ermentrout, M. A. Whittington, R. D. Traub, *Proc. Natl. Acad. Sci. U.S.A.* **97**, 1867 (2000).

31. Supported by NSF grant SBE0354378 and National Institute of Neurological Disorders and Stroke grant R01NS035145. We thank S. Henrickson, J. Roy, and M. Wicherski for comments on the manuscript; W. Asaad and K. Maccully for technical and other support; and E. N. Brown for help with the statistical analyses.

Supporting Online Material

www.sciencemag.org/cgi/content/full/315/5820/1860/DC1
Materials and Methods
Figs. S1 to S5
Table S1

28 November 2006; accepted 7 March 2007
10.1126/science.1138071

Cellular Membrane Stain

LavaCell stain is suitable for visualizing cellular membranes in live or fixed cells. LavaCell is a small, neutral, cell-permeable bright orange stain. It has a long Stokes shift, reacts with free amine groups, and does not stain nucleic acids, making it suitable for multiplexing.

Active Motif For information 877-222-9543 www.activemotif.com

Chemotaxis Slide

A new slide for the optical analysis of slow-migrating cells allows the motion tracking of cells such as chemotactic active cancer cells in gradients. Previous comparable cell-based assays have allowed only the tracking of fast-migrating cells such as neutrophils or dictiostelia. The new μ-Slide series allows the formation of long-term stable gradients over a 48-hour period, which enables the user to follow the motion of cells moving at a speed of one cell-length per hour.

ibidi For information +49 (0) 89 57 00 18 06
www.ibidi.com

Electrophysiology Measurements

The NeuroStar, for in vivo electrophysiology experiments, is a comprehensive system that controls recording impedance, stimulation, and data acquisition. From setting up experiments to preparing data for publication, NeuroStar allows researchers to take in vivo experiments from start to finish. A pilot feature provides unassisted exploration for single-unit neuronal activity; NeuroStar software provides automatic database management, where data can be mapped on either a two-dimensional or three-dimensional atlas in real time.

Stoelting For information 630-860-9700
www.stoeltingco.com/physio

Fluorescent Secondary Proteins

New fluorescent secondary antibodies conjugated to the Chromeo line of dyes offer high intensity, low background, and limited photobleaching effects. Chromeo fluorescent secondary antibodies are available in anti-mouse and anti-rabbit formats in 488 nm, 494 nm, 546 nm, and 642 nm wavelengths.

Active Motif For information 877-222-9543
www.activemotif.com

Ultraviolet Detector

The ActiPix D100 is a miniature multiplexed capillary ultraviolet (UV) imaging area detector. Using a capillary as combined sample vessel and optical element, the ActiPlex D100 detector provides inherent spatial separation of sample and reference beams, resulting in a unique self-referencing system in a miniature format. Allowing minute (picoliter to nanoliter) volumes to be measured with high sensitivity without sacrificing spatial resolution, the ActiPix D100 is a suitable detector for capillary liquid chromatography and capillary electrophoresis systems. With an active pixel area sensor to capture measurements, imaging of single or multiple capillaries is achieved on a single sensor. Simultaneous measurement of multiple capillaries allows high throughput of samples. Sensitive and linear over five orders of magnitude dynamic range, applications for the ActiPix D100 include monitoring nanoscale biocatalytic reactions.

Paraytec For information +44 1904 526270
www.paraytec.com

Gel Imaging Software

A new tool converts slab gel TIFF, BIP, JPEG, and TXT files into a standard format for importing electrophoresis data into GeneMarker software. The jelMarker tool was developed in response to the growing demand for software that can analyze fluorescence, chemiluminescence, and autoradiography gel image files, especially those from Li-Cor's 4300 DNA Analyzer and Kodak's Image Station 4000R. Researchers can convert and import the files to take advantage of GeneMarker's rapid analysis in a Windows environment. The jelMarker can import up to two gel image files for simultaneous analysis of two-color data. The software also features easy lane and band modification via a point-and-click methodology.

SoftGenetics For information 814-237-9340
www.softgenetics.com

Proteomic Sample Preparation

Dynabeads SCX for proteomic sample preparation are designed with a surface optimized for binding and fractionation of intricate protein and peptide mixtures. Featuring strong cationic exchange (SCX), these magnetic beads precisely separate proteomic samples based on isoelectric point and net charge differences, in preparation for downstream analyses such as mass spectrometry, high performance liquid chromatography, one-dimensional gel electrophoresis, or two-dimensional gel electrophoresis. Dynabeads SCX add further functionality to Dynal's magnetic bead chromatography product line, which includes products for cation exchange, anion exchange, and hydrophobic capture. Beads with different surface characteristics can be combined to isolate different fractions from the same sample, allowing for step-wise reduction of sample complexity.

Invitrogen For information 800-955-6288
www.invitrogen.com/dynal

Knife for Frozen Hydrated Specimens

A new diamond knife for the sectioning of frozen hydrated specimens features a 25 degree angle for the least possible compression and the best structural preservation. With a cutting range from 25 to 200 nm, it is available in a 3.0-mm diamond width. The triangular holder, suitable for dry sectioning, and the trough, for sectioning using fluids, are both made from a special copper-nickel alloy for good heat conduction. A cold-resistant epoxy resin is used for the seal.

Diatome For information 215-412-8390
www.emsdiasum.com

Newly offered instrumentation, apparatus, and laboratory materials of interest to researchers in all disciplines in academic, industrial, and government organizations are featured in this space. Emphasis is given to purpose, chief characteristics, and availability of products and materials. Endorsement by *Science* or AAAS of any products or materials mentioned is not implied. Additional information may be obtained from the manufacturer or supplier.

POSITIONS OPEN

CURATOR of ANTHROPOLOGY
Position Announcement

The California Academy of Sciences invites applications for the Irvine Chair of Anthropology in its Department of Anthropology. This is a full-time, regular Faculty Position on a ten month annual basis. Applications are solicited from individuals with primary interest in, and commitment to, active field-and-collection-oriented research in any field of systematics-based physical or biological anthropology, using contemporary techniques. Research preferably should be broadly based and multidisciplinary. Successful candidate will have oversight responsibilities for curation, use, and growth of a modest, but important, ethnographic collection (nearly 17,000 objects with particular strengths in the U.S. Southwest, California, Alaska, and Oceania) and will contribute to the varied educational and administrative activities of the Institution, including exhibit development, lecturing, and supervising of departmental support staff. Teaching opportunities at several Bay Area institutions are also possible. Ph.D. is required, and prior experience in museum setting is desirable.

Salary is commensurate with experience and includes an excellent benefits package. To apply, send a letter of interest, curriculum vitae, and a description of research goals, along with the names, mail and e-mail addresses, as well as telephone and fax numbers of three references by June 8, 2007, to: **California Academy of Sciences, Human Resources, Department CA, 875 Howard Street, San Francisco, CA 94103.**

The California Academy of Sciences is a natural history museum, aquarium, planetarium, and research institution presently located in downtown San Francisco. Staff will begin moving into a new facility at the Academy's former location in Golden Gate Park in early 2008, with the facility scheduled for public opening in late 2008. For more information, visit our **website: http://www.calacademy.org** and click on the employment opportunities link. *The California Academy of Sciences is an Equal Opportunity Employer committed to diversity.*

CARDIOVASCULAR MOLECULAR BIOLOGIST

Applications are being accepted for a tenure-track position at the rank of **ASSISTANT/ASSOCIATE PROFESSOR** in the Department of Biomedical Sciences **(website: http://www.dbms.missouri.edu)** and the Dalton Cardiovascular Research Center **(website: http://dalton.missouri.edu)** at the University of Missouri, Columbia. Requirements include M.D., D.V.M., and/or Ph.D. degree. The successful candidate must have proven expertise in molecular biology technologies and have extramural support or demonstrate exceptional potential for the development of a vigorous, sustained research program. Potential for collaborative interactions with current faculty include vascular cell biology, exercise, microcirculation, neural cardiorespiratory control, sex differences, vascular cell-matrix interactions, cardiac function, and large mammal models of cardiovascular disease. Preference will be placed on those whose research utilizes state-of-the-art in vivo and in vitro molecular approaches to cardiovascular and/or exercise-related problems, although outstanding applicants in other related aspects of molecular biology are encouraged to apply. Teaching responsibilities involve molecular biology related lectures to first-year veterinary and graduate students. Review of completed applications will begin July 1, 2007, and continue until the position is filled. Applicants should submit current curriculum vitae; a statement of professional goals, emphasizing research and teaching; and the names of four references to: **Dr. Doug Bowles, Search Committee Chair, E102 Veterinary Medicine, University of Missouri-Columbia, Columbia, MO 65211.** Electronic applications in PDF format may be submitted to **e-mail: bowlesd@missouri.edu.** *The University of Missouri is an Affirmative Action/Equal Opportunity Employer. Applications from women and minorities are strongly encouraged. To request ADA accommodations, please contact our* ***ADA Coordinator*** *at* ***website: http://ada.missouri.edu/index.html.***

POSITIONS OPEN

G. P. WILDER VISITING CHAIR in BOTANY

The Department of Botany, University of Hawai'i Manoa, seeks a **DISTINGUISHED BOTANIST** for the G.P. Wilder Chair. This appointment is available for a period ranging from one semester to an academic year. Applications are sought from individuals in any field of botany with expertise complementary to departmental faculty. Primary duties include sharing of expertise through interactions with faculty and students in the Botany Department and offering a seminar series or course in their specialty area. Salary is competitive and research support may be provided; arrangements will be tailored to the requirements of each Chair holder within the purposes and limits specified by the endowment. Additional information about this position and the Botany Department can be found at **website: http://www.botany.hawaii.edu.** Submit curriculum vitae, contact information (e-mail, phone, fax), a statement of planned activities for the period of appointment, and the names and contact information for three references to: **Dr. Alan Teramura, Chair, Department of Botany, University of Hawai'i Manoa, 3190 Maile Way, Honolulu, HI 96822-2279.** Review of applications will begin April 15, 2007, for fall 2008 and October 15, 2007, for spring 2009. Inquiries by e-mail should be addressed to **e-mail: teramura@hawaii.edu; fax: 808-956-3923.**

The University of Hawai'i at Manoa is an Affirmative Action/Equal Opportunity Employer. Women and members of minority groups are strongly encouraged to apply.

FACULTY POSITION in NEUROSCIENCE
at New Princeton Institute

Princeton University is seeking to make the first of several anticipated new faculty appointments in neuroscience, as part of its new Institute in this area and its growing focus on quantitative approaches to understanding neural coding and dynamics. The position is at the **ASSISTANT PROFESSOR** level, to begin as soon as September 2007, for a **THEORIST** in systems and/or cognitive neuroscience. The appointment will be joint between the Institute and a department appropriate to the individual's background and interests, with possibilities including (but not limited to) psychology, molecular biology, mathematics, physics, electrical engineering or computer science. Applicants should be prepared to teach both an undergraduate and a graduate level course in neuroscience. Please send curriculum vitae, a one-page research description, and three letters of recommendation to the: **Search Committee, Neuroscience Institute, Princeton University, Princeton, NJ 08544,** or by **e-mail: tosearch@neuroscience.princeton.edu.** Materials should be submitted as soon as possible. Applications will be considered on a rolling basis, and the search will remain open until the position is filled. For information about applying to Princeton and how to self-identify, please link to **website: http://web.princeton.edu/sites/dof/ApplicantsInfo.htm.** *Princeton is an Equal Opportunity, Affirmative Action Employer.*

BIOINFORMATICS CONSULTANT

The University of Minnesota Supercomputing Institute seeks to hire a Bioinformatics Consultant to join a dynamic group that provides a high level of technical support for researchers at the University of Minnesota Supercomputing Institute. This is an exciting opportunity to participate in a successful program that provides technical support to a broad range of development efforts and applications in computational bioinformatics and genomics.

Apply directly at the University of Minnesota employment **website: http://employment.umn.edu.** You will need to create an account, and then please apply directly to job # 146937.

The University of Minnesota is an Equal Opportunity Educator and Employer.

Positions @ NIH

THE NATIONAL INSTITUTES OF HEALTH

STAFF SCIENTIST OR STAFF CLINICIAN NEUROIMAGING

The National Institute of Neurological Disorders and Stroke is recruiting for a STAFF SCIENTIST or STAFF CLINICIAN, with a Ph.D. or M.D., respectively, with skills in neuroimaging (MRI/PET, particularly fMRI) and possibly also EEG/MEG. The individual will work in the HMCS, MNB, and collaborate in research projects relating to the normal control of movement and the pathophysiology of movement disorders.

Interested individuals should contact: **Mark Hallett, M.D., Chief, Human Motor Control Section, Medical Neurology Branch, NINDS, NIH, DHHS; Building 10, Room 5N226, 10 Center Drive, MSC 1428, Bethesda, MD 20892-1428. Telephone: 301-496-9526; Facsimile: 301-480-2286; e-mail: hallettm@ninds.nih.gov**. NINDS is a component of the National Institutes of Health, Department of Health and Human Services. Applications must be received by **May 31, 2007**.

Staff Scientist Position

The National Cancer Institute (NCI), Center for Cancer Research (CCR), Vaccine Branch (VB), seeks a Staff Scientist on a renewable appointment to manage a Flow Cytometry Core equipped for sorting of live infected cells and analysis in support of research on HIV/AIDS and Cancer. The Core will have two BD FACSCaliburs, a BD LSRII, and a BD FACSAria with room for expansion. The Staff Scientist will supervise the Core, provide training, maintain up-to-date knowledge of flow cytometry applications and reagents, trouble-shoot new procedures, maintain the instrumentation and establish SOPs. He/She may collaborate, however the position does not include independent resources for investigator initiated research. Minimum qualifications include a Ph.D. and extensive experience in flow cytometry. Salary is commensurate with experience. Applicants should submit a curriculum vitae, bibliography, brief statement of relevant background, and arrange for three letters of recommendation to be sent to:

Ms. Jacqueline McPhail, National Institutes of Health, National Cancer Institute, 41 Medlars Drive, Building 41, Room D804, Bethesda, MD, 20892-1578 , Email:mcphailj@mail.nih.gov. All applications must be received by **April 20, 2007**.

NCI/NIH/DHHS is an equal opportunity employer.

Deputy Director
Fogarty International Center (FIC)

The NIH is seeking exceptional candidates for the position of Deputy Director, Fogarty International Center (FIC) to advance health through international scientific cooperation and to promote and support scientific research and training internationally to reduce disparities in global health. This position offers a unique opportunity for the right individual to assist the Director, FIC in providing strong and visionary leadership to an organization dedicated to international health and global collaboration. This position serves as Deputy to the Director, FIC in coordination of all activities related to the mission and functions of the Center, in the development and execution of plans and policies of the FIC and in the allocation of resources. The Deputy Director provides expert advice and counsel to the Director on the development of and opportunities for international research and research capacity building; on the development and coordination of international agreements in which the NIH participates; and on the development and dissemination of information, nationally and internationally, on the Center's international research and training initiatives. Applicants may browse the FIC Home Page at http://www.fic.nih.gov. Applicants must possess an M.D., Ph.D., or equivalent degree and be an experienced administrator with a broad international programmatic or scientific background; able to interact with full authority; have the demonstrated capability to plan and direct programs of international importance; and have the ability to communicate with and obtain cooperation of the public, private and international organizations and individuals from the international sector. Salary is commensurate with his/her qualifications and experience. Full Federal benefits including leave, health and life insurance, long-term care insurance, retirement, and savings plan (401k equivalent) will be provided. A detailed vacancy announcement that includes application procedures is available at: **http://www.jobs.nih.gov (under vacancy announcement FIC-07-174209)**. Questions may be addressed to **Ms. Yolette Lee, 301-594-2792 e-mail: leeyol@mail.nih.gov**. CV and bibliography, including a statement addressing the qualifications, must be received by **April 30, 2007**.

Health Scientist Administrator

The National Institute of Drug Abuse is recruiting for an energetic, experienced research scientist in the area of clinical, behavioral, social science, or health services research with the ability to synthesize and present science information to a wide variety of audiences. This position is located in Bethesda, Maryland. The successful candidate will be a respected, accomplished scientist with maturity, integrity and outstanding communication skills. Requirements include an M.D. or a Ph.D. degree in clinical, behavioral, social sciences, or health services research or equivalent training and experience. A record of independent research accomplishments documented by an outstanding publication/presentation record and/or administrative experience is desirable.

As a Health Scientist Administrator, you will develop position statements on scientific issues, serve as an authority in the field, represent the Institute before professional, scientific and public interest groups, work as part of a team to develop publications, and actively participate in a wide variety of planning, evaluation, and dissemination activities with NIDA senior staff.

Compensation is commensurate with research experience and accomplishments, and a full Civil Service package of benefits is available (including retirement and 401K equivalent plans as well as health, life, and long-term care insurance).

For additional information about this opportunity as a Health Science Administrator at NIDA, please visit **www.usajobs.gov** where detailed information may be found under Announcement **NIDA-07-177430**. Supplemental documentation must be submitted to **JoAnn Suthill, National Institutes of Health, 111 Alexander Drive, Mail Drop NH-01, Research Triangle Park, N.C. 27709, or faxed to 919-541-3659**.

WWW.NIH.GOV

Announcement of an NIH Roadmap Research Funding Opportunity
ASSAY DEVELOPMENT FOR HIGH THROUGHPUT SCREENING
Request for applications RM-07-008

This RFA is one component of the NIH Roadmap Molecular Libraries and Imaging Initiative (http://nihroadmap.nih.gov/molecularlibraries/). Its goal is to stimulate pharmacological probe design by funding development of scientifically novel and technologically robust assays that can be miniaturized, automated, and used to interrogate small molecule libraries. Investigators are asked to state a biological question that can be addressed through the use of a pharmacological small molecule probe, to further identify the requisite features that should be encompassed in its design, and develop a screening plan of assays that can be used to identify small molecules with essential probe attributes.

Assay development proposals should aim to develop assay protocols for novel molecular targets and phenotypes and provide plans to transition them to a high throughput screening format. Investigators should additionally define and characterize a screening project plan to include secondary and counter-screening assays. Emphasis will be placed on screening targets for which an inadequate array of selective and potent small molecule modulators are available to the public. Support will be provided via a R21 mechanism with $125,000 in direct costs available.

The RFA is intended to promote the development of automated screening projects that enter the Roadmap Molecular Libraries Screening Center Network. Funded applications will be able to directly request screening by the MLSCN following project completion. The overall goal of the Molecular Libraries and Imaging Initiative is to create a public database of biological information about small molecule chemical structures (see PubChem; http://pubchem.ncbi.nlm.nih.gov), which will further seed the development of small molecule pharmacological tools for biological research.

It is anticipated that 20 projects will be funded (for $4 million) in response to this RFA. Further announcements are planned in succeeding years. Investigators should submit a letter of intent by May 2 for the next submission date of May 16, 2007. Additional information about the announcement can be obtained at the following website: http://grants.nih.gov/grants/guide/rfa-files/RFA-RM-07-008.html, or, by contacting Program Director Mark Scheideler, Ph.D., by email at: scheidelerm@ninds.nih.gov

ASSISTANT/ASSOCIATE PROFESSOR OF IMMUNOLOGY

the City College of New York

FLSA Status: Exempt

Compensation: $38,001 - $79,220

College Web Site: www.ccny.cuny.edu

Notice Number: FY - 12848

Closing Date: Open until filled with review of applications to begin 04/01/07.

POSITION DESCRIPTION AND DUTIES: The Biology Department of The City College of New York is undergoing a dynamic growth phase, with many new recent additions. To broaden and strengthen our focus of immunology research, we are looking for a scientist who studies T or B cells or who studies innate immunity in vertebrates or in invertebrate model systems. We welcome applications from individuals studying molecular aspects of signaling mechanisms involved in normal (or dysfunctional) innate immune responses or issues relating to how the innate immune system influences the adaptive immune system.

QUALIFICATION REQUIREMENTS: A Ph.D. and one or more years of postdoctoral work experience. The successful applicant will have demonstrated a record of research productivity and will be expected to work independently and develop an active externally funded research program.

The City College of New York has a strong institutional commitment to diversity. In that spirit, we are particularly interested in receiving applications from a broad spectrum of people, including women and members of under-represented ethnic groups.

TO APPLY: Send curriculum vitae and a letter detailing research interests, and the names and contact information for three references to: **Professor Jerry Guyden, Chair of Search Committee - FY 12848, City College of New York, Department of Biology, MR 633, 160 Convent Avenue, New York, N.Y. 10031, E-mail: jguyden@ccny.cuny.edu.**

Information on the CCNY Science Division can be found at the City College website, **www.sci.ccny.cuny.edu**

The City University of New York is an Equal Employment Opportunity/Affirmative Action/Immigration Reform and Control Act/ Americans with Disabilities Act Employer

CITY COLLEGE IS CUNY

UNIVERSITY of VIRGINIA HEALTH SYSTEM

FACULTY POSITIONS

School of Medicine

Center for Public Health Genomics

The Center for Public Health Genomics at the University of Virginia invites applications for positions at the Assistant to Full Professor level with research interests in human molecular genetics, bioinformatics, genetic epidemiology, or statistical genetics. Primary targets of recruitment are those individuals with interest in the genetics of complex human disease.

Rank of appointment is dependent upon prior experience and research accomplishment. These faculty positions are being jointly recruited in the new multidisciplinary Center for Public Health Genomics with primary academic appointment in an existing Department within the University of Virginia School of Medicine. Candidates who complement existing research strengths in cardiovascular disease, cancer, metabolic disorders, obesity and neurodegenerative diseases are particularly encouraged to apply.

Candidates should have a Ph.D. and/or MD degree and exceptional potential for establishing both collaborative and independent research. Newly renovated, high-quality laboratory space in an exceptional computing support environment will be provided.

Positions are available immediately. Applications should include curriculum vitae, email address, a brief statement of proposed research program, and names and addresses of three references. Please send materials to:

Stephen S. Rich, Ph.D.
Director, Center for Public Health Genomics
University of Virginia School of Medicine, P.O. Box 800717
Charlottesville, VA 22908-0717
email: cphg-search@virginia.edu

The University of Virginia is an Equal Opportunity, Affirmative Action Employer. Women and members of minority groups are strongly encouraged to apply.

Rosalind Franklin University of Medicine and Science
Department of Physiology and Biophysics
Seeking Assistant/Associate Professors

The Department of Physiology and Biophysics in the Chicago Medical School at Rosalind Franklin University of Medicine and Science is seeking applications to fill two tenure-track faculty positions at the Assistant/Associate Professor level. The successful candidates will be expected to develop meritorious extramurally funded research programs and have a strong commitment to medical and graduate student education. We are particularly interested in individuals who will complement existing departmental and institutional strengths, including: membrane transport, protein trafficking, protein structure, cell biology, virology, neuroscience, and cardiovascular and respiratory physiology. The Department is located in a new, state-of-the-art research building designed for multidisciplinary research group interactions.

The University has begun an expansion campaign to fill twenty-five new faculty slots, all with nationally competitive salaries and start-up packages.

Rosalind Franklin University of Medicine and Science is located in North Chicago, IL, a suburb approximately 40 miles north of the city of Chicago. Nearby tollways and train stations provide easy access to the many cultural and recreational amenities of metropolitan Chicago.

Please submit a *curriculum vitae* along with a one-page summary of research and teaching interests and future plans. The review of applicants will begin **April 16, 2007**, and continue until the positions are filled. Applications and nominations should be submitted by mail or email to: **Robert J. Bridges, Ph.D., Chairman, Department of Physiology and Biophysics, Rosalind Franklin University of Medicine and Science, Chicago Medical School, 3333 Green Bay Road, North Chicago, IL 60064, bob.bridges@rosalindfranklin.edu**.

Rosalind Franklin University of Medicine and Science is an Equal Employment Opportunity/Affirmative Action Employer.

The University of Edinburgh

The University of Edinburgh is an exciting, vibrant, research-led academic community offering opportunities to work with leading international academics whose visions are shaping tomorrow's world.

Chair of Developmental Biology and Anatomy

£48,162 – £80,887

This newly created post will be held in the School of Biomedical Sciences (SBMS). You will have a particular commitment to, and academic responsibility for, the discipline of Anatomy within the College. You will make a major contribution to the academic leadership of the School and be encouraged to draw on excellent opportunities for collaboration within the School, College and University. An established international reputation for excellence in research in Developmental Biology is required.

Further information may be obtained by contacting either Professor John Savill, Head of College (headcmvm@ed.ac.uk) or Professor Tony Harmar, Head of School, (head.SBMS@ed.ac.uk).

Please note that this is a re-advertisement. Previous applicants should not apply.

Apply online, view further particulars or browse more jobs at our website. Alternatively, telephone the recruitment line on 0131 650 2511. Ref: 3007169SI. Closing date: 27 April 2007.

Committed to Equality and Diversity

www.jobs.ed.ac.uk

The Faculty of Science of the University of Fribourg/Switzerland
(Department of Geosciences)

invites applications for the positions of

one **FULL PROFESSOR**
and one
ASSOCIATE PROFESSOR
in Physical Geography

The successful candidates should have expertise in (1) physical processes and environmental changes concerning the cryosphere in mountain regions, and/or in (2) geomorphological processes controlling mass transfers and landscape evolution in mountain regions. He or she must have an excellent scientific record and will develop a competitive research programme. Teaching involves courses in Physical Geography at the BSc, MSc, and PhD levels.

Candidates are requested to submit their application by **May 31, 2007**, according to the information and guidelines provided under:

www.unifr.ch/geosciences/geographie/newposition.pdf

DIRECTOR, INDIANA UNIVERSITY CENTER FOR REGENERATIVE BIOLOGY AND MEDICINE INDIANA UNIVERSITY-PURDUE UNIVERSITY INDIANAPOLIS

The Department of Biology in the School of Science at Indiana University-Purdue University Indianapolis (IUPUI) seeks outstanding applicants for the Directorship of the Indiana University Center for Regenerative Biology and Medicine (CRBM). The successful applicant will have an established research program in developmental or regenerative biology commensurate with appointment at the rank of Associate or Full Professor. The Director is expected to take a leadership role in building the research capacity and external funding of the CRBM and to further develop graduate programs and technology transfer in regenerative biology and medicine. Candidates must be sensitive to the needs of, and possess an interest in, working in an academic community that is diverse with regard to gender, race, ethnicity, nationality, sexual orientation, and religion. Salary will be commensurate with experience and start-up funds will be available.

The CRBM is a collaborative effort between the School of Science, the School of Medicine, and industry. The goal of the CRBM is to understand the mechanisms of tissue, organ, and limb regeneration and translate that understanding into clinical regenerative therapies. The CRBM interacts with other centers on campus that have overlapping research interests and has access to numerous core facilities, including facilities for flow cytometry and imaging, computational molecular science, transgenic and knockout mice, DNA and protein synthesis and sequencing, translational genomics, and proteomics. For more information, see the CRBM website at **www.regen.iupui.edu**. The state of Indiana is engaged in a major life sciences initiative that unites the expertise of academic institutions and private industry. As part of this initiative, regenerative biology and medicine is a research area of high priority for the Department of Biology. For information on the department, visit **www.science.iupui.edu**.

IUPUI is the Indianapolis campus of Indiana University. The campus enrolls 29,000 students in over 185 degree programs and is the top generator of research funding in the state. For more information on IUPUI, visit **www.iupui.edu**. Indianapolis is the 14th largest city in the United States, with a metropolitan area population of 1.6 million, a relatively low cost of living and many cultural, recreational and educational venues.

Letters of application, a curriculum vitae, and the names of three references, should be directed electronically to **David L. Stocum** at **dstocum@iupui.edu**. Our mailing address is: **Department of Biology, IUPUI, 723 W. Michigan St., Indianapolis, IN, 46202**. Applications will be accepted until **May 15, 2007** or until a suitable candidate has been identified.

IUPUI is an Affirmative Action/Equal Opportunity Employer.

OPPORTUNITIES FOR SCIENTISTS OF INDIAN ORIGIN

GOVERNMENT OF INDIA
MINISTRY OF SCIENCE & TECHNOLOGY
DEPARTMENT OF BIOTECHNOLOGY RAMALINGASWAMI FELLOWSHIP

Applications/nominations are invited for **"Ramalingaswami Fellowship"**, a scheme newly instituted by the Department of Biotechnology, Ministry of Science & Technology, Government of India. The scheme is for scientists , physician researchers and bio-engineers of Indian origin working outside the country all over the world in various fields of biotechnology, life sciences, bio-engineering, translational science and other related disciplines who are interested in taking up scientific research positions in India.

The applicant should possess a higher degree or equivalent, such as PhD in Life Sciences/ Agriculture, Bioinformatics, Engineering, Masters in Engineering or Technology/ Medicine etc. and outstanding track record reflected in publications and other recognitions. The duration of the fellowship will be for a period of five years, extendable by another 5 years.

NATURE OF SUPPORT:

- The amount of the fellowship will be Rs.50,000/- per month for the first 3 years and Rs.60,000/- per month during the last two years. Each awardee will, in addition, receive a contingency grant of Rs. 5.00 lakh per annum.
- Ramalingaswami Fellows could work in any of the scientific institutions / universities in the country. They would also be eligible for fast track and regular research grants through extramural and other research schemes of various S&T agencies of the Government of India.

Nominations/applications should be sent post or email to :
Dr. Meenakshi Munshi,
Joint Director
Department of Biotechnology,
Block-2, 6-8th Floor, CGO Complex,
Lodi Road, New Delhi - 110 003.
Email: meenakshi29@dbt.nic.in

The applications/nominations may be sent with consent of the proposed host institute **latest by 20th April, 2007.** In the event, assistance is required for locating a host institute, facilitation will be provided upon request. **For application format and other details please visit the website of the Department: www.dbtindia.gov.in**

PROFESSOR OF NANOPHOTONICS

the City College of New York

Position Detail: Tenure Track - Assistant/Associate/ Full Professor

Compensation: Commensurate with Experience

College Web Site: www.ccny.cuny.edu

Notice Number: FY - 13111

Closing Date: Position is open until filled, with review of applications to begin on May 1, 2007.

POSITION DESCRIPTION AND DUTIES: The Division of Science seeks researchers in the areas of nanoscale photonic materials synthesis, near-field microscopic characterization, nanoscale photonic device fabrication, bio-photonics and/or quantum information sciences. The successful candidate is expected to develop a vigorous externally funded research program and interact synergistically with ongoing nanoscale photonics research activities at the college and with colleagues at other City University of New York campuses that are active in the CUNY Photonics Initiative.

QUALIFICATION REQUIREMENTS: Ph.D. required for appointment in all professoriate ranks. Depending on applicant's qualifications and experience, appointment will be made at assistant, associate or full professor level.

TO APPLY: Applicants should provide a CV with a list of publications, a description of future research plans, teaching interests and experience, and 3 letters of recommendation sent independently to: **Dean Maria Tamargo, Nanophotonics Faculty Search, Attention: Ms. Wildys Rosario, The City College of New York, 160 Convent Ave., Division of Science, Room #MR-1320, New York, NY 10031. Or, by email to: wrosario@ccny.cuny.edu.**

For CCNY website posting see: **http://www1.ccny.cuny.edu/positions.**

The City University of New York is an Equal Employment Opportunity/Affirmative Action/Immigration Reform and Control Act/ Americans with Disabilities Act Employer

CITY COLLEGE IS CUNY

Northeastern University

Higher Learning. Richer Experience.

Northeastern University (**http://www.biology.neu.edu/index.html**). The successful candidate will lead and expand an evolving department that plays a key role in the research and educational missions of the University.

We are seeking nationally recognized leaders who have an on-going record of competitive research funding. The **Biology Department** has 28 faculty and is currently searching to fill two additional **tenure track positions**. The Department's undergraduate programs enroll 450 biology majors and 270 undergraduates in two interdepartmental programs, biochemistry and behavioral neuroscience. Graduate programs serve 50 PhD students. There are also professional MS programs in Bioinformatics, Biotechnology, and Marine Biology.

Research interests in the department are diverse and span the spectrum from organismal to molecular studies. The successful candidate will complement these areas or will bring his/her own theme and cluster of key hires. We are especially interested in an individual who will foster and expand collaborative and interdisciplinary research. Existing interdisciplinary initiatives include Biotechnology, Neurobiology, Sensing and Imaging, and Nanotechnology, with participants from Chemistry and Chemical Biology, Physics, Engineering and the College of Health Sciences. As part of the University's continuing growth as a research institution, Northeastern is in the process of hiring 30 outstanding faculty to pursue interdisciplinary research and teaching.

A competitive start-up package will be provided. Please send a letter of application, curriculum vitae, the names and contact information for five references, and a brief description of research interests. The earliest anticipated start date is fall of 07, and the search will continue until the position is filled. Applications should be submitted electronically to **biojobs@neu.edu**.

Northeastern University is an Equal Opportunity/Affirmative Action Employer. Candidates from groups underrepresented in science are especially encouraged to apply.

Tenure-Track Faculty Position
The Department of Microbiology and Immunology
Medical University of South Carolina
Charleston, South Carolina

The Department of Microbiology and Immunology at the Medical University of South Carolina is seeking applicants for tenure-track positions at the Assistant Professor level in the areas of tumor vaccine development and/or tumor gene therapy. New faculty will have access to a competitive salary and startup funds and benefit from protected time for the establishment of a nationally competitive research program. Independent funding is highly desirable. Relocation of established funded research programs in tumor vaccines or tumor gene therapy will be considered. In 2006, new laboratory space opened in the Hollings Cancer Center. The Department provides teaching to multiple colleges within the University, and all Faculties participate in professional and graduate education as well as maintain an active research program.

The Medical University of South Carolina is a rapidly growing research environment. Extramural research support has consistently increased over the past 10 years, topping $189 million in 2006. Research centers include the Hollings Cancer Center and the Center for Cell, Gene, and Vaccine Therapy. State-of-the-art research facilities include X-ray crystallography, mass spectrometry, proteomics, microarrays, functional imaging, and confocal microscopy. A BSL-3 small animal/wet lab is completed and will be commissioned by the fall. A major new facility in biomolecular NMR is under development. The Charleston area provides an outstanding quality of life in a historic coastal community offering excellent opportunities in the arts, sports, recreation, and cuisine.

Please reply to **www.jobs.musc.edu** or **www.musc.edu/hrm** position **#043499**, or send curriculum vitae, research interests, and send three letters of recommendation addressing both research and teaching potential to: **Tumor Immunology Search Committee, c/o Katherine Lindley, Department of Microbiology and Immunology, Medical University of South Carolina, 173 Ashley Avenue, PO Box 250504, Charleston, SC 29425.**

The Medical University of South Carolina is an Affirmative Action/Equal Opportunity Employer.

NATIONAL JEWISH
Medical and Research Center

Global Leader in Lung, Allergic and Immune Diseases

FACULTY POSITION:

The Integrated Department of Immunology and Division of Mycobacterial and Respiratory Infections at National Jewish Medical and Research Center and the University of Colorado at Denver and Health Sciences Center invites applications for a faculty position at the Assistant or Associate Professor level.

The successful candidate will be expected to develop a competitive research program studying the host immune responses to pathogens. Candidates should have a Ph.D. and/or M.D. degree and at least three years of post-doctoral experience.

Please send your curriculum vitae and statement of research interests and arrange for three letters of reference to be sent to:

Dr. Phillippa Marrack, Chair, Search Committee
National Jewish Medical and Research Center
1400 Jackson Street, 5th Floor, Goodman Building, Denver, Colorado 80206
marrackp@njc.org

The University of Colorado and National Jewish Medical and Research Center are Affirmative Action/Equal Opportunity employers.

University of Colorado Health Sciences Center

Featured Employers

Search **ScienceCareers.org** for job postings from these employers. Listings updated three times a week.

Abbott Laboratories www.abbott.com

Amgen www.amgen.com

Elan Pharmaceuticals www.elan.com/careers

Genentech www.gene.com

Kelly Scientific Resources
www.kellyscientific.com

Novartis Institutes for BioMedical Research
www.nibr.novartis.com

Pfizer Inc.
www.pfizer.com

Philip Morris
www.cantbeattheexperience.com

Pioneer Hi-Bred
www.pioneer.com

If you would like to be a featured employer, call 202-326-6543.

ScienceCareers.org
We know science AAAS

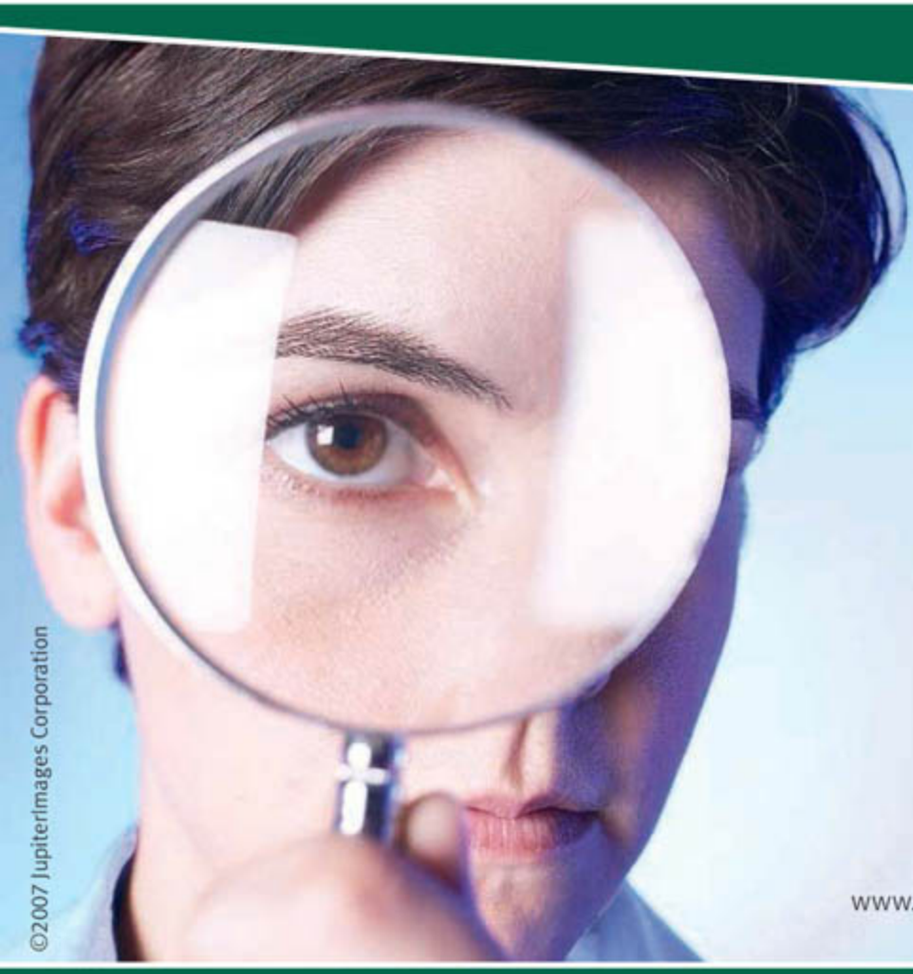

Looking for Career Advice?

Find a wealth of information relevant to your current career and future employment decisions in the *Science* Career Features.

UPCOMING FEATURES:

April 6: Careers in Cancer Research

April 20: Postdoctoral Careers: Transferable Skills

April 27: Biotech and Pharma

Also available online at:
www.sciencecareers.org/businessfeatures

ScienceCareers.org
We know science AAAS

U.S. Environmental Protection Agency
Office of Research and Development
National Exposure Research Laboratory (NERL)

Branch Chief (Supervisory Biologist/Supervisory Physical Scientist), GS-14/15

The U.S. Environmental Protection Agency is seeking qualified applicants for a Branch Chief position located in the National Exposure Research Laboratory (NERL), Environmental Sciences Division (ESD), Las Vegas, NV(**http://www.epa.gov/esd**). The incumbent of this position will serve as the Chief of the Landscape Ecology Branch and is expected to work both as a Supervisory Biologist/Supervisory Physical Scientist and to conduct research as a nationally and/or internationally recognized expert in his/her field of research related to the ESD's and NERL's mission. The incumbent will be responsible for the administrative management of the Branch, which conducts research in the field of landscape ecology and related disciplines, develops landscape assessment and characterization applications, and devises tools and methods for the solution of regional environmental problems, specifically regarding the vulnerability of ecosystems and watersheds to human-induced and natural stress. The incumbent serves as a first-line supervisor for a staff of about 20-25 researchers, technicians, and support staff located primarily in Las Vegas.

This is a permanent, full-time position requiring U.S. citizenship. Candidates must meet U.S. Office of Personnel Management qualification requirements including specific educational course work. Desirable applicants will have a degree in the areas of biology, landscape ecology or related biological and/or physical sciences disciplines. Salary ranges from $79,115 to $120,981 and is commensurate with qualifications. The selected candidate will be eligible for a full benefits package, including relocation, health insurance, life insurance, retirement, and vacation and sick leave.

HOW TO APPLY: This position will be advertised through the Federal Government's job web site: **http://www.usajobs.gov**. For additional information regarding the application process, please contact: **Ms. Barbara Howard** at **(800) 433-9633** or via email at **howard.barbara@epa.gov**.

The U.S. EPA is an Equal Opportunity Employer.

Do what you love.

Love what you do.

www.sciencecareers.org

ScienceCareers.org
We know science AAAS

Get the experts behind you.

www.ScienceCareers.org

now part of ScienceCareers.org

- Search Jobs
- Next Wave
- Job Alerts
- Resume/CV Database
- Career Forum
- Career Advice
- Meetings and Announcements
- Graduate Programs

All features on ScienceCareers.org *are FREE to job seekers.*

ScienceCareers.org
We know science AAAS

Q AAAs

Katherine Socha, Ph.D.
I got interested in math rather late. But I liked diagramming sentences in high school. In college, I found a similar sort of architectural approach to mathematics and science.

S. James Gates Jr., Ph.D.
When I was six my father gave me some books on rockets and stars, and my universe exploded.

Leonard Susskind, Ph.D.
My father had no idea what a physicist was until I told him I wanted to be like Einstein.

Why did you become a scientist?

We would love to know. E-mail us with the answers to the following questions and you could appear in an advertisement in *Science*: What first made you want to be a scientist? How did you get into science? And what are the most important aspects of your work and how will it impact the future?

Find out more at www.aaas.org/stories

AAAS
ADVANCING SCIENCE, SERVING SOCIETY

International Society for Stem Cell Research

5th ISSCR Annual Meeting

The world's premier stem cell research event

June 17–20, 2007

Cairns Convention Centre
Cairns, Queensland, Australia

REGISTER NOW

Attend the Premier Meeting in Stem Cell Research

Early Registration Discount Deadline:
April 17

Details Available at
www.isscr.org

Australian StemCell Centre

Co-Sponsored by
the Australian Stem Cell Centre

POSITIONS OPEN

DENNING FAMILY PROFESSOR of SUSTAINABLE DEVELOPMENT

Columbia University in the City of New York seeks to hire a Professor of Sustainable Development, at the **ASSOCIATE PROFESSOR LEVEL or HIGHER,** whose research and education focuses on sustainability science. This endowed Professorship, made possible by a gift from the Denning Family, is associated with the establishment of the Denning Family Program in Sustainable Development. The candidate is expected to develop a vigorous program of externally funded research in environmental sustainability and contribute to the establishment of an undergraduate major in sustainable development. Columbia University is a world leader in sustainable development with an existing, highly competitive Ph.D. program in sustainable development, an undergraduate concentration in sustainable development, and an increasing number of faculty and research associates in economics, international and public affairs, the Business School, Barnard College, the Lamont-Doherty Earth Observatory, and the Earth Institute involved with sustainable development. The appointment will be in the Department of Ecology, Evolution, and Environmental Biology. A Ph.D. in the natural sciences or related field is required. Application screening begins May 15, 2007. Please send electronically the following five items in application for the position; (1) a curriculum vitae, (2) statement of research, (3) statement of education, (4) conceptualization of a program in sustainable development, and (5) list of three reference contacts (name, institution, and e-mail address) to: **Shahid Naeem, Chair of the Denning Family Search Committee, Department of Ecology, Evolution, and Environmental Biology, Columbia University, e-mail: sn2121@columbia.edu.** For further information, see **website: http://www.columbia.edu/cu/e3b/denning.html.**

Applications from women and minorities are encouraged. Columbia University is an Equal Opportunity/Affirmative Action Employer.

ANATOMIST

The Department of Health Sciences at East Tennessee State University (ETSU) seeks applications for a tenure-track position at the **ASSISTANT PROFESSOR** level opening in August 2007. The position requires teaching undergraduate lecture and laboratory courses in anatomy/physiology and upper-division human anatomy. Development of a fundable research program that complements the mission of the Department is expected. Ph.D. preferred, however, candidates holding other graduate degrees with extensive University-level teaching experience in anatomy may be considered. Application review will begin immediately. Salary will depend on qualifications and experience. Please submit ETSU application, curriculum vitae, a description of research interests, and the names of three references to: **Dr. Michael Gallagher, Professor and Chair, East Tennessee State University, Department of Health Sciences, P.O. Box 70673, Johnson City, TN 37614-1709, e-mail: gallaghe@etsu.edu.**

ASSOCIATE RESEARCH SCIENTISTS
Columbia University Institute for Cancer Genetics

Associate Research Scientist positions available to study molecular pathogenesis of various cancers including breast, lymphoid, prostate, Wilms tumor, acute leukemias, and brain cancers. Ph.D. or M.D. and extensive related research experience required. Please send statement of research interests, curriculum vitae, availability, and names of references to: **Dr. Linda Lowenstein, Institute for Cancer Genetics, Columbia University, 1130 St. Nicholas Avenue, Room 508, New York, NY 10032.**

Columbia University is an Affirmative Action/Equal Opportunity Employer.

POSITIONS OPEN

The U.S. Army Engineer Research and Development Center Environmental Laboratory (ERDC-EL) has career opportunities for **COMPUTATIONAL BIOLOGISTS and BIOINFORMATICISTS** in a fully funded program in toxicogenomics and predictive toxicology. We are expanding our traditional ecotoxicology studies using toxicogenomic (genomics, proteomics, and metabonomics) and computational toxicology methods to assess and predict effects on ecological receptors (rats, birds, fish, and earthworms). Master's or Ph.D.-level researchers are needed to direct, develop, and execute bioinformatics and computational biology/toxicology efforts within this program. Fields of interest include, but are not limited to: (1) Biological networks (e.g., approaches for the analysis of metabolic and signaling pathways, and regulatory networks); (2) Comparative and functional genomics (e.g., protein and genome evolution; transcriptional and metabolite profiling); (3) Metagenomics (e.g., analysis of microbial consortia); (4) Structural bioinformatics (e.g., analysis of protein structural domains; homology modeling); (5) Knowledge discovery and data mining (e.g., biological data integration, cluster analysis, pattern discovery, biological ontologies); (6) Predictive toxicological modeling. Salaries will be competitive and financial recruitment incentives are available. The positions are available and will remain open until filled. To apply, send or e-mail a letter containing a statement of career objectives and research interests, a resume, and examples of recent publications, along with the names, telephone numbers, and e-mail addresses of three references to: **Dr. Ed Perkins (e-mail: edward.j.perkins@us.army.mil), Environmental Laboratory, U.S. Army Engineer Research and Development Center, 3909 Halls Ferry Road, Vicksburg, MS 39180.**

DIRECTOR
Natural Sciences

Southeastern Natural Sciences Academy, a leader in environmental research and education, seeks an exceptionally qualified scientist with a Ph.D. in ecology or related field, with extensive experience in managing a research and education institute, credentials to serve as Principal Investigator on major research projects related to river basin and restoration ecology, proven ability to build collaborative research and education programs, and strong administrative and management experience, to serve as Director and Chief Scientific Officer of the Academy. The ideal candidate will be visionary in evaluating critical natural resources issues, skilled in formulating plans to develop programs around those issues, and have expertise in technical grant writing. In addition, the Director will develop and maintain effective local and regional networks, and academic affiliations. Salary is commensurate with experience and accomplishments, and a package of benefits (including retirement and health insurance) is available. Applicants should send curriculum vitae, statement of research interests, and contact information for three references, preferably by e-mail, by April 20, 2007, to: **Director Search Committee, Southeastern Natural Sciences Academy, 1858 Lock and Dam Road, Augusta, GA 30906. E-mail: jobs@naturalsciencesacademy.org.**

For more information about the Academy and a full position description, please visit our **website: http://www.naturalsciencesacademy.org.**

A cardiovascular laboratory in Temple University School of Medicine is looking for **POSTDOCTORAL FELLOWS** to study mechanisms of cardiovascular disease, **website: http://develop.temple.edu/medicine/faculty/w/wangh.asp.** The applicants should have strong background in molecular biology and cardiovascular science. Lipid or animal work experience is preferred. Send curriculum vitae and three references to: **Dr. Hong Wang, 3420 N. Broad Street, Philadelphia, PA 19140** or **e-mail: hongw@temple.edu.**

POSITIONS OPEN

POSTDOCTORAL FELLOW in BIOINFORMATICS
University of Washington
Seattle, Washington

The bioinformatics group of the Northwest Regional Center of Excellence for Biodefense and Emerging Infectious Diseases Research and the Samuel I. Miller Laboratory at the University of Washington consists of outstanding biologists and computer experts who combine their specific skills to provide computational solutions to biological problems while working closely with bacterial pathogenesis researchers. The research focus for this position involves comparative genomics of gram-negative bacteria in conjunction with proteomics and microarray data analysis to find genes or genetic polymorphisms that have consequences for pathogenicity in humans. This position provides an opportunity for a Biologist with laboratory experience to develop bioinformatics programming skills using Perl scripts, the statistical language R, or other programming languages. Candidates with strong analytical skills and a track record of accomplishment in a biological discipline are encouraged to apply. A Ph.D. in microbiology, molecular and cellular biology, genetics, or a related biological science is required. Prior programming experience is desired but not essential. To apply, send curriculum vitae, a list of three references, and a brief statement of research interests and goals to **Dr. Mitchell Brittnacher** at **e-mail: mbrittna@u.washington.edu.**

POSTDOCTORAL FELLOWSHIP in DRUG DELIVERY
Harvard University

Applications are invited for a Postdoctoral position in the School of Engineering and Applied Sciences, Harvard University. The research focus is on targeted liposome delivery and determining the cellular response to chemical cues. We study the impact of chemical cues on cell protein regulation for clinical applications. Prior hands-on experience in the areas of polymer chemistry, molecular and cellular biology, and in vivo testing a plus. We are seeking a highly motivated candidate with an experimental background, strong academic record and publications. The candidate should have a Ph.D. (or expect to graduate by June 2007) in chemical engineering, bioengineering, materials science, or related disciplines. The candidate is expected to start in summer 2007. Applicants should send their curriculum vitae, list of publications, and names of three references to: **Debra Auguste (e-mail: auguste@seas.harvard.edu).**

Harvard is an Equal Opportunity/Affirmative Action Employer. We strongly welcome applications from qualified women and minority group members.

POSTDOCTORAL POSITIONS

Up to four Postdoctoral positions are available to study the role of complement and inflammation in: (1.) Ischemia/reperfusion injury, (2.) Organ transplantation and, (3.) Apoptosis-based therapy of cancer. A background in immunology is preferred and, for organ transplantation projects, experience in small animal surgery is essential (preferably mouse cardiac transplantation). Experience in molecular biology techniques and/or recombinant protein expression would also be helpful for some projects. Skills in oral and written communications are essential. These positions are being offered in the Laboratories of **Drs. Stephen Tomlinson and James Norris.** Please reply to **websites: http://www.jobs.musc.edu** or **www.musc.edu/hrm** position #043495 or send curriculum vitae and research interests by **e-mail: tomlinss@musc.edu. Stephen Tomlinson, Ph.D., Medical University of South Carolina, Department of Microbiology and Immunology, P.O. Box 250504, 173 Ashley Avenue, Charleston, SC 29466.**

POSITIONS OPEN

POSTDOCTORAL FELLOWSHIP
Wellesley College

Wellesley College invites applications for a Postdoctoral Fellowship (two to three years) for projects on neuropeptidases and steroid hormones in brain. The Fellow will work with an interdisciplinary (biological chemistry and neuroscience) team of faculty mentors and our undergraduate students on localization and role of an endopeptidase in brain. Experience in biochemistry and molecular biology, including enzymology or immunohistochemistry, is desirable. The Fellow will have opportunities for mentored teaching assignments. Applications, including curriculum vitae, statement of research experience and research interests, and three letters of recommendation, should be sent to: **Adele Wolfson, Office of the Dean of the College, Wellesley College, 106 Central Street, Wellesley, MA 02481,** or **e-mail: awolfson@wellesley.edu.** Review of applications will begin on April 30, 2007. Wellesley College has been a leader in the education of women for more than 130 years, and continues to be one of the top liberal arts colleges in the country. Located near Boston, the College provides outstanding resources for teaching and research. *Wellesley College is an Affirmative Action/Equal Opportunity Employer, and we are committed to increasing the diversity of the College community and the curriculum. Candidates who believe that they can contribute to that goal are encouraged to apply.*

POSTDOCTORAL POSITIONS available immediately to investigate molecular mechanisms in acute myeloid leukemia using the mouse as a model system. Our Laboratory focuses on the zinc finger oncoprotein EVI1. We have developed a number of genetic models to investigate its function. Please send curriculum vitae and names of three references to: **Archibald S. Perkins, M.D., Ph.D.,** at **e-mail: archibald.perkins@yale.edu.**

MARKETPLACE

What if staying up to date with the latest technology published in journals and patents were as easy as pushing a button?

It is.

With the "Keep Me Posted" alerting feature, SciFinder sends you automatic updates on areas you—and your competitors—are interested in.

You can monitor specific research topics, companies, authors, substances, or sequences, and choose how frequently you receive notifications: daily, monthly, or weekly.

The service isn't just convenient, it's incredibly current. Journal article records often appear in SciFinder before they're even in print. New references, substances, and sequences are added daily. Patents from all the major offices are added within two days of issuance.

As with all SciFinder features, Keep Me Posted is integrated with your workflow. At any point in a search (including the beginning), simply click on the Keep Me Posted button. SciFinder tracks your steps and will generate the appropriate alert—even for complex topics. When you receive a notification, you can follow each reference as you would in a search: find citing or cited articles (with links to the electronic full text), and follow referenced substances and reactions for further information.

Comprehensive, intuitive, seamless—SciFinder doesn't just alert you, it's part of the process. To find out more, call us at 800-753-4227 (North America) or 614-447-3700 (worldwide) or visit www.cas.org/SCIFINDER.

SciFinder®

Part of the process.™

In flow cytometry, every dot tells a story . . .

The ImageStream® system

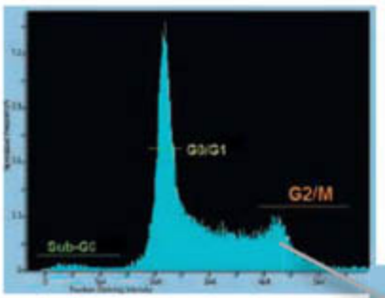

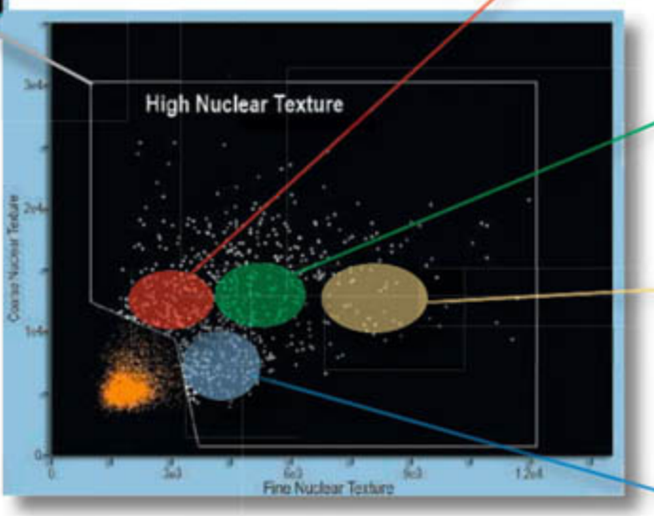

HLA60 cells were labeled with AF488 anti-HLA to reveal the cell membrane and with DRAQ5™ to stain the nucleus. Labeled cells were analyzed on the ImageStream system. The DNA content histogram (above) cleanly separates the major cell cycle subpopulations. G2/M cells were plotted (right) to display the high nuclear texture fraction, from which cells in the progressive stages of mitosis were identified and highlighted on the plot. Composite cell images (far right) show HLA and nuclear staining.

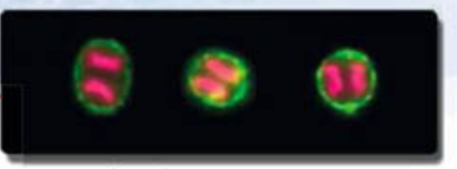

Anaphase

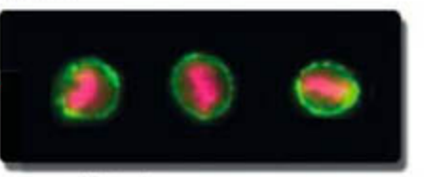

Metaphase

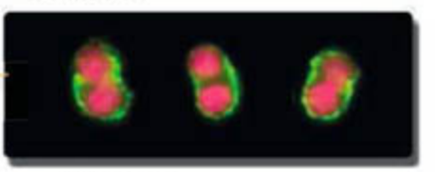

Telophase

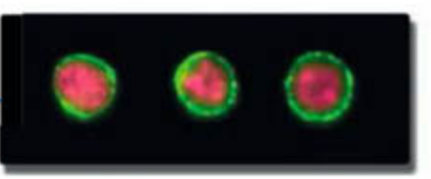

Prophase

For over 30 years, flow cytometry has been about the dots. But behind every dot is a cell, rich in morphological complexity. Now, the ImageStream imaging flow cytometer from Amnis makes this wealth of biological information directly accessible. By combining quantitative microscopy and the statistical power of flow cytometry in a single platform, the ImageStream offers you completely new options for cell analysis.

Study the intracellular distribution of markers, analyze interactions between cells, quantitate subtle morphologic changes in the cell and its structures, and much more. The range of applications is extensive, as is the growing list of published science.

While we can't guarantee that every experiment you do with the ImageStream system will turn into a publication, we do guarantee that when you analyze your cells on the ImageStream you will see more -- and know more -- than you ever thought possible.

To learn more, visit www.amnis.com or call 800-730-7147 toll-free in the US or +1 206-374-7000 outside the US.

ImageStream. Think outside the dot.

amnis®